

PE&RS

September 2021

Volume 87, Number 9

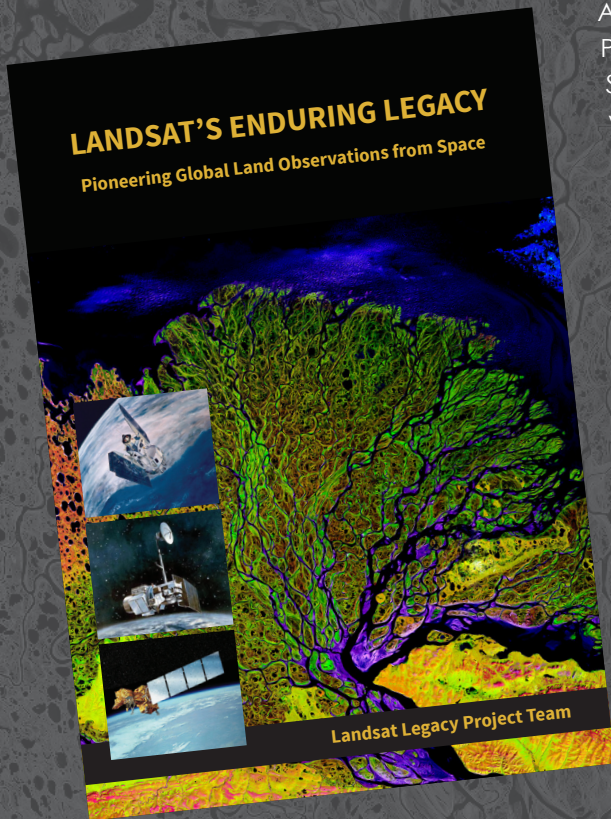
The official journal for imaging and geospatial information science and technology

PHOTOGRAMMETRIC ENGINEERING & REMOTE SENSING



LANDSAT'S ENDURING LEGACY

PIONEERING GLOBAL LAND OBSERVATIONS FROM SPACE



After more than 15 years of research and writing, the Landsat Legacy Project Team is about to publish, in collaboration with the American Society for Photogrammetry and Remote Sensing (ASPRS), a seminal work on the nearly half-century of monitoring the Earth's lands with Landsat. Born of technologies that evolved from the Second World War, Landsat not only pioneered global land monitoring but in the process drove innovation in digital imaging technologies and encouraged development of global imagery archives. Access to this imagery led to early breakthroughs in natural resources assessments, particularly for agriculture, forestry, and geology. The technical Landsat remote sensing revolution was not simple or straightforward. Early conflicts between civilian and defense satellite remote sensing users gave way to disagreements over whether the Landsat system should be a public service or a private enterprise. The failed attempts to privatize Landsat nearly led to its demise. Only the combined engagement of civilian and defense organizations ultimately saved this pioneer satellite land monitoring program. With the emergence of 21st century Earth system science research, the full value of the Landsat concept and its continuous 45-year global archive has been recognized and embraced. Discussion of Landsat's future continues but its heritage will not be forgotten.

The pioneering satellite system's vital history is captured in this notable volume on Landsat's Enduring Legacy.

Landsat Legacy Project Team

Samuel N. Goward
Darrel L. Williams
Terry Arvidson
Laura E. P. Rocchio
James R. Irons
Carol A. Russell
Shaida S. Johnston

Landsat's Enduring Legacy

Hardback, 2017, ISBN 1-57083-101-7

Student	\$60*
Member	\$80*
Non-member	\$100*

* Plus shipping

SAVE 40%

VISIT THE ASPRS BOOKSTORE at ASPRS.ORG

ANNOUNCEMENTS

North Dakota Department of Transportation recently acquired a **GeoCue True View 640 3D Imaging System (3DIS®)** for their UAS program. GeoCue's True View 3D Imaging Sensors allow for both drone lidar and imagery to be collected in a single flight on most UAS platforms. The simultaneous data collection, bundled fusion processing software and data management package offers a fully integrated solution giving NDDOT a significant advantage over traditional lidar/camera systems as they can single-pass collect, process, and deliver high quality fused 3D data without leaving the True View ecosystem.

NDDOT's UAS Program is responsible for conducting small Unmanned Aircraft System (sUAS) surveys for the design and construction of highways and bridges, asset management and natural disaster survey/monitoring across the state. The State of North Dakota's use of this cutting-edge technology will facilitate ongoing sUAS projects to help the department gather important analytic data.

Examples of derived products from the True View 3DIS include colorized 3D point clouds, breakline enforced 3D models, profiles, cross sections, topographic contours, volumetric analysis, classified ground models and more. These products serve as base data layers for analysis and planning. Bordering state departments of transportation have also acquired GeoCue's 3DIS technology, enabling easy collaboration between state departments on coordination, training, and development of best practices.

NDDOT Representative, Derek Pfeifer, Program Manager - Design Division said, "We are excited that the True View System is now part of the NDDOT UAS program and look forward to its capabilities in the very near future."

"We are very pleased to be selected by NDDOT as their UAS drone lidar/Camera system supplier," said Lewis Graham, President/CTO of GeoCue Group. "The DOTs literally keep America moving and we are honored to be an integral part of that mission."

The URISA Exemplary Systems in Government (ESIG) awards were first presented in 1981 to recognize outstanding achievement by government agencies in the use of geospatial information technology. This exemplary achievement is defined as the effective application of geospatial technologies and data that result in improved government service delivery and increased benefits to citizens. The award competition is international in nature and open to all public agencies at the local, regional, state/provincial and federal levels.

Since their commencement 40 years ago, the ESIG awards have gained considerable prestige and there is always substantial publicity given to the winning systems – both by URISA as well as the nominating jurisdictions concerned. In many cases, the awards have been the key to enabling further budget support to be provided for the systems, as well as in-house acknowledgment and acceptance of their excellence.

Nominations are made in one of two categories: Enterprise Systems which are used by multiple agencies, and Single Process Systems which are used by one agency. Nominations are required to address specific award criteria associated with system design and implementation, organizational impact and use of resources to create the system. The number of nominations received varies from year to year and in 2021 a total of nine nominations were received. Four entries were received in the Single process category and five were received in the Enterprise Systems category.

A volunteer ESIG Awards Committee is formed each year to handle the entry judging tasks and this year there were 15 people serving on the committee. They were: Dr Gary Hunter (chair); Patrick Baber; Eva Cancino; Nicole Dogan; Mike Edelson; Dianne Haley; Steve Holmes; Ian Kidner; Asher McNicol; John Nerge; Rachel Parrinello; Curtis Pulford; Carolynne Saxton; Michael Shean and Alice Wilson. URISA extends its thanks to the committee members for the time and effort they have put into the judging of this year's ESIG submissions.

The 2021 ESIG Awards winners are:

Single Process Systems

- Winner: Arizona Department of Environmental Quality: "Mobile Compliance Inspections for Waste Programs." Submitted by Julie Mikolajczyk, GIS Manager, Arizona Department of Environmental Quality, Phoenix, Arizona.
- Distinguished System: Commonwealth of Virginia 9-1-1 & Geospatial Services Bureau, Virginia Department of Emergency Management: "Virginia's Next Generation 9-1-1 Dashboard." Submitted by Matthew Gerike, PhD, GISP, Geospatial Program Manager, Commonwealth of Virginia 9-1-1 & Geospatial Services Bureau, Virginia Department of Emergency Management, North Chesterfield, Virginia.
- Distinguished System: Stark County, Ohio: "Restart Stark." Submitted by Skyler Dewey, GISP, GIS Team Lead, Stark County, Canton, Ohio.

Enterprise Systems

- Winner: United States Virgin Islands: "United States Virgin Islands GIS Division Territorial GIS Platform & Applications." Submitted by L. Christopher George, GIS Administrator, Office of Lt. Governor, United States Virgin Islands GIS Division, St. Thomas, USVI.
- Distinguished System: North Carolina Department of Transportation: "Project ATLAS – Advancing Transportation through Linkages, Automation and Screening." Submitted by Leilani Paugh, Environmental Program Manager, Division of Highways, North Carolina Department of Transportation, Raleigh, North Carolina.
- Distinguished System: Raleigh-Durham Airport Authority: "RDU's GeoPortal." Submitted by Kristin Johnston, GISP, GIS Administrator, Raleigh-Durham Airport Authority, Morrisville, North Carolina.

UP42 has signed an agreement with HEAD Aerospace of Beijing to make image data from more than 40 innovative Chinese Earth Observation satellites available on the UP42 marketplace. The broad selection of imaging capabilities from the constellations dramatically expands the range of applications in multiple sectors, with the most significant benefits expected in Infrastructure, Transportation, Utilities, Agriculture, Government.

The UP42 marketplace currently contains more than 50 geospatial data sets, including satellite imagery from six international organizations. The newly added satellites' diverse and often unique imaging capabilities include wide-swath imaging at very high resolution, nighttime acquisitions, frequent intraday revisits, tri-stereo collection, and hyperspectral imaging.

"This partnership is an important milestone for us as a company but, more importantly, for our customers. By diversifying our data sets, we are unlocking a broader spectrum of use cases for our users in multiple sectors. This is the true meaning of 'democratizing access to Earth insights,'" said UP42 CEO Sean Wiid.

HEAD Aerospace is the international distributor of satellite imagery collected by commercial Earth Observation missions. The UP42-HEAD agreement includes imagery from multiple constellations, including SuperView, Earthscanner, Gaofen-7, DailyVision, NightVision, Hyperscan, and Tri-Stereo ZY3. These seven constellations will total more than 80 satellites by the end of 2021.

"Sharing a similar approach facilitating users' easy access to an agnostic data source by a centralized portal with a wide choice of satellite attributes, we are glad to have partnered with UP42. This partnership represents another new milestone for us in expanding our global network." said Kammy Brun, Managing Director of HEAD Aerospace.

While each satellite constellation was designed with one or more imaging specialties, a remarkable variety of operational capabilities are shared across the constellations to support numerous applications and industries.

HawkEye 360 Inc. announced the successful launch of its Cluster 3 radio frequency geolocation microsattellites built by Space Flight Laboratory (SFL). Carried aboard the June 30 SpaceX Transporter 2 mission, the Cluster 3 formation-flying microsattellites join in orbit the HawkEye 360 Cluster 2 and Cluster 1 Pathfinder satellites – all built by SFL.

The HawkEye 360 launch brings to 20 the total number of

SFL satellites placed into orbit in less than a year. The Cluster 3 satellites were built on SFL's space-proven 30-kg DEFIANT microsattellite bus.

"SFL congratulates HawkEye 360 on developing the world's first commercial satellite constellation for radio frequency (RF) signal intelligence," said SFL Director Dr. Robert E. Zee. "Contact has been made with all three Cluster 3 microsattellites. They are healthy and undergoing commissioning."

The HawkEye 360 Constellation detects and geolocates RF signals for maritime situational awareness, emergency response, national security, and spectrum analysis applications. Cluster 3 significantly expands HawkEye 360's global revisit and collection capacity, stated the Herndon, Va., company.

HawkEye 360 selected SFL due to the importance of formation flying by multiple satellites for successful RF geolocation. SFL is the acknowledged leader in developing and implementing high-performance attitude control systems that make it possible for relatively low-cost nanosatellites and microsattellites to fly in stable formations while in orbit.

The previous HawkEye 360 satellite clusters built by SFL were the Pathfinder launched in 2018 and Cluster 2 in January 2021. Each Cluster is comprised of three satellites.

Other launches of SFL-built satellites in just the past year include missions developed for the Norwegian Space Agency (NOSA) in Norway, the Dubai-based Mohammed Bin Rashid Space Centre (MBRSC) in the United Arab Emirates, GHGSat Inc. of Canada, Space-SI of Slovenia, and a Canada-based telecommunications company.

SFL is a unique microspace provider that offers a complete suite of nano-, micro- and small satellites – including high-performance, low-cost CubeSats – that satisfy a broad range of mission types from 3 to 500 kilograms. SFL's heritage of on-orbit successes includes 72 satellites and distinct missions related to Earth observation, atmospheric monitoring, ship tracking, communication, technology demonstration, space astronomy, solar physics, space plasma, and other scientific research.

Since 1998, SFL has developed CubeSats, nanosatellites, and microsattellites that have achieved more than 150 cumulative years of operation in orbit. These microspace missions have included SFL's trusted attitude control and, in some cases, formation-flying capabilities. Other core SFL-developed components include modular (scalable) power systems, on-board radios, flight computers, and control software.

CALENDAR

- 3-6 October, **GIS-Pro 2021**, Baltimore, Maryland. For more information, visit www.urisa.org/gis-pro.
- 27-28 October, 7th International Conference on Engineering and Emerging Technologies, Istanbul, Turkey. For more information, visit www.iceet.net.
- 8-12 November, **URISA GIS Leadership Academy**, St. Petersburg, Florida. For more information, visit www.urisa.org/education-events/urisa-gis-leadership-academy/.
- 14-18 December, **30th International Cartographic Conference & International Cartographic Exhibition**, Florence, Italy. For more information, visit <https://icaci.org/icc2021>.



597 Photogrammetry and Electrical Resistivity Tomography for the Investigation of the Clandestine Graves in Colombia

By Jonathan Drake, Carlos Martín Molina, Edier Fernando Avila, and Alejandra Baena

SECTORINSIGHT. *edu*

606 SectorInsight.edu— Making a Difference in a Developing Country—One Student at a Time

COLUMNS

- 605 GIS Tips & Tricks—Another Trick with “Hot-Keys”
- 606 SectorInsight.edu—Making a Difference in a Developing Country—One Student at a Time
- 609 Grids and Datums Update
This month we look at the United Kingdom

ANNOUNCEMENTS

- 608 New ASPRS Members
Join us in welcoming our newest members to ASPRS.
- 613 In Memoriam—John Dwyer
- 614 Headquarters News

DEPARTMENTS

- 593 Industry News
- 594 Calendar
- 682 In-Press *PE&RS* Articles
- 683 Who’s Who in ASPRS
- 684 ASPRS Sustaining Members

615 Gaussian Mixture Model of Ground Filtering Based on Hierarchical Curvature Constraints for Airborne Lidar Point Clouds

Longjie Ye, Ka Zhang, Wen Xiao, Yehua Sheng, Dong Su, Pengbo Wang, Shan Zhang, Na Zhao, and Hui Chen

This article proposes a Gaussian mixture model of a ground filtering method based on hierarchical curvature constraints.

631 Detecting Geo-Positional Bias in Imagery Collected Using Small UASs

Jonathan B. Thayne, Aaron M. Paque, and Megan C. Maher

In this article, statistical methods for detecting bias in global positioning system (GPS) error are presented and applied to imagery collected using three common unmanned aerial systems (UASs).

639 Double Adaptive Intensity-Threshold Method for Uneven Lidar Data to Extract Road Markings

Chengming Ye, Hongfu Li, Ruilong Wei, Lixuan Wang, Tianbo Sui, Wensen Bai, and Pirasteh Saied

Due to the large volume and high redundancy of point clouds, there are many dilemmas in road-marking extraction algorithms, especially from uneven lidar point clouds. To extract road markings efficiently, this article presents a novel method for handling the uneven density distribution of point clouds and the high reflection intensity of road markings.

649 Estimating Regional Soil Moisture with Synergistic Use of AMSR2 and MODIS Images

Majid Rahimzadegan, Arash Davari, and Ali Sayadi

Soil moisture content (SMC), product of Advanced Microwave Scanning Radiometer 2 (AMSR2), is not at an adequate level of accuracy on a regional scale. This article introduces a simple method to estimate SMC while synergistically using AMSR2 and Moderate Resolution Imaging Spectroradiometer (MODIS) measurements with a higher accuracy on a regional scale.

661 Optimal Regularization Method Based on the L-Curve for Solving Rational Function Model Parameters

Guoqing Zhou, Man Yuan, Xiaozhu Li, Hongjun Sha, Jiasheng Xu, Bo Song, and Feng Wang

Rational polynomial coefficients in a rational function model (RFM) have high correlation and redundancy, especially in high-order RFMs, which results in ill-posed problems of the normal equation. For this reason, this article presents an optimal regularization method with the L-curve for solving rational polynomial coefficients.

669 Scene-Change Detection Based on Multi-Feature-Fusion Latent Dirichlet Allocation Model for High-Spatial-Resolution Remote Sensing Imagery

Xiaoman Li, Yanfei Zhong, Yu Su, and Richen Ye

With the continuous development of high-spatial-resolution ground observation technology, it is now becoming possible to obtain more and more high-resolution images, which provide us with the possibility to understand remote sensing images at the semantic level. Compared with traditional pixel- and object-oriented methods of change detection, scene-change detection can provide us with land use change information at the semantic level, and can thus provide reliable information for urban land use change detection, urban planning, and government management. Most of the current scene-change detection methods are based on the visual-words expression of the bag-of-visual-words model and the single-feature-based latent Dirichlet allocation model. In this article, a scene-change detection method for high-spatial-resolution imagery is proposed based on a multi-feature-fusion latent Dirichlet allocation model.

See the Cover Description on Page 596

COVER DESCRIPTION

Communities in Germany, Belgium, and The Netherlands are reeling after extreme July rainfall swamped parts of Western Europe. Some of the worst-hit areas saw as much as two months of rain within 24 hours—enough to break precipitation records, push rivers to new heights, and trigger devastating flash floods.

Nighttime downpours on July 14-15, 2021, proved especially damaging. Many people were asleep when the most intense rain fell, and they were caught off guard as rivers raged, dams failed, and floodwaters inundated homes. News media estimated that 196 people were killed by flooding and thousands more were injured. Hundreds of people are still listed as missing.

On July 18, 2021, the Operational Land Imager (OLI) on Landsat 8 captured this image of flooding along the Meuse and Roer rivers. As water levels rose, nearly 5,000 people were forced to evacuate from Roermond, a city in The Netherlands near the border with Germany. A dam breach on the Roer contributed to the extensive flooding.

While it will take some time for experts to analyze whether this event was influenced by human-caused global warming, scientists have amassed data showing that warming has led to more intense and frequent downpours in many parts of the world. Some researchers and meteorologists have also suggested that warming may be changing the jet stream in ways that make atmospheric “blocking” patterns—like the one that prolonged these downpours—more likely.

For more information and to compare the image acquired on June 16 2021 to this one, visit <https://landsat.visibleearth.nasa.gov/view.php?id=148598>.

NASA Earth Observatory images by Lauren Dauphin, using Landsat data from the U.S. Geological Survey. Story by Adam Voiland.



PHOTOGRAMMETRIC ENGINEERING & REMOTE SENSING

JOURNAL STAFF

Publisher ASPRS

Editor-In-Chief Alper Yilmaz

Assistant Director — Publications Rae Kelley

Electronic Publications Manager/Graphic

Artist Matthew Austin

Photogrammetric Engineering & Remote Sensing is the official journal of the American Society for Photogrammetry and Remote Sensing. It is devoted to the exchange of ideas and information about the applications of photogrammetry, remote sensing, and geographic information systems. The technical activities of the Society are conducted through the following Technical Divisions: Geographic Information Systems, Photogrammetric Applications, Lidar, Primary Data Acquisition, Professional Practice, and Remote Sensing Applications. Additional information on the functioning of the Technical Divisions and the Society can be found in the Yearbook issue of *PE&RS*.

Correspondence relating to all business and editorial matters pertaining to this and other Society publications should be directed to the American Society for Photogrammetry and Remote Sensing, 425 Barlow Place, Suite 210, Bethesda, Maryland 20814-2144, including inquiries, memberships, subscriptions, changes in address, manuscripts for publication, advertising, back issues, and publications. The telephone number of the Society Headquarters is 301-493-0290; the fax number is 225-408-4422; web address is www.asprs.org.

PE&RS. *PE&RS* (ISSN0099-1112) is published monthly by the American Society for Photogrammetry and Remote Sensing, 425 Barlow Place, Suite 210, Bethesda, Maryland 20814-2144. Periodicals postage paid at Bethesda, Maryland and at additional mailing offices.

SUBSCRIPTION. For the 2021 subscription year, ASPRS is offering two options to our *PE&RS* subscribers — an e-Subscription and the print edition. E-subscribers can plus-up their subscriptions with printed copies for a small additional charge. Print and Electronic subscriptions are on a calendar-year basis that runs from January through December. We recommend that customers who choose both e-Subscription and print (e-Subscription + Print) renew on a calendar-year basis.

The rate of the e-Subscription (digital) Site License Only for USA and Non-USA is \$1000.00 USD. e-Subscription (digital) Site License Only for Canada* is \$1049.00 USD. e-Subscription (digital) Plus Print for USA is \$1365.00 USD. e-Subscription (digital) Plus Print for Canada* is \$1424.00 USD. e-Subscription (digital) Plus Print for Non-USA is \$1395.00 USD. Printed-Subscription Only for USA is \$1065.00 USD. Printed-Subscription Only for Canada* is \$1124.00 USD. Printed-Subscription Only for Non-USA is \$1195.00 USD. *Note: e-Subscription/Printed-Subscription Only/e-Subscription Plus Print for Canada include 5% of the total amount for Canada's Goods and Services Tax (GST #135123065). **PLEASE NOTE: All Subscription Agencies receive a 20.00 USD discount.**

POSTMASTER. Send address changes to *PE&RS*, ASPRS Headquarters, 425 Barlow Place, Suite 210, Bethesda, Maryland 20814-2144. CDN CPM # (40020812)

MEMBERSHIP. Membership is open to any person actively engaged in the practice of photogrammetry, photointerpretation, remote sensing and geographic information systems; or who by means of education or profession is interested in the application or development of these arts and sciences. Membership is for one year, with renewal based on the anniversary date of the month joined. Membership Dues include a 12-month electronic subscription to *PE&RS*. Or you can receive the print copy of *PE&RS* Journal which is available to all member types for an additional fee of \$60.00 USD for shipping USA, \$65.00 USD for Canada, or \$75.00 USD for international shipping. Dues for ASPRS Members outside of the U.S. will now be the same as for members residing in the U.S. Annual dues for Regular members (Active Member) is \$150.00 USD; for Student members \$50.00 USD for USA and Canada \$53.00 USD; \$60.00 USD for Other Foreign members. A tax of 5% for Canada's Goods and Service Tax (GST #135123065) is applied to all members residing in Canada.

COPYRIGHT 2021. Copyright by the American Society for Photogrammetry and Remote Sensing. Reproduction of this issue or any part thereof (except short quotations for use in preparing technical and scientific papers) may be made only after obtaining the specific approval of the Managing Editor. The Society is not responsible for any statements made or opinions expressed in technical papers, advertisements, or other portions of this publication. Printed in the United States of America.

Be a part of ASPRS Social Media:



facebook.com/ASPRS.org



linkedin.com/groups/2745128/profile



twitter.com/ASPRSoorg



youtube.com/user/ASPRS



PHOTOGRAMMETRY AND ELECTRICAL RESISTIVITY TOMOGRAPHY FOR THE INVESTIGATION OF THE CLANDESTINE GRAVES IN COLOMBIA

Jonathan Drake, Carlos Marín Molina, Edier Fernando Avila, and Alejandra Baena

Photogrammetric Engineering & Remote Sensing
Vol. 87, No. 9, September 2021, pp. 597–604.
0099-1112/21/597–604

© 2021 American Society for Photogrammetry
and Remote Sensing

doi: 10.14358/PERS.87.9.597

INTRODUCTION

Forced disappearances are a serious crime against humanity. A forced disappearance consists of the deprivation of liberty of an individual and the refusal to recognize or give information related to their whereabouts (CED, 2017; MP, 2020). Presently, Colombia has approximately 100,000 missing people, among which, 26,000 are forced disappearances. It is assumed that most, probably about one-half, are related to armed conflicts in Colombia between the government and guerrilla and paramilitary groups (INML, 2020). Unfortunately, the primary sources of information in Colombia contain conflicting data; therefore, it is possible that there are more missing people than reported in databases. (RUV, 2020; INML, 2020).

Located in the central-eastern region of Colombia, the Casanare Province was one of the many zones strongly impacted by armed conflicts. Probably more than 150 people were forced to disappear from Chámeza and Recetor, two small towns in the southwest area of the Casanare Province. These disappearances were from 2002-2003 and attributed to one of the illegal armed groups in Colombia. These groups are well known as Paramilitaries or the United Self Defense of Casanare (AUC, by its Spanish abbreviation) (EQUITAS, 2015). Until now, the remains of only 14 forced disappearances have been found and returned to their families. The main causes of these disappointing numbers are the lack of integrated information and the non-sophisticated search methods that are being employed in the process of finding victims (FGN, 2020).

Presently, Colombia is in a peace process to end the armed conflict with the Revolutionary Armed Forces of Colombia (FARC-EP), complying with the peace agreement signed in 2016. During the peace negotiation process, access to the truth was a crucial step for the reparation to the victims. This was an important step towards justice after the conflict (OACP, 2020). Consequently, finding the victims contributes to the reparation process. To investigate human rights infringement in Chámeza and Recetor, a non-profit association, EQUITAS, an independent forensic team, developed a strategic regional plan to aid in the search for victims. This plan, Predictive Spatial and Statistical Modelling (MESP, by its Spanish abbreviation), produced a predictive heatmap model that indicated the areas with the highest probability to find clandestine graves (EQUITAS, 2015).

To take advantage of the information provided by MESP and accomplish our goal properly, it was important that a field procedure was developed prior to starting a controlled excavation. This procedure included several types of analyses: surface geomorphology changes, soil

type, visual observation of the vegetation variations and near-surface geophysics (Ruffell and McKinley, 2014). In the process of investigating, there are a variety of geophysical methods that can be used. Ground Penetrating Radar GPR, the most commonly used in forensic search, has several limitations related to environmental features such as soil moisture, waterlogged, clayrich (Pringle et al., 2012). In our case studies, the zones with wooded topography and difficult terrain access were not suitable for GPR. Therefore, Electrical Resistivity Tomography (ERT) was evaluated as a more reliable method in this investigation. ERT is a near-surface geophysical method and permits surveying in wooded terrain. Furthermore, it has been widely used for the detection of clandestine graves (Pringle et al., 2012), ancient burials (Dick et al., 2015) and controlled experiments (France et al., 1992).

ERT is based on the application of an electric current penetrating into the ground to measure the intensity of the electric resistivity generated in the response. We were able to obtain information on the electric resistivity properties of the analyzed material, passing an electrical current and applying Ohm's law ($R = V/I$) where R is the electrical resistance, V is the potential difference between the electrodes and I the current intensity. The use of ERT as a complement to other geophysical methods has been very useful in various applications, such as water search, plume detection, location of leaks, soil study in agriculture and determination of geological strata.

Given the above, a multidisciplinary approach has been proposed using modeling and high-resolution techniques to study the cases in Casanare Colombia (Molina et al., 2019). This integration of technologies guarantees the appropriate scientific methodology is used to assist the investigators in Colombia in finding missing people (Brilis, 2001; Grip et al., 2000). Furthermore, it could be very advantageous to start with a large-scale method such as, remote sensing and photogrammetry, before the near-surface method. Doing this could offer digital support to the preliminary visual observations and allows for the appropriate fieldwork planning.

Geospatial information is a useful tool for field researchers, and over the past decade has been employed extensively in human rights research. Along with traditional data products such as maps, photographs, and field sketches, remotely-sensed data in the form of satellite imagery has increasingly been a key component of this research. This is due to remotely-sensed data ability to provide information about remote, dangerous, or otherwise inaccessible locations (AAFS, 2013; Marx and Goward, 2013). With a ground sample distance of 30 centimeters per pixel even the highest-resolution commercial satellite

imagery is limited when the subject of interest is on the scale of individual clandestine burials. In places like Colombia the difficulties associated with this data product are further compounded by local factors such as frequent cloud cover, and/or the presence of continuous forest canopy. In situations like these, however, many of the difficulties associated with satellite imagery can be overcome by conducting photogrammetric mapping on-site.

The use of photogrammetry to enhance field research has already proven useful in a number of fields, including geology, civil engineering, and city planning (Shugar et al., 2017). Additional applications of these tools have also emerged in the fields of archaeology where they have been useful in reconstructing damaged cultural heritage sites, and in law enforcement where they have supplemented the traditional role of the crime-scene photographer in preserving evidence (Al-Ruzouq et al., 2012). While these latter applications are in many ways similar to the documentation of clandestine grave sites in the human rights context, multi-image photogrammetry has yet to be applied to this type of investigation.

In the context of research on clandestine graves, photogrammetry has the potential of benefiting investigations in three primary ways: by providing field researchers with enhanced situational awareness; by facilitating the identification of potential burial sites; and by enhancing the documentation of gravesites once they have been discovered. Traditionally, satellite imagery has been used in the first and second roles, however as mentioned above, its use is limited by weather, tree cover, and resolution. Therefore, its usefulness in investigations is often limited to the very largest of gravesites or providing historical or contemporary context about the surrounding terrain. The output of photogrammetry may be able to transcend these limitations. For example, when the input images contain geotags in their EXIF data, which many GPS-enabled cameras generate automatically, the processing software can use this information to produce fully georeferenced orthomosaics and digital surface models (DSMs) with significantly higher resolution than comparable satellite data.

This article presents the study of two places of interest to detect graves and find missing people in Casanare Colombia. It was organized as follows: Materials and Methods describes the features of the zones of interest we studied and the methodologies used to study and explore these sites. Results presents the results from the multidisciplinary approach with focus on clandestine graves detection. Discussion and Perspectives expounds the advantages and limitations of the reported methodologies and techniques for this kind of human rights projects.

MATERIALS AND METHODS

Study Sites

Chámeza Zone

The first study site determined by MESP is located at an altitude of 2018 meters above sea level with coordinates $5.0^{\circ} 8.0' 4.4''$ N and $72^{\circ} 51' 2.0''$ E. The San José Mountain Ridge is at this location. Due to the steep, densely wooded terrain and lack of roads access is difficult and the only practical means of accessing the site is via pack horse or mule train using a narrow, winding path. The topography is undulating, covered with dense vegetation and many rock fragments as shown in Figure 1a. The environment is a humid tropical forest with predominately clay soil.

To begin the search, first the ground zone was evaluated. Observations of the soil showed the presence of extensive leaf litter of between 0.1m to 0.15m in thickness, which was necessary to remove before the use of ERT. This was done to establish good contact of the ERT electrodes with the ground. The soil presents a black color for the first 0.1m of depth, which indicates the presence of organic matter. Below this, a second stratum of 0.1m to 0.2m in thickness, exhibited gray color. This was in turn underlaid by yellow clay. In Figure 1b, a picture of an ERT line at the location is presented.



Figure 1. The study site in the Chameza Zone. a) The place indicated by the families of the victims as a possible location of interest; b) ERT line within the search area.

Receptor Zone

The second area of interest identified by MESP is located at an altitude of 1658 meters above sea level with coordinates $5.0^{\circ} 9.0' 46''$ N and $72^{\circ} 55' 24''$ E. This specific site is known as Tequita Alta, and referred to as “The School” by the local inhabitants due to its former use as a training camp for illegal armed groups. This site is illustrated in Figure 2a. Access to this site was less difficult than Chámeza and motorized transport was possible, although the roads are unpaved. The landscape presented smooth slopes with “isolated” vegetation. The methods used to conduct the initial search were the same as at Chámeza. Figure 2b, shows the electrical resistivity tomography ERT GEOAMP 202 in the location where animal bones were found.



Figure 2. The study site in the Recetor Zone. a) Topography at the area of interest in Recetor. b) Electrical Resistivity Tomography (ERT) with GEOAMP 202 equipment at the site where a grave containing animal bones was found.

Photogrammetry

Alongside ERT, this investigation attempted to apply both air and ground-based photogrammetry to the two sites of interest, which were selected by MESP as having the highest probabilities of finding the remains of missing people. The first goal of the investigation was to evaluate the technique's usefulness as a tool for enhancing the situational awareness of field researchers conducting forensic investigations in rugged, unfamiliar terrain.

The Recetor Zone called Teguita Alta 1, and Teguita Alta 2, consisted of open fields, which allowed the mapping to be conducted using UAS. At these sites, a stock DJI Phantom 4 was used for this purpose. The UAS was controlled using a tablet computer attached to its remote-control unit, which allowed for automated flight with the possibility of manual intervention at any time. Two different applications were used to upload flight plans to the aircraft, Pix4DCapture and DroneDeploy. Both Pix4DCapture and Drone Deploy would normally rely on internet access to retrieve online maps to facilitate the process of defining the survey area. As no connectivity was available at the sites, the area was defined using a laser rangefinder and, where possible, by walking the perimeter of the site while holding the tablet, thereby establishing its boundaries using the tablet's built-in GPS.

The survey flights were conducted under computer control, without direct pilot input except in case of emergency. In order to ensure that the UAS would not be in danger of encountering any obstacles during these autonomous flights, a manual test flight was conducted prior to each survey flight. This test flight established the minimum altitude at which the aircraft could safely fly without encountering trees, terrain, or other obstructions. The final parameter of the flight involved defining the exact path followed by the UAS. The flight over the first site, conducted using DroneDeploy, was defined as a single-grid mission followed by a single circular orbit of the site. For the second site, controlled by Pix4DCapture, a double-grid mission was flown, in which the flight path consisted of overlapping grid paths, rotated at ninety degrees to one-another. At both sites, the amount

of visual overlap between subsequent images was defined as 80%. Whenever possible, the area to be mapped was cleared of personnel prior to each flight to minimize the potential for error caused by motion in the scene. When this was not possible, everyone in the mapped area was asked to remain still.

The San José site in the Chameza Zone was located under dense forest canopy, on the side of a north-south facing hill slope where dense vegetation precluded the automated flight of the UAS. Manual flight, while possible, was deemed too risky due to the potential for crashing the UAS. For this reason, mapping at this site was performed on the ground using a Canon 6D Digital Single-Lens Reflex Camera with a Sigma 8mm circular fisheye lens; the camera's built-in GPS provided geolocation data. This lens provided a 180-degree field of view, which allowed for the maximum possible amount of overlap between successive images. The mapping proceeded on foot in an over-lapping grid pattern, with the first pass covering the site through a series of traverses in an east-west direction at right angles to the slope, followed by a second series that covered the site via traverses in a north-south direction. Photographs were taken at approximately one-meter intervals, though the pattern often diverged from a perfect grid due to the practical considerations associated with navigating the uneven terrain on foot. The locations of the images acquired at this site are shown in Figure 3a.

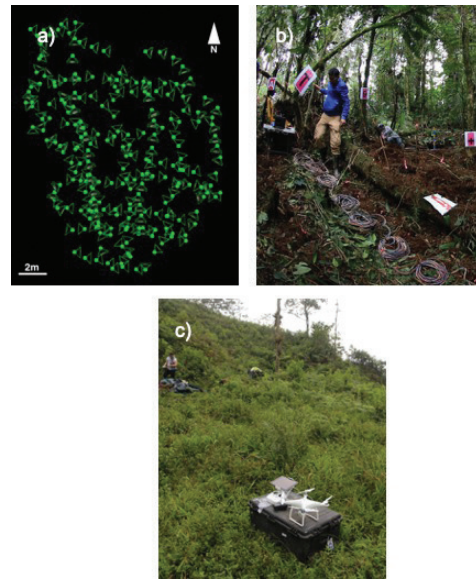


Figure 3. Photoogrammetry at San Jose. a) Locations of images acquired; the pattern of overlapping grids is crude, but visible. b) Photograph showing the alignment markers used to facilitate 3-D reconstruction, as well as the challenges of overhanging vegetation. c) The DJI Phantom UAS used for conducting aerial mapping.

Due to the high level of visual complexity associated with the jungle terrain, the similarity of many features (e.g., leaves, tree branches, etc.), as well as the frequent rain showers, it was considered highly likely that automated matching of the images would fail. In order to correct for this, large color-coded alphanumeric markers were placed on the sides of trees and logs at a variety of elevations throughout the site

to provide unique, easily identifiable 3-D reference points during processing, as shown in Figure 3b. Although these markers were placed at high density throughout most of the study area, in order to evaluate whether it was possible to use natural features as manual tie-points in this type of terrain, none were placed in the northeast quadrant of the study area.

Once collected, the data was downloaded and processed using Pix4D Desktop. For UAS flights, the default processing parameters for 3-D mapping produced good results from automatic image alignment. The adjustment process gave a maximum of only 2.5 percent of images uncalibrated; it was because there was no overlap of the edge of the images, which primarily corresponds to outside the study area where the images included a significant presence of trees. As expected, for the ground-based mapping, automatic image alignment was far less successful. As a result, the images were manually calibrated with one another using the alphanumeric markers described above. Following this manual process, 221 out of 236 images were correctly calibrated. Since total station or survey-grade GPS was not available at the three sites, ground control points, used to improve the geolocation data generated by the cameras onboard GPS, were not available. Instead, Pix4D's "scale and orient" tool was used to adjust the size and rotation of the model by referencing stakes and measurement tapes that had been placed on the ground in the field site for this purpose. The 15 images that failed to calibrate even after manual matching were located almost exclusively in the northeast quadrant where artificial references had been deliberately omitted. The calibrated images were then processed into a 3-D point cloud using Pix4D's standard matching algorithm. The resulting point cloud contained a large number of points that corresponded to overhanging vegetation, and which interfered with interpretation of the scene. In order to simplify the resulting model, the point cloud was manually edited to remove features that were not of interest to the investigation, including branches, leaves, and other elements that had the potential of obscuring the surface of the terrain in the final mosaic. The lower ends of tree trunks, however, were preserved, as were logs already on the ground, because both of these are part of the landscape and can serve as useful reference points should the model be used to guide subsequent investigations. The edited point cloud was then processed into a 3-D model using a custom set of processing parameters that maximized the number of triangles in the completed mesh.

Geophysics

There is little existing literature on applying forensic geophysical methods to clandestine burials sites in South America (Sagripanti et al., 2013; Molina et al., 2015). The few studies that do exist in this area have shown good results with detecting simulated graves using methods similar to the ones discussed in this article in controlled conditions.

However, the success of these techniques depends on many factors, such as time since burial, burial style, local soil type, vegetation, and the locations climate (Molina et al., 2016). In the current investigation, ERT was used to explore the areas of interest determined by MESP. This method enables the exploration of remote, difficult to access areas with mountainous terrain and challenging environmental conditions as described above (Molina et al., 2013).

Electrical Resistivity Tomography (ERT)

In the study zone, the data were acquired by a GeoAmp 303 electric tomography apparatus using the Wenner method. In Chámeza, the experimental design consisted of eight tomography lines, each being 15.5 m long and separated by 0.5m between successive lines. This configuration was chosen in order to obtain data every 0.30m. Earthimager Software v. 2.4.1 (<https://www.agiusa.com/>) was used to process the data in direct mode.

In the Recetor Zone, only one-line of ERT was made, using the same configuration as in Chámeza. At this site, the results of the line enabled the detection of a grave containing animal bones.

RESULTS

Photogrammetry

The aerial data collected using UAS produced high-quality mosaics and digital elevation models with minimum effort. Ground sample distance in the orthomosaics produced by autonomous flight was approximately 2 cm per pixel, over 10 times better than the best available satellite imagery. After being generated by Pix4D, the 3-D Analyst Toolbox in Esri ArcMap was used to convert the digital surface models (DSMs) into slope maps, which were able to reveal several small depressions and areas of level ground that were not immediately obvious or accessible to the team in the field. These could be promising future targets for investigation using subsurface tomography. Examples of airborne-derived DSMs are shown in Figure 4.

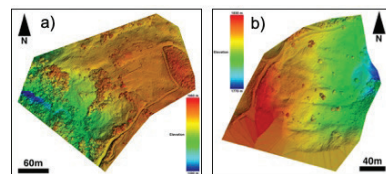


Figure 4. Digital Surface Models derived from UAS imagery. a) Teguita Alta site one and (b) site two.

Following point cloud editing, the 3-D model generated from the ground-based images acquired at San José successfully reproduced the essential features of the landscape, including fallen logs, tomographic equipment, and test pits dug during the course of the fieldwork. At the highest magnification, many areas of this model's texture map were blurry, or contain multiple overlapping "ghosts" of the same feature. This

is likely due to the large number of images that overlap a given point in this model, combined with small errors in the manual image calibration. Nonetheless, features as small as the heads of tomography electrodes are easily distinguishable as such in the model. Based on the dimensions of these features, the model's texture map has an estimated spatial resolution of approximately 0.01 m per pixel. Despite the qualitative fidelity of the 3-D model, however, the orthomosaic generated from the ground-based images contained numerous image artifacts that could not be eliminated using the editing tools available in Pix4D. In order to produce a useful mosaic, the 3-D model, which was not subject to these errors, was viewed in orthographic projection at high magnification. By stitching together multiple vignettes and georeferencing the resulting mosaic according to the model's geolocation data, a more faithful orthomosaic was produced. This output depicts the terrain located beneath the jungle canopy as it appeared during the collection of subsurface tomography data, and can inform the placement of subsequent tomography soundings. An overview of this mosaic is shown in Figure 5a. As described above, the lack of data in the northeast quadrant is due to failed image calibration resulting from a lack of alignment markers in that region. The artifacts associated with the orthomosaic did not extend to the digital surface model derived from the ground-based photography. This output, like the 3-D model, reproduced the contours of the terrain and associated features, as shown in Figure 5b. Measurements conducted on objects of known length within this model show that the geometric corrections applied by the "scale and orient" tools did result in a model that faithfully reproduces their dimensions at a local scale. However, due to the lack of ground control points in this case whether geometric consistency applies over greater distances could not be validated. Similarly, the elevations of the DSM, being solely based on the camera's built-in GPS, may vary significantly from the terrain in an absolute sense.

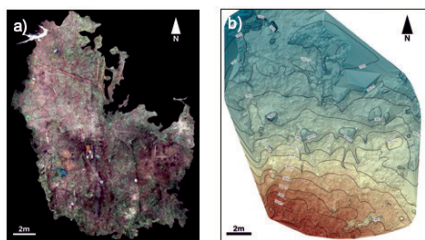


Figure 5. Two views of the San José site. a) Orthomosaic with overhanging vegetation digitally removed and b) digital surface model with elevation contours. Both results were derived from ground-based imagery.

Geophysics

Chámeza

ERT produced eight-lines of tomographic data, each of which show the apparent electrical resistivity along a transect of the area of interest in 2D. Between lines one and two, there is a negative anomaly visible as an area of blue color within the black circle in Figure 6. The rest of the tomography lines did not produce resistivity profiles of any interest.

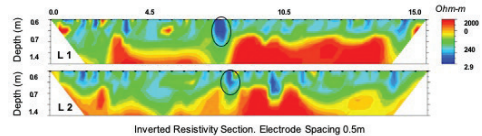


Figure 6. Tomographic data from ERT Lines one and two, which show a negative (blue) anomaly of interest, indicated by a black circle on both transects. The anomaly was attributed to rock fragments found at the corresponding location.

Recetor

The ERT line identified a significant positive anomaly at this location. As a result, a grave 0.60 m x 0.50 m x 1.40 m was detected. Instead of the remains of victims of forced disappearance, however, this grave contained animal bones, as shown in Figure 7. Furthermore, subsequent data processing identified two small additional anomalies (not shown), which could be interesting to verify during the next field season.

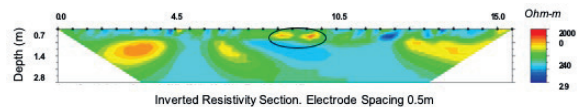


Figure 7. Tomography data from ERT Line. The black circle highlights the positive anomaly related to animal bones found.

DISCUSSION AND PERSPECTIVES

This work demonstrates that photogrammetry, in addition to enhancing the situational awareness of field teams in remote environments, is a powerful and effective tool in facilitating the search for and documentation of gravesites in the context of human rights.

Where the terrain is sufficiently clear of obstacles to allow for automated flight operations, UAS-based photogrammetry can be a valuable tool for providing a broad overview of a site at a resolution significantly higher than the best available satellite imagery. Under dense tree cover, ground-based imagery can also be used for this purpose. However, this method can be time-consuming in both the set-up phase (alignment markers are essential to the technique's success and must be carefully placed beforehand, and low-lying vegetation must be cleared to allow for walking), and the processing phase (the resulting images must be manually aligned and calibrated). Due to the amount of effort necessary to create good results using ground-based photogrammetry in jungle terrain, it therefore cannot be recommended as a tool for surveying a large area. In all cases, confidence in the results of photogrammetric surveys would be significantly enhanced through the use of ground control points to constrain the resulting model. These results would be further improved by using a real-time kinematic (RTK) GPS receiver to calibrate a total station, rather than the handheld units available for this work.

The multidisciplinary approach of integrating geophysics techniques such as ERT alongside photogrammetry using remote sensors is a very important and useful tool for investi-

gators. The possibility of visualizing and locating depressions or subsidence in the area of interest can be consistent with the anomalies identified via ERT; thus, both results together could enable a robust detection of probable locations for a mass grave.

Electrical Resistivity Tomography (ERT) is a recommended geophysical method for searching for clandestine graves in forested or otherwise difficult-to-access areas, which are the features of many places in Colombia. In Chameza and Recetor it was possible to detect anomalies associated with objects buried under the soil such as rock fragments and animals remain; therefore, the findings demonstrate that ERT is a valuable technique when searching for clandestine graves in these particular conditions. Furthermore, its handling will permit access to other wooded zones revealed by MESP and proposed by testimonies from victim's families.

The MESP model is likewise important, as it enables a significant reduction in the search area, and correspondingly, the time spent searching for gravesites. Because of this, such desk-based work is highly important before going out into the field.

Currently, American Association for the Advancement of Science AAAS is exploring a number of applications of this technique that have the potential to increase its value to human rights advocates in the future. One such application involves correlating the orthomosaics generated from modern photogrammetric surveys with declassified US government satellite imagery acquired around the time that many of these graves were suspected to have been dug. Preliminary work suggests it may improve the interpretability of contemporary data by providing relevant historical context. Another application involves using photogrammetry, not just to document remains as they are exhumed in the field, but in the laboratory as well. When the model resulting from these experiments was shared with a professional medical examiner, he indicated that the level of detail was sufficient to come to a forensic conclusion about the remains. In the future, this technique could be an important way of preserving the record of trauma associated with the remains, even after they have been returned to families for re-interment. Such models might even be 3-D printed, so that an accurate physical representation of the remains can be presented in court cases where the remains themselves are no longer accessible.

The potential use of this evidence in court raises another important issue associated with this technique. As an emerging technology that continues to evolve, developing consistent, workable standards and best practices for collecting and analyzing photogrammetric evidence in a legal context will be essential if its use in human rights investigations is to expand beyond the current proof-of-concept as shown in Figure 8a and Figure 8b. To do this, conversations will need to take place among geospatial technologists, forensic scien-

tists, human rights practitioners, lawyers, and members of the judiciary regarding the potential legal implications of the methods used to create these models. Training will necessarily be an important component of these conversations. Through these and similar efforts, the continued exploration of this and other emerging technologies will continue to improve the landscape of human rights practice, and form a core component of the Scientific Responsibility, Human Rights, and Law Program promoted by the American Association of the Advancement of Science. Additionally, fostering and facilitating the responsible practice and applications of science is contributing to the program of the truth, justice, and reparation of victims in the context of the peace agreements in Colombia.



Figure 8. Proof-of-concept for the use of photogrammetry for forensic documentation of human remains in a laboratory context. a) Photograph of a human skull with a traumatic injury; one of a series taken from a stationary camera while the skull rotates on a turntable. b) View of the 3-D model resulting from photogrammetry, enabling measurements of the bullet wound (in this case, 0.017 m), even after the remains are reinterred.

REFERENCES

- AAFS, 2013. Human rights applications of remote sensing. American Association for the Advancement of Science.
- Al-Ruzouq, R. I., Al-Rawashdeh, S. B., Tommalieh, O. A. and Ammar, M. S., 2012. Photogrammetry and gis for three-dimensional modeling of the dome of the rock. *Applied Geomatics* 4(4), pp. 257–267.
- Brilis, G., 2001. Remote sensing tools assist in environmental forensics: part ii—digital tools. *Environmental Forensics* 2(3), pp. 223–229.
- CED, 2017. United nations organization force disappearance group. <https://www.ohchr.org/EN/AboutUs/Pages/WhoWeAre.aspx>.
- Dick, H. C., Pringle, J. K., Sloane, B., Carver, J., Wisniewski, K. D., Haffenden, A., Porter, S., Roberts, D. and Cassidy, N. J., 2015. Detection and characterisation of black death burials by multi-proxy geophysical methods. *Journal of Archaeological Science* 59.
- EQUITAS, 2015. Un radar para encontrarlos. <http://equitas.org.co/blog/mesp-un-radar-para-encontrarlos>.
- FGN, 2020. Fiscalía general de la nación. <https://www.fiscalia.gov.co/colombia/>.
- France, D. L., Griffin, T. J., Swanburg, J. G., Lindemann, J. W., Davenport, G. C., Trammell, V., Armbrust, C. T., Kondratieff, B., Nelson, A., Castellano, K. and et al.,

1992. A multidisciplinary approach to the detection of clandestine graves. *Journal of Forensic Sciences*.
- Grip, W. M., Grip, R. W. and Morrison, R. D., 2000. Application of aerial photography and photogrammetry in environmental forensic investigations. *Environmental Forensics* 1(3).
- INML, 2020. Registro nacional de desaparecidos inml. <https://www.medicinalegal.gov.co/rnd-registro-de-desaparecidos>.
- Marx, A. and Goward, S., 2013. Remote sensing in human rights and international humanitarian law monitoring: Concepts and methods. *Geographical Review* 103(1).
- Molina, C. M., Hernandez, O. and Pringle, J., 2013. Experiments to Detect Clandestine Graves from Interpreted High Resolution Geophysical Anomalies. In: *AGU Spring Meeting Abstracts*, Vol. 2013, pp. NS21C–03.
- Molina, C. M., Pringle, J. K., Saumett, M. and Evans, G. T., 2016. Geophysical monitoring of simulated graves with resistivity, magnetic susceptibility, conductivity and gpr in colombia, south america. *Forensic Science International* 261, pp. 106–115.
- Molina, C. M., Pringle, J. K., Saumett, M. and Hernandez, O., 2015. Preliminary results of sequential monitoring of simulated clandestine graves in colombia, south america, using ground penetrating radar and botany. *Forensic Science International* 248, pp. 61–70.
- Molina, C. M., Wisniewski, K. D., Drake, J., Baena, A., Guatame, A. and Pringle, J. K., 2019. Testing application of geographical information systems, forensic geomorphology and electrical resistivity tomography to investigate clandestine grave sites in colombia, south america. *Journal of Forensic Sciences* 65(1), pp. 266–273.
- MP, 2020. For memory, truth and justice. <http://www.desaparecidos.org/main.html>.
- OACP, 2020. Oficina del alto comisionado para la paz. <http://www.altocomisionadoparalapaz.gov.co>.
- Pringle, J. K., Holland, C., Szkornik, K. and Harrison, M., 2012. Establishing forensic search methodologies and geophysical surveying for the detection of clandestine graves in coastal beach environments. *Forensic Science International*.
- Ruffell, A. and Mckinley, J., 2014. Forensic geomorphology. *Geomorphology* 206, pp. 14–22.
- RUV, 2020. Ruv registro unico de víctimas. <https://www.unidadvictimas.gov.co>.
- Sagripanti, G., Villalba, D., Aguilera, D. and Giaccardi, A., 2013. Geología forense: Métodos aplicados en la búsqueda de desaparecidos en la región central de Argentina. *Revista Asociación Geológica de Argentina*.
- Shugar, D. H., Clague, J. J., Best, J. L., Schoof, C., Willis, M. J., Copland, L. and Roe, G. H., 2017. River piracy and drainage basin reorganization led by climate-driven glacier retreat.

AUTHORS

Jonathan Drake, American Association for the Advancement of Science, 1200 New York Ave NW, Washington, DC. jdrake@aaaas.org.

Carlos Martín Molina, Instituto Nacional de Medicina Legal y Ciencias Forenses, Bogotá, Colombia and Universidad Antonio Nariño, Facultad de Ingeniería Ambiental y Civil, Bogotá, Colombia. martin.molina@uan.edu.co.

Edier Fernando Avila, Universidad de Cundinamarca, Facultad de Ciencias Agropecuarias, Colombia. efernando-avila@ucundinamarca.edu.co.

Alejandra Baena, Universidad Antonio Nariño, Facultad de Ciencias, Bogotá, Colombia. alejandra.baena@uan.edu.co.



Too young to drive the car? Perhaps!

But not too young to be curious about geospatial sciences.

The ASPRS Foundation was established to advance the understanding and use of spatial data for the betterment of humankind. The Foundation provides grants, scholarships, loans and other forms of aid to individuals or organizations pursuing knowledge of imaging and geospatial information science and technology, and their applications across the scientific, governmental, and commercial sectors.

Support the Foundation, because when he is ready so will we.

asprsfoundation.org/donate



Another Trick with “Hot-Keys”

In previous columns, we have highlighted using “hotkeys” in several GIS software programs including the Esri suite, Global Mapper, and Intergraph. Hotkeys are sometimes referred to as shortcut keys because of their ability to easily trigger an action. Most people are familiar with a few basic shortcut commands such as Ctrl+C to copy and Ctrl+V to paste that have become ubiquitous in most Windows-based software. While we have discussed the “built-in” hotkeys, those that the software vendor thinks you need, one great feature about hotkeys that many people do not realize is that they, too, are customizable. Setting your own hotkeys is quick, easy and a great way to streamline common processes.

In the Esri ArcGIS Desktop suite, it is as simple as:

1. Click the Customize menu and click Customize Mode.
2. In the Customize window (Figure 1) that appears, click the Keyboard button on the customize dialog box.

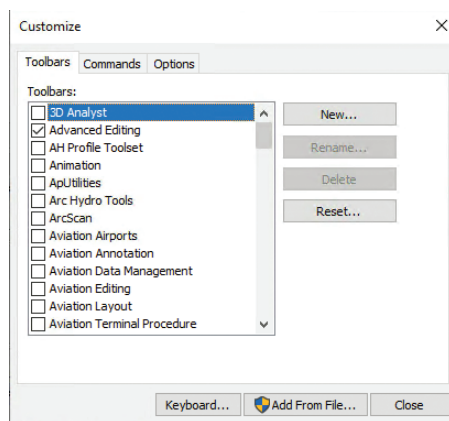


Figure 1. The Esri Customize dialog box

3. From the Customize Keyboard dialog (Figure 2) click the category in the left-hand side panel containing the command you want to modify. You can also search for commands from the ‘Show Commands Containing box’.
4. Click the command to which you want to add a keyboard shortcut.
5. Click in the Press new shortcut key text box and press the keys on the keyboard that you want to use for a shortcut. Once that command is pressed, it will appear in the Press New Shortcut Key box. For this example, to assign Ctrl+M to the Merge features tool on the editor toolbar; press the Ctrl key and the M key at the same time to make that appear in the dialogue box. One tool can have multiple shortcuts, but a shortcut

command can only be assigned to a single tool. If those keys have been assigned to another command, that command’s name will appear below under the Currently Assigned to dialogue area.

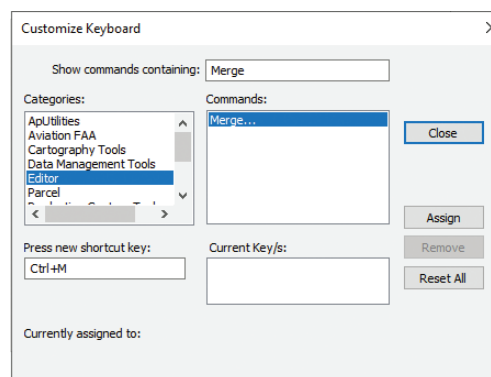


Figure 2. The Esri Customize Keyboard dialog box.

6. Click Assign if the keys aren’t currently assigned to another command (Figure 3). The new shortcut appears in the Current Key/s list. If the shortcut key you typed for the selected command is currently assigned to a different command and you press the Assign button, the original command/key assignment will be overridden. When you use that shortcut key, the new command will be executed instead of the command to which this shortcut was previously assigned.

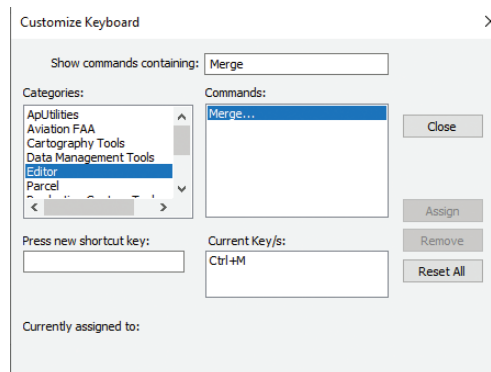


Figure 3. Customize Keyboard Dialog box showing the “Ctrl+M” shortcut assigned.

continued on page 608

Photogrammetric Engineering & Remote Sensing
Vol. 87, No. 9, September 2021, pp. 605–608.
0099-1112/21/605–608

© 2021 American Society for Photogrammetry
and Remote Sensing
doi: 10.14358/PERS.87.9.605

*Jennifer Murphy*

Making a Difference in a Developing Country – One Student at a Time

As background, I began my Geomatics career in 1977 working at the Canada Centre for Remote Sensing (CCRS) on the absolute radiometric calibration and relative correction of data from the Multispectral Scanner and the Thematic Mapper on the Landsat satellites. Our small team of Radiometry Specialists, including Dr. Frank Ahern and with ideas from Dr. Murray Strome, contributed to the production of Landsat products on tape and on film that were highly regarded for their accuracy (Murphy et al, 1985). In preparation for the launch of Landsat 4, CCRS developed an interim processing system to analyze in detail all the inflight data including calibration information. We were also able to qualify and quantify various anomalies that had not been predicted before launch. For the Landsat Image Data Quality Assessment (LIDQA) Symposium, we chose one random scene (that happened to include President Ronald Reagan's Ranch...) to exemplify, with considerable success, all these anomalies and our proposed correction method, as described by Murphy et al. (1985). I later worked as a Science and Technology Policy Advisor to an Assistant Deputy Minister and the Minister in Natural Resources Canada.

In 2009 I was 18 months into retirement, and it was time for a new challenge. After a whirlwind tour of Nepal in 2007, I began annual treks there in 2009 using the company, Three Sisters (also known as Empowering Women of Nepal), based in Pokhara about 300kms west of Kathmandu. It was founded by the Chhetri sisters in 1999 to train local young women to be trekking guides and assistants. I took the Teaching English as a Second Language (TESL) course in Canada and volunteered to teach English to these young women in January each year. This was a marvelous opportunity to support an organization that was actively encouraging young women in a developing country. I felt a wonderful sense of achievement when I later encountered on a trek in the mountains some of my students, with eyes sparkling, who seemed to be totally at ease with their clients. My pattern for the next six years was to spend two months in Nepal, teaching English in January, and then trekking in the mountains.

More opportunities in Nepal related to my remote sensing career were on the horizon. In 2012, Dr. Bob Ryerson gave me the contact information for two eminent Nepalese geomatics

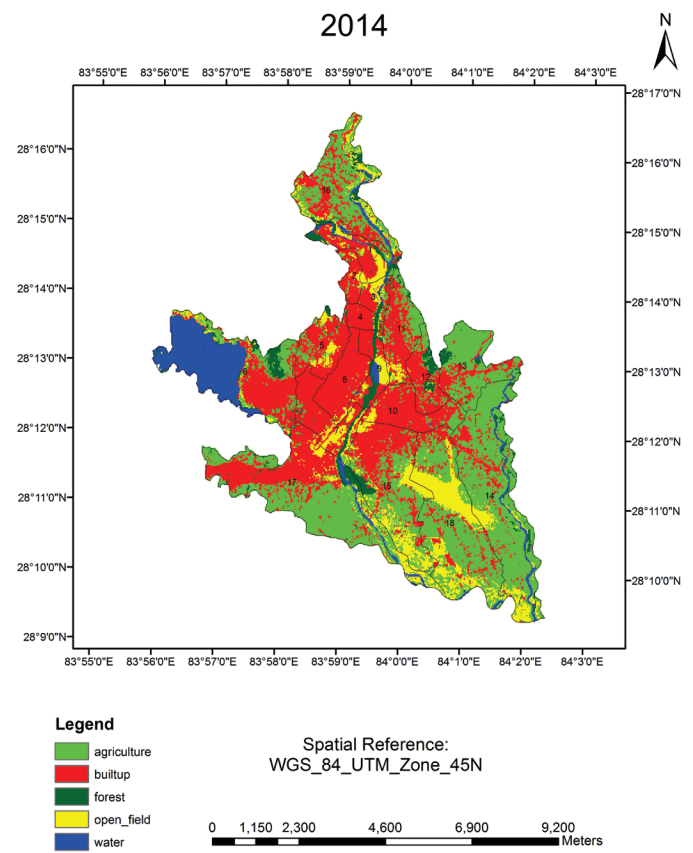
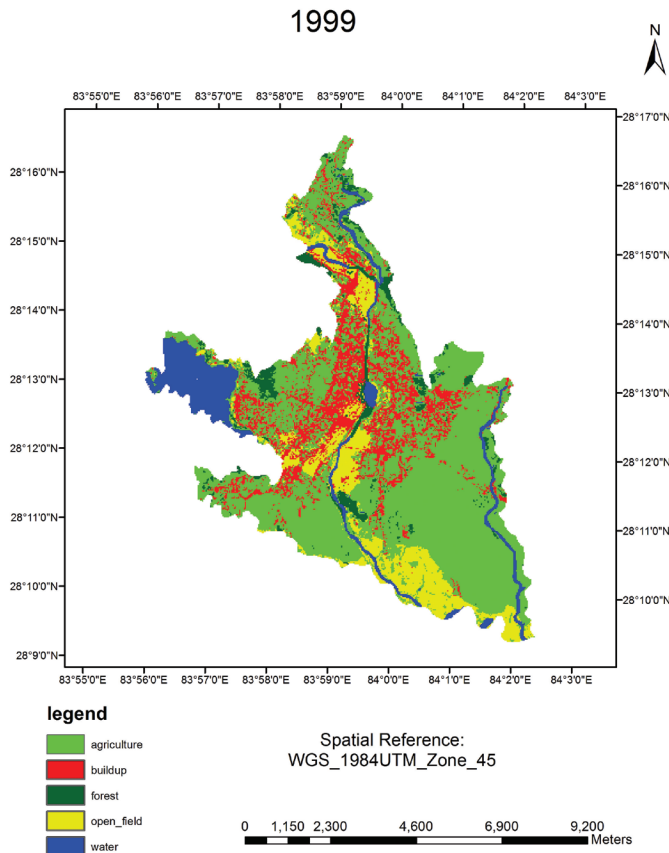
scholars whom he had met at various international conferences. Within a year, I had started a series of informal meetings in Kathmandu with Dr. Rabin Sharma, the President of the Nepal Society for Photogrammetry and Remote Sensing. In 2013 Professor Krishna Bhandari, at that time a Ph.D. student in Thailand and a lecturer at the Paschimanchal Engineering Campus of Tribuvhan University, invited me for a tour of their campus, located in Pokhara, and we met with several of the faculty. He later returned the favour by joining my English class at Three Sisters, participating in some of the activities, and explaining to my students why science and mathematics are important.

When I returned home, I asked myself how it could be possible to teach geomatics on a campus that had none of the hallmarks normally associated with hi-tech subjects. There is an added challenge for the entire country since most of the power is hydroelectric. The electrical system works well during the monsoon season, but in the winter and spring, the power supply is intermittent at best and often non-existent for several hours a day as the rivers dry up. I decided that it must be the dedication of the Professors and the students that make the program feasible. They understand how desperately Nepal needs geomatics technology, not only on a routine basis to map resources, the landscape, and social infrastructure, but also during times of natural disasters such as earthquakes, mudslides, and glacial melting. I vowed that my next retirement project would involve setting up a scholarship to help deserving young students in Nepal in their quest to participate in Geomatics.

The Canada Nepal Geomatics Advancement Foundation (CNGAF) was registered in 2016 as a Charity with Canada's tax agency, the Canada Revenue Agency (CRA). Our work is challenging since we speak no Nepali, and the CRA requires a raft of forms and record-keeping to be archived, including details of the students, their technical work, and their

Photogrammetric Engineering & Remote Sensing
Vol. 87, No. 9, September 2021, pp. 606–608.
0099-1112/21/606–608

© 2021 American Society for Photogrammetry
and Remote Sensing
doi: 10.14358/PERS.87.9.606



The two maps above from 1999 and 2014 are from a project to map land use change in the area of Pokhara, Nepal over five time periods using Landsat data. The work by undergraduate student Sudip Kuikel (now a government officer in Nepal) was supervised by Dr. Bhandari and supported by the Canada Nepal Geomatics Advancement Foundation.

expenses. I visited with Dr. Bhandari three more times, and I gave a short lecture to the geomatics students about the CNGAF Scholarship. I had several meetings with various Nepalese University officials, and we were finally successful in having the Foundation ratified there in February 2016, marked by a Certificate of Appreciation signed by Dr. Bhandari, Coordinator of the Research Management Unit, and by Associate Professor Gautam, Paschimanchal Campus Chief. We sent scholarships to our first two deserving young students in 2017 in their graduating year, which marked the first graduating class for the Geomatics program on that campus. Dr. Bhandari has subsequently extended the program to include a master's degree and was instrumental in setting up the related Centre for Space Science and Geomatics Studies (CSSGS). (See <https://www.facebook.com/wrc.cssgs/> for more details.) Dr. Bhandari is also using the CNGAF Scholarships to leverage collaboration with other universities, and he cites an MOU with the Centre for Spatial Information Science at the University of Tokyo.

By mid-2021, the CNGAF has already provided scholarships to eight students. Their Research Projects are varied and have included a study on land pooling to improve agriculture production. Another included a 3-D spatial information system for the recently upgraded Pokhara Airport. One student did a carbon stock estimation of above-ground tree biomass using geospatial technology. Another reported that the scholarship gave him the means to travel to Chandigar, India, to present his paper "Participatory Geographic Information System for Sustainable Ecotourism in Mountainous Area" at the International Conference on "Global Frameworks in the Local Context: Challenges and Way Forward." As a bonus, he was able to attend the related two-day Pre-Conference Workshop. Yet another is now studying in the master's program in Geoinformation Science and Earth Observation. Immediately after completing his bachelor's degree with a CNGAF scholarship, this student received an additional scholarship from the CSSGS. This allowed him to travel to Thailand to work as a Research Associate at the Asian Institute of Technology, where he worked on projects such as Global Navi-

gation Satellite Systems data analysis which could lead to the prediction of an earthquake. One of the first recipients worked on Land Use and Land Cover (LULC) using GIS and Landsat data to evaluate changes over time, due to human and natural causes, and another worked on visualization of public vehicle routes. These last two CNGAF scholarship recipients are both currently employed as Survey Officers in the Nepal Government.

One major goal of this scholarship is to foster local growth and to encourage the scholarship recipients to remain in Nepal after graduation so that these valuable skills remain in their home country, where they are so desperately needed. The Foundation has now settled into a routine of supporting three students a year, one in each year of Geomatics specialization, with a new student being selected each year based on their academic evaluations and their project proposal. The quality and content of their reports testify that they are contributing in a meaningful way to the wellbeing of their beautiful country. Despite the challenges of the Covid-19 epidemic, the University is persevering in training young people in the valuable discipline of geomatics.

I feel honoured and privileged to be able to contribute in this way to the scientific discipline that I found so satisfying, and to people in a country who are richly deserving of this support. I hope this Insight into our program encourages others in our profession to support students in other developing countries. For further information contact the CNGAF at cngaf@bell.net.

Reference

Murphy, J.M., Ahern, F.J., Duff, P.F., and Fitzgerald, A.J., 1985. Assessment of Radiometric Accuracy of Landsat-4 and Landsat-5 Thematic Mapper Data Products from Canadian Production Systems, *Photogrammetric Engineering and Remote Sensing*, vol. LI, No. 9 (September), pp. 1359-1369.

Jenny Murphy (BSc Physics 1966, MSc Radioastronomy 1967, UK) specialized in the radiometric correction of Landsat satellite data at the Canada Centre for Remote Sensing and was later the Science Policy Advisor in Natural Resources Canada. In retirement she has taught English in Nepal to female trainee trekking guides and is the Founder of the Canada Nepal Geomatics Advancement Foundation registered charity. She anticipates completing her Bachelor of Humanities at Carleton University in 2023.

GIS Tips & Tricks, continued from page 605

- Click Close on the Customize Keyboard dialog box (Figure 3). Click Close on the Customize dialog box (you will be returned to Figure 1). Once you have assigned a shortcut to a tool, that shortcut will appear to the right of the tool if the tool appears in a menu (Figure 4).

Remember that you can also assign shortcuts to key combinations for when you run out of options. And that is all there is to making custom hotkeys.

Please feel free to share your Tips & Tricks with us. Send your questions, comments, and tips to GISTT@ASPRS.org.

Sara Hedrick is a geospatial analyst with the Dewberry Office in Denver. She works extensively with the Esri suite of software. Al Karlin, Ph.D., CMS-L, GISP, as a senior geospatial scientist in the Dewberry – Tampa office, works with all aspects of lidar, remote sensing, photogrammetry, and GIS-related projects.

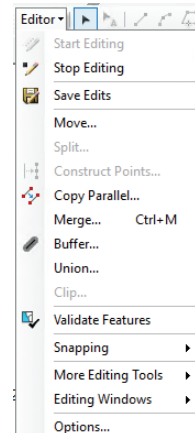


Figure 4. Editor menu showing the "Ctrl-M" shortcut assigned to the "Merge..." function.

NEW ASPRS MEMBERS

ASPRS would like to welcome the following new members!

Russell Aicher
 Niklas Anderson, GISP
 Jimmie M. Austin, Jr.
 Heath Babb
 Matthew Bauld
 John Broz
 Andrew Byron
 Jon Caris
 Carey Johnston
 Arthur W. Mohr, Jr.
 Angel Murillo
 Dakota Nichols
 Richard Allon Pickett
 Luke Skowronek
 David Ryan Stephens
 Erin Storey

FOR MORE INFORMATION ON ASPRS MEMBERSHIP, VISIT
[HTTP://WWW.ASPRS.ORG/JOIN-NOW](http://www.asprs.org/join-now)



& GRIDS & DATUMS

BY Clifford J. Mugnier, CP, CMS, FASPRS

UNITED KINGDOM

The Grids & Datums column has completed an exploration of every country on the Earth. For those who did not get to enjoy this world tour the first time, *PE&RS* is reprinting prior articles from the column. This month's article on the United Kingdom was originally printed in 2003 but contains updates to their coordinate system since then.

The United Kingdom includes England, Scotland, Wales, and Northern Ireland. The latter was included in a previous column on the entire island of Ireland (*PE&RS*, March 1999). Evidence from pre-Roman times includes Neolithic mound-tombs and henge monuments as well as Bronze Age Beaker culture tools, graves, and the famous Stonehenge monument. Brythonic-speaking Celtic peoples arrived during migrations of the first millennium B.C., according to *Webster's Geographical Dictionary*. England has existed as a unified entity since the 10th century. The union between England and Wales was begun in 1284 and formalized in 1536. England and Scotland agreed to join as Great Britain in 1707 and with Ireland in 1801. The present name of Great Britain and Northern Ireland was adopted in 1927. The area of Great Britain is slightly smaller than Oregon; the kingdom has a 12,429 km coastline and the lowest point is Fenland (-4 m), the highest point is Ben Nevis (1,343 m). Great Britain is only 35 km from France and is linked by the "Chunnel." Because of the heavily indented coastline, no location in the country is more than 125 km from tidal waters!

Thanks to the web site of the Ordnance Survey, "England was squeezed between rebellion in Scotland and war with France when King George II commissioned a military survey of the Scottish highlands in 1746. The job fell to William Roy, a far-sighted young engineer who understood the strategic importance of accurate maps. Walk into Ordnance Survey's Southampton headquarters and you'll see Roy's



name engraved on the curved glass entrance doors, yet his vision of a national military survey wasn't implemented until after his death in 1790. By then Europe was in turmoil, and there were real fears that the French Revolution might sweep across the English Channel.

Realizing the danger, the government ordered its defense ministry – the Board of Ordnance – to begin a survey of England's vulnerable southern coasts. In June 1791, the Board purchased a huge new Ramsden theodolite, and surveyors began mapping southern Britain from a baseline that Roy himself had measured several years earlier.

"The first one-inch map of Kent was published in 1801, and a similar map of Essex followed – just as Nelson's victory at Trafalgar made invasion less likely! Within twenty years about a third of England and Wales had been mapped at the one-inch scale. If that seems slow in these days of aerial sur-

Photogrammetric Engineering & Remote Sensing
Vol. 87, No. 9, September 2021, pp. 609–613.
0099-1112/21/609–613

© 2021 American Society for Photogrammetry
and Remote Sensing
doi: 10.14358/PERS.87.9.609

veys and global positioning, spare a thought for Major Thomas Colby – later Ordnance Survey’s longest serving Director General – who walked 586 miles in 22 days on a reconnaissance in 1819. In 1824, Parliament ordered Colby and most of his staff to Ireland, to produce a detailed six-inch to the mile valuation survey. Colby designed specialist measuring equipment, established systematic collection of place names, and reorganized the map-making process to produce clear, accurate plans. But Colby the perfectionist also traveled with his men, helped to build camps, and arranged mountaintop feasts with huge plum puddings at the end of each surveying season.

“Soon after the first Irish maps began to appear in the mid-1830s, the demands of the Tithe Commutation Act provoked calls for similar six-inch surveys in England and Wales. The government prevaricated but, by then, there was a new power in the land. This was the era of railway mania and if the one-inch map was unsuitable for calculating tithes, it was virtually useless for the new breed of railway engineers. To make matters worse, mapping of England and Scotland remained incomplete and, in 1840, the Treasury agreed that the remaining areas should be surveyed at the six-inch scale. Now, surveyors needed greater access than ever before; and so, in 1841, the Ordnance Survey Act gave them a legal right to ‘enter into and upon any land’ for survey purposes. A few months later Ordnance Survey’s cramped Tower of London offices were at the centre of a national catastrophe when fire swept through the Grand Storehouse, threatening to engulf the Crown Jewels in the Martin Tower. Miraculously, the Jewels were saved, and most of Ordnance Survey’s records and instruments were also carried to safety. But the blaze highlighted the Survey’s desperate need for more office space, and prompted a move to Southampton. “The scene was now set for two decades of wrangling over scales. Throughout this period, Victorian reforming zeal was creating an acute need for accurate mapping. The issue was settled piecemeal until, by 1863, scales of six inches and twenty-five inches to the mile had been approved for mountain and moorland, and rural areas respectively. The one-inch map was retained, and detailed plans at as much as ten feet to the mile were introduced for built-up areas.

“By now, Major-General Sir Henry James – perhaps Ordnance Survey’s most eccentric and egotistical Director General – was midway through his twenty-one year term. James quickly saw how maps could be cheaply and quickly enlarged or reduced using the new science of photography, and he designed an elaborate glass studio at Southampton for processing photographic plates. James planted his name on everything he touched, and later claimed to have invented photo zincography, a photographic method of producing printing plates. In fact, the process had been developed by two of his staff. By 1895 the twenty-five inch survey was complete.

“The twentieth century brought cyclists and motorists

swarming onto the roads, and the new Director General, Colonel Charles Close, prepared to exploit this expanding leisure market. But by now, the tide of history was sweeping Ordnance Survey back to its roots. As Britain entered the First World War, surveyors, draughtsmen and printers from Ordnance Survey were posted overseas. Working in appalling conditions alongside the troops, surveyors plotted the lines of trenches and, for the first time, aerial photography was used to capture survey information.

“After the war, Sir Charles, as he now was, returned to his marketing strategy and appointed a professional artist to produce eye-catching covers for the one-inch maps. Ellis Martin’s classic designs boosted sales to record levels, but the war had taken its toll; behind their bright new covers, the maps were increasingly out of date. In an uncanny echo of the mid-nineteenth century, a whole raft of new legislation brought demands for accurate, up-to-date mapping.

“Matters came to a head in 1935, and the Davidson Committee was established to review Ordnance Survey’s future. That same year, a far-sighted new Director General, Major-General Malcolm MacLeod, launched the retriangulation of Great Britain. Surveyors began an Olympian task, building the now familiar concrete triangulation pillars on remote hilltops throughout Britain. Deep foundations were dug by hand, and staff dragged heavy loads of materials over isolated terrain by lorry, packhorse and sheer brute force. The Davidson Committee’s final report set Ordnance Survey on course for the 21st century. The National Grid reference system was introduced, using the metre as its measurement. An experimental new 1:25,000 scale map was launched, leaving only the one-inch unscathed. It was almost forty years before this popular map was superseded by the 1:50,000 scale series, first proposed by William Roy more than two centuries earlier.

“In 1939, war intervened once again. The Royal Artillery was now responsible for its own field surveys, but over a third of Ordnance Survey’s civilian staff were called up, and its printing presses were kept busy with war production. It wasn’t a soft option. Enemy bombing devastated Southampton in November 1940 and destroyed most of Ordnance Survey’s city centre offices. Staff were dispersed to other buildings, and to temporary accommodation at Chessington. But the military appetite remained insatiable – the Norman- dy landings alone devoured 120 million maps!

“After the war, Ordnance Survey returned to Davidson’s agenda; the retriangulation was completed, and metric maps began to appear along National Grid sheet lines. Aerial survey helped speed up the new continuous revision strategy, and up-to-date drawing and printing techniques were introduced. But the organization was still fragmented, scattered across southern England in a battered collection of worn-out buildings. All that changed in 1969, when Ordnance

Survey moved to its present, purpose-built headquarters on the outskirts of Southampton. Four years later, the first computerized large-scale maps appeared; the digital age had begun. Ordnance Survey digitized the last of some 230,000 maps in 1995, making Britain the first country in the world to complete a programme of large-scale electronic mapping. Computers have transformed the map-making process, and electronic data is now routinely available to customers within 24 hours of being surveyed. The public still knows Ordnance Survey for its comprehensive range of printed leisure maps, yet electronic data now accounts for some 80% of Ordnance Survey's turnover. Independent estimates show that the national mapping agency's data now underpins up to £136 billion-worth of economic activity in Britain – everything from crime-fighting and conservation to marketing and mobile phones.”

“OS was founded in 1791 by the Master General of Ordnance [equivalent to the Minister of Defense today], Charles Lennox, Duke of Richmond. His Grace had been an outspoken supporter of the American colonists in the House of Lords. In December 1775 he declared that the resistance of the colonists was “neither treason nor rebellion, but it is perfectly justifiable in every possible political and moral sense.” Yet less than 10 years later he was a government minister – I think anywhere else in Europe he would have been executed or exiled! He was succeeded as Master General by Lord Cornwallis, who didn't appear to have suffered any long-term political damage by that unfortunate incident at Yorktown. An early Director General of OS, William Mudge, had served on Cornwallis's staff in the southern colonies.”

~ Russell Fox, Ordnance Survey

The original triangulation of Britain was carried out between 1783 and 1853 and is known as the “Principal Triangulation.” Jesse Ramsden, a gifted but dilatory gentleman, built the theodolite where the overall size of the horizontal circle measured 3 feet in diameter and was divided to a precision of a tenth of an arc second! (That's the same precision as the Wild Heerbrugg T-4 astronomical theodolite still manufactured as recently as the 1980s). Major General William Roy once wrote, “On one occasion he (Ramsden) attended at Buckingham Palace precisely as he supposed at the time named in the Royal mandate. The King remarked that he

was punctual as to the day and hour, while late by a whole year!” The genius responsible for the final adjustment and computation of the Principal Triangulation of 1783-1853 was Colonel Alexander Ross Clarke who also computed the Clarke ellipsoids of 1858, 1866, and 1880. The network selected by Clarke was an interlocking system of well-conditioned triangles. In 1967, the Ordnance Survey wrote, “This network was geometrically of great strength since it involved no fewer than 920 condition equations to find corrections to 1,554 observed directions subsequently used to fix 218 points.” The One-Inch map series referred to a map scale of one inch equals one mile. The One-Inch Scottish Bonne projection (1852-1936) was based on the Principal Triangulation and had a central meridian $\lambda_0 = 4^\circ \text{ W}$, a latitude of origin $\varphi_0 = 57^\circ 30' \text{ N}$, a scale factor of unity, and with no false Origin. The One-Inch English and Welsh Cassini projection (1919-1936) was also based on the Principal Triangulation and had a central meridian $\lambda_0 = 2^\circ 41' 03.5620'' \text{ W}$, a latitude of origin $\varphi_0 = 53^\circ 13' 17.2740'' \text{ N}$, a scale factor of unity, and with no false Origin.

The counties of the United Kingdom were based on local Cassini-Soldner projections that had the typical scale factor equal to unity, no false origin, and a single triangulation station as the projection origin. System Ben Auler ($\varphi_0 = 56^\circ 48' 50.3889'' \text{ N}$, $\lambda_0 = 4^\circ 27' 49.7064'' \text{ W}$) served the counties Canna, Eigg, Muck, Rhum, Sanday, and Skye of the Inner Hebrides and Inverness of Scotland. System Ben Cleuch ($\varphi_0 = 56^\circ 11' 08.8438'' \text{ N}$, $\lambda_0 = 3^\circ 46' 05.2765'' \text{ W}$) served the counties Clackmannan and Perth of Scotland. System Ben Clibrig (1839) ($\varphi_0 = 58^\circ 14' 07.8780'' \text{ N}$, $\lambda_0 = 4^\circ 24' 35.3627'' \text{ W}$) served the county of Sutherland, Scotland. System Black Down (1797, 1840) ($\varphi_0 = 50^\circ 41' 10.3186'' \text{ N}$, $\lambda_0 = 2^\circ 32' 52.4856'' \text{ W}$) served the counties Dorset and Somerset of England. System Bleasdale ($\varphi_0 = 53^\circ 54' 55.351'' \text{ N}$, $\lambda_0 = 2^\circ 37' 20.752'' \text{ W}$) served the county of Lancashire, England. System Brandon (1822) ($\varphi_0 = 52^\circ 24' 19.820'' \text{ N}$, $\lambda_0 = 0^\circ 37' 21.040'' \text{ W}$) served the counties Durham and Northumberland of England. System Broadfield ($\varphi_0 = 55^\circ 47' 59.8320'' \text{ N}$, $\lambda_0 = 4^\circ 32' 20.5920'' \text{ W}$) served the county of Rentfrew, Scotland. System Brown Carrick ($\varphi_0 = 55^\circ 24' 26.5714'' \text{ N}$, $\lambda_0 = 4^\circ 42' 41.1291'' \text{ W}$) served the counties Ayr, Wigtown, and Kirkcudbright, Scotland. System The Buck ($\varphi_0 = 57^\circ 17' 51.1940'' \text{ N}$, $\lambda_0 = 2^\circ 58' 32.0297'' \text{ W}$) served the counties Aberdeen, Banff, East Lothian, Fife, Kincardine, Kinross, Midlothian, and West Lothian of Scotland. System Cairn Glasher ($\varphi_0 = 57^\circ 20' 22.8895'' \text{ N}$, $\lambda_0 = 3^\circ 50' 30.5116'' \text{ W}$) served the county of Nairn, Scotland. System Cleisham (1840) ($\varphi_0 = 57^\circ 57' 50.6850'' \text{ N}$, $\lambda_0 = 6^\circ 48' 41.4340'' \text{ W}$) served the Outer Hebrides. System Craigowl ($\varphi_0 = 56^\circ 32' 52.4204'' \text{ N}$, $\lambda_0 = 3^\circ 00' 48.5178'' \text{ W}$) served the county of Angus, Scotland. System Cruach-na-Sleagh ($\varphi_0 = 56^\circ 07' 08.9328'' \text{ N}$, $\lambda_0 = 5^\circ 43' 34.1145'' \text{ W}$) served the counties Argyle, Arran, and Bute of Scotland and Coll, Islay, Jura, Mull, and Tiree of the Inner Hebrides. System Cryn-y-Brain (1852, 1853) ($\varphi_0 = 53^\circ$

02' 16.8715" N, $\lambda_0 = 3^\circ 10' 22.2907''$ W) served the counties Denbighshire and Flintshire of Wales. System Danbury (Church) Spire (1844), ($\phi_0 = 51^\circ 42' 57.9220''$ N, $\lambda_0 = 0^\circ 34' 32.9299''$ E) served the counties Cambridgeshire and Isle of Ely, Huntingdonshire, Soke of Peterborough, Norfolk, and Suffolk of England. System Derrington Great Law ($\phi_0 = 55^\circ 26' 08.9646''$ N, $\lambda_0 = 2^\circ 26' 34.6838''$ W) served the county of Berwick, Scotland. System Ditchling (1793, 1845) ($\phi_0 = 50^\circ 54' 04.0149''$ N, $\lambda_0 = 0^\circ 06' 21.7531''$ W) served the county of Sussex, England. System Dunnet Head (1838) ($\phi_0 = 58^\circ 40' 10.1679''$ N, $\lambda_0 = 3^\circ 22' 13.4365''$ W) served the county of Caithness, Scotland. System Dunnose (1793, 1844) ($\phi_0 = 50^\circ 37' 03.7288''$ N, $\lambda_0 = 1^\circ 11' 50.1015''$ W) served the counties Berkshire, Buckingham, Derby, Hampshire, Isle of Wight, Leicester, Lincoln, Northampton, Nottingham, Oxford, Rutland, Warwick, Wiltshire, Worcester, and Stafford of England. System Dunrig (1816, 1850) ($\phi_0 = 55^\circ 47' 59.832''$ N, $\lambda_0 = 4^\circ 32' 20.592''$ W) served the county of Peebleshire, Scotland. System Finlay Seat ($\phi_0 = 57^\circ 34' 42.2883''$ N, $\lambda_0 = 3^\circ 14' 26.5655''$ W) served the county of Moray, Scotland. System Forest Hill ($\phi_0 = 54^\circ 25' 30.700''$ N, $\lambda_0 = 2^\circ 43' 41.593''$ W) served the county Westmorland of England. System Foula (1821) ($\phi_0 = 60^\circ 08' 26.2436''$ N, $\lambda_0 = 2^\circ 05' 38.4808''$ W) served the counties Orkney, and Zetland, Scotland. System Hart Fell (1816, 1847) ($\phi_0 = 55^\circ 24' 28.9742''$ N, $\lambda_0 = 3^\circ 24' 00.1634''$ W) served the county of Dumfries, Scotland. System Hensbarrow (1790, 1843) ($\phi_0 = 50^\circ 22' 58.8532''$ N, $\lambda_0 = 4^\circ 49' 05.1029''$ W) served the counties Cornwall, and Isles of Scilly, England. System Highgate ($\phi_0 = 51^\circ 41' 10''$ N, $\lambda_0 = 4^\circ 50' 10''$ W) served the county of Pembroke, Wales. System High Pike ($\phi_0 = 54^\circ 42' 19.3478''$ N, $\lambda_0 = 3^\circ 03' 26.5277''$ W) served the county of Cumberland, England. System Hollingbourne ($\phi_0 = 51^\circ 16' 10.380''$ N, $\lambda_0 = 0^\circ 39' 55.564''$ W) served the county of Kent, England. System Lanark Church Spire ($\phi_0 = 55^\circ 40' 20.8037''$ N, $\lambda_0 = 3^\circ 46' 19.8904''$ W) served the counties Dumbarton, Lanark, Stirling, and Roxburgh of Scotland. System Leith Hill Tower (1792, 1822, 1824) ($\phi_0 = 51^\circ 10' 32.8895''$ N, $\lambda_0 = 0^\circ 22' 10.9797''$ W) served the county of Surrey, England. System Llangeinor ($\phi_0 = 51^\circ 38' 26.6535''$ N, $\lambda_0 = 3^\circ 34' 17.0360''$ W) served the counties Anglesey, Brecknock, Caer narvon, Car digan, Car marthen, Glamorgan, Merioneth, Montgomery, and Radnor of Wales and Hereford, Monmouth, and Salop of England. System Nantwich Church Tower ($\phi_0 = 53^\circ 04' 00.3405''$ N, $\lambda_0 = 2^\circ 31' 09.1414''$ W) served the county of Cheshire, England. System Rippon Tor ($\phi_0 = 50^\circ 33' 57.0563''$ N, $\lambda_0 = 3^\circ 46' 12.0872''$ W) served the county of Devon, England. System St. Paul's (1848) ($\phi_0 = 51^\circ 28' 15.9830''$ N, $\lambda_0 = 0^\circ 22' 47.6011''$ W) served the counties of Bedford, Essex, Hertsford, London, and Middlesex, England. System Sandhope Heights ($\phi_0 = 55^\circ 30' 10.253''$ N, $\lambda_0 = 3^\circ 02' 31.092''$ W) served the county of Selkirk, Scotland. System Scour-na-Lapach (1846) ($\phi_0 = 57^\circ 22' 10.3858''$ N, $\lambda_0 = 5^\circ 03' 31.5613''$ W) served the counties of Ross and Cromarty, Scotland. System South Berule (1846) ($\phi_0 = 54^\circ 08' 57.5699''$ N, $\lambda_0 = 4^\circ 40' 05.2960''$ W) served the Isle of Man, England.

System York Minster (1846) ($\phi_0 = 53^\circ 57' 43.1879''$ N, $\lambda_0 = 1^\circ 04' 49.7302''$ W) served the counties York and Yorkshire, England.

The retriangulation of Great Britain was not based on a single origin point. However, it was not based on any new length measurements, either. The overall size of the network was constrained to agree with the old 18th century Principal Triangulation using the old coordinates of 11 primary stations adjusted by Clarke. Therefore, the Ordnance Survey of Great Britain 1936 datum (OSGB36) does not have a single origin point. The ellipsoid of reference is the Airy 1830 where $a = 6,377,563.396$ m and $b = 6,356,256.910$ m. The overall size of the OSGB36 is based on the measurement of a single distance between two stations on Hounslow Heath in 1784 using 18-foot glass rods! The error incurred by using this scale constraint yielded an error in the length of the entire country of only 20 meters! The War Office Grid (1927-1950) was based on the Cassini-Soldner projection and had a central meridian $\lambda_0 = 1^\circ 11' 50.1360''$ W, a latitude of origin $\phi_0 = 50^\circ 37' 03.7480''$ N, a scale factor of unity, False Easting = 500 km, and False Northing = 100 km. Introduced in 1931, the English Yard Belt Transverse Mercator ($m_0 = 0.9996$, False Easting and False Northing = 1,000,000 yds.) was short-lived and was replaced by a slightly different metric version in 1945 and it continues to be used. The current system is the National Grid. Although the equations published appear to be a Gauss-Krüger expansion to the 5th derivative, they are cast as *latitude differences* from the False Northing latitude of true origin = 49° N. The central meridian = 2° W, and the scale factor at the central meridian, commonly mistaken for that of the TM Yard Grid and the UTM Grid, is different in that by definition, $m_0 = 0.9996012717... \equiv \text{Log}_{10} m_0 = 1.99982680$, exactly. I would love to find out where that number came from. The False Easting is 400 km and the False Northing is -100 km.

The Ordnance Survey seven-parameter transformation from OSGB36 to WGS84 modified to the standard American rotation convention used by the National Geodetic Survey (NGS) and by the National Imagery and Mapping Agency is $DX = +446.448$ m, $DY = -125.157$ m, $DZ = +542.060$ m, $\text{scale} = -20.4894 \cdot 10^{-6}$, $R_X = -0.1502''$, $R_Y = -0.2470''$, and $R_Z = -0.8421''$. "OSGB36 is an inhomogeneous Terrestrial Reference Frame by modern standards. Do not use this transformation for applications requiring better than 5 metre (*sic*) accuracy in the transformation step, either vertically or horizontally. Do not use it for points outside Britain." The above transformation parameters were extracted from A Guide to Coordinate Systems in Great Britain, a "pdf" file downloaded from the Ordnance Survey's web site, www.gps.gov.uk. Higher accuracy transformations are possible utilizing the free software available from the Ordnance Survey in the form of OSTN02, a bi-linear interpolation package similar in concept to the NADCON package of the NGS. The British Geoid

Model, OSGM02, is available and is free from the Ordnance Survey. The stated vertical accuracy is 2 cm in mainland UK and 4 cm for other areas. I hope that other nations will follow the example of the United Kingdom, Australia, Mexico, and the United States in making critical national geodetic transformation models available at no charge to the public. I am indebted to Russell Fox, soon to retire from the Ordnance Survey, and to John W. Hager, now retired from NIMA, for their patience over the years in helping me to compile this mass of data on the UK.

United Kingdom Update

The Ordnance Survey of the United Kingdom has published an up-to-date document that covers all of the current coordinate systems and recommended transformation methods and parameters as of 2020:

<https://www.ordnancesurvey.co.uk/documents/resources/guide-coordinate-systems-great-britain.pdf>

The contents of this column reflect the views of the author, who is responsible for the facts and accuracy of the data presented herein. The contents do not necessarily reflect the official views or policies of the American Society for Photogrammetry and Remote Sensing and/or the Louisiana State University Center for GeoInformatics (C⁴G). This column was previously published in *PE&RS*.

ASPRS WORKSHOP SERIES



It's not too late to earn Professional Development Hours

Miss an ASPRS Workshop or GeoByte? Don't worry! Many ASPRS events are available through our online learning catalog.

<https://asprs.prolearn.io/catalog>

Image Priscilla Du Preez on Unsplash.

In Memoriam

John Dwyer

1955-2021



John Dwyer, who started working at EROS in 1980 and retired in 2019 as Chief of the Science and Applications Branch, passed away Sunday, July 4, of complications from ALS. He was 65.

John started as a contract data analyst in Science and Applications. Among his accomplishments during his time at EROS, he earned a master's degree in geological sciences and did some Ph.D. coursework; became a Federal employee of USGS; worked two detail positions at Reston, VA; served as contract department manager for, and built up, the then-new Satellite Systems Branch; and built the Landsat Satellites Data System (LSDS) Science Research and Development (LSRD) project team. He also earned the Distinguished Service Award from the Department of the Interior.

John was the Landsat project scientist through the development of Landsat 8 and formulation of Landsat 9. Throughout his career at EROS, he was instrumental in the hiring and development of many key staff. "John had a unique ability to bring out the best in the people he worked with," said Brian Sauer, Landsat Engineering and Development Manager.

John's obituary can be found at www.millerfh.com/obituary/john-dwyer.

Who at ASPRS Do I Contact for help with...

Membership/PE&RS Subscription
office@asprs.org

Advertising/Exhibit Sales
Bill Spilman — bill@innovativemediasolutions.com

PE&RS Editor-in-Chief
Alper Yilmaz — PERSeditor@asprs.org

Calendar — calendar@asprs.org

ASPRS Bookstore — office@asprs.org

ASPRS Foundation — foundation@asprs.org

425 Barlow Place, Suite 210, Bethesda, MD 20814
301-493-0290, 225-408-4422 (fax), www.asprs.org

JOURNAL STAFF

Editor-In-Chief

Alper Yilmaz, Ph.D., PERSeditor@asprs.org

Associate Editors

Rongjun Qin, Ph.D., qin.324@osu.edu
Michael Yang, Ph.D., michael.yang@utwente.nl
Petra Helmholz, Ph.D., Petra.Helmholz@curtin.edu.au
Bo Wu, Ph.D., bo.wu@polyu.edu.hk
Clement Mallet, Ph.D., clemallet@gmail.com
Jose M. Pena, Ph.D., jmpena@ica.csic.es
Prasad Thenkabail, Ph.D., pthenkabail@usgs.gov
Ruisheng Wang, Ph.D., ruisheng@ucalgary.ca
Desheng Liu, Ph.D., liu.738@osu.edu
Valérie Gouet-Brunet, Ph.D., valerie.gouet@ign.fr
Dorota Iwaszczuk, Ph.D., dorota.iwaszczuk@tum.de
Qunming Wang, Ph.D., wqm1111@126.com
Filiz Sunar, Ph.D., fsunar@itu.edu.tr
Norbert Pfeifer, np@ipf.tuwien.ac.at
Jan Dirk Wegner, jan.wegner@geod.baug.ethz.ch
Hongyan Zhang, zhanghongyan@whu.edu.cn
Dongdong Wang, Ph.D., ddwang@umd.edu
Zhenfeng Shao, Ph.D., shaozhenfeng@whu.edu.cn
Ribana Roscher, Ph.D., ribana.roscher@uni-bonn.de
Sidike Paheding, Ph.D., spahedin@mtu.edu

Contributing Editors

Highlight Editor

Jie Shan, Ph.D., jshan@ecn.purdue.edu

Feature Articles

Michael Joos, CP, GISP, featureeditor@asprs.org

Grids & Datums Column

Clifford J. Mugnier, C.P., C.M.S., cjmce@lsu.edu

Book Reviews

Sagar Deshpande, Ph.D., bookreview@asprs.org

Mapping Matters Column

Qassim Abdullah, Ph.D., Mapping_Matters@asprs.org

Sector Insight

Lucia Lovison-Golob, Ph.D., lucia.lovison@sat-drones.com
Bob Ryerson, Ph.D., FASPRS, bryerson@kimgeomatics.com

GIS Tips & Tricks

Alvan Karlin, Ph.D., CMS-L, GISP akarlin@Dewberry.com

ASPRS Staff

Assistant Director — Publications

Rae Kelley, rkelly@asprs.org

Electronic Publications Manager/Graphic Artist

Matthew Austin, maustin@asprs.org

Advertising Sales Representative

Bill Spilman, bill@innovativemediasolutions.com

THE ASPRS BOARD OF DIRECTORS ANNOUNCES THE APPOINTMENT OF KAREN SCHUCKMAN AS THE NEXT EXECUTIVE DIRECTOR OF ASPRS

“After a thorough and extensive search process, the ASPRS Board of Directors has named Karen Schuckman as its next Executive Director. Karen in her previous positions in ASPRS has demonstrated an incredible commitment to seeing the Society succeed, and we look forward to her continuing to help us make ASPRS the best society possible”, says Jason Stoker, President of ASPRS.

The Executive Director is the senior operating officer of the Society and reports directly to the Board of Directors. The responsibilities of the Executive Director are outlined in the Bylaws, in Article XI Section 3. Schuckman succeeds Acting Executive Director Jesse Winch, who announced his retirement from ASPRS, effective June 30, 2021.

“I am pleased and honored to continue serving the Society and the profession in the role of Executive Director. I will miss the daily interaction I had with Jesse over the past 5 years as Managing Director, but I appreciate the Board’s vote of confidence as I step into his role. ASPRS has been and continues to be the cornerstone of my professional life, and my goal as Executive Director is to ensure that it continues to thrive, supporting evolving interests and needs of the geospatial community for decades to come”, says Schuckman.

Schuckman’s involvement with ASPRS began in 1990 as a member of the California State University, Fresno Student Chapter. She has since served the Society in a wide variety of elected regional and national positions and is a Past President and Fellow of ASPRS, former Director of the Photogrammetric Applications Division and Professional Practice Division, Certified Photogrammetrist, and Certified Mapping Scientist-Lidar. She has won numerous awards from ASPRS including the 2018 Outstanding Service Award.

ASPRS ADDS SUPPLEMENTAL MATERIAL FEATURE TO *PE&RS*

Photogrammetric Engineering & Remote Sensing (PE&RS) the monthly journal of the American Society for Photogrammetry and Remote Sensing (ASPRS) has added a supplemental material feature to *PE&RS*. This feature will be available in the digital version of *PE&RS* hosted by Ingenta Connect.

“This feature will increase the exposure of authors’ work and provide the reader with presentation materials and data files used in the published research; thus, increasing the number of citations to the published papers,” said Dr. Alper Yilmaz, Editor-In-Chief, *PE&RS*.

The implementation of this feature will give authors the opportunity to include a presentation with their *PE&RS* article as well as share files that support their research including videos, terrain models, images, presentations, audio files, and many more.

All supplemental files will be open access and available on the *PE&RS* publication page through Ingenta Connect.

For more information, contact Rae Kelley, Director of Publication, rkelly@asprs.org.

Gaussian Mixture Model of Ground Filtering Based on Hierarchical Curvature Constraints for Airborne Lidar Point Clouds

Longjie Ye, Ka Zhang, Wen Xiao, Yehua Sheng, Dong Su, Pengbo Wang, Shan Zhang, Na Zhao, and Hui Chen

Abstract

This paper proposes a Gaussian mixture model of a ground filtering method based on hierarchical curvature constraints. Firstly, the thin plate spline function is iteratively applied to interpolate the reference surface. Secondly, gradually changing grid size and curvature threshold are used to construct hierarchical constraints. Finally, an adaptive height difference classifier based on the Gaussian mixture model is proposed. Using the latent variables obtained by the expectation-maximization algorithm, the posterior probability of each point is computed. As a result, ground and objects can be marked separately according to the calculated possibility. 15 data samples provided by the International Society for Photogrammetry and Remote Sensing are used to verify the proposed method, which is also compared with eight classical filtering algorithms. Experimental results demonstrate that the average total errors and average Cohen's kappa coefficient of the proposed method are 6.91% and 80.9%, respectively. In general, it has better performance in areas with terrain discontinuities and bridges.

Introduction

Airborne light detection and ranging (lidar) systems measure the distance between the target and the instrument reference center through calculating the round-trip time of the laser pulse. When given the ground reference system, dense, geo-referenced, and accurate point clouds are generated (Meng *et al.*

Ka Zhang, Yehua Sheng are with the Key Laboratory of Virtual Geographic Environment (Nanjing Normal University) of Ministry of Education, School of Geography, Nanjing Normal University, the Jiangsu Center for collaborative Innovation in Geographical Information Resource Development and Application, the State Key Laboratory Cultivation Base of Geographical Environment Evolution (Jiangsu Province), No.1, Wenyuan Road, Nanjing, China; and the Key Laboratory of Urban Land Resources Monitoring and Simulation of Ministry of Natural Resources, No. 69, News Road, Shenzhen, China (zhangka81@126.com; shengyehua@njnu.edu.cn).

Longjie Ye, Dong Su, Pengbo Wang, Shan Zhang and Na Zhao are with the Key Laboratory of Virtual Geographic Environment (Nanjing Normal University) of Ministry of Education, School of Geography, Nanjing Normal University, No.1, Wenyuan Road, Nanjing, China.

Wen Xiao is with the School of Engineering, Newcastle University, NE1 7RU, Newcastle upon Tyne, United Kingdom (co-first author).

Hui Chen is with the School of Geography and Ocean Science, Nanjing University, No. 163, Xianlin Avenue, Nanjing, China.

Contributed by Zhenfeng Shao, August 28, 2020 (sent for review January 14, 2021; reviewed by Nan Yang, Bin Hu).

2010). Compared with photogrammetric methods, lidar systems have the advantage of not being affected by the weather, being able to penetrate vegetation and obtain a large amount of spatial information efficiently (Meng *et al.* 2009). Currently, airborne lidar has been applied to many fields, including digital terrain model (DTM) construction (Chen *et al.* 2017; Ozcan and Unsalan 2017), three-dimensional building model generation (Yang *et al.* 2013; Huang *et al.* 2013; Zhou and Zhou 2014), road extraction (Hui *et al.* 2016), forest stand parameters estimation (Hyypä *et al.* 2012), forest and urban vegetation biomass estimation (Shao *et al.* 2017; Zhang *et al.* 2019; Zhang and Shao 2021), etc. In most applications, to distinguish ground and nonground objects from lidar measurements, filtering must be performed.

Airborne lidar technology has revolutionized the way to acquire DTM/digital surface model (DSM) due to its high efficiency, high precision, and penetrability (Mongus *et al.* 2014; Zhang *et al.* 2016). In recent years, many scholars have proved the effectiveness of lidar derived elevation modeling (Hingee *et al.* 2019; Vassilaki and Stamos 2020). Since the airborne lidar system provides an optimal solution for large-area, high-resolution terrain surface surveying and mapping, many studies have focused on using lidar data to extract terrain information. To construct DTM, one critical step is to filter out nonground point clouds, including those on bridges, buildings, vegetation, etc. Although the airborne lidar system can acquire a massive amount of data in a short time, the processing of lidar data requires a high time cost. According to previous research, about 60–80% of the postprocessing time is spent on manual filtering and classification (Flood 2001). Hence, it is invaluable to improve the efficiency of lidar filtering algorithms and reduce the complexity of parameter adjustment.

Many researchers have proposed dozens of filtering algorithms in the past two decades. However, accurate filtering still remains a challenge. A comparative experiment was conducted by Sithole and Vosselman (2004) to test the performance of eight classic filtering methods in both city and rural sites. They pointed out that the eight algorithms filter precisely in flat rural scenes. However, the results of all filters are not satisfactory in urban regions with variant terrains. On the whole, surface-based filters produce better results in terms of filtering strategy. It is because they use more contextual information of lidar data than other filters. Since then, the 15 sample data sets have become a benchmark for testing the accuracy and performance of ground filtering algorithms.

Most of the existing filtering algorithms need to adjust parameters according to the complex terrain environment, which is not user friendly. Our algorithm is based on the surface

Photogrammetric Engineering & Remote Sensing
Vol. 87, No. 9, September 2021, pp. 615–630.
0099-1112/21/615–630

© 2021 American Society for Photogrammetry
and Remote Sensing
doi: 10.14358/PERS.87.20-00080

filtering strategy and provides a set of more general parameters for filtering. The adjustment in the parameter is handed over to the expectation-maximization (EM) algorithm for automatic optimization. Therefore, our algorithm makes the task easier for inexperienced users. In this paper, an adaptive height difference classifier based on the Gaussian mixture model is proposed to maximize filter efficiency in areas with terrain discontinuities or steep slope. Compared with previous work (Hui *et al.* 2019), our approach has mainly two innovative points: (1) It uses the thin plate spline (TPS) function instead of low-order polynomial coefficients for iterative surface interpolation. Therefore, the proposed method can better fit the terrain. It is worth noting that only ground control points are used in the fitting process. (2) While solving the Gaussian mixture model, hierarchical curvature results are applied to initialize the probabilistic model parameters. In order to classify more accurately, the relative elevation is substituted into the Gaussian mixture model. By computing the posterior probability of each point, we can determine which lidar point belongs to the ground. Since the subsequent optimization process is based on probabilistic reasoning, the algorithm does not require a prior knowledge for parameter adjustment. Moreover, it can well overcome the influence of terrain gradient through the interpolation surface constructed by TPS.

Related Work

There are mainly four types of methods to filter airborne lidar point clouds: slope comparison, mathematical morphology, surface interpolation, and segmentation strategies. Alternatively, it is a wise strategy to choose a combination of several of them to filter the point cloud. For example, Chen *et al.* (2016) first used the regional growth method to obtain more ground seeds and then applied a surface interpolation method to filter out objects from the original lidar measurement. Hui *et al.* (2016) adopted Kriging interpolation to construct a surface corresponding to the change morphology window. In their method, the slope gradient based on the constructed surface is combined with the morphological opening operation for filtering. The results show that their approach can well preserve the detailed features of the terrain.

Vosselman (2000) first adopted the slope of the line between two points in the lidar point clouds and set a threshold for filtering. This method is based on the hypothesis that the gradient of the ground will be much smaller than that of non-terrain (bridges, trees, etc.). However, this hypothesis limits the application of this method to gentle slope terrains. To overcome this limitation, many filters with an adaptive slope threshold have been proposed. Such filtering methods include the adaptive parameter approaches (Sithole 2001; Tseng *et al.* 2004; Susaki 2012), knowledge classifiers (Wang and Shan 2009), and directional filters (Wang and Tseng 2010). Generally, the slope-based method can perform well in areas where the gradient of the slope changes gently. However, it will fail in terrain where the slope varies sharply (cliffs) (Mongus and Žalik 2012). Furthermore, because contextual information of lidar point clouds other than slope is not considered, these methods will become unreliable in complex terrains.

By rasterizing lidar data and taking the elevation as the gray value of a raster image, the morphological method can be transferred and applied to the filtering. In this type of filtering algorithm, morphological opening operations are widely used. Under the premise of the constant slope, Zhang *et al.* (2003) adopted a combined filtering strategy of gradually increasing morphological structural elements and height difference threshold. In each iteration, the first step is to use the open operation of the current structure element to obtain the filtered grid gray value. Then, by calculating the difference with the original grid elevation value and comparing it with the height difference threshold, ground points are selected if less than the threshold. Chen *et al.* (2007) considered that the slope of

the real terrain is not constant, and the slope of the building boundary changes drastically. They adopted a group of adjustable parameters to determine the height difference threshold. Then, most of the buildings were removed through morphological opening operations with a set of increasing structural elements. Li (2013) introduced a morphological filtering algorithm to remove object points while preserving ground points well by using multi-gradient analysis. Other methods, such as sloped brim (Li *et al.* 2014), differential morphological profiles (Mongus *et al.* 2014), and image inpainting (Pingel *et al.* 2013) are alternative strategies. Moreover, morphological methods can be used as an effective tool to filter out outliers (Hui *et al.* 2019) and modify filtering results (Bayram *et al.* 2018; Liu and Lim 2018). Briefly, the advantage of the morphological filtering method is that it is easy to implement and has high accuracy.

The methods of surface interpolation generally require obtaining ground seeds first. Then, the elevation difference is calculated according to the constructed surface to filter with a given threshold. For example, Kraus and Pfeifer (1998) introduced a method of dynamic weight determination. They first built a reference surface with all points initially of the same weight. Since the surface is located between the ground and the objects, the ground points will have a negative residual to get more weight, while the nonterrain point will be the opposite. Finally, points with smaller weights will be removed to complete the filtering. Axelsson (2000) adopted a progressive densification strategy. In their method, a sparse triangular irregular network (TIN) is first constructed based on the control points obtained by the local minimum method. Then, if the point meets predefined conditions, including the angle threshold and distance threshold, it will be included in the ground point. The algorithm finishes filtering until all points are less than the threshold. Evans and Hudak (2007) proposed a multi-scale curvature classification method. In this method, the TPS is iteratively used to classify ground points that are less than curvature thresholds. Chen *et al.* (2013) improved this method by comparing all the residuals in the moving window instead of the mean residuals and using a voting strategy. Other than that, many multi-resolution interpolation filtering methods performed well (Mongus and Žalik 2012; Hu *et al.* 2014; Su *et al.* 2015). Recently, Hui *et al.* (2019) presented a threshold-free filtering method according to the quadratic polynomial surface. On the basis of the revised elevation, the filtering method automatically extracts the ground to construct DTM. Through the use of unsupervised classification, this method reduces the extra time for parameter adjustment. In general, the surface-based approach can accomplish the filtering task excellently. However, it is generally accompanied by higher processing time due to repeated updates of the surface.

Different from point-by-point classification methods, the filter based on the segmentation strategy first clusters the point cloud into segments according to the homogeneity criterion. Then, according to the heterogeneity between terrain segments, they classify all segments into terrain segments and nonterrain segments. Sithole and Vosselman (2004) first segmented the point cloud into several smooth segments. Then, they divided the segments into the ground and objects according to the elevation difference between neighboring segments. Tóvári and Pfeifer (2005) proposed an interpolation function for point cloud groups. It iteratively updates the weights of all segments to fit the surface. It completes the classification of all segments according to the size of the final weight. Yan *et al.* (2012) introduced an object-oriented feature filtering criterion. At first, the lidar returns are rasterized and divided into segments based on a region growing algorithm. Then, the ground segments are separated according to the topology and size information of the object. Lin and Zhang (2014) proposed a progressive densification algorithm for terrain segments. Firstly, it performs segmentation according to the smoothness of local point cloud clusters. Then, it iteratively adds

segments to the terrain seed segment on the basis of angle and distance constraints. The essence of the segmentation-based method is to cluster before classifying. It generally requires the segments obtained by initial clustering to be as under-segmented as possible but to maintain homogeneity. Segmentation-based algorithms can capture more contextual information, so this type of algorithm performs well at terrain boundaries. However, the accuracy of clustering methods limits the application of segmentation methods.

In addition to the four categories of methods mentioned above, many new theories have been introduced to advance the filtering of airborne lidar data, such as cloth simulation filter (CSF) (Zhang *et al.* 2016; Yang *et al.* 2020), spectrum method (Bayram *et al.* 2018), etc. The basic idea of the CSF method is to invert the lidar point cloud and then cover it with a rigid cloth. Finally, the ground points are extracted by judging the positional relationship between the lidar point clouds and the cloth surface. The spectral method regards the lidar data as the graph node and determines the weight of the connected edge of each node by calculating the spatial distance of each point. Then the graph signal is filtered through the Laplacian operator in the spectral graph. The final graph nodes are regarded as ground points. However, the latest methods still cannot perform well where terrain is discontinuous. To filter robustly on those terrains, this paper proposes a Gaussian mixture model of a ground filtering method based on hierarchical curvature constraints for lidar point clouds.

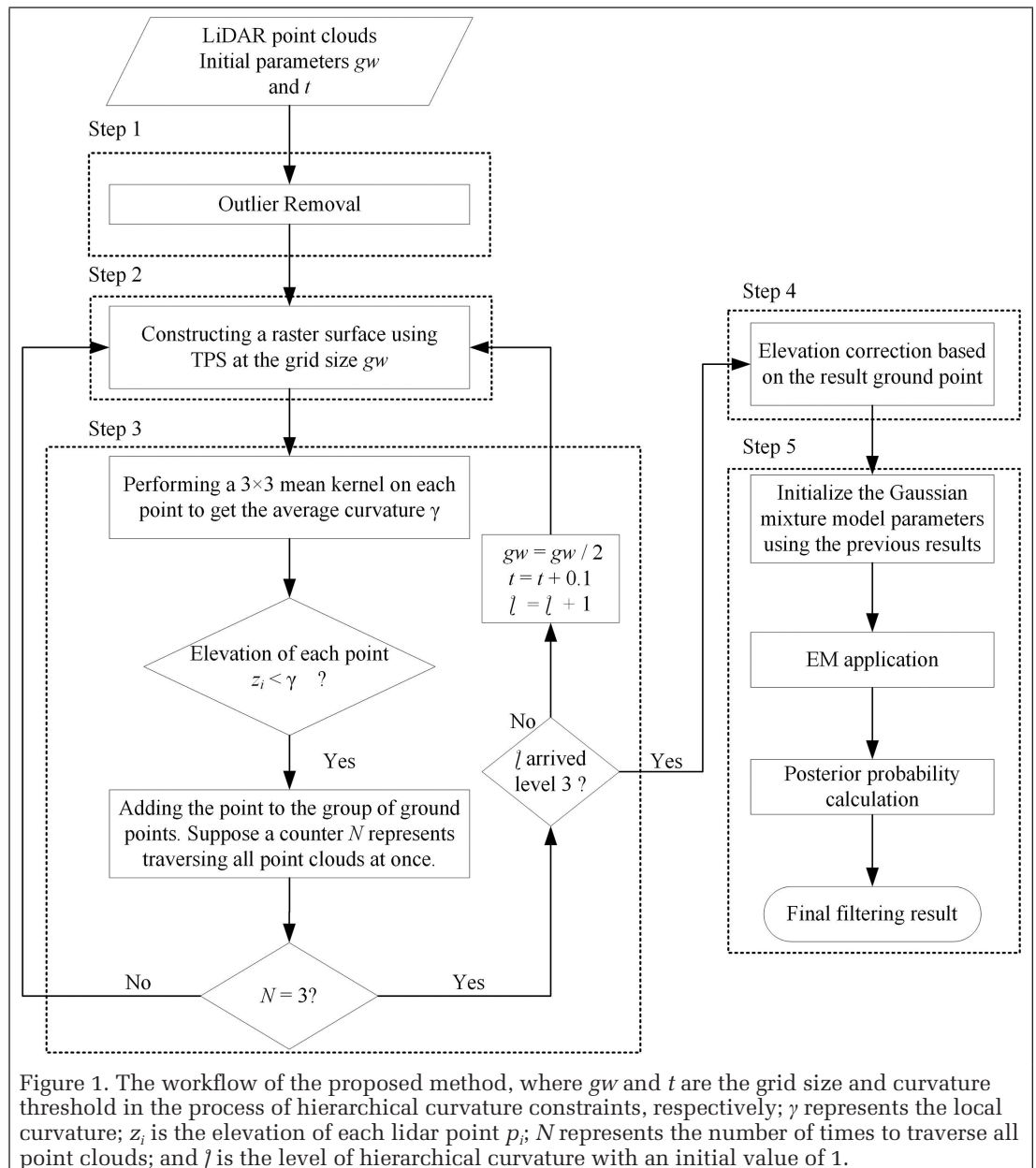
Method

The proposed method extracts the ground points from lidar data based on the Gaussian mixture model because normal distribution can be used to approximate lidar returns, according to the central limit theorem (Bartels *et al.* 2006). Separating the ground points from the other objects could be regarded as the process of solving the Gaussian mixture model. First, we use TPS interpolation based on a hierarchical curvature to construct the fitted surface. It is worth noting that our interpolation surface construction is based on ground seeds. Then, according to the results of the interpolation, two groups of appropriate initial values are derived by calculating the Gaussian distribution parameters of the ground and nonground points, respectively. Therefore,

using the EM algorithm to solve the Gaussian mixture model reduces the possibility of falling into a locally optimal solution. The proposed method mainly includes five steps (Figure 1): (1) outlier removal; (2) surface interpolation by TPS; (3) constraints of iterative hierarchical curvature; (4) relative elevation calculation; (5) ground points extraction using the EM algorithm.

Outlier Removal

Due to the internal error of the lidar system and the presence of particles in the atmosphere, outliers always exist in lidar returns. In particular, low outliers will lead to wrong ground seeds selection. However, in most of the current filtering algorithms, the assumption is that the lowest point in the local area must belong to the ground (Sithole and Vosselman 2004). This assumption will cause that the filtered DTM is not able to approximate the real ground. Consequently, we used the statistical outlier removal (SOR) algorithm to remove outliers from an intuitive point of view that they are generally scattered far away from their neighbors (Rusu *et al.* 2007). Its core



idea is that in a local neighborhood, the average distance of outliers will be significantly larger than other points.

We compute the average distance d_i^K of each point p_i ($i = 1, 2, \dots, n$) based on K -nearest neighbors (KNN). By traversing each point p_i , if d_i^K of it does not exceed the sum of the average distance and η times the standard deviation, then we label it as an outlier point. The maximum distance threshold can be defined as Equation 1.

$$D_{max} = D_{mean} + \eta \times \sigma \quad (1)$$

where D_{max} denotes the max distance threshold; D_{mean} is the mean value of KNN average distance of all points; σ is the corresponding standard deviation; and η is the standard deviation multiplication factor.

Because the average distance of KNN obeys a normal distribution, the standard deviation multiplier η can be selected according to its probability density function curve. According to the three sigma rule, when η is equal to 3, the proportion of the number of regular lidar points is about 99.73% (Pukelsheim 1994). Generally, a large value of η may result in more outliers in filtering. In contrast, a small value of η may cause a lower number of processing points. Also, the value of K must be large enough to avoid mistakes in calculating the average distance of KNN. Obviously, for different lidar point clouds densities, appropriate K value needs to be adjusted to remove outliers based on visual inspection. The specific workflow of the SOR algorithm to remove outliers is shown in Figure 2. The blue ellipse represents KNN, and the SOR algorithm traverses each point and calculates its KNN. By comparing the average distance of KNN at point p_i with the distance threshold, the high and low outliers are eliminated. According to previous research (Carrilho *et al.* 2018), no algorithm can eliminate all outliers, so manual corrections are needed with visual inspection.

Surface Interpolation by Using TPS

We use a surface interpolation strategy to deal with the influence of the drastically changing terrain slope in the filtering algorithm (Mongus and Žalik 2012). Generally, interpolated surfaces should accurately approximate the terrain and be sufficiently smooth. According to previous research (Evans and Hudak 2007), the TPS function is most suitable for interpolating spatial data. Given a set $C \{c_s(x_s, y_s, z_s) | s = 1, 2, \dots, n\}$ containing n three-dimensional control points, TPS fits an interpolation function $f(x, y)$ that passes through control points precisely and minimizes the so-called bending energy. In a two-dimensional space, the bending energy \mathcal{E}_f is defined as the integral on the square of the second derivative, as shown in Equation 2 (Wahba 1990).

$$\mathcal{E}_f = \iint_{\mathbb{R}^2} \left[\left(\frac{\partial^2 f}{\partial x^2} \right)^2 + 2 \left(\frac{\partial^2 f}{\partial x \partial y} \right)^2 + \left(\frac{\partial^2 f}{\partial y^2} \right)^2 \right] dx dy$$

where f is the interpolation function $f(x, y)$ and (dx, dy) is the

differential of $f(x, y)$ in the x and y directions. Therefore, to meet the above conditions, the interpolation function $f(x, y)$ can be expressed as Equation 3.

$$f(x, y) = a_1 + a_2 x + a_3 y + \sum_{s=1}^n w_s \varphi(\|(x_s, y_s) - (x, y)\|) \quad (3)$$

where a_1, a_2, a_3 are coefficients reflecting the overall trend of the interpolation surface; w_s denotes the weight related to the control points; n is the number of control points; and (x_s, y_s) is the x, y coordinate value of control point c_s . $\varphi(\cdot)$ is the radial basis kernel $\varphi(r) = r^2 \ln r$ corresponding to TPS. As mentioned before, only if $f(x, y)$ meet Equation 4, it has square-integrable second derivatives.

$$\sum_{s=1}^n w_s = \sum_{s=1}^n w_s x_s = \sum_{s=1}^n w_s y_s = 0 \quad (4)$$

To solve the unknown TPS weights column vector \mathbf{w} (composed of $w_s, s \in \{1, 2, \dots, n\}$) and trend coefficients column vector \mathbf{a} (composed of a_1, a_2, a_3), the following linear system of TPS interpolation can be used:

$$\begin{bmatrix} \mathbf{U} & \mathbf{P} \\ \mathbf{P}^T & \mathbf{0} \end{bmatrix} \begin{bmatrix} \mathbf{w} \\ \mathbf{a} \end{bmatrix} = \begin{bmatrix} \mathbf{v} \\ \mathbf{0} \end{bmatrix} \quad (5)$$

where \mathbf{U} is a matrix defined by $U_{ij} = \varphi(\|(x_i, y_i) - (x_j, y_j)\|)$, $i, j \in \{1, 2, \dots, n\}$; (x_i, y_i) and (x_j, y_j) are the x and y coordinate values of the i th control point c_i and j th control point c_j , respectively. \mathbf{P} and \mathbf{v} can be represented as Equation 6.

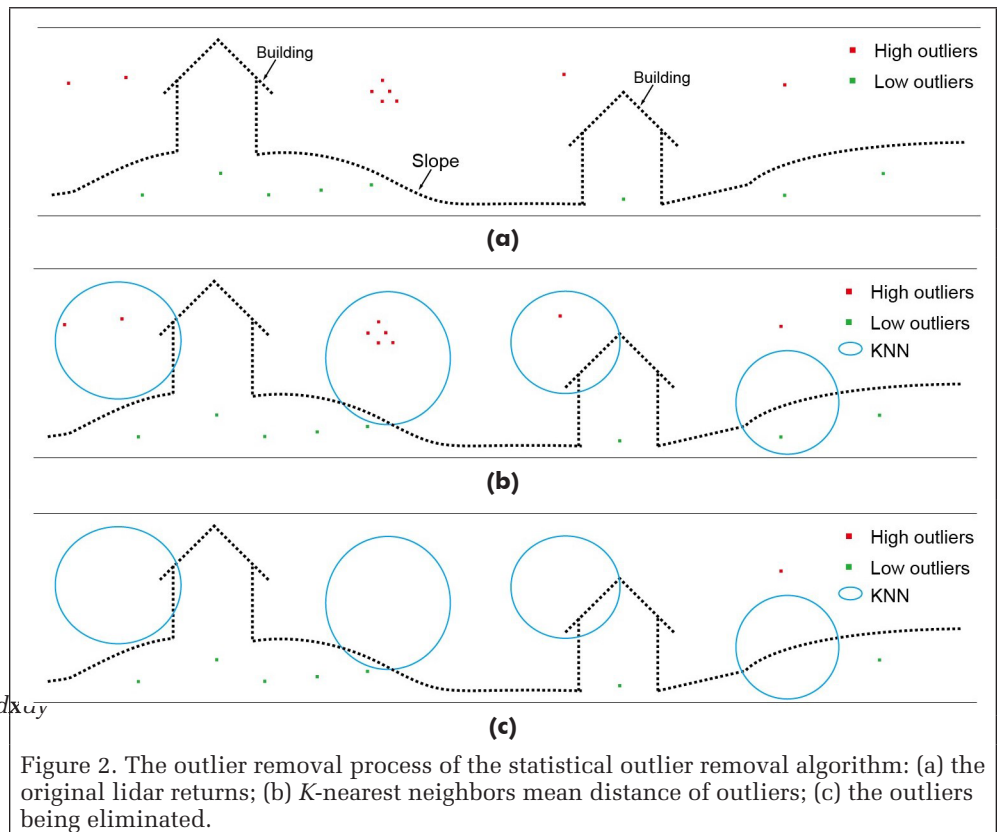


Figure 2. The outlier removal process of the statistical outlier removal algorithm: (a) the original lidar returns; (b) K -nearest neighbors mean distance of outliers; (c) the outliers being eliminated.

$$\mathbf{P}_{n \times 3} = \begin{bmatrix} 1 & x_1 & y_1 \\ 1 & x_2 & y_2 \\ \vdots & \vdots & \vdots \\ 1 & x_n & y_n \end{bmatrix}; \mathbf{v}_{n \times 1} = \begin{bmatrix} z_1 \\ z_2 \\ \vdots \\ z_n \end{bmatrix} \quad (6)$$

where the elements in the matrix come from the coordinate values of control points set $C \{c_s(x_s, y_s, z_s) | s = 1, 2, \dots, n\}$; n is the number of control points.

The calculation complexity of the global interpolation of TPS is relatively high. Generally speaking, we only select the neighbor of the interpolation point as the control point for the local calculation. In this article, we choose the KNN of the interpolation point as the neighborhood. After experimental analysis, we set K to 12 by default. We represent the terrain characteristics of the lidar point clouds by DSM (Figure 3). According to the TPS interpolation method described, the interpolation surface can thus be built. Note that the constructed surface passes through all control points in the variable neighborhood.

Constraints of Iterative Hierarchical Curvature

In this step, the used surface-based filter repeatedly traverses and processes all points at each level λ of the hierarchy. As shown in Figure 4b–d, both the grid size gw and the curvature threshold t simultaneously change from level 1–3. We adopt the local minimum algorithm of the maximum window size W to initialize ground seeds at level $\lambda = 1$. The more ground points are added in each λ , the closer the constructed surface is to the ground. In general, the criterion is to set an

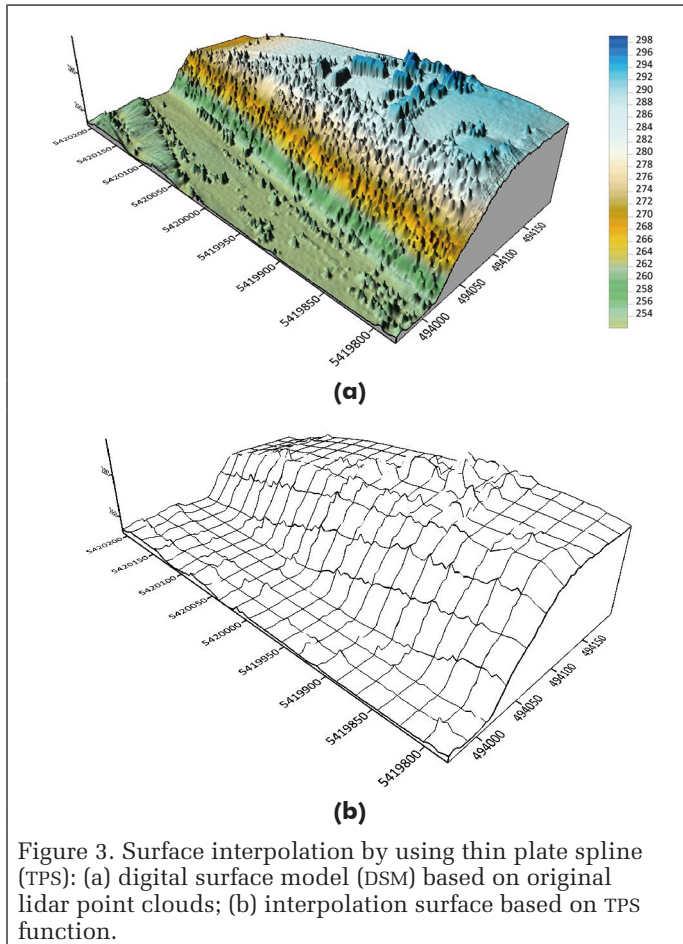


Figure 3. Surface interpolation by using thin plate spline (TPS): (a) digital surface model (DSM) based on original lidar point clouds; (b) interpolation surface based on TPS function.

appropriate distance threshold in the local neighborhood of a point. That is, the curvature threshold value t is added to the local average elevation value to obtain the local curvature γ . Therefore, nonground points can be filtered out as many as possible by comparing the elevation of the measuring point and the corresponding local curvature γ . After the final iteration is completed, we will get a rough DTM. The gw and t values change at each level to effectively cope with the influence of drastically changing terrain slope.

The detailed process of the hierarchical curvature filtering for lidar point clouds is as follows:

1. A surface grid ξ is constructed by using TPS function and ground control points. The two input parameters are the grid size gw and the curvature threshold t , which are specified by the user.
2. Calculating curvature at each level λ . A 3×3 moving mean window is passed over ξ . Similar to the process of image convolution, the new pixel value $z'(m, n)$ is thus calculated. Therefore, the corresponding local curvature γ is as follows.

$$\gamma(m, n) = z'(m, n) + t \quad (7)$$

where $z'(m, n)$ represents the grid cell in the m th row and n th column calculated by the 3×3 mean kernel; t is the corresponding curvature threshold at the current λ .

3. Ground points are separated according to local curvature. By traversing each point $p_i(x_i, y_i, z_i)$, if it meets the following conditions, it will be marked as a ground point and added to the control point set C .

$$\text{if } z_i < \gamma, \text{ then classify as ground point} \quad (8)$$

where γ is the corresponding local curvature.

4. According to the updated C , a new interpolated surface grid ξ' is constructed using TPS. It is based on a strategy of progressive encryption to produce precise results.
5. Repeat steps 2–5 until the iteration number of the nested loop arrives three (namely, the traversal counter N reaches 3). This is to avoid over-fitting the ground.
6. Repeat steps 2–6. Both the grid size gw and the curvature threshold t simultaneously change from the current λ to the next one. Specifically, $gw = gw/2$ while $t = t + 0.1$, $\lambda = \lambda + 1$.

Relative Elevation Calculation

The height difference is an important indicator to distinguish between ground and nonground. The algorithm assumes that if the height difference of a point is higher than its neighbors it is thus considered as nonground points. However, it will fail when encountering terrains with sharp gradients such as steep slopes or cliffs. We will calculate the relative elevation point by point to enhance the ability of the filter to identify terrain details. Similar to the traditional definition of relative elevation, our method selects the aforementioned interpolation surface as the reference surface. The distance along the plumb line from each point in the lidar point clouds to the reference surface is called relative elevation. In this paper, we choose the ground points obtained by the hierarchical curvature in the section “Constraints of Iterative Hierarchical Curvature” as the control points. Then, TPS is used to interpolate to generate a reference surface. Therefore, the relative elevation of a point can be expressed as Equation 9:

$$\Delta H = H - H_\xi \quad (9)$$

where H is the coordinate value of each point $p_i(x_i, y_i, z_i)$ in the z -direction; H_ξ is the interpolated elevation of the

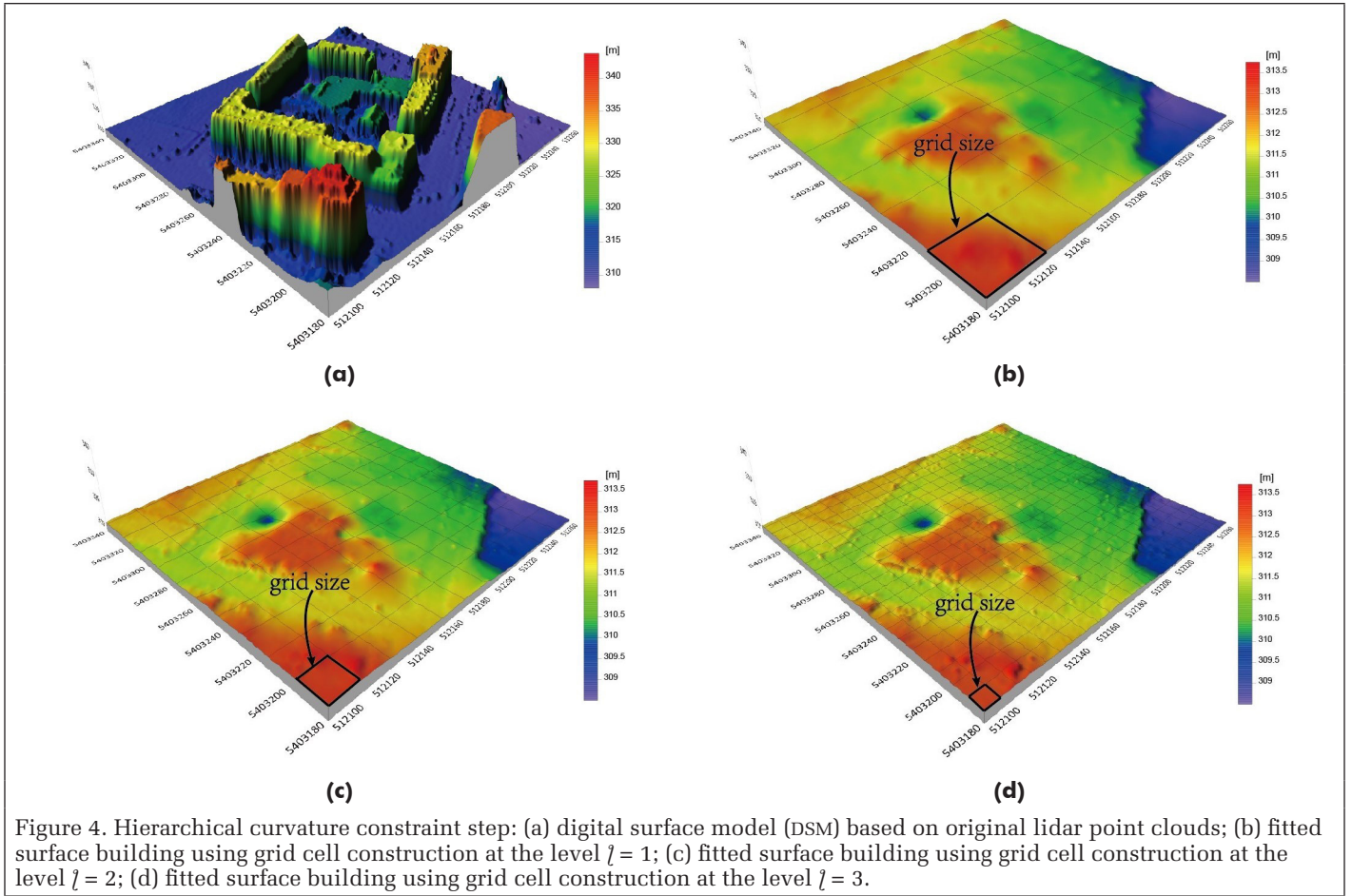


Figure 4. Hierarchical curvature constraint step: (a) digital surface model (DSM) based on original lidar point clouds; (b) fitted surface building using grid cell construction at the level $l = 1$; (c) fitted surface building using grid cell construction at the level $l = 2$; (d) fitted surface building using grid cell construction at the level $l = 3$.

reference surface grid \mathcal{S} corresponding to p_i ; and ΔH is the relative elevation.

The reference surface is denoted as a black dashed line, while the real terrain surface is represented as a solid black line in Figure 5. Based on the relative elevation formula, we can calculate the relative elevation of the ground and objects, which is represented by the red straight line with two arrows. Intuitively, by comparing the relative elevations of all points, we can easily extract the ground points from the lidar returns. It is because even if a point is located in a steep slope area, its relative elevation will still be smaller than a point situated in a building or tree. In this way, the proposed filtering algorithm can well maintain the detailed features of the earth while removing objects.

Ground Points Extraction Using the EM Algorithm

Based on statistical methods, the posterior probability of each point p_i belonging to a specific category can be calculated to achieve adaptive filtering, as expressed in Equation 10 and Equation 11.

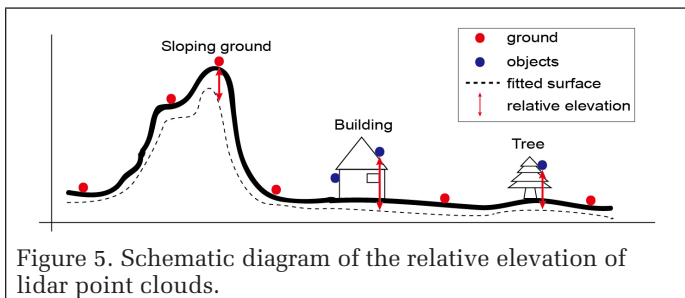


Figure 5. Schematic diagram of the relative elevation of lidar point clouds.

$$P(G|p_i) = \frac{P(p_i|G)P(G)}{P(p_i)} \quad (10)$$

$$P(NG|p_i) = \frac{P(p_i|NG)P(NG)}{P(p_i)} \quad (11)$$

where $P(G|p_i)$ and $P(NG|p_i)$, respectively, denotes the posterior probability of a ground point (G) and a nonground point (NG), $P(G)$ represents the prior probability of G , and $P(NG)$ is the prior probability of NG . $P(p_i) = P(p_i|G)P(G) + P(p_i|NG)P(NG)$, which is calculated according to the total probability theorem.

If $P(G|p_i)$ is larger than 0.5, we will regard p_i as G . Since there are only two classes (ground and objects) as Gaussian mixture model components. According to the Bayesian formula, the posterior probability of p_i belonging to each category will be calculated indirectly by calculating the conditional probability of each category as follows:

$$P(p_i|\theta) = \sum_{k=1}^2 \alpha_k \phi(\Delta H_i | \theta_k) \quad (12)$$

where α_k is the mixing coefficient and $\alpha_k \geq 0$; ΔH_i is the relative elevation of the point p_i ; $\phi(\cdot)$ is the Gaussian probability density function; and $\theta_k = (\mu_k, \sigma_k)$ is its parameters. μ_k denotes the mean of ΔH_i , while σ_k is the standard deviation of ΔH_i . We express the Gaussian probability density function as Equation 13.

$$\phi(\Delta H_i|\theta_k) = \frac{1}{\sqrt{2\pi}\sigma_k} \exp\left(-\frac{(\Delta H_i - \mu_k)^2}{2\sigma_k^2}\right) \quad (13)$$

Because of the probability model used, there are both observable variables ΔH_i and latent variables G and NG . Therefore, the maximum likelihood method cannot be used directly for parameter estimation. The EM algorithm provides an approximate solution for probability models with latent variables. Four main steps are employed to realize the EM algorithm (Dempster *et al.* 1977).

1. Initialize input parameters, including α_k , μ_k , and σ_k , $k = 1, 2$.
At first, we initialize α_1 as the proportion of the number of ground seeds at $l = 3$ in the section “Constraints of Iterative Hierarchical Curvature”, while α_2 is the proportion of the final number of nonground points. Note that $\alpha_1 + \alpha_2 = 1$. $\mu_1, \mu_2, \sigma_1, \sigma_2$ can be determinate according to Equation 14 based on the relative elevations of G and NG .

$$\begin{cases} \mu = \frac{1}{n} \sum_{i=1}^n \Delta H_i \\ \sigma = \sqrt{\frac{1}{n} \sum_{i=1}^n (\Delta H_i - \mu)^2} \end{cases} \quad (14)$$

where ΔH_i is the relative elevation; n is the total number of lidar points; μ is the mean of ΔH_i ; and σ is the standard deviation of ΔH_i .

2. E step: Calculating the membership probability expectations of the submodel to the observed data points including $P(G|p_i)$ and $P(NG|p_i)$.
3. M step: Calculating the model parameters (α_k, μ_k and σ_k , $k = 1, 2$) of the new iteration of the Gaussian mixture model.

The M step in the iteration is to look for the maximum value of the membership probability expectations in the E step to calculate the new iteration parameters. The algorithm calculates its partial derivative to the parameters separately and makes it 0. The updated parameter value can be expressed by the following Equations 15–17.

$$\begin{cases} \alpha_1 = \frac{\sum_{i=1}^n P(G|p_i)}{\sum_{i=1}^n P(G|p_i) + \sum_{i=1}^n P(NG|p_i)} \\ \alpha_2 = \frac{\sum_{i=1}^n P(NG|p_i)}{\sum_{i=1}^n P(G|p_i) + \sum_{i=1}^n P(NG|p_i)} \end{cases} \quad (15)$$

where α_1, α_2 are the updated percentage coefficients in the Gaussian mixture model; $P(G|p_i)$ and $P(NG|p_i)$ are the posterior probability of a ground point (G) and a nonground point (NG), respectively; and n is the total number of lidar points.

$$\begin{cases} \mu_1 = \frac{\sum_{i=1}^n P(G|p_i) \Delta H_i}{\sum_{i=1}^n P(G|p_i)} \\ \mu_2 = \frac{\sum_{i=1}^n P(NG|p_i) \Delta H_i}{\sum_{i=1}^n P(NG|p_i)} \end{cases} \quad (16)$$

where ΔH_i is the relative elevation and μ_1, μ_2 are the updated mean value of the relative elevation of ground points and nonground points.

$$\begin{cases} \sigma_1^2 = \frac{\sum_{i=1}^n P(G|p_i) (\Delta H_i - \mu_1)^2}{\sum_{i=1}^n P(G|p_i)} \\ \sigma_2^2 = \frac{\sum_{i=1}^n P(NG|p_i) (\Delta H_i - \mu_2)^2}{\sum_{i=1}^n P(NG|p_i)} \end{cases} \quad (17)$$

where σ_1, σ_2 are the updated standard deviation of the relative elevation of ground points and nonground points.

4. Convergence conditions of the EM algorithm.

The EM algorithm repeats steps 1–4 until the model parameters no longer change, i.e., the algorithm will stop computing until the updated parameters of the current calculation are equal to the parameters of the last iteration.

Experiment and Discussion

Data Set and Accuracy Measure Index

We selected 15 data samples provided by the International Society for Photogrammetry and Remote Sensing (ISPRS), Commission III, Working Group III, for algorithm assessment (Sithole and Vosselman 2003). These data were collected in the rural area of Vaihingen and the urban area of Stuttgart. The sample point spacing in urban areas is 1–1.5 m, while that in rural areas is 2–3.5 m. Since the original intention of the data set is to test the robustness of the filter algorithms, it contains many challenging and complex terrains. The specific terrain details are described in Table 1 (Sithole and Vosselman 2004).

Table 1. Characteristics of 15 samples provided by the International Society for Photogrammetry and Remote Sensing.

Region	Sample	Features
Urban	11	Mixture of vegetation and buildings on hillside
	12	Buildings on hillside
	21	Large buildings and bridge
	22	Irregularly shaped buildings
	23	Large, irregularly shaped buildings
	24	Steep slopes
	31	Complex buildings
	41	Data gaps
Rural	42	Railway station with trains
	51	Mixture of vegetation and buildings on hillside
	52	Buildings on hillside
	53	Large buildings and bridge
	54	Irregularly shaped buildings
	61	Large, irregularly shaped buildings
	71	Steep slopes

The filtering effect of the proposed algorithm is accurately calculated by comparing it with the labels of the test data set. We choose following four commonly used indicators for analysis: Type I error (E_{I}), Type II error (E_{II}), total error (E_t), and Cohen’s kappa coefficient. Among them, kappa is a useful indicator for the consistency of classification results, so it is often used to assess the classification of remote sensing images (Congalton 1991). Based on the confusion matrix, the four accuracy indicators can be calculated by the formulas in Table 2. It is worth noting the four essential elements (TP, FN, FP, TN) in the confusion matrix, where TP and TN represent the numbers for correctly classified ground and nonground points, respectively, while FN and FP, respectively, denote the numbers of wrongly classified ground and nonground points.

Table 2. Formulas of the four indicators E_I, E_II, E_t, and kappa.

	Filtered		Intermediate Parameters
	Ground	Nonground	$e = TP + FN + FP + TN$
Reference			
Ground	TP	FN	$P(a) = (TP + TN)/e$
Nonground	FP	TN	$P(e) = ((TP + FP) * (TP + FN) + (FP + TN) * (FN + TN)) / (e * e)$
Metric formula			
	$E_I = FN / (TP + FN)$		
	$E_{II} = FP / (FP + TN)$		
	$E_t = (FN + FP) / e$		
	$kappa = (P(a) - P(e)) / (1 - P(e))$		

Table 3. Parameters and descriptions.

Parameter	Description	Range
W	The selection of W is based on the largest building size in the test area, when the local minimum algorithm is used to select the initial ground seed points. If the value is too small, it is easy to include nonground points; if it is too large, few ground points will be obtained.	6–130 m
gw	The value represents the size of the surface grid constructed using the thin plate spline function, which is used to accurately approximate the real bare earth surface for curvature constraints.	2–4 m
t	t represents curvature threshold, which determines whether a measurement point belongs to the ground. The selection rule is that the smaller the value, the smaller the terrain gradient. Therefore, a propriate t can eliminate the influence of terrain slope changes and filter nonground points.	0.4–1.7 m

Results and Discussion

Parameter Analysis

In this section, we discuss the effects of using different parameters. The proposed algorithm mainly involves three parameters: the maximum window size W , the surface grid size gw , and the curvature threshold t . The specific description is shown in Table 3.

Two typical cases, samp21 and samp41, are used to analyze the change pattern of kappa value in order to optimize the choice of the three parameters. As shown in Figure 6, gw and W have insignificant changes on kappa value of each sample. The reason may be that the distribution pattern of nonground points is relatively uniform in each sample area. Another possible reason is that the ground points are the majority among those samples. On the one hand, W is used to initialize the ground seed point and the recommended value is the largest building size in the area in order to ensure that the local area can obtain the ground points. On the other

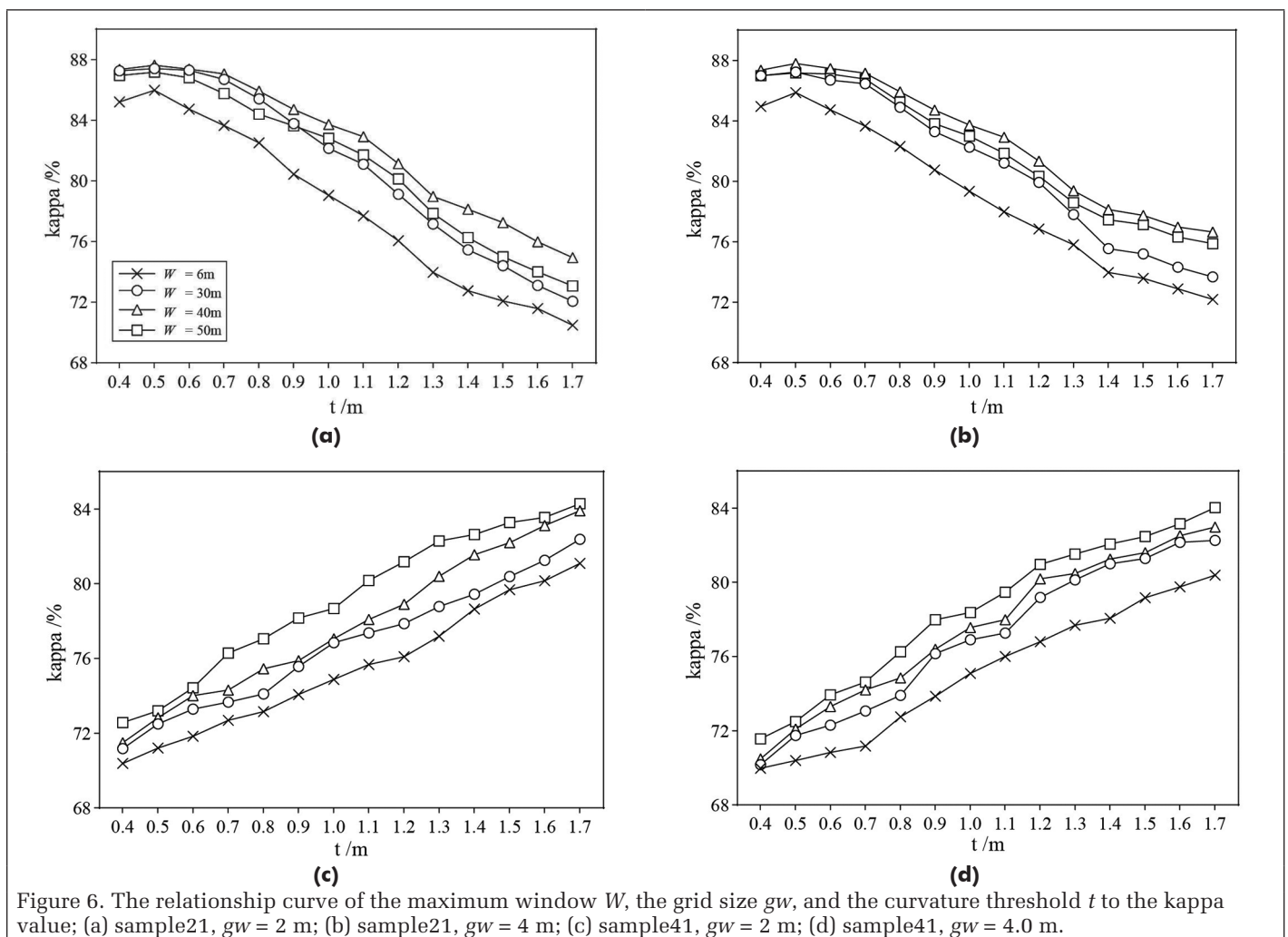


Figure 6. The relationship curve of the maximum window W , the grid size gw , and the curvature threshold t to the kappa value; (a) sample21, $gw = 2$ m; (b) sample21, $gw = 4$ m; (c) sample41, $gw = 2$ m; (d) sample41, $gw = 4.0$ m.

hand, since gw is a parameter used to interpolate the surface grid of the TPS function, it can be set to 4 m when the nonground points in the area are more uniformly distributed. The reason for this is that the number of interpolation grid cells is decreased and thus the filtering efficiency is improved due to reduced computational complexity.

In comparison, t has a relatively large influence on κ . Take samp21 as an example (Figure 6a and 6b); t only needs to be 0.5 to achieve a κ value above 80%, as the overall terrain gradient barely changes. However, when t is greater than 0.5, as t increases, more nonground points are mistakenly regarded as ground points. It results in a decrease in the κ value. On the contrary, since samp41 is located in a rugged terrain zone, it is characterized by large changes in topographic gradient. When the t value gradually increased to 1.7 m, the κ value of samp41 continued to increase. On the whole, t can compensate for the influence of terrain gradient during filtering.

Quality Evaluation

To test the best performance of the proposed method, the optimal set of parameters W , gw , and t were determined by minimizing κ . The optimized results for each of the fifteen samples is shown in Table 4. In general, the numerical range of the initial grid size is from 2 m to 4 m. This setting is compatible with the point spacing of the sample area. The curvature threshold t is ranging from 0.4 m to 1.7 m. It is the only parameter that needs to be set according to the terrain of the test region. In rural sites with forests, we usually choose more than 0.7 m due to the drastically changing terrain. The maximum window size of the initial ground seed varies from 6 m to 130 m, which is set according to the largest building size in the test area.

In these samples, the value of E_t ranges from 1.09% to 11.84%. Regarding specific samples, the algorithm performs the worst in samp53. It is mainly because the large buildings and bridges in the area cause more E_{II} errors on their borders. Excluding this sample, the algorithm has achieved excellent results in most rural areas (samp51, samp52, samp54,

samp61, samp71). It proves that our algorithm is robust enough in rugged terrain with vegetation, thus performing well in complicated terrain, such as samp11 (a sloped area mixed with vegetation and buildings), a kind of terrain that usually troubles other filters (Zhang *et al.* 2016). Overall, the average E_t and κ of the algorithm are 6.91% and 80.9%, respectively.

It is worth mentioning that each E_{II} of samp11, samp24, and samp52 is significantly higher than E_I , for two reasons. First, a large part of the buildings is located on relatively steep terrain, which leads to insignificant differences between the edges of these buildings and the ground. Second, the number of terrain points is larger than that of nonterrain points. According to the calculation formula of E_{II} , even if a few nonterrain points are misclassified, it will finally cause a larger E_{II} .

Figures 7–10 show the DTM and error spatial distribution obtained by our filtering algorithm on each sampled ground. Through comparative observation, we found that steep terrain that mixes vegetation and buildings is a significant challenge for the proposed filter. As depicted in samp11(d), samp51(d), and samp52(d), the error is mainly distributed in the narrow strip along the edge of the building facade. The reason for this error is that the gradient difference between the ground and objects is tiny on steep terrain. Therefore, the classification criteria of the adaptive filter will not work in this case. The rugged mountain landscape, such as sharp ridges and rapidly changing cliffs, is another challenge to our approach. As shown in Figures 9 and 10, samp52(d) and samp53(d) show many E_I along the ridgeline. It is consistent with the performances of most algorithms (Bayram *et al.* 2018; Liu and Lim 2018; Shi *et al.* 2018). Although the terrain with drastic gradient changes can be preserved as much as possible through the calculation of relative elevation, it is difficult to ultimately maintain its morphological characteristics due to the grid resolution. Furthermore, it is manifested that the filtered DTM is thus smoothed in the ridge and steep slope regions. However, the proposed method can still maintain the main terrain features while suppressing E_I .

Seen from samp53 (d) and samp61 (d) in Figure 10, our method treats some small vegetation points mistakenly as ground. It is because of the high density of low vegetation in rural areas, which makes it challenging to obtain accurate ground seed points. Conversely, inaccurately interpolated surfaces cause more vegetation points to be wrongly regarded as ground points. Besides, the height difference of low vegetation is not significant enough. These two reasons together lead to E_{II} in samp53 and samp61. Nevertheless, most of the forest landscape is still effectively removed. It indicates that our method is sufficiently robust to the shape and size of nonground points.

In general, the ability of our method to preserve discontinuous terrain is attributed to the reduction of E_I , which can be demonstrated through the hierarchical curvature constraint step. Through the initial ground seed, the fitted surface gradually approaches the real terrain. Therefore, the relative elevation difference between the ground and nonground points is highlighted. Besides, due to the subsequent optimization process of the EM algorithm, the final result is controlled within an acceptable range.

In the 15 study sites, the DTM filtered by our algorithm is almost the same as the reference DTM in terms of the main morphological structure. These results indicate that our algorithm can well preserve terrain features while filtering out most objects. Besides, the distributions of E_I and E_{II} are sparse in general, which demonstrates that the proposed algorithm is robust to various complex environments.

Table 4. Four accuracy indicators of optimized results and corresponding parameter sets.

Study Site	Parameter Set (m)			Optimized Results (%)			
	W	gw	t	E_I	E_{II}	E_t	κ
samp11	35	2	0.9	6.26	16.64	10.42	78.03
samp12	30	2	0.6	5.88	4.31	5.17	89.59
samp21	40	4	0.5	3.52	4.95	3.78	87.8
samp22	40	2	0.9	7.67	9.62	8.22	80.33
samp23	24	2	1.3	6.71	9.73	8.09	83.67
samp24	24	2	0.9	7.77	18.4	10.27	72.08
samp31	50	4	0.4	2.99	1.78	2.47	94.96
samp41	50	2	1.7	11.79	3.63	7.87	84.28
samp42	130	4	0.9	5.58	1.98	2.95	92.48
samp51	30	4	0.8	9.09	8.11	8.91	83.41
samp52	30	4	0.7	7.21	17.41	7.95	76.09
samp53	6	4	0.9	11.64	18.49	11.84	45.05
samp54	30	4	0.7	5.1	4.3	4.69	90.61
samp61	6	4	0.7	0.9	9.94	1.09	76.72
samp71	20	2	0.7	6.71	8.41	6.85	84.17
Avg	— ^a	—	—	7.07	8.95	6.91	80.9

^aDashes indicate xxxx.

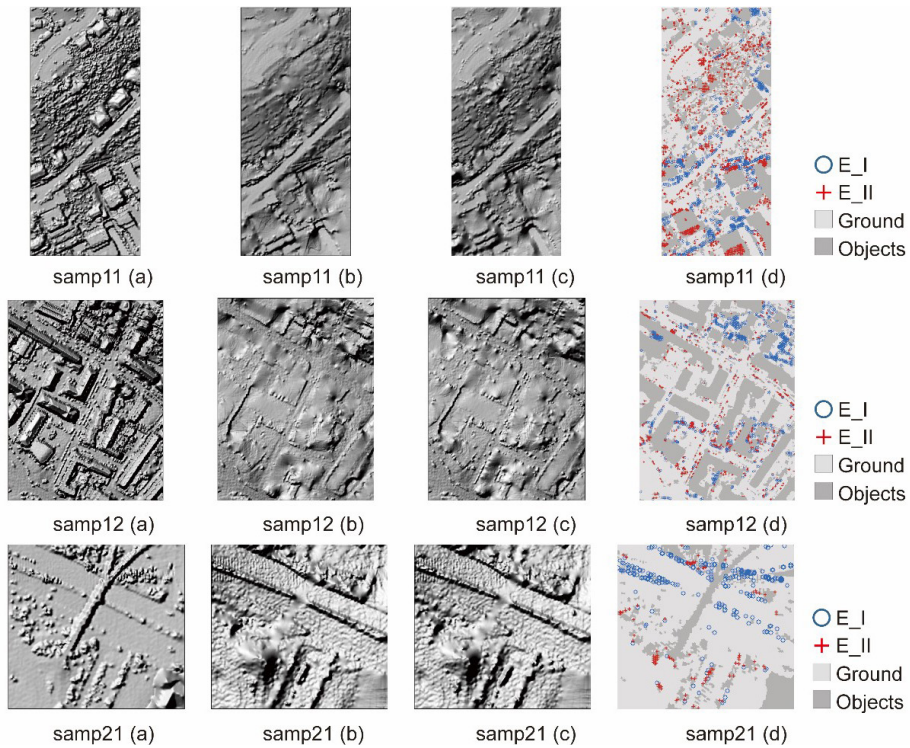


Figure 7. Visualization of filtering results and error distribution for samp11-21: (a) digital surface model constructed based on the original point cloud; (b) digital terrain model (DTM) built based on real terrain points; (c) DTM built based on filtered terrain points; (d) the distributions of E_I and E_{II} .

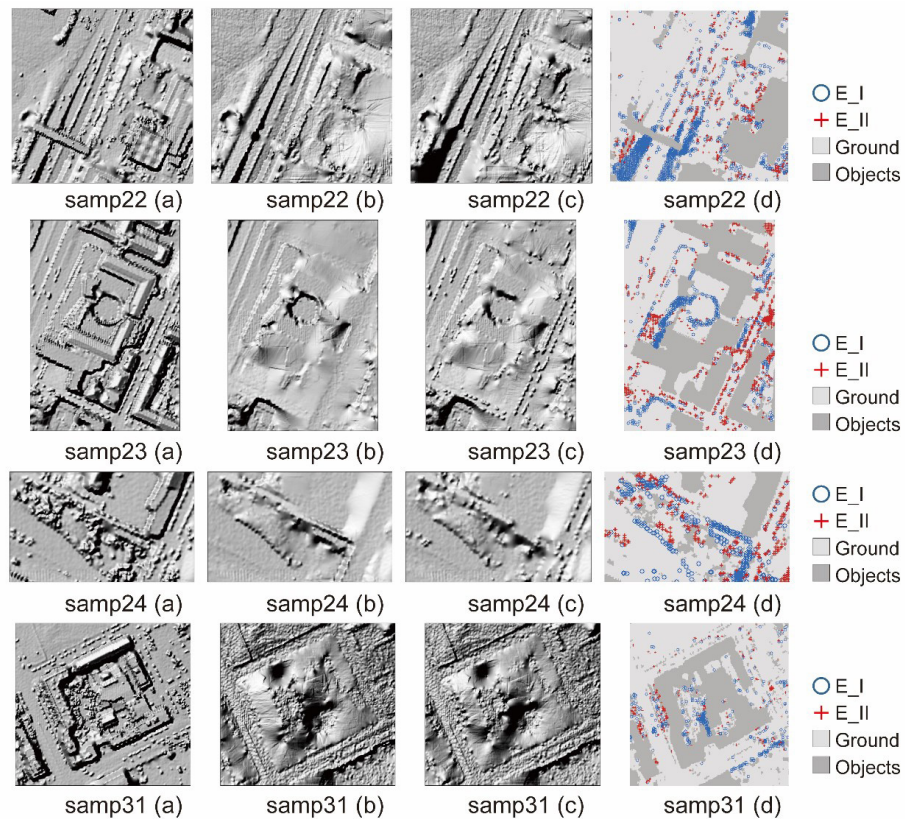


Figure 8. Visualization of filtering results and error distribution for samp23-31: (a) digital surface model constructed based on the original point cloud; (b) digital terrain model (DTM) built based on real terrain points; (c) DTM built based on filtered terrain points; (d) the distributions of E_I and E_{II} .

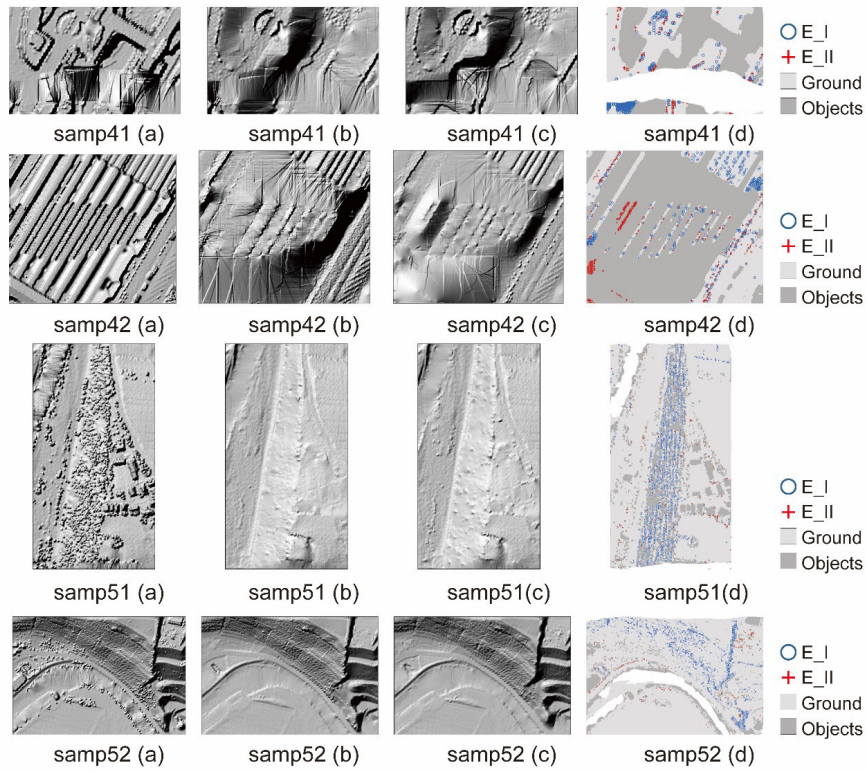


Figure 9. Visualization of filtering results and error distribution for samp41-52: (a) digital surface model constructed based on the original point cloud; (b) digital terrain model (DTM) built based on real terrain points; (c) DTM built based on filtered terrain points; (d) the distributions of E_I and E_{II} .

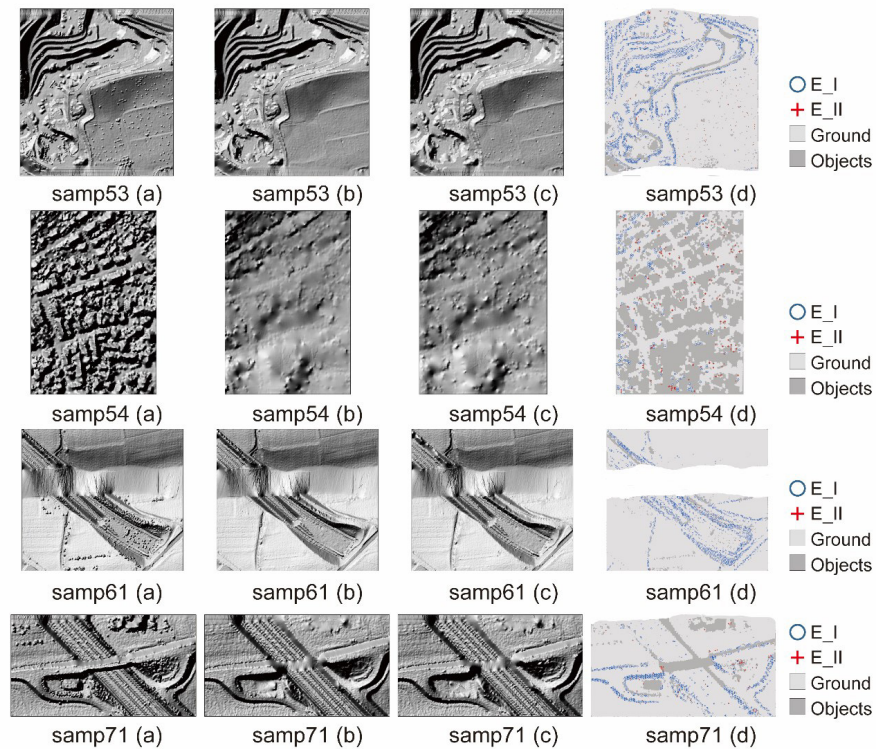


Figure 10. Visualization of filtering results and error distribution for samp53-71: (a) digital surface model constructed based on the original point cloud; (b) digital terrain model (DTM) built based on real terrain points; (c) DTM built based on filtered terrain points; (d) the distributions of E_I and E_{II} .

Method Comparison

Table 5 shows the E_t of our algorithm and eight classical filtering algorithms in 15 test samples. In general, all algorithms can achieve good performance in relatively flat areas but are not satisfactory for complex terrains. Compared with the other eight algorithms, our algorithm is the second-best overall (Figure 11 and Figure 12). Furthermore, it reached

the lowest E_t in three out of the 15 samples. Among the remaining twelve samples, Axelsson's algorithm and Pfeifer's algorithm reached 10 and 2 lowest E_t , respectively.

In particular, the proposed algorithm performs the best on samp11, samp41, and samp61. These results demonstrate that our method has superior adaptability when dealing with terrain with data gaps and bridges. In order to confirm

Table 5. Comparison of E_t of our method and eight classic filtering algorithms for 15 study sites (%).^a

Study Site	Elmqvist	Sohn	Axelsson	Pfeifer	Brovelli	Roggero	Wack	Sithole	Ours
samp11	22.4	20.49	10.76	17.35	36.96	20.8	24.02	23.25	10.42
samp12	8.18	8.39	3.25	4.50	16.28	6.61	6.61	10.21	5.17
samp21	8.53	8.80	4.25	2.57	9.30	9.84	4.55	7.76	3.78
samp22	8.93	7.54	3.63	6.71	22.28	23.78	7.51	20.86	8.22
samp23	12.28	9.84	4.00	8.22	27.80	23.2	10.97	22.71	8.09
samp24	13.83	13.33	4.42	8.64	36.06	23.25	11.53	25.28	10.27
samp31	5.34	6.39	4.78	1.80	12.92	2.14	2.21	3.15	2.47
samp41	8.76	11.27	13.91	10.75	17.03	12.21	9.01	23.67	7.87
samp42	3.68	1.78	1.62	2.64	6.38	4.30	3.54	3.85	2.95
samp51	23.31	9.31	2.72	3.71	22.81	3.01	11.45	7.02	8.91
samp52	57.95	12.04	3.07	19.64	45.56	9.78	23.83	27.53	7.95
samp53	48.45	20.19	8.91	12.60	52.81	17.29	27.24	37.07	11.84
samp54	21.26	5.68	3.23	5.47	23.89	4.96	7.63	6.33	4.69
samp61	35.87	2.99	2.08	6.91	21.68	18.99	13.47	21.63	1.09
samp71	34.22	2.20	1.63	8.85	34.98	5.11	16.97	21.83	6.85
Avg	20.87	9.35	4.82	8.02	25.78	12.35	12.04	17.48	6.91

^aBoldface represents the algorithm with the lowest E_t .

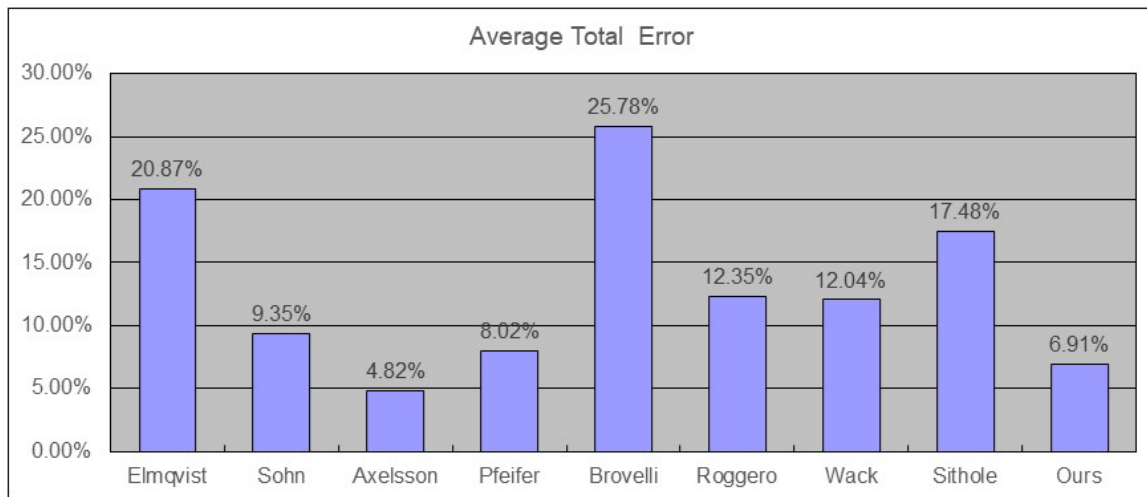


Figure 11. Histogram of the average E_t of eight classic filtering algorithms.

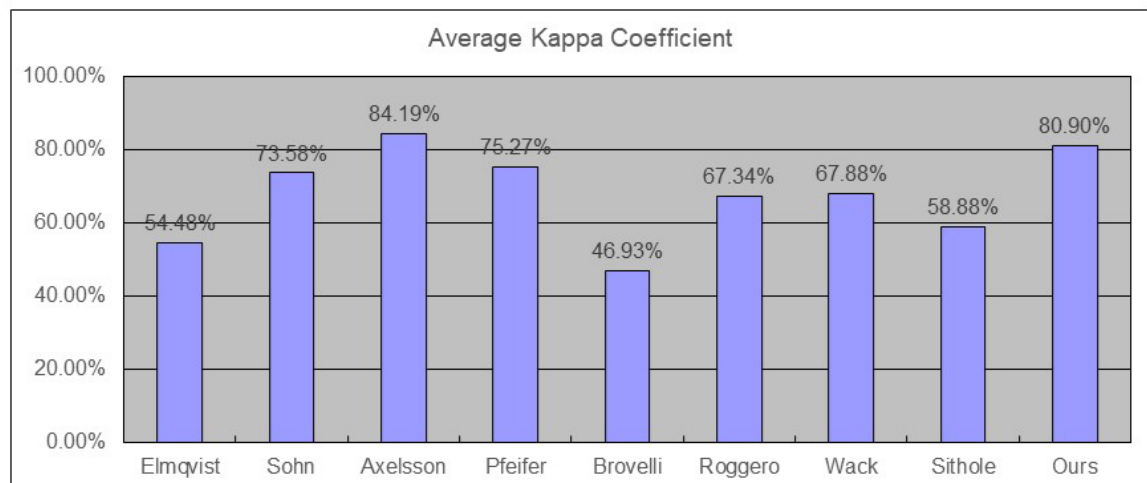
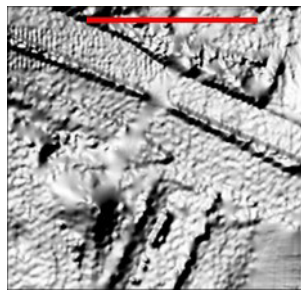
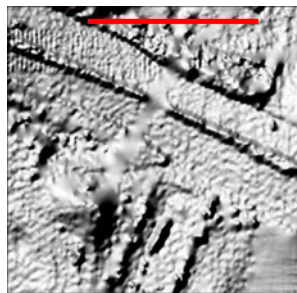


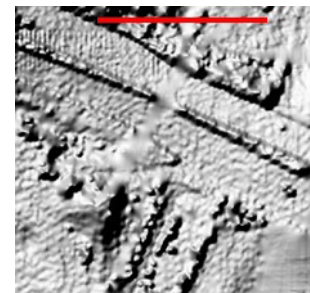
Figure 12. Histogram of the average kappa of eight classic filtering algorithms.



(a) Reference DTM



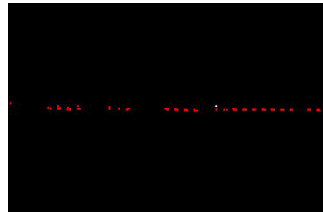
(b) Our DTM



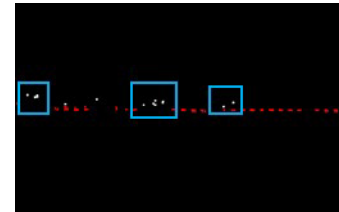
(c) Axelsson's DTM



(d) Reference cross-section



(e) Our cross-section

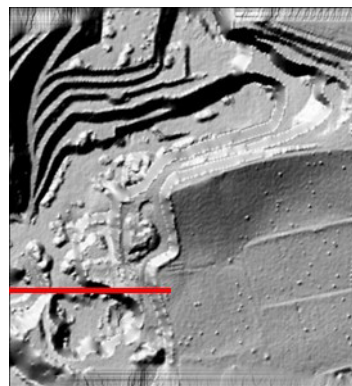


(f) Axelsson's cross-section

Figure 13. Comparison of our method, Axelsson's method and reference data regarding maintaining terrain discontinuities. Shaded relief terrain of samp21 generated using (a) reference data, (b) ours, and (c) Axelsson's. The filtered cross section is identified by the red horizontal line from (d) reference data, (e) ours, and (f) Axelsson's. White points denote nonground point, orange-red points denote ground points, and blue rectangle represents E_II error.



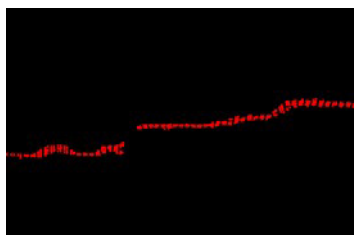
(a) Reference DTM



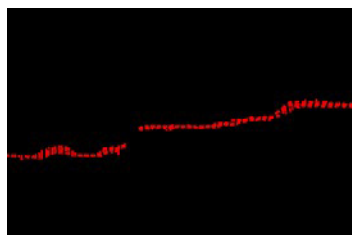
(b) Our DTM



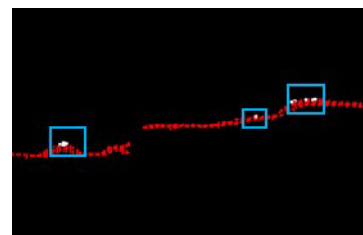
(c) Axelsson's DTM



(d) Reference cross-section



(e) Our cross-section



(f) Axelsson's cross-section

Figure 14. Comparison of our method, Axelsson's method and reference data regarding maintaining terrain discontinuities. Shaded relief terrain of samp53 generated using (a) reference data, (b) ours, and (c) Axelsson's. The filtered cross section is identified by the red horizontal line from (d) reference data, (e) ours, and (f) Axelsson's. White points denote nonground points, orange-red points denote ground points, and blue rectangle represents E_II error.

that, we use the DTM and cross-section results from samp21 and samp53 for analysis (Figures 13 and 14). The display of the cross-sectional details shows that our method can well distinguish the ground point in the discontinuous area after filtering. However, Axelsson's method cannot adapt well to drastic changes in terrain. The reason may be that the dense triangular patch is severely distorted when the gradient changes drastically, which makes the criterion of this area invalid. Specifically, in the bifurcation area of the bridge (Figure

13), the DTM formed by Axelsson's method is relatively rough, and the cross-section indicates that some points on the bridge cannot be filtered out, resulting in E_II error. Moreover, nonground points on steep hills and fault lines cannot be well filtered out either (Figure 14f). In contrast, our method can adapt to terrain gradient changes due to the introduction of a multi-level curvature constraint process. Therefore, the topological terrain obtained by our method matches the reference data set very well in those scenarios.

There are two main reasons for the better overall performance of Axelsson's method. One possible reason is that the TIN constructed based on ground seed points can approximate the real terrain with high accuracy. The more ground points are added, the denser the TIN is constructed. Therefore, most nonground points can be filtered out after the iteration is completed. Another possible reason is that their method has two parameters, iteration distance and angle, which can be adjusted according to local seed points. In the case of sufficient ground seed points, adaptive parameters make the filtering result robust enough. However, when there are insufficient ground seed points in some areas, it is difficult to choose a suitable angle threshold to maintain the terrain. In this case, our method performs better because it is less restricted by ground points.

Although the overall performance of the proposed algorithm is not as good as Axelsson's, it requires fewer parameters to be adjusted and thus is easier to use. Axelsson's algorithm requires users to set four parameters: iterative angle, distance, terrain gradient, and maximum building size. The settings of iterative angle and distance threshold depend greatly on user's filtering experience. In contrast, the proposed method requires users to set the maximum window size, grid size, and curvature threshold. In the parameter analysis section, we pointed out that the key parameter of the algorithm is curvature threshold t , which is proportional to the test area and its value lies between 0.4–1.7 m. In other

words, optimized results can be obtained by only adjusting the t value in most scenes.

The performance of our algorithm on most samples is better than the other seven algorithms. There are two main reasons for this. First, our algorithm uses an interpolation strategy. According to an early report (Sithole and Vosselman 2004), interpolation-based algorithms can better use the contextual information in the lidar point cloud and can well overcome the influence of terrain gradient. Second, due to the use of relative elevation in the calculation of the Gaussian mixture model, our algorithm can remove objects while maintaining terrain features with much complex topography.

Further Algorithm Verification

The ISPRS test data set used earlier was obtained decades ago. In recent years, due to the development of lidar measurement systems, the accuracy and density of the acquired point clouds have been continuously improved. An increase in data density usually means higher challenge for filters. Thus, we choose an area in Rudong, China, with an average point density of 1.92 points/m² to test the filtering performance of the proposed method. The length and width of this area are 0.4 km and 0.6 km, respectively, with a total of 293 909 points. The topographical features of the study area include buildings, bridges, and dense vegetation. We present the DTM and cross-sections to analyze the filter performance of the study area in Figure 15. With the help of orthophotos, we use CloudCompare software, version x.x (year) to label the ground points for accuracy assessment manually. The comparison

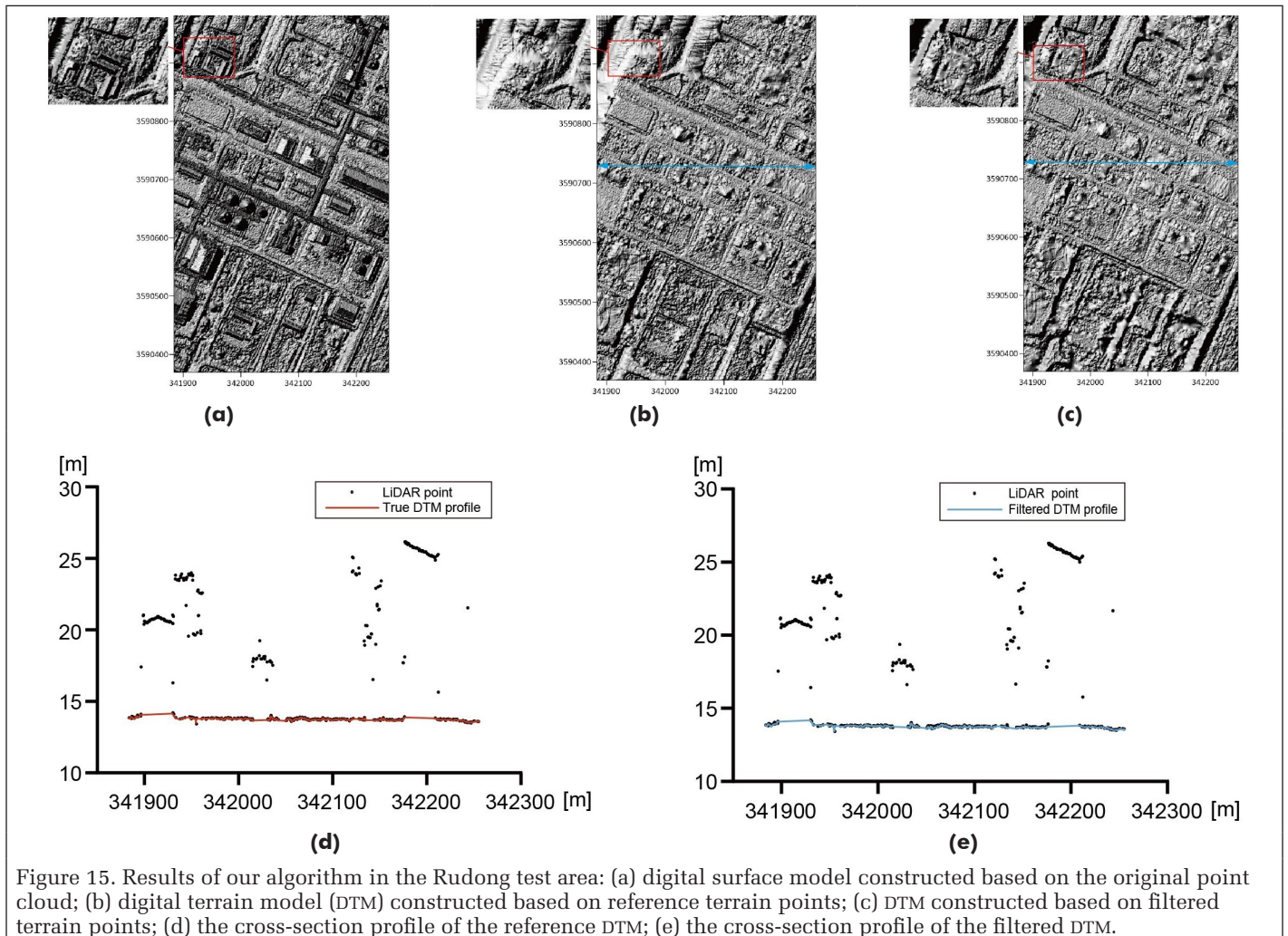


Figure 15. Results of our algorithm in the Rudong test area: (a) digital surface model constructed based on the original point cloud; (b) digital terrain model (DTM) constructed based on reference terrain points; (c) DTM constructed based on filtered terrain points; (d) the cross-section profile of the reference DTM; (e) the cross-section profile of the filtered DTM.

result demonstrates that our method works effectively in urban regions where multiple types of buildings and bridges are present. Besides, we found out that the algorithm will produce E_{II} error in terrains with fewer ground points (the red rectangle in Figure 15c). During the construction of the fitting surface, if not enough ground seed points can be used for fitting, it will indirectly cause the subsequent calculation of relative elevation to be inaccurate.

Table 6 shows the proposed method and the comparison of E_t and kappa between the two different methods for Rudong data. The results indicate that our method is more precise than other methods. In terms of all quantitative indicators, E_I, E_{II}, E_t, kappa are 5.81%, 17.45%, 8.23%, and 87.62%, respectively. This shows that our algorithm can achieve good performance on high-density lidar data. The possible reason is that the higher the density of measurement points, the more ground control points are added. Interpolation surface based on control points and TPS can fit the terrain well. Besides, the assumption that lidar point clouds can be regarded as a Gaussian mixture model is valid regardless the data density. With its powerful ability to fit data distribution, we can separate ground points from other lidar data. In general, the proposed method is robust in filtering in urban areas of various bridges and buildings.

Table 6. Compare the proposed method and two different methods for Rudong data (%).

Method	E _t	kappa
Axelsson (2000)	8.35	85.43
Cloth simulation filter (Zhang <i>et al.</i> 2016)	9.74	79.91
Ours	8.23	87.62

Conclusion

In this paper, a robust and automatic algorithm that can extract ground points from the airborne lidar point clouds is proposed. In the proposed method, an optimized strategy for classification is adopted. (1) To overcome terrain gradient effects, a hierarchical curvature pyramid is built using the TPS function. Both the grid size and the curvature tolerance simultaneously change from the bottom level to the top level. After the iteration, rough ground seeds can thus be obtained. (2) The iterative hierarchical curvature result is applied to initialize the Gaussian mixture model parameters, and the EM algorithm is subsequently used to automatically solve the posterior probability of each point belonging to the ground. By comparing the likelihood with a threshold of 0.5, the category of the point is determined. The proposed method combines the advantages of interpolation filtering and statistical filtering. It is tested on the ISPRS benchmark data set and compared with eight classical filtering algorithms. Experimental results demonstrate that our method has a significant improvement in terrains with discontinuities and bridges. Future work will be focused on maintaining the detailed features of the terrain while adding echo or spectral information to enhance the accuracy of the algorithm.

Acknowledgments

This work was supported by National Natural Science Foundation of China (grant numbers 41631175 and 42071301), the Natural Science Foundation of Jiangsu Province (grant number BK20201372), the Open Fund of Key Laboratory of Urban Land Resources Monitoring and Simulation, Ministry of Natural Resources (grant number KF-2019-04-003), the Marine Science and Technology Innovation

Project of Jiangsu Province (grant number HY2018-3), the National Key Research and Development Plan of China (grant number 2017YFB0503500, 2017YFB0503504), and the Priority Academic Program Development of Jiangsu Higher Education Institutions (grant number 164320H116). The authors would like to acknowledge the provision of the data sets by ISPRS WG III/3.

References

- Axelsson, P. 2000. DEM generation from laser scanner data using adaptive TIN models. *International Archives of Photogrammetry and Remote Sensing* 33:111–118.
- Bartels, M., H. Wei and D. C. Mason. 2006. DTM generation from LIDAR data using skewness balancing. Pages 566–569 in *Proceedings 18th International Conference on Pattern Recognition I*, held in Hong Kong, China.
- Bayram, E., P. Frossard, E. Vural and A. Alatan. 2018. Analysis of airborne LiDAR point clouds with spectral graph filtering. *IEEE Geoscience and Remote Sensing Letters* 15(8):1284–1288.
- Chen, C. and Y. Li. 2012. A robust method of thin plate spline and its application to DEM construction. *Computers & Geosciences* 48:9–16.
- Chen, C., Y. Li, W. Li and H. Dai. 2013. A multiresolution hierarchical classification algorithm for filtering airborne LiDAR data. *ISPRS Journal of Photogrammetry and Remote Sensing* 82:1–9.
- Chen, C., Y. Li, C. Yan, H. Dai, G. Liu and J. Guo. 2016. An improved multi-resolution hierarchical classification method based on robust segmentation for filtering ALS point clouds. *International Journal of Remote Sensing* 37(4):950–968.
- Chen, Q., P. Gong, D. Baldocchi and G. Xie. 2007. Filtering airborne laser scanning data with morphological methods. *Photogrammetric Engineering & Remote Sensing* 73(2):175–185.
- Chen, Z., B. Gao and B. Devereux. 2017. State-of-the-art: DTM generation using airborne LIDAR data. *Sensors* (Basel) 17(1).
- CloudCompare, version x.x. Year. 3D point cloud and mesh processing software Open Source project. <<https://www.danielgm.net/cc/>>
- Congalton, R. G. 1991. A review of assessing the accuracy of classifications of remotely sensed data. *Remote Sensing of Environment* 37(1):35–46.
- Dempster, A. P., N. M. Laird and D. B. Rubin. 1977. Maximum likelihood from incomplete data via the EM algorithm. *Journal of the Royal Statistical Society* 39(1):1–38.
- Evans, J. S. and A. T. Hudak. 2007. A multiscale curvature algorithm for classifying discrete return LiDAR in forested environments. *IEEE Transactions on Geoscience and Remote Sensing* 45(4):1029–1038.
- Flood, M. 2001. LiDAR activities and research priorities in the commercial sector. *International Archives of Photogrammetry and Remote Sensing* (Part 3/W4) 34:678–684.
- Hingee, K. L., P. Caccetta and L. Caccetta. 2019. Modelling discontinuous terrain from DSMs using segment labelling, outlier removal and thin-plate splines. *ISPRS Journal of Photogrammetry and Remote Sensing* 155:159–171.
- Hu, H., Y. Ding, Q. Zhu, B. Wu, H. Lin, Z. Du, Y. Zhang and Y. Zhang. 2014. An adaptive surface filter for airborne laser scanning point clouds by means of regularization and bending energy. *ISPRS Journal of Photogrammetry and Remote Sensing* 92:98–111.
- Huang, H., C. Brenner and M. Sester. 2013. A generative statistical approach to automatic 3D building roof reconstruction from laser scanning data. *ISPRS Journal of Photogrammetry and Remote Sensing* 79:29–43.
- Hui, Z., Y. Hu, S. Jin and Y. Z. Yevenyo. 2016a. Road centerline extraction from airborne LiDAR point cloud based on hierarchical fusion and optimization. *ISPRS Journal of Photogrammetry and Remote Sensing* 118:22–36.
- Hui, Z., Y. Hu, Y. Z. Yevenyo and X. Yu. 2016b. An improved morphological algorithm for filtering airborne LiDAR point cloud based on multi-level kriging interpolation. *Remote Sensing* 8(1).

- Hui, Z., D. Li, S. Jin, Y. Y. Ziggah, L. Wang and Y. Hu. 2019. Automatic DTM extraction from airborne LiDAR based on expectation-maximization. *Optics & Laser Technology* 112:43–55.
- Hyyppä, J., M. Holopainen and H. Olsson. 2012. Laser scanning in forests. *Remote Sensing* 4(10):2919–2922.
- Kraus, K. and N. Pfeifer. 1998. Determination of terrain models in wooded areas with airborne laser scanner data. *ISPRS Journal of Photogrammetry and Remote Sensing* 53(4):193–203.
- Li, Y. 2013. Filtering airborne LiDAR data by an improved morphological method based on multi-gradient analysis. *ISPRS International Archives of the Photogrammetry, Remote Sensing and Spatial Information Sciences* 41:21–24.
- Li, Y., B. Yong, H. Wu, R. An and H. Xu. 2014. An improved top-hat filter with sloped brim for extracting ground points from airborne Lidar point clouds. *Remote Sensing* 6(12):12885–12908.
- Lin, X. and J. Zhang. 2014. Segmentation-based filtering of airborne LiDAR point clouds by progressive densification of terrain segments. *Remote Sensing* 6(2):1294–1326.
- Liu, L. and S. Lim. 2018. A voxel-based multiscale morphological airborne lidar filtering algorithm for digital elevation models for forest regions. *Measurement* 123:135–144.
- Maguya, A. S., V. Junttila and T. Kauranne. 2014. Algorithm for extracting digital terrain models under forest canopy from airborne LiDAR data. *Remote Sensing* 6(7):6524–6548.
- Meng, X., N. Currit and K. Zhao. 2010. Ground filtering algorithms for airborne LiDAR data: A review of critical issues. *Remote Sensing* 2(3):833–860.
- Meng, X., L. Wang, J. L. Silván-Cárdenas and N. Currit. 2009. A multi-directional ground filtering algorithm for airborne LIDAR. *ISPRS Journal of Photogrammetry and Remote Sensing* 64(1):117–124.
- Mongus, D., N. Lukač and B. Žalik. 2014. Ground and building extraction from LiDAR data based on differential morphological profiles and locally fitted surfaces. *ISPRS Journal of Photogrammetry and Remote Sensing* 93:145–156.
- Mongus, D. and B. Žalik. 2012. Parameter-free ground filtering of LiDAR data for automatic DTM generation. *ISPRS Journal of Photogrammetry and Remote Sensing* 67:1–12.
- Ozcan, A. H. and C. Unsalan. 2017. LiDAR data filtering and DTM generation using empirical mode decomposition. *IEEE Journal of Selected Topics in Applied Earth Observations and Remote Sensing* 10(1):360–371.
- Pingel, T. J., K. C. Clarke and W. A. McBride. 2013. An improved simple morphological filter for the terrain classification of airborne LIDAR data. *ISPRS Journal of Photogrammetry and Remote Sensing* 77:21–30.
- Pukelsheim, F. 1994. The three sigma rule. *The American Statistician* 48(2):88–91.
- Rusu, R. B., N. Blodow, Z. Marton, A. Soos and M. Beetz. 2007. Towards 3D object maps for autonomous household robots. In *Proceedings IEEE International Conference on Intelligent Robots and Systems*, held in San Diego, Calif.
- Shao, Z., L. Zhang and L. Wang. 2017. Stacked sparse autoencoder modeling using the synergy of airborne LiDAR and satellite optical and SAR data to map forest above-ground biomass. *IEEE Journal of Selected Topics in Applied Earth Observations and Remote Sensing* 10(12):5569–5582.
- Shi, X., H. Ma, Y. Chen, L. Zhang and W. Zhou. 2018. A parameter-free progressive TIN densification filtering algorithm for lidar point clouds. *International Journal of Remote Sensing* 39(20):6969–6982.
- Sithole, G. 2001. Filtering of laser altimetry data using a slope adaptive filter. *International Archives of Photogrammetry and Remote Sensing* 34:203–210.
- Sithole, G. and G. Vosselman. 2003. *ISPRS Test on Extracting DEMs from Point Clouds: A Comparison of Existing Automatic Filters*. Technical report. <http://www.itc.nl/isprswgiii-3/filtertest/report.htm>. Accessed day Month year.
- Sithole, G. and G. Vosselman. 2004. Experimental comparison of filter algorithms for bare-Earth extraction from airborne laser scanning point clouds. *ISPRS Journal of Photogrammetry and Remote Sensing* 59(1–2):85–101.
- Su, W., Z. Sun, R. Zhong, J. Huang, M. Li, J. Zhu, K. Zhang, H. Wu and D. Zhu. 2015. A new hierarchical moving curve-fitting algorithm for filtering lidar data for automatic DTM generation. *International Journal of Remote Sensing* 36(14):3616–3635.
- Susaki, J. 2012. Adaptive slope filtering of airborne LiDAR data in urban areas for digital terrain model (DTM) generation. *Remote Sensing* 4(6):1804–1819.
- Tóvári, D. and N. Pfeifer. 2005. Segmentation based robust interpolation—A new approach to laser data filtering. *ISPRS Workshop Laser Scanning* 36:79–84.
- Tseng, Y., M. Wang and F. Chou. 2004. Dem generation using 3d rasterized airborne lidar data. Page 20 in *Proceedings of ISPRS 20th Congress (Commission III)*, held in Istanbul, Turkey, 12–23 July 2004. Edited by Orhan Altan.
- Vassilaki, D. I. and A. A. Stamos. 2020. TanDEM-X DEM: Comparative performance review employing LIDAR data and DSMs. *ISPRS Journal of Photogrammetry and Remote Sensing* 160:33–50.
- Vosselman, G. 2000. Slope based filtering of laser altimetry data. *International Archives of Photogrammetry and Remote Sensing* 33 (Part B3/2) 33:935–942.
- Wahba, G. 1990. *Spline Models for Observational Data*. Philadelphia, Pa.: SIAM.
- Wang, C. K. and Y. H. Tseng. 2010. Dem generation from airborne lidar data by an adaptive dual-directional slope filter. *Remote Sensing and Spatial Information Sciences* 38:628–632.
- Wang, J. and J. Shan. 2009. Segmentation of lidar point clouds for building extraction. Pages 9–13 in *Proceedings ASPRS 2009 Annual Conference*, held in Baltimore, Md.
- Yang, A., Z. Wu, F. Yang, D. Su, Y. Ma, D. Zhao and C. Qi. 2020. Filtering of airborne LiDAR bathymetry based on bidirectional cloth simulation. *ISPRS Journal of Photogrammetry and Remote Sensing* 163:49–61.
- Yang, B. S., Z. Wei, Q. Q. Li and J. Li. 2013. Semiautomated building facade footprint extraction from mobile LiDAR point clouds. *IEEE Geoscience and Remote Sensing Letters* 10(4):766–770.
- Zhang, K., S. Chen, D. Whitman, M. Shyu, J. Yan and C. Zhang. 2003. A progressive morphological filter for removing nonground measurements from airborne LIDAR data. *IEEE Transactions on Geoscience and Remote Sensing* 41(4):872–882.
- Zhang, L., Z. Shao, J. Liu and Q. Cheng. 2019. Deep learning based retrieval of forest aboveground biomass from combined LiDAR and Landsat 8 data. *Remote Sensing* 11(12).
- Zhang, W., J. Qi, P. Wan, H. Wang, D. Xie, X. Wang and G. Yan. 2016. An easy-to-use airborne LiDAR data filtering method based on cloth simulation. *Remote Sensing* 8(6):501–522.
- Zhang, Y. and Z. Shao. 2021. Assessing of urban vegetation biomass in combination with LiDAR and high-resolution remote sensing images. *International Journal of Remote Sensing* 42(3):964–985.
- Zhang, Z. 1994. Iterative point matching for registration of free-form curves and surfaces. *International Journal of Computer Vision* 13(2):119–152.
- Zhou, G. and X. Zhou. 2014. Seamless fusion of LiDAR and aerial imagery for building extraction. *IEEE Transactions on Geoscience and Remote Sensing* 52(11):7393–7407.

Detecting Geo-Positional Bias in Imagery Collected Using Small UASs

Jonathan B. Thayn, Aaron M. Paque, and Megan C. Maher

Abstract

Statistical methods for detecting bias in global positioning system (GPS) error are presented and applied to imagery collected using three common unmanned aerial systems (UASs). Imagery processed without ground control points (GCPs) had horizontal errors of 1.0–2.5 m; however, the errors had unequal variances, significant directional bias, and did not conform to the expected statistical distribution and so should be considered unreliable. When GCPs were used, horizontal errors decreased to less than 5 cm, and the errors had equal variances, directional uniformity, and they conformed to the expected distribution. The analysis identified a longitudinal bias in some of the reference data, which were subsequently excluded from the analysis. Had these data been retained, the estimates of positional accuracy would have been unreliable and inaccurate. These results strongly suggest that examining GPS data for bias should be a much more common practice.

Introduction

The use of low-altitude aerial imagery collected using small unmanned aerial systems (UASs) is growing (Colomina and Molina 2014; Whitehead and Hugenholtz 2014) and is expected to keep growing (Tang and Shao 2015) as more advanced electronics and image processing methods overcome the limitations of earlier systems (Hardin and Jensen 2011; Hardin *et al.* 2019). Although there are many excellent reviews of methods for assessing the geo-positional accuracy of UAS data (Barry and Coakley 2013; Gabrlik *et al.* 2018; Gómez-Candón *et al.* 2011; Hugenholtz *et al.* 2016; Zandbergen 2008), most of them rely heavily on comparing coordinates extracted from the imagery with corresponding field-collected coordinates using the root-mean-square error (RMSE) and related measures (Whitehead and Hugenholtz 2015).

The RMSE is an excellent measure of geo-positional error, but only if the data are unbiased. Bias in global positioning system (GPS) data refers to any systematic or predictable pattern in the errors and most published data standards, e.g., the National Standard for Spatial Data Accuracy (NSSDA) (FGDC 1998), do not include recommendations for assessing positional accuracy when data are biased (Zandbergen 2008). This paper recommends a series of statistical procedures for detecting bias in GPS data. When bias is absent, and only random noise is present, the errors can be appropriately measured using the RMSE. However, if bias is found, (1) the errors should be corrected or new, unbiased data should be collected before

Jonathan B. Thayn is with Illinois State University, Department of Geography, Geology, and the Environment, Normal, IL 61790-4400 (jthayn@ilstu.edu).

Aaron M. Paque is with DeWitt County, Illinois, Arrowsmith, IL 61722.

Megan C. Maher is with GEOMAP, Department of Geography, Geology, and the Environment, Illinois State University, Normal, IL 61790-4400.

Contributed by Sidike Paheding, December 28, 2020 (sent for review January 27, 2021; reviewed by Peter Tian-Yuan Shih, Dora Roque).

the project continues, and/or (2) the results of the proposed tests should be included to contextualize RMSE values.

Positional errors are composed of two parts, the distance of the errors and the direction of the errors. GPS locations can be considered unbiased if:

1. The longitude and latitude of the errors have equal variances.
2. The distances of the errors conform to a Rayleigh distribution.
3. The directions of the errors are uniform, i.e., they are dispersed randomly around the compass rather than clustered in a specific direction.

The longitude and latitude of GPS errors should exhibit equal variances, i.e., the data should measure north-south errors just as accurately as east-west errors. Although most GPS data do not have perfectly equal variances, in part due to variability caused by poor satellite visibility that increases with latitude (Parkinson 1996), large departures from equality indicate bias that should be considered carefully.

The error distances should conform to a Rayleigh distribution (Wilson 2006), particularly when the distances are less than one meter (Zandbergen 2008). The Rayleigh distribution occurs when a two-dimensional vector's orthogonal components are normally and independently distributed. Its values range from 0 to infinity and are positively skewed with most values near zero, whereas a diminishing number fall farther away (Figure 1). Error distances conform to the Rayleigh distribution because most points fall reasonably close to their accurate location, with fewer larger errors. The probability distribution and cumulative distribution functions of the Rayleigh distribution are presented in the appendix.

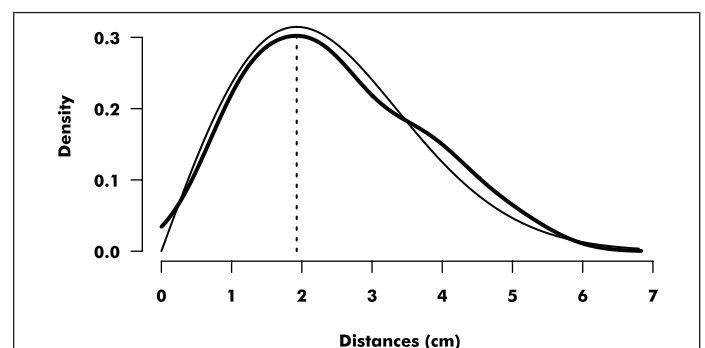


Figure 1. A Rayleigh distribution, based on the distance error data from the DJI Matrice unmanned aerial systems flown at 200 feet above ground level.

Photogrammetric Engineering & Remote Sensing
Vol. 87, No. 9, September 2021, pp. 631–638.
0099-1112/21/631–638

© 2021 American Society for Photogrammetry
and Remote Sensing
doi: 10.14358/PERS.20-00124

The error directions should be uniform, or distributed in all directions, rather than concentrated in one or more directions. In our experience, pronounced directional clustering is usually the result of poor registration, projection errors, or improperly calibrated GPS units. We are not aware of any published data standards that recommend assessing the directions of errors, despite the clear negative consequences of directionally biased data and the relative ease of correcting the data.

Methods

GPS Data

The ground-reference GPS points were collected over the football field of a large midwestern university on a sunny, windless day in October 2019. Reference locations were collected where the 0, 10, 20, 30, 40, and 50 yard-lines intersected with the sidelines and on the hash marks at the middle of the field at the 5, 15, 25, 35, 45, and 50 yard-lines (Figure 2). One hash mark on the 5 yard-line near the southern end zone was excluded because the mark was hidden by researchers collecting GPS data while the UAS data were collected. The GPS data were collected using a Trimble R8, with a real-time kinematic base station. The coordinates for each location were averaged for 10 seconds. The Trimble R8 has a horizontal accuracy of 1 cm and a vertical accuracy of 2 cm (Trimble 2009, p. 50). The data were collected in the Illinois East Projection based on the North American Datum of 1983. The units of this projection are feet, rather than meters, and it is used primarily by surveyors and engineers. The Trimble R8 was borrowed from a municipal public works department that was interested in the spatial accuracy of UAS data and plans to use them to inventory and assess infrastructure. Although the civil engineers preferred data in feet, the GPS errors were converted from imperial to metric units for this paper.

UAS Imagery

The UAS images were collected on the same date as the GPS data using three common and affordable UASs, all produced by SZ DJI Technology Co., Ltd. (www.dji.com): the Mavic Pro, the Phantom 4 Pro, and the Matrice 200. According to the specifications on the DJI website, these three drones have the same hover accuracy range: ± 0.5 m vertically and ± 1.5 m horizontally without downward vision positioning (DVP) and ± 0.1 m vertically and ± 0.3 m horizontally with DVP. DVP was enabled during all flights. Each UAS completed two flights, one at 61 m (200 ft) above ground level (AGL) and a second at 122 m (400 ft) AGL, with 80% side-lap and front-lap between images. The onboard GPS units were calibrated prior to each flight.

Aerial images collected at low altitudes are very susceptible to relief displacement (Breckenridge and Dakins 2011; Zhang *et al.* 2011), so UAS images should be mosaicked stereoscopically using structure-from-motion software (Westoby *et al.* 2012) like PhotoScan Pro (Agisoft 2017). PhotoScan systematically examines neighboring images to detect locations that are identifiable in at least two images. The locations are stereopairs and the elevation of each identified location is then calculated using the location of the UAS when each image was collected. These elevation data are used by PhotoScan Pro to correct topographic displacement as the images are mosaicked. Turner *et al.* (2014) includes an excellent discussion of the structure-from-motion process and of PhotoScan Pro; they found PhotoScan Pro to be more accurate than other commonly used orthophotomosaicking software. Successfully correcting topographic relief displacement requires identifying as many paired locations as possible. For the UAS flights at 200 ft AGL, PhotoScan Pro detected a mean of nearly 800 locations m^{-2} , which resulted in a mean nominal spatial resolution of 2.24 cm for the mosaicked images. A mean of nearly 200 points m^{-2} were discovered in the images flown at 400 ft AGL, for a mean mosaicked spatial resolution of 4.39 cm (Table 1).



Figure 2. The study area. The coordinates of the white dots on the sidelines and on the hash marks on the field were the reference points used to assess the locational accuracy of the mosaicked unmanned aerial systems images. The white stars were the ground control points used to orthophotomosaic some of the images.

Table 1. The details of the orthophotomosaicking process done using Agisoft PhotoScan Pro.

UAS	Flying Height (ft)	Number of Photos	Points	Area (m^2)	Points (m^{-2})	Spatial Resolution (cm)
Mavic	200	392	9 977 059	15 705	635	2.56
Mavic	400	90	3 430 391	16 707	205	4.72
Phantom	200	413	6 959 761	11 854	587	2.45
Phantom	400	189	2 338 346	15 705	149	4.84
Matrice	200	92	13 320 911	10 428	1277	1.53
Matrice	400	20	2 922 893	12 538	233	3.39

UAS = unmanned aerial systems.

Two mosaics were created for each UAS flight. The first was based solely on the coordinates recorded by the onboard GPS unit. The second used eight ground control points (GCPs) to improve the spatial positioning of the mosaicked image. The eight points were the four collected at the extreme corners of the football field and the four collected in the center of the study area at the hash marks on the 45 yard-lines (Figure 2).

Coordinates were extracted manually from the mosaicked UAS images for comparison against the Trimble R8 reference data using Quantum GIS (QGIS 2019) at a scale of 1:20. Each hash mark in the middle of the field had a vertical and a horizontal line, making accurately pinpointing the center of the mark in the UAS images relatively straightforward. The marks on the sidelines however, had only a horizontal line since the yard-lines stopped some centimeters short of the sidelines. The horizontal position of these was obscured by mixed pixels in the UAS imagery. This introduced more horizontal error than vertical error to the locational data extracted along the sidelines. With this in mind, comparison statistics were calculated three times for each flight: (1) using all of the reference locations and the images mosaicked without GCPs, (2) using the reference points (minus those used as GCPs) and the images mosaicked with GCPs, and (3) using only the reference points from the middle of the field, i.e., those that did not have introduced longitudinal error, and the images mosaicked using GCPs.

Statistical Analysis

All statistical procedures were performed in the R Statistical Environment (R Core Team 2019). The tests below are discussed in more detail in the appendix.

Measuring Positional Accuracy

The RSME of the longitude (RMSE_x), of the latitude (RMSE_y), and of the longitude and latitude together (also called the radial root-mean-square error, RMSE_r) were used to measure positional accuracy. Per the recommendation of the NSSDA, the RMSE_r 95%, or the radius of a circle centered on the measured or uncertain location that contains the true or accurate location 95% of the time, was also calculated. This is estimated by multiplying the RMSE_r by 1.7308 (Greenwalt and Shultz 1962). This calculation assumes that the latitude and longitude of the errors are normally and independently distributed and that their variances are equal (Hugenholtz *et al.* 2016; Whitehead and Hugenholtz 2015).

Equal Variances of the Longitude and Latitude

F-tests were used to assess equality of variances between the longitude and latitude components of the positional errors.

Characterizing the Distribution of the Error Distances

The Anderson-Darling test was used to determine if the error distances conform to a Rayleigh distribution (Al-Omari and Zamanzade 2016). The original test returns an A^2 statistic and a modified version returns a V^2 statistic. The A^2 statistic has a longer historical precedence, but the V^2 statistic is more powerful (Best *et al.* 2010).

Although the Anderson-Darling test is the most commonly used procedure for assessing conformity to a Rayleigh distribution, a recently proposed version of the Hellinger distance test seems to be more powerful (Jahanshahi *et al.* 2016). The test statistic, D_H , is the integral of the squared difference of the density function of the errors and the Rayleigh density function fitted to the errors. Values of D_H get smaller as the errors more closely conform to a Rayleigh distribution.

Assessing the Directional Uniformity of the Errors

The mean error direction, $\bar{\theta}$, ranges from 0° to 360° and indicates the direction of the error if systematic directional bias is present. The mean resultant length of the directions,

$\bar{\rho}$, is a measure of circular dispersion or clustering. It ranges from 0, indicating a perfectly uniform or random distribution of directions, to 1, indicating a perfectly clustered distribution with a single modal direction. A probability value for $\bar{\rho}$ can be found using the Rayleigh test (Landler *et al.* 2018; Mardia and Jupp 2000, p. 94). The null hypothesis is that the directions are uniformly distributed, so large p-values suggest that the directions are random and uniform, whereas small p-values suggest that the directions are strongly clustered in a single direction. Axial data, i.e., directional data with two clusters pointing in opposite directions, can be assessed by doubling the angles before submitting them to the Rayleigh test (Batschelet 1981, p. 51).

Assessing Vertical Errors

Vertical GPS errors should be normally distributed with a mean near zero. The RMSE_z and RMSE_z 95%, which is found by multiplying the RMSE_z by 1.9600 (FGDC 1998; Greenwalt and Shultz 1962), were used to measure vertical errors. The median vertical errors were also calculated (Hamshaw *et al.* 2019). The Shapiro-Wilks test was used to assess the normality of the vertical errors.

Results

Images Mosaicked without GCPs

The error distances and directions of the images mosaicked without GCPs are shown by UAS and by altitude in Figure 3. The origin of this plot is the reference locations recorded using the precise Trimble R8 GPS unit. The results of the F-Tests show that none of these errors exhibit equal variances (Table 2), suggesting strong bias in the imagery mosaicked without GCPs. The F -statistics of the Mavic data and the Matrice data were larger than 1, indicating larger variance in the longitude than in the latitude. The most egregious were the errors of the Matrice flown at 200 AGL, which displayed seven times larger variance in its longitude than in its latitude. The F -statistics of the Phantom flights were less than one, indicating that the variance of the latitude of the errors was greater than that of the longitude of the errors.

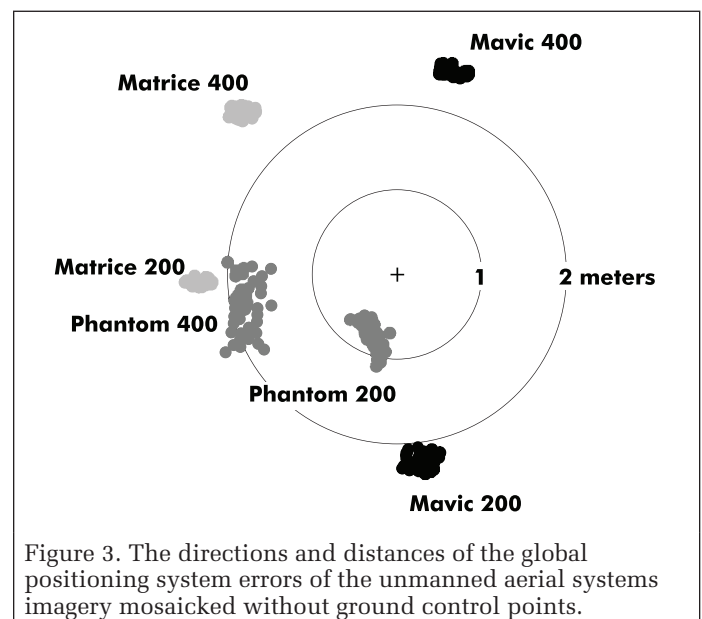


Figure 3. The directions and distances of the global positioning system errors of the unmanned aerial systems imagery mosaicked without ground control points.

Table 2 contains estimates of error distance, error direction, and the results of the goodness-of-fit tests used to determine if the errors fit a Rayleigh distribution. The rows labeled with the UAS name and flight altitude are those of the images

Table 2. The first section contains the results of F-tests of equal variances; the second section includes common root-mean-square error (RMSE) values and the $\hat{\beta}$ value of the fitted Rayleigh distribution; the third section includes the mean circular direction ($\bar{\theta}$), the mean resultant length ($\bar{\rho}$), and the p-value of the Rayleigh test of circular uniformity; and the fourth section contains the results of the goodness-of-fit tests performed on the global positioning system distance errors, the Anderson-Darling test (A^2 and V^2), and the Hellinger test (D_H). The statistics associated with significant fits at a critical probability of 0.05 are indicated in bold typeface.

Image	n	Variances		Error Distance (cm)					Error Direction					Error Distance Distribution			
		F	p-value	RMSE _x	RMSE _y	RMSE _r	r 95%	$\hat{\beta}$	$\bar{\theta}$	$\bar{\rho}$	p-value	Axial $\bar{\rho}$	p-value	A^2	V^2	D_H	
Mavic 200	42	2.022	0.027	29.975	221.030	223.054	386.062	157.723	172.864	0.999	<0.000				16.639	8.269	0.797
Mavic 200 GCP	34	6.809	<0.000	7.118	2.807	7.652	13.244	5.411	299.964	0.162	0.411	0.317	0.031		0.820	0.280	0.127
Mavic 200 GCP Limited	17	0.192	0.002	2.287	3.268	3.989	6.904	2.821	274.050	0.465	0.023	0.272	0.287		0.553	0.264	0.130
Mavic 400	43	6.871	<0.000	68.041	236.945	246.521	426.678	174.316	15.474	0.999	<0.000				18.654	9.463	0.878
Mavic 400 GCP	35	2.216	0.023	8.501	5.655	10.209	17.671	7.219	263.470	0.235	0.144	0.282	0.061		0.685	0.176	0.095
Mavic 400 GCP Limited	17	0.701	0.701	3.894	3.715	5.382	9.315	3.805	247.812	0.638	<0.000	0.173	0.610		0.396	0.132	0.104
Phantom 200	42	0.331	0.001	29.627	76.647	82.173	142.226	58.106	201.596	0.987	<0.000				9.272	4.043	0.493
Phantom 200 GCP	35	15.935	<0.000	7.618	1.904	7.852	13.591	5.552	274.160	0.068	0.853	0.471	<0.000		5.383	1.089	0.195
Phantom 200 GCP Limited	17	1.056	0.914	1.914	1.670	2.540	4.396	1.796	266.117	0.238	0.387	0.046	0.966		0.843	0.317	0.134
Phantom 400	43	0.191	<0.000	178.759	49.144	185.391	320.875	131.091	257.997	0.988	<0.000				14.112	6.721	0.674
Phantom 400 GCP	35	10.199	<0.000	7.326	2.298	7.678	13.290	5.429	249.859	0.224	0.172	0.459	<0.000		6.144	1.416	0.211
Phantom 400 GCP Limited	17	1.097	0.855	1.817	1.348	2.262	3.915	1.599	290.777	0.550	0.004	0.307	0.204		0.306	0.137	0.081
Matrice 200	43	7.189	<0.000	234.595	9.429	234.784	406.364	166.018	267.821	1.000	<0.000				17.172	8.551	0.811
Matrice 200 GCP	34	21.126	<0.000	6.671	1.755	6.898	11.939	4.878	310.161	0.390	0.005	0.666	<0.000		0.177	0.448	0.149
Matrice 200 GCP Limited	16	1.539	0.413	2.398	1.295	2.725	4.717	1.927	295.323	0.843	<0.000	0.501	0.016		0.284	0.089	0.056
Matrice 400	42	3.515	<0.000	184.449	190.853	265.417	459.385	187.679	316.024	1.000	<0.000				17.332	8.694	0.834
Matrice 400 GCP	35	20.972	<0.000	6.942	1.583	7.121	12.324	5.035	330.239	0.233	0.150	0.396	0.004		5.080	1.114	0.200
Matrice 400 GCP Limited	17	0.630	0.365	1.409	1.644	2.165	3.747	1.531	314.963	0.513	0.010	0.404	0.061		0.348	0.128	0.097

GCP = ground control points; RMSE_x = RSME of the longitude; RMSE_y = RMSE of the latitude; RMSE_r = the longitude and latitude together (also called the radial root-mean-square error).

mosaicked without GCPs. The rows labeled with “GCP” are those mosaicked with GCPs and assessed using all of the reference points (minus those used as GCPs). The rows labeled with “GCP Limited” are those of the images mosaicked with GCPs but assessed with only the more reliable hash mark reference points from the middle of the football field.

Notice that the directional bias of the errors of images mosaicked without GCPs is very pronounced. The error directions were all strongly clustered, with Rayleigh test values greater than or equal to 0.987 with p-values <0.000 (Table 2). The most dramatic example was the data collected by the Matrice at 400 ft AGL, which was incorrectly positioned 2.65 m to the northwest ($\bar{\theta} = 316^\circ$, $\bar{\rho} = 1.000$, $p < 0.000$). When the same data were mosaicked using GCPs the image was off by only 0.07 m in random directions ($\bar{\rho} = 0.223$, $p = 0.150$). The strong directional clustering suggests that the bias is very systematic; therefore, it should be easy to repair during postprocessing using any of the geo-rectification procedures common to most image processing software. None of these errors conformed to a Rayleigh distribution (Table 2). The RMSE values for these data are included in Table 2 for comparison purposes, but because of their unequal variances, strong directional bias, and non-Rayleigh distribution, they are unreliable.

Images Mosaicked with GCPs

The errors of the images mosaicked using GCPs are shown in Figure 4, where each circle plot is labeled with the name of the UAS and with the altitude at which the data were collected. The gray dots and lines are the errors assessed using the dubious sideline reference points and the black dots and lines are the errors measured using the more reliable hash mark points from the middle of the field.

When assessed using only the reliable hash mark reference points, the longitude and latitude of most of these errors exhibited equal variances (Table 2). The only exception was the Mavic data collected at 200 ft AGL ($F = 0.192$, $p = 0.002$). As expected, when the dubious sideline reference points were included in the assessment, the variances were strongly unequal, with large F ratios confirming that the longitudinal variances were greater than the latitudinal variances. This is surely the result of inaccurately extracted reference coordinates rather than a poorly positioned image, as explained earlier.

The results of the Rayleigh tests conducted using the dubious sideline reference points initially seem to suggest that the error directions are uniform, with the exception of the Matrice data collected at 200 AGL ($\bar{\rho} = 0.390$, $p = 0.005$). However, the Rayleigh test assesses the error directions against a single cluster, and the plots in Figure 4, and the results of

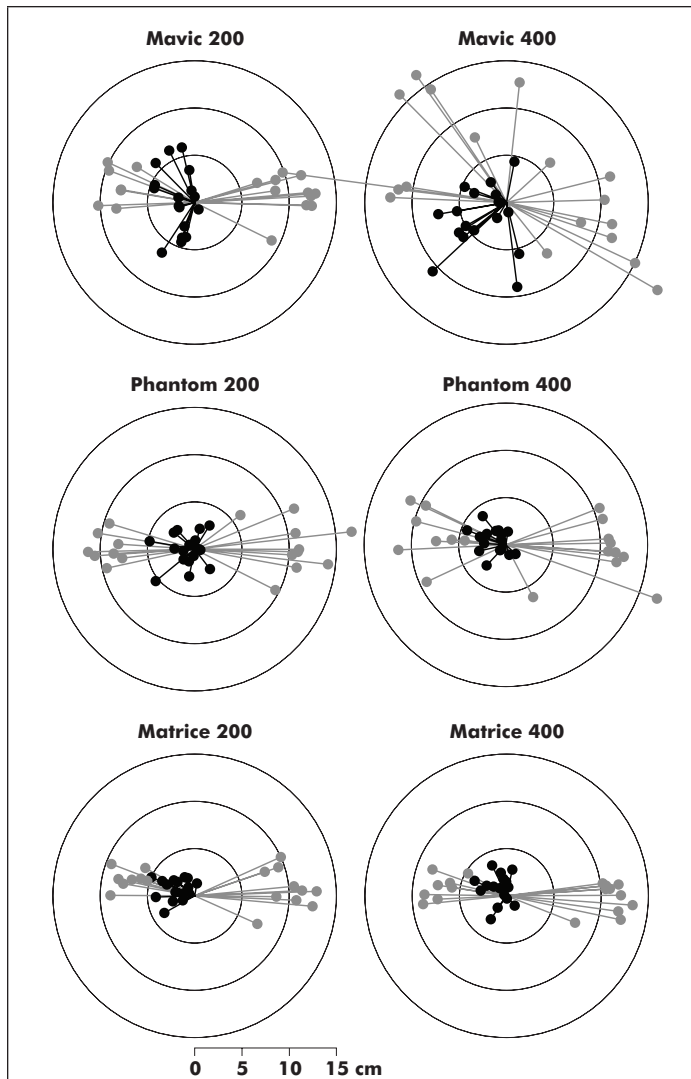


Figure 4. The directions and distances of the global positioning system errors of the unmanned aerial systems imagery mosaicked with ground control points. The gray dots are the sideline reference points and the black dots are those of the hash mark reference points (see Figure 2).

the F-tests, show that these data have two opposing clusters, one pointing east and one pointing west. The results of axial Rayleigh tests show unmistakable clustering. The least significantly clustered data was that of the Mavic flown at 400 ft AGL, but it was still strongly clustered ($Axial \bar{p} = 0.282$, $p = 0.061$). The strong axial nature of the error directions confirm that the sideline reference points are biased and unreliable.

When assessed using only the reliable hash mark reference points, all of the images processed using GCPs had errors that conformed to a Rayleigh distribution (Table 2). This result was unanimous across the three fit statistics: A^2 , V^2 , and D_H .

Positional Accuracy

The $RMSE_x$, $RMSE_y$, $RMSE_r$, and $RMSE_r$ 95% are presented for all image mosaics in Table 2, which also shows the $\hat{\beta}$ values of the fitted Rayleigh distributions. The $\hat{\beta}$ is the measure of central tendency for the Rayleigh distribution and could be a useful metric of positional accuracy, but only for those errors that conform to a Rayleigh distribution. The vertical dashed line in Figure 1 is $\hat{\beta}$ for the Rayleigh distribution fitted to the error distances of the Matrice data collected at 200 ft AGL,

mosaicked using GCPs, and assessed using only the reliable hash mark reference points. In that example, the $\hat{\beta}$ is equal to 1.93 cm, the $RMSE_r$ is equal to 2.73 cm and the $RMSE_r$ 95% is equal to 4.72 cm. The mean error distance is 2.47 cm. These data have equal variances and conform to a Rayleigh distribution (Table 2).

The $RMSE_r$ value of the Mavic UAS, when flown at 400 ft AGL and mosaicked with GCPs, was 5.38 cm or 1.14 pixels, with a 95% reliability of 9.32 cm. The same UAS flown at 200 ft AGL and mosaicked with GCPs produced an $RMSE_r$ of 3.99 cm or 1.56 pixels, with a 95% reliability of 6.90 cm. This compares favorably to Barry and Coakley (2013), who used PhotoScan Pro with images collected from a fixed-wing UAS flown at 90 m AGL and 10 ground control points and achieved a 95% horizontal reliability of 4.1 cm.

The Phantom UAS, flown at 400 ft AGL and mosaicked using GCPs produced an $RMSE_r$ value of 2.26 cm or just under half a pixel width, with a horizontal 95% reliability of 3.92 cm. When flown at 200 ft AGL, the $RMSE_r$ was 2.54 cm or just over 1 pixel width, with a 95% horizontal reliability of 4.40 cm. When flown at 400 ft AGL, the Matrice data produced an $RMSE_r$ of 2.17 cm or 0.64 pixels, with a horizontal 95% reliability of 3.75 cm. The Matrice flown at 200 ft AGL had an $RMSE_r$ of 2.73 or 1.78 pixels, with a 95% reliability of 4.72 cm. At 400 ft AGL, the Matrice produced an $RMSE_r$ of 2.17 cm or 0.64 pixels, with a 95% reliability of 3.75 cm.

Vertical Accuracy

The elevation values that PhotoScan Pro generates to correct relief displacement can be output as a separate raster. Only the elevation values of the images mosaicked using GCPs were assessed (Table 3). The mean of the $RMSE_z$ values for the imagery collected at 200 ft AGL was 2.3 cm, whereas that of the imagery collected at 400 ft AGL was just over 3.5 cm. The data collected using the Mavic UAS at 400 ft AGL had the largest $RMSE_z$. The Mavic 400 data contained several outliers, which were removed from the data before calculating the statistics in Table 3. Only the data from the Phantom flown at 200 ft AGL were not normally distributed ($W = 0.898$, $p < 0.000$).

Table 3. Measures of vertical global positioning system error, including the Shapiro-Wilks normality test results.

UAS	AGL	$RMSE_z$	$RMSE_z$ 95%	\bar{e}	W	p-value
Mavic	200	1.677	3.287	-0.410	0.991	0.973
	400	5.170	10.132	-0.493	0.976	0.555
Phantom	200	3.707	7.266	-2.564	0.898	<0.000
	400	3.685	7.222	-2.121	0.966	0.172
Matrice	200	1.518	2.975	-0.265	0.974	0.349
	400	1.849	3.625	-0.737	0.969	0.230

UAS = unmanned aerial systems; AGL = above ground level; $RMSE_z$ = root-mean-square vertical errors.

The $RMSE_z$ value of the Mavic UAS, when flown at 400 ft AGL, was 5.17 cm and a 95% reliability of 10.13 cm. The same UAS flown at 200 ft AGL produced an $RMSE_z$ of 1.68 cm with a vertical 95% reliability of 3.29 cm. Again, this compares favorably to Barry and Coakley (2013), who achieved a 95% vertical reliability of 6.8 cm.

The Phantom UAS, flown at 400 ft AGL, produced an $RMSE_z$ of 3.69 cm with a vertical 95% reliability of 7.22 cm. At 200 ft AGL, the $RMSE_z$ was 3.71 cm with a 95% reliability of 7.27 cm. The Matrice data, when flown at 400 ft AGL, produced an $RMSE_z$ of 1.85 cm and a vertical 95% reliability of 3.63 cm. When flown at 200 ft AGL, the Matrice produced an $RMSE_z$ of 1.52 cm with a vertical 95% reliability of 2.98 cm.

Discussion and Conclusions

Across the three UASs, image mosaics collected at lower altitudes were geo-positioned more accurately than images collected at higher altitudes. Approximately four times more images were required to capture the study area when the UASs were flown at 200 ft AGL than when they were flown at 400 ft, but this resulted in approximately four times more stereo-locations used to correct the topographic displacement and about four times more pixels in the final image (Table 1).

The RMSE_r values of the images mosaicked without GCPs ranged from about 1 m to a bit more than 2.5 m; however, the errors had consistently unequal variances, exhibited very significant directional bias (Figure 3), and did not conform to the expected Rayleigh distribution (Table 2). Because of these faults, the data are biased and their RMSE values should be considered cautiously.

The proposed statistical methods identified the bias of the faulty sideline reference points. The longitude and latitude of their errors exhibited strongly unequal variances; their error directions were significantly clustered eastward and westward (a result of the difficulty of identifying the longitude of these points in the mosaicked imagery); and only half of them conformed to a Rayleigh distribution (Table 2). All of these items suggest biases that make the positional accuracy of these data suspect. These data were collected in the field as precisely as possible and it was not until the data were being processed that their faults became apparent. In particular, the plots in Figure 4 and the F-tests made the east/west bias obvious, which was subsequently confirmed by the axial Rayleigh test results (Table 2). If all of the reference points had suffered from these problems, an accurate assessment of positional accuracy would have required collecting new reference data. Fortunately, half of the points were reliable. Researchers who do not assess their GPS data for bias would not have detected this problem.

When assessed using the reliable hash mark reference points, the images mosaicked using GCPs demonstrated consistently equal variances and conformity to the expected Rayleigh distribution (Table 2). However, only the error directions of the data from the Phantom flown at 200 ft AGL were distributed uniformly ($\bar{\rho} = 0.238$, $p = 0.387$). The others were all biased towards the east. The mean directions ranged from 248° to 315°, all with p-values less than 0.05. This is also apparent in the plots in Figure 4. The cause of this eastward trend is unknown. It could have been caused by the steep sides of the football stadium, which blocked visibility to the east and the west and may have impeded communication between the satellites and the GPS receiver. The RMSE_x of these images range from nearly 1.5 cm to just under 4.0 cm, so the bias, although consistent, is slight. Researchers who encounter similar issues with their data should report the statistical results along with the RMSE values, as we have done here, to give a more complete representation of the errors and their bias.

The discussion and results presented here strongly suggest that GPS data should be routinely assessed for bias, certainly in projects where positional accuracy is critical. The clear picture of the errors that these procedures produce is, at least, a useful description of the errors or, at most, a strong indication that data need to be corrected or replaced. Geospatial professionals would benefit from making bias assessments a part of their routine data processing.

Appendix: Statistical Methods for Assessing GPS Errors

The equations for RMSE_x, RMSE_y, and RMSE_r are not included here, but they can be found in Whitehead and Hugenholtz (2015). Thorough reviews of circular statistical procedures can be found in Batschelet (1981), Fisher (1993), Mardia (1975), and Mardia and Jupp (2000).

Assessing the Direction of GPS Errors

The Rayleigh test of circular uniformity (Rayleigh 1880) is based on two circular descriptive statistics: the circular mean, a measure of central tendency, and the mean resultant length, a measure of circular dispersion. Calculating circular statistics involves transforming the data from circular values to linear ones using the sine and cosine trigonometric functions. The statistic is then calculated using the transformed data and the result is back-transformed to a circular value using the arctangent function.

The directions, θ , entered into Equation 1 below must be expressed in radians. Most geographic data begin in degrees, which are converted to radians through multiplication by $\pi/180$. Angles expressed in radians, like the mean returned from Equation 2, can be transformed to degrees through multiplication by $180/\pi$.

The circular mean is found by first summing the sines and cosines of the angles,

$$\begin{aligned} s &= \sum \sin(\theta_i) \\ c &= \sum \cos(\theta_i) \end{aligned} \quad (1)$$

and then reverting to a circular value using

$$\bar{\theta} = \begin{cases} \tan^{-1}\left(\frac{s}{c}\right), & \text{if } s > 0, c > 0 \\ \tan^{-1}\left(\frac{s}{c}\right) + \pi, & \text{if } c < 0 \\ \tan^{-1}\left(\frac{s}{c}\right) + 2\pi, & \text{if } s < 0, c < 0 \end{cases} \quad (2)$$

The circular mean is a useful descriptive statistic only if the directions are nonuniform and clustered around a single direction. Circular dispersion is most appropriately measured using the mean resultant length,

$$\bar{\rho} = \frac{1}{n} \sqrt{s^2 + c^2} \quad (3)$$

where s and c are calculated according to Equation 1. Notice that $\bar{\rho}$ remains a linear value, ranging from zero to one. Values near zero indicate circular uniformity, whereas values near one indicate that the errors are clustered in one direction. $\bar{\rho}$ can be used in an inferential test of circular uniformity called the Rayleigh test, where the null hypothesis is that the directions are uniform. If the test statistic is too large, the null hypothesis should be rejected. $\bar{\rho}$ is converted to a test statistic by

$$z = n\bar{\rho}^2 \quad (4)$$

with a p-value of

$$p = e^{-z} \left(1 + \frac{2z - z^2}{4n} - \frac{24z - 132z^2 + 76z^3 - 9z^4}{288n^2} \right) \quad (5)$$

if n is less than 50, and e^{-z} if n is equal to or larger than 50.

A large p-value returned from a Rayleigh test performed on GPS error directions indicates that the errors are systematic, or that the direction of the errors is biased and predictable. A low p-value indicates that the error directions are uniform and unpredictable, which is the expectation for GPS errors. The R functions for finding the circular mean, the mean resultant length, and its corresponding p-value are found in the R “circular” package (Agostinelli and Lund 2017).

Axial data, or data with two clusters pointing in opposite directions, can be assessed by doubling the angles prior to submitting them to the Rayleigh test. The null hypothesis is that the data are uniform and the alternate hypothesis is that they exhibit two clusters that are 180° apart.

Rayleigh Distribution Goodness-of-Fit Tests

The Rayleigh distribution is the best known approximation of GPS error distances (Wilson 2006; Zandbergen 2008) and is composed of a two-dimensional vector whose orthogonal components (longitude and latitude) are normally and independently distributed. The Rayleigh distribution ranges from zero to infinity and is positively skewed (Figure 1). The peak of the distribution is located at the scale factor, $\hat{\beta}$, which can be estimated using (Jahanshahi *et al.* 2016),

$$\hat{\beta} = \sqrt{\frac{\sum x_i^2}{2n}} \quad (6)$$

Its probability density function is

$$f(x, \beta) = \frac{x}{\beta^2} e^{-x^2/(2\beta^2)} \quad (7)$$

and the cumulative distribution function (CDF) has the form,

$$F(x, \beta) = 1 - e^{-x^2/(2\beta^2)} \quad (8)$$

Simulating a sample that follows a Rayleigh distribution can be done using

$$R(y, \beta) = \beta \sqrt{-2 \ln(y)} \quad (9)$$

where y is a set of randomly selected numbers that range from 0 to 1.

The Anderson-Darling Test

The Anderson-Darling test (Anderson and Darling 1952) has been recommended as a goodness-of-fit test for the Rayleigh distribution (Abd-Elfattah 2011; Al-Omari and Zamanzade 2016; Best *et al.* 2010). The null hypothesis is that the data conform to a Rayleigh distribution. If the statistic is too large, the null hypothesis should be rejected. The sample must be sorted so that $x_1 \leq x_2 \leq \dots \leq x_n$. Then,

$$A^2 = -n - \frac{1}{n} \sum (2i - 1) [\ln(d_i) + \ln(1 - d_{n+1-i})] \quad (10)$$

where d is the CDF (Equation 8) of each observation in the sorted sample. The modified Anderson-Darling statistic is calculated according to (Anderson *et al.* 1954):

$$V^2 = \frac{n}{2} - 2 \sum d_i - n \sum \left[\left(2 - \frac{2i-1}{n} \right) \ln(1 - d_i) \right] \quad (11)$$

V^2 has been shown to be slightly more powerful than the A^2 statistic (Abd-Elfattah 2011; Rahman *et al.* 2006).

Critical values of A^2 and V^2 do not belong to a defined statistical distribution and are unique for every combination of sample size and scale factor (Best *et al.* 2010); although some tables of critical values have been generated using Monte Carlo simulations (Abd-Elfattah 2011; Best *et al.* 2010; Rahman *et al.* 2006). (Note that Abd-Elfattah (2011) used the cumulative distribution function from the Weibull distribution, which is similar to the Rayleigh distribution.) These tables are limited

to specific combinations of sample sizes and scale factors. In the current analysis, critical values were found by simulating Rayleigh-distributed samples as described below.

The Hellinger Distance Test

Hellinger's distance (Hellinger 1909) has not been used as often as the Anderson-Darling test for characterizing Rayleigh distributions, but it has been shown to be more powerful (Jahanshahi *et al.* 2016). It is based on the integral of the squared difference between two density functions:

$$D_H = \frac{1}{2} \int_0^{\infty} (\sqrt{f(x)} - \sqrt{f(x, \beta)})^2 \quad (12)$$

where $f(x)$ is the density function of the sample being assessed and $f(x, \beta)$ is the density function for the Rayleigh Distribution, Equation 7, using the scale factor derived from the sample using Equation 6. If D_H is too large, the null hypothesis should be rejected and the error distances should be assumed to not conform to a Rayleigh distribution. In the current analysis, $f(x)$ was estimated using the "densityfun" function from the "statip" R package (Poncet 2019). The "integrate" function was used to calculate the integral. Like the Anderson-Darling test statistics, critical values for D_H are unknown (Jahanshahi *et al.* 2016) and are unique to each combination of sample size and $\hat{\beta}$.

Critical values for the Anderson-Darling and Hellinger distance test statistics were estimated according to the method outlined in Abd-Elfattah (2011) and Jahanshahi *et al.* (2016). For each combination of sample size and scale factor, 5000 samples were simulated from a generalized Rayleigh distribution (Equation 9) and the A^2 , V^2 , and D_H test statistics were calculated using Equations 10, 11, and 12. The value of the 95th quantile of the simulated samples' statistics was found and used as the critical value. If the test statistic was less than the critical value, the GPS error distances were considered to fit the Rayleigh distribution.

References

- Abd-Elfattah, A. M. 2011. Goodness of fit test for the generalized Rayleigh distribution with unknown parameters. *Journal of Statistical Computation and Simulation* 81(3):357–366.
- Agisoft. 2017. *PhotoScan Professional*. St. Petersburg, Russia.
- Agostinelli, C. and U. Lund. 2017. R package "circular": Circular statistics (version 0.4–93). <<https://r-forge.r-project.org/projects/circular/>> Accessed day Month year.
- Al-Omari, A. and E. Zamanzade. 2016. Different goodness of fit tests for Rayleigh distribution in ranked set sampling. *Pakistan Journal of Statistics and Operation Research* 12(1):25–39.
- Anderson, T. W. and D. A. Darling. 1952. Asymptotic theory of certain "goodness of fit" criteria based on stochastic processes. *The Annals of Mathematical Statistics* 23(2):193–212.
- Anderson, T. W. and D. A. Darling. 1954. A test of goodness of fit. *Journal of the American Statistical Association* 49(268):765–769.
- Barry, P. and R. Coakley. 2013. Accuracy of UAV photogrammetry compared with network RTK GPS. *International Archives of the Photogrammetry, Remote Sensing and Spatial Information Sciences* 2:27–31.
- Batschelet, E. 1981. *Circular Statistics in Biology*. New York, N.Y.: Academic Press.
- Best, D. J., J. C. W. Rayner and O. Thas. 2010. Easily applied tests of fit for the Rayleigh distribution. *Sankhya B* 72(2):254–263.
- Breckenridge, R. and M. Dakins. 2011. Evolution of bare ground on rangelands using unmanned aerial vehicles: A case study. *GIScience & Remote Sensing* 48(1):74–85.
- Colomina, I. and P. Molina. 2014. Unmanned aerial systems for photogrammetry and remote sensing: A review. *ISPRS Journal of Photogrammetry and Remote Sensing* 92:79–97.

- FGDC (Federal Geographic Data Committee). 1998. *Geospatial Positioning Accuracy Standards Part 3: National Standard for Spatial Data Accuracy*, edited by F.G.D. Committee, 28. Reston, Va.: U.S. Geological Survey.
- Fisher, N. 1993. *Statistical Analysis of Circular Data*. Cambridge, England: Cambridge University Press.
- Greenwalt, C. R. and M. E. Shultz. 1962. *Principles of Error Theory and Cartographic Applications*. St. Louis, Mo.: Aeronautical Chart and Information Center.
- Hamshaw, S. D., T. Engel, D. M. Rizzo, J. O'Neil-Dunne and M. M. Dewoolkar. 2019. Application of unmanned aircraft system (UAS) for monitoring bank erosion along river corridors. *Geomatics, Natural Hazards and Risk* 10(1):1285–1305.
- Hardin, P. and R. R. Jensen. 2011. Small-scale unmanned aerial vehicles in environmental remote sensing: Challenges and opportunities. *GIScience and Remote Sensing* 48(1):99–111.
- Hardin, P. J., V. Lulla, R. R. Jensen and J. R. Jensen. 2019. Small unmanned aerial systems (sUAS) for environmental remote sensing: Challenges and opportunities revisited. *GIScience & Remote Sensing* 56(2):309–322.
- Hellinger, E. 1909. Neue Begründung der Theorie quadratischer Formen von unendlichvielen Veränderlichen. *Journal für die reine und angewandte Mathematik* 1909(136):210–271.
- Jahanshahi, S.M.A., A. H. Rad and V. Fakoor. 2016. A goodness-of-fit test for Rayleigh distribution based on Hellinger distance. *Annals of Data Science* 3(4):401–411.
- Landler, L., G. D. Ruxton and E. P. Malkemper. 2018. Circular data in biology: Advice for effectively implementing statistical procedures. *Behavioral Ecology and Sociobiology* 72(8):128–128.
- Mardia, K. V. 1975. Statistics of directional data. *Journal of the Royal Statistical Society* 37(3):349–393.
- Mardia, K. V. and P. E. Jupp. 2000. *Directional Statistics*. West Sussex, England: John Wiley and Sons.
- Parkinson, B. 1996. GPS error analysis. In *Global Positioning Systems: Theory and Applications*, edited by B. Parkinson and J. Spiler Jr. Washington, D.C.: American Institute of Aeronautics.
- Poncet, P. 2019. statip: Statistical Functions for Probability Distributions and Regression (version 0.2.3). <<https://CRAN.R-project.org/package=statip>> Accessed .
- QGIS (Quantum Geographic Information System) DT. 2019. *QGIS Geographic Information System*. Open Source Geospatial Foundation Project. <<https://www.qgis.org/en/site/>> Accessed .
- R Core Team. 2019. *R: A Language and Environment for Statistical Computing*. Vienna, Austria: R Foundation for Statistical Computing.
- Rahman, M., L. M. Pearson and H. C. Heinen. 2006. A modified Anderson-Darling test for uniformity. *Bulletin of the Malaysian Mathematical Sciences Society* 2(29):11–16.
- Rayleigh, L. 1880. XII. On the resultant of a large number of vibrations of the same pitch and of arbitrary phase. *The London, Edinburgh, and Dublin Philosophical Magazine and Journal of Science* 10(60):73–78.
- Tang, L. and G. Shao. 2015. Drone remote sensing for forestry research and practices. *Journal of Forestry Research* 26(4):791–797.
- Trimble. 2009. *User Guide: Trimble R8 GNSS Receiver*. Dayton, Ohio: Trimble Navigation Limited.
- Turner, D., A. Lucieer and L. Wallace. 2014. Direct georeferencing of ultrahigh-resolution UAV imagery. *IEEE Transactions on Geoscience and Remote Sensing* 52(5):2738–2745.
- Westoby, M. J., J. Brasington, N. F. Glasser, M. J. Hambrey and J. M. Reynolds. 2012. “Structure-from-Motion” photogrammetry: A low-cost, effective tool for geoscience applications. *Geomorphology* 179:300–314.
- Whitehead, K. and C. H. Hugenholtz. 2014. Remote sensing of the environment with small unmanned aircraft systems (UASs), part 1: A review of progress and challenges. *Journal of Unmanned Vehicle Systems* 02(03):69–85.
- Whitehead, K. and C. H. Hugenholtz. 2015. Applying ASPRS accuracy standards to surveys from small unmanned aircraft systems (UAS). *Photogrammetric Engineering & Remote Sensing* 81(10):787–793.
- Wilson, D. 2006. *GPS Horizontal Positional Accuracy*. <<http://users.erols.com/dlwilson/gpsacc.htm>>, Accessed: 2008.
- Zandbergen, P. A. 2008. Positional accuracy of spatial data: Non-normal distributions and a critique of the national standard for spatial data accuracy. *Transactions in GIS* 12(1):103–130.
- Zhang, Y., J. Xiong and L. Hao. 2011. Photogrammetric processing of low-altitude images acquired by unpiloted aerial vehicles. *The Photogrammetric Record* 26(134):190–211.

Double Adaptive Intensity-Threshold Method for Uneven Lidar Data to Extract Road Markings

Chengming Ye, Hongfu Li, Ruilong Wei, Lixuan Wang, Tianbo Sui, Wensen Bai, and Pirasteh Saied

Abstract

Due to the large volume and high redundancy of point clouds, there are many dilemmas in road-marking extraction algorithms, especially from uneven lidar point clouds. To extract road markings efficiently, this study presents a novel method for handling the uneven density distribution of point clouds and the high reflection intensity of road markings. The method first segments the point-cloud data into blocks perpendicular to the vehicle trajectory. Then it applies the double adaptive intensity-threshold method to extract road markings from road surfaces. Finally, it performs an adaptive spatial density filter based on the density distribution of point-cloud data to remove false road-marking points. The average completeness, correctness, and F measure of road-marking extraction are 0.827, 0.887, and 0.854, respectively, indicating that the proposed method is efficient and robust.

Introduction

With the rapid development of 3D laser scanning and acquisition equipment, point clouds have become the essential spatiotemporal data source after vector maps and image data, according to the European Geospatial Business Outlook Report (Geospatial Media and Communications 2018). Many researchers have studied point-cloud data obtained from 3D laser scanning systems (especially mobile laser scanning systems [MLSs]), mainly focusing on 3D reconstruction, forest resource survey, geological disasters, automatic driving, and construction of 3D high-definition (HD) maps (Aijazi *et al.* 2013; Guan *et al.* 2015; Pirasteh and Li 2017; Balado *et al.* 2018; Wang *et al.* 2018; Che *et al.* 2019; Pirasteh *et al.* 2019, 2020; Ye *et al.* 2020). Compared with two-dimensional (2D) standard maps, a 3D HD map characterizes roads more completely and accurately, and can fulfill the requirements of new challenging road safety applications (Bétaille and Toledo-Moreo 2010; Pu *et al.* 2011; Soilán *et al.* 2017). Traffic signs, particularly including road markings, are the most important safety elements in a 3D HD map. They provide information about limits and directions, and warn drivers about potential dangers (Kumar *et al.* 2014; Holgado-Barco *et al.* 2015; Wen *et al.* 2019). Therefore, robustly and accurately extracting road markings from MLS data is a key problem in constructing 3D

HD maps and automatic driving. However, due to the large volume, high redundancy, and nonlinear error distribution of point-cloud data, the development of automated algorithms for efficient extraction from point-cloud data lags behind compared to advances in hardware systems for mobile lidar (B. Yang *et al.* 2012, 2017).

Extracting road markings from MLS data mainly involves two very different steps: extracting the road surface from raw point-cloud data and extracting road markings from the road surfaces. Researchers have discussed road-surface extraction in-depth, and there are many algorithms available, such as curb-based road-surface extraction (Bartels and Wei 2010; Boyko and Funkhouser 2011; Kumar *et al.* 2013; Rodríguez-Cuenca *et al.* 2015; Yadav *et al.* 2017). Therefore, we concentrate in this study on extracting road markings from road-surface point clouds.

Based on different data formats, road-marking extraction methods can be mainly categorized into two groups: 2D feature image-based extraction and 3D point-based extraction.

At early stages, 2D feature image-based extraction is more popular, because many advanced image-processing algorithms can be used after georeferenced feature images are generated from point-cloud data. B. Yang *et al.* (2012) have presented a method for extracting road markings from georeferenced reflectance intensity images, created by inverse distance-weighted interpolation. The extraction results showed that their method is efficient. Guan *et al.* (2014; see also Ma *et al.* 2019) have proposed an adaptive approach based on reflection intensity variation to extract road markings from feature images. They have improved the traditional intensity threshold method with their discovery that the reflection intensity of point clouds from MLS data is affected by scanning angle and scanning distance—and a better result was gained. Cheng *et al.* (2017) have converted point clouds into radiometrically corrected and enhanced 2D intensity imagery of road surfaces, with pavement markings automatically extracted using Otsu's thresholding, neighbor-counting filtering, and region-growing algorithm based on reflection intensity. Moreover, Jung *et al.* (2019) have used an image-segmentation algorithm to separate lane markings from pavement after rasterizing road-surface point clouds. Topologically similar lane markings were associated with each other by computing line parameters to rectify occlusions or worn portions caused by moving vehicles. In general, this type of method can extract road markings fast using advanced image-processing algorithms, but it may lead to incompleteness and incorrectness when converting 3D point clouds to 2D feature images.

By contrast, the precision and 3D information of point clouds can be preserved by using a 3D point-based extraction method to extract road markings. This type of approach

Chengming Ye, Hongfu Li, Ruilong Wei, Lixuan Wang, and Tianbo Sui are with the Key Laboratory of Earth Exploration and Information Technology of Ministry of Education, Chengdu University of Technology, Chengdu, China (leehungu@sina.com).

Wensen Bai is with Chengdu Sefon Software Company Limited, Chengdu, China.

Pirasteh Saied is with the GeoAI Smarter Map and LiDAR Lab, Department of Geoinformatics and Surveying, Faculty of Geosciences and Environmental Engineering, Southwest Jiaotong University, Chengdu, China.

Contributed by Zhenfeng Shao, October 19, 2020 (sent for review February 9, 2021; reviewed by Gui Cheng, Cheng Zhong).

Photogrammetric Engineering & Remote Sensing
Vol. 87, No. 9, September 2021, pp. 639–648.
0099-1112/21/639–648

© 2021 American Society for Photogrammetry
and Remote Sensing
doi: 10.14358/PERS.20-00099

relies on prior knowledge to a large extent, such as geometric distribution, reflection intensity, and morphological features. Soilán *et al.* (2018; see also Yu *et al.* 2015; M. Yang *et al.* 2018) have detected road markings using a single reflection intensity threshold or multi-threshold based on the high reflectiveness of road markings. Using integrated gray information generated from RGB signals, reflection intensity, and differential intensity, Gao *et al.* (2017) have presented a method to extract road markings from point-cloud data. Wang *et al.* (2018) have excluded points outside the road markings from block-based local coordinate systems within a threshold, then used a statistical filter to remove outliers. Rastiveis *et al.* (2020) have used a Hough transform algorithm to detect candidate lane markings and then extracted true lane markings by extracting geometric and radiometric descriptors for the clusters of probable lane markings and analyzing them in a fuzzy inference system. Yan *et al.* (2016) have proposed a scan-line-based method to extract road markings from mobile lidar point clouds. In this method, the isolated points are removed, and point-cloud data are organized according to scan lines. Then road markings are extracted by the Edge Detection and Edge Constraint method. As already mentioned, the morphological and reflection-intensity features of road markings are widely considered in extracting road markings. However, the characteristics of the point-cloud data themselves, such as uneven density distribution, are ignored in most cases of extracting road markings directly from a 3D point cloud, giving these methods poor adaptability and robustness.

In contrast to all these methods, this study proposes a robust double adaptive reflection intensity-threshold method to extract road markings directly from 3D point cloud data, taking in consideration both the high reflection intensity of road markings and the uneven density of the original point-cloud data. The following sections cover data profiling, the methodology of the study, results and discussion, and conclusions.

Data Profiling

The MLS data sets used in this study were acquired by a RIEGL VMX-450 mobile lidar system in Xiamen, China. The point clouds collected were preprocessed and saved as LAS files. There are three data sets used in this article, containing respectively 5 524 429, 865 532, and 2 098 391 points. We chose Data set 1 as sample data for interpreting our method; road markings in this set mainly contain boundary lines, centerlines, word markings, and zebra crossings (Figure 1).

The VMX-450 system is integrated with two full-view VQ-450 laser scanners, four high-resolution digital cameras, an inertial measurement unit, two global navigation satellite system antennae, and a wheel-mounted distance measurement indicator. The system can achieve a maximum effective measurement rate of 1.1 million points/s. With a speed of 50 km/h, close to the scanning center, the MLS point density is as high as 4000–7000 points/m².

Method

This study presents a double adaptive reflection intensity-threshold approach based on high reflection intensity and uneven density distribution, to extract road markings from road-surface point-cloud data. The method mainly includes preprocessing, road-marking extraction, and adaptive spatial density filtering (Figure 2).

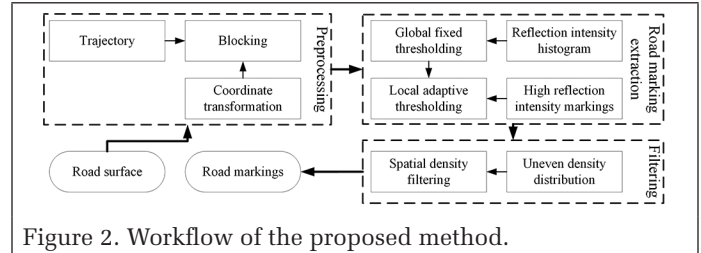


Figure 2. Workflow of the proposed method.

Preprocessing

Coordinate Transformation

The coordinate system of the point-cloud data obtained by an MLS system is arbitrary. For user-friendly visualization and quick calculation, we transform the arbitrary coordinate system to a local relative coordinate system (Figure 1). First a rotation transformation function is used to make sure that the front of the vehicle is roughly parallel to the x-axis and the y-axis points to the left of the vehicle (Equation 1), and; then the data are moved close to their original point by translation (Equation 2):

$$\begin{pmatrix} x_2 \\ y_2 \end{pmatrix} = \begin{pmatrix} \cos \theta & \sin \theta \\ -\sin \theta & \cos \theta \end{pmatrix} \times \begin{pmatrix} x_1 \\ y_1 \end{pmatrix} \quad (1)$$

$$\begin{pmatrix} x_2 \\ y_2 \end{pmatrix} = \begin{pmatrix} x_1 \\ y_1 \end{pmatrix} - \begin{pmatrix} x_m \\ y_m \end{pmatrix} \quad (2)$$

where (x_1, y_1) and (x_2, y_2) are point coordinates before and after the transformation, respectively, θ is the rotation angle between the trajectory and the x-axis, and (x_m, y_m) are the minimum values of x and y after rotation, respectively.

Blocking

Road markings show higher reflection intensity than other surrounding road surfaces in point clouds, because they are painted on asphalt road surfaces using highly reflective objects (Figure 1). However, the reflection intensity of point clouds also depends on material properties of the scanned objects, the range between the laser sensor and the target, and incidence angles of the laser beam, which all cause the reflection intensity value to be unevenly distributed. A profile of the y-direction is generated perpendicular to the trajectory, recorded by the on-board navigation module while the MLS system collects data. As Figure 3 illustrates, the reflection

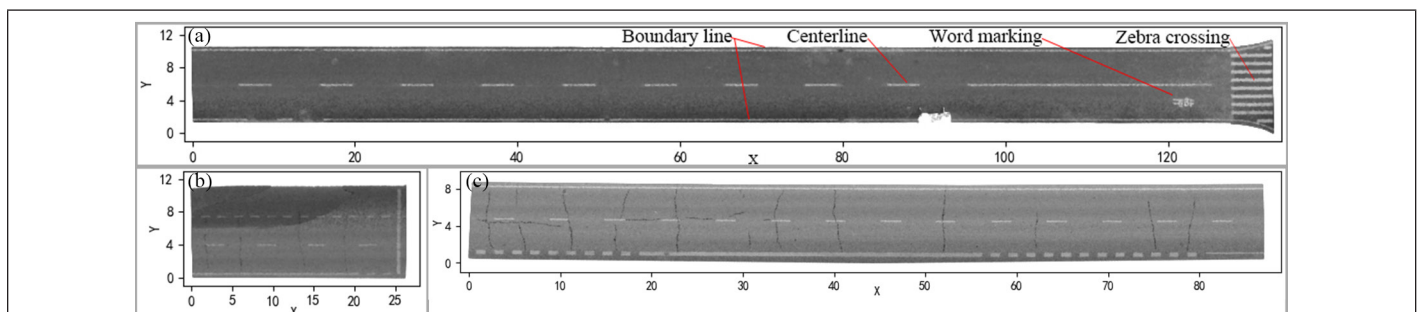


Figure 1. Experiment road-surface point cloud after coordinate transformation. (a) Data set 1, (b) Data set 2, (c) Data set 3.

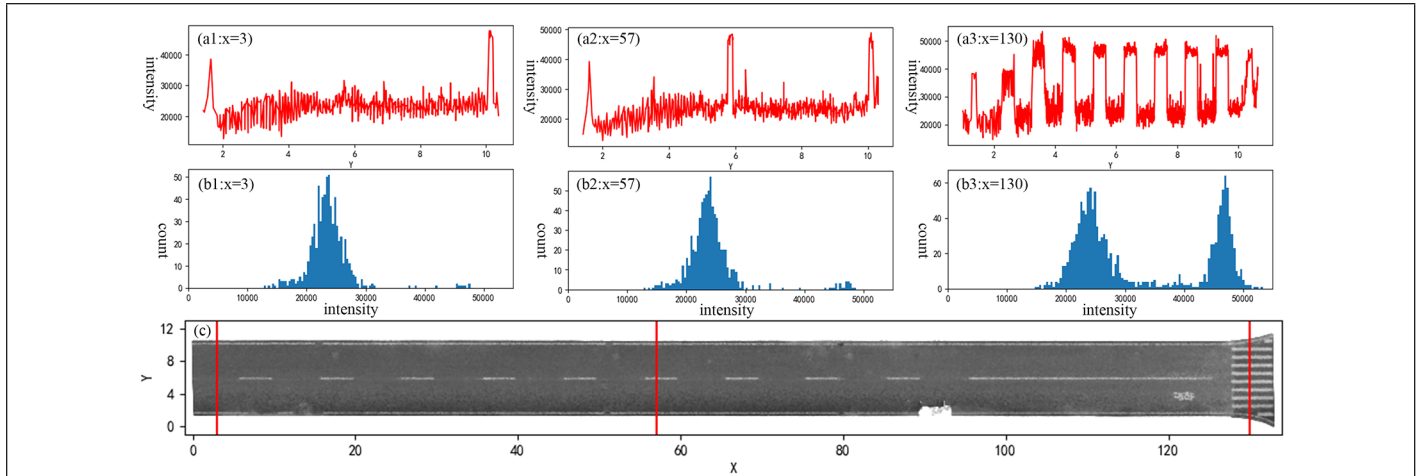


Figure 3. Profile analysis perpendicular to the trajectory for Data set 1. (a) Reflection intensity of profiles, (b) reflection intensity histogram of profiles, (c) road-surface point cloud with profiles.

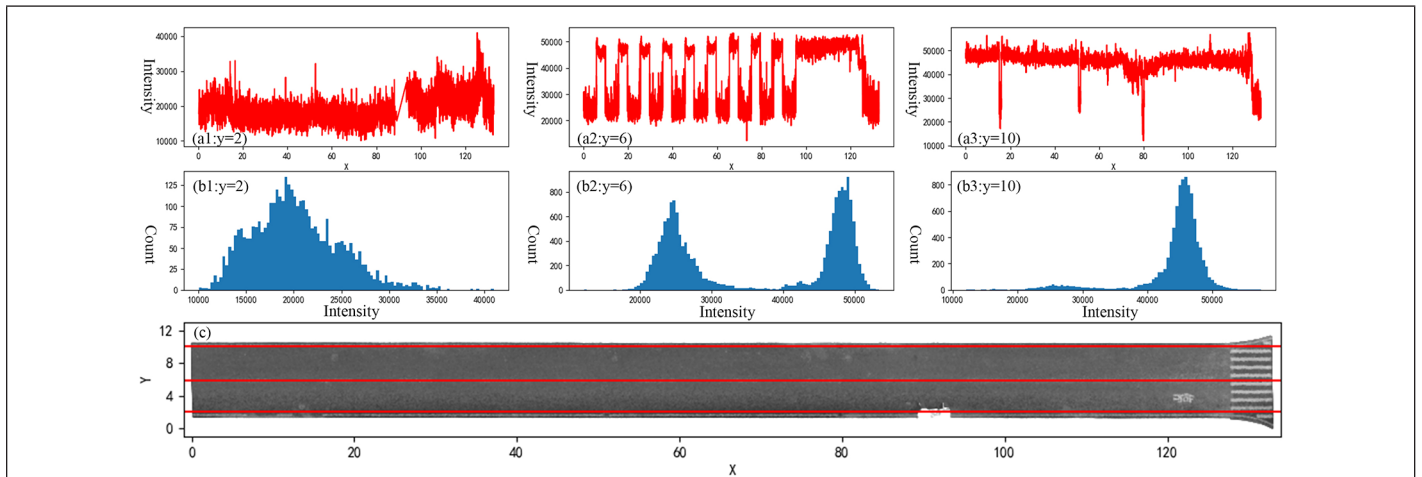


Figure 4. Profile analysis along the trajectory for Data set 1. (a) Reflection intensity of profiles, (b) reflection intensity histogram of profiles, (c) road-surface point cloud with profiles.

intensity of the road surface fluctuates violently, and is slightly greater at the upper part of the road surface than at the bottom. In addition, the (relative) reflection intensity value of road markings is nearly 2000 higher than that of the road surface. A similar phenomenon occurs in Figure 4, a profile of the x-direction along the trajectory. In this study, the uneven reflection intensity is what must be overcome for better results in road-marking extraction. Therefore, to avoid interference from local high-reflection-intensity road surface (considered noise) far away from the markings, we partition the road-surface point-cloud data into a set of blocks perpendicular to the trajectory (Figure 5). The width W of a block is fixed.

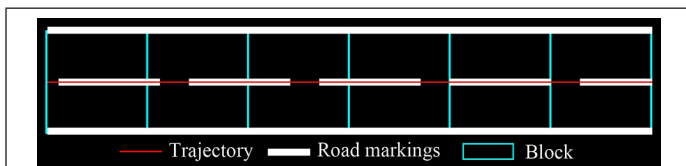


Figure 5. Block model perpendicular to the trajectory.

Road-Marking Extraction

Although the effect of uneven reflection intensity along the trajectory is decreased by the blocking operation, it still exists in each block perpendicular to the trajectory. The proposed double adaptive intensity-threshold method is an efficient

way to restrain the influence of uneven reflection intensity. In the first instance, we use a global fixed reflection intensity threshold to remove points of low reflection intensity. In the second, we extract road markings from each block by a local adaptive reflection intensity threshold.

Global Fixed Thresholding

We divided the road-surface points into three categories to extract road markings efficiently. In this study, we categorized the reflection intensity of point clouds as either low, medium, or high. As Figure 6 depicts, point clouds were categorized as having low reflection intensity when their reflection intensity was lower than the first crest of the histogram. Medium reflection intensity meant the value was between the first crest of the histogram and the local adaptive threshold. The remainder were categorized as having high reflection intensity—and regarded as road markings. In this article, we aim to find an optimal reflection intensity threshold to maximize the differences between medium-reflection-intensity points and road markings. In theory, the optimal threshold is a fixed value for each block and will not be affected by low-reflection-intensity points. But in practice, these low-reflection-intensity points extend the range of reflection intensity, making the optimal reflection intensity smaller. Therefore, low-reflection-intensity points are considered noise and are removed from the road surface before road markings are extracted using a global fixed reflection intensity threshold.

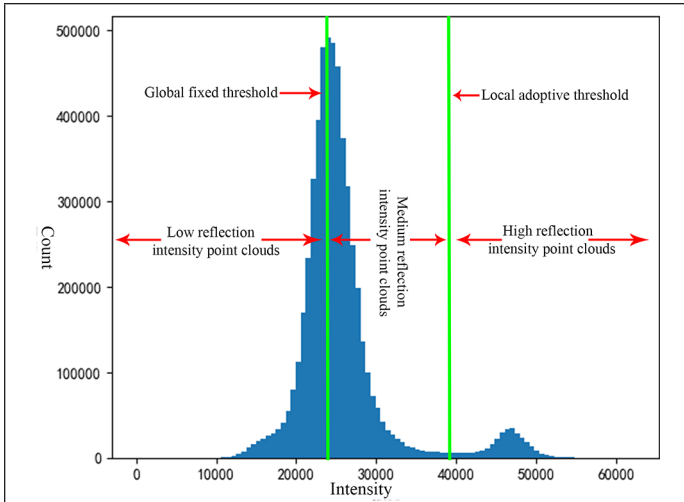


Figure 6. Reflection-intensity classification of road surface based on the histogram of Data set 1.

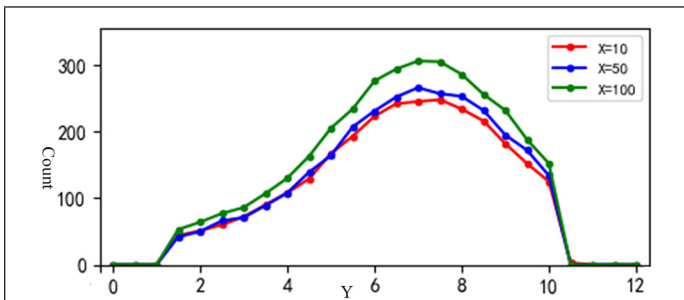


Figure 7. Number of points in a square neighborhood with side length 0.1 m.

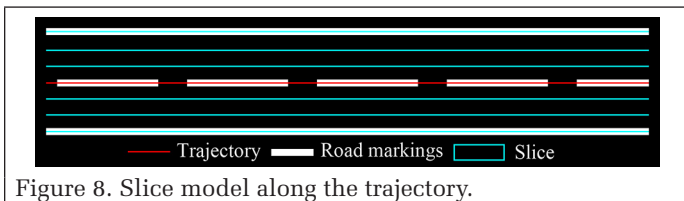


Figure 8. Slice model along the trajectory.

Local Adaptive Thresholding

After low-reflection-intensity points are removed from the road surface, we aim to find an optimal local threshold between the remaining road surface and road markings in each block. We applied the Otsu (1979) thresholding algorithm to determine local adaptive thresholds. The Otsu thresholding algorithm aims to find an optimal threshold between background and foreground by maximizing the ratio of between-classes variance, defined as

$$\sigma = w_0 \cdot w_1 (u_1 - u_0) \quad (3)$$

where w_0 and w_1 are the respective occurrence probabilities of non-traffic-marking points (background) and road-marking points (foreground) and u_0 and u_1 are the corresponding mean reflection intensity values.

The detailed steps of the Otsu thresholding algorithm are as follows: 1) Suppose an optimal threshold, estimate the values of the parameters w_0 , w_1 , u_0 , and u_1 , and compute the value of σ . 2) Iterate all reflection intensities using a given step value and repeat step 1. 3) Find the maximum value of σ ; the optimal reflection intensity threshold is the corresponding hypothesis threshold.

Adaptive Spatial Density Filtering

We extracted road markings using the double adaptive intensity-threshold method. However, there was still much high-reflection-intensity noise (false road-marking points), which were dispersed and irregularly distributed. To remove these from the extracted road markings, we used an adaptive spatial density filter based on the density distribution of point-cloud data. This method eliminates noises by setting a fixed density threshold D_f in a neighborhood R_n and comparing it with the practical density D_p . If a point's D_p in R_n is smaller than D_f , the point is regarded as noise and removed:

$$\begin{cases} \text{noise} & \text{if } D_p < D_f, \\ \text{road marking} & \text{otherwise} \end{cases} \quad (4)$$

We found that the density distribution of the point-cloud data was uneven, with much higher density near trajectory, causing dense noise near trajectory and sparse noise away from it (Figure 7). Due to this uneven distribution, false road-marking points cannot be easily eliminated by a spatial density filter using a fixed density threshold. Hence, we improved the method based on an uneven density distribution. First, we partitioned the road surface into slices parallel to the trajectory (Figure 8). Then, to efficiently eliminate both dense and sparse noise, we determined the density threshold for each slice by the density value of its road-surface point-cloud data:

$$\begin{cases} \text{noise} & \text{if } D_p < (D_o/k), \\ \text{road marking} & \text{otherwise} \end{cases} \quad (5)$$

where D_p is the practical density of the point-cloud data after extracting road markings; D_o , regarded as the density threshold, is the density of origin point clouds before extracting road markings, with a different value for each slice; and k is a coefficient to reduce the gap between D_p and D_o , because the density of point clouds after road markings are extracted is definitely lower.

Results and Discussion

Road-Marking Extraction

As low-reflection-intensity points were already defined, we set the first crest value of the reflection intensity histogram as a global fixed reflection intensity threshold. The shaded parts of the surface (highlighted in red in Figure 9) are removed using a global fixed reflection intensity threshold, and the distinction between road markings and road surface is still clear visually. After that, we extracted road markings using a local adaptive threshold for each data block. The width W of each block was set as 2 m according to our experiments—but it is also fine if W is a little bigger or smaller. As Figure 10 shows, we extracted the road markings very well and the uneven reflection intensity was efficiently constrained, except in Data set 2. There is a shadow in Figure 10b1 (highlighted in green), reducing the reflection intensity there, so road-marking extraction results there are terrible. And there is still much dispersed noise in all three data sets. According to the origin point-cloud data, we can see that the reflection intensity values of the road surface are higher in these areas, causing this dense noise.

We compared our road-marking extraction results with the results of the extraction methods of Yu *et al.* (2015) and Otsu (1979). The Yu *et al.* method partitions the point clouds into a set of data blocks along the trajectory and uses a multi-segment thresholding strategy, whereas Otsu's method segments the data into blocks perpendicular to the trajectory

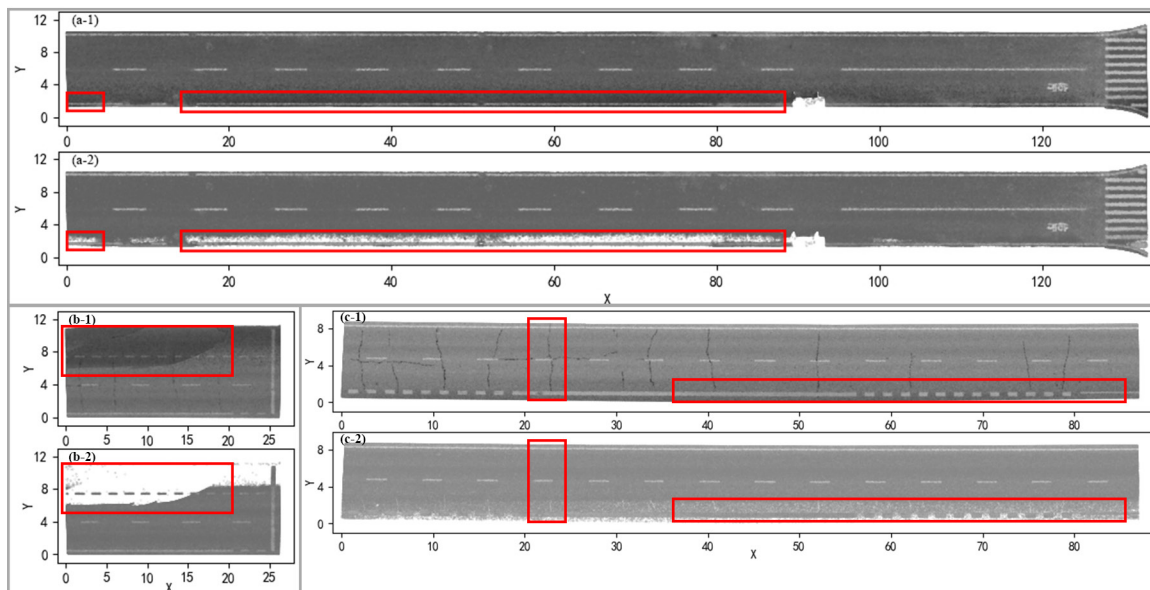


Figure 9. Removal of low-reflection-intensity point clouds. (a1, b1, c1) Original data for Data sets 1, 2, and 3, respectively. (a2, b2, c2) Corresponding results after removal of low-reflection-intensity point clouds.

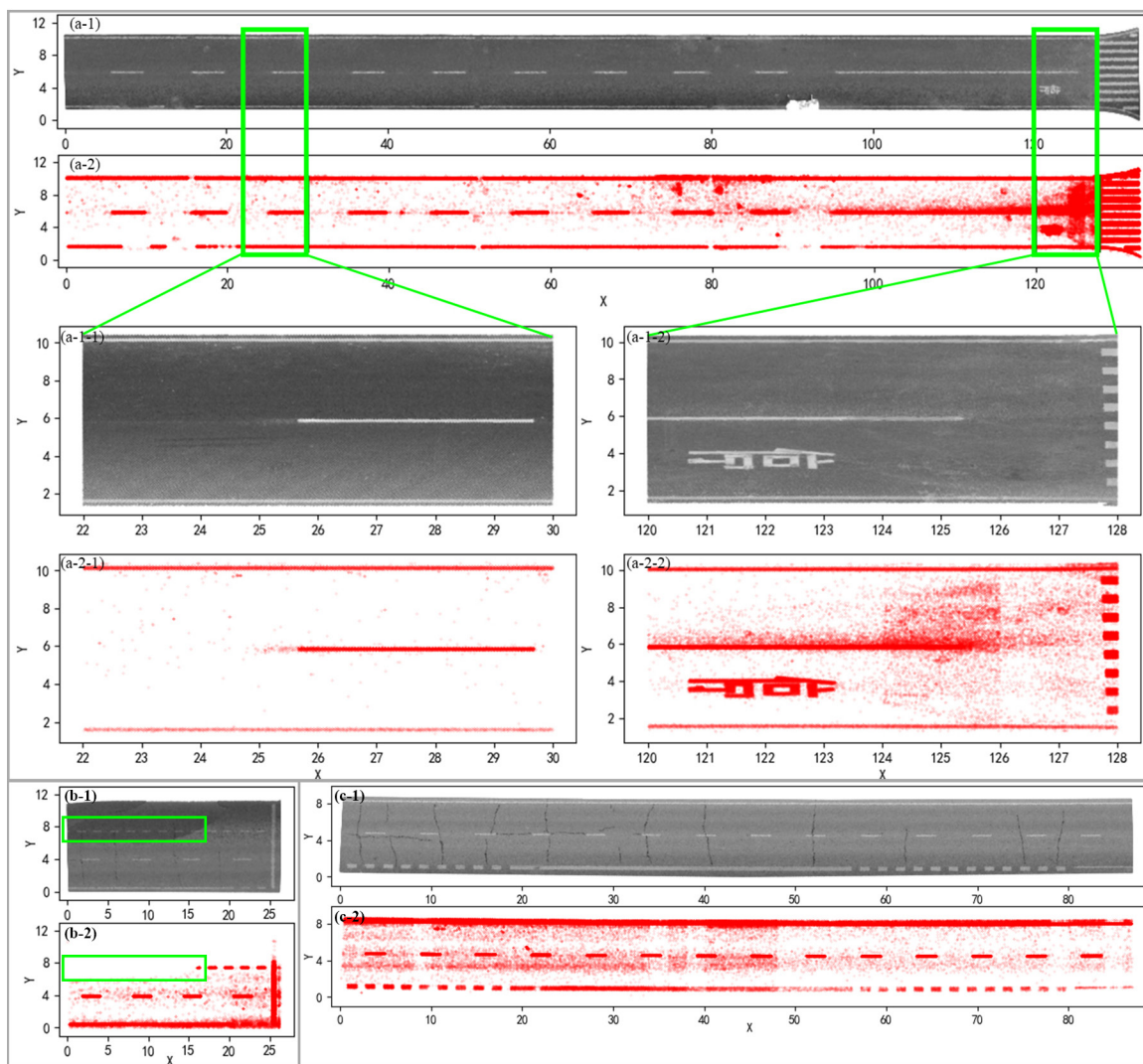


Figure 10. Road-marking extraction. (a1, b1, c1) Original data for Data sets 1, 2, and 3, respectively. (a2, b2, c2) Corresponding results after road-marking extraction.

and uses adaptive reflection intensity thresholding only once. As Figure 11 shows, our proposed method is more sensitive to high-reflection-intensity noise and extracts road markings more efficiently and accurately. There is more noise in Figure 11 for the Yu *et al.* and Otsu methods because a large number of low-reflection-intensity points exists in the road surface. In addition, both of those methods use adaptive intensity thresholding only once, reducing the adaptive reflection intensity threshold below normal. If the differences between road surface and markings are great, those methods may nevertheless attain good road-marking extraction results, as in most of Figure 11a2 and the upper part of Figure 11a3.

To further quantitatively evaluate our experimental results obtained using different methods, we converted our 3D road-marking extraction results to 2D georeferenced images and then computed completeness E_{cpt} , correctness E_{crt} , and the F measure E_f based on manually labeled reference road markings:

$$E_{cpt} = \frac{TP}{TP + FN} \quad (6)$$

$$E_{crt} = \frac{TP}{TP + FP} \quad (7)$$

$$E_f = \frac{2 \times E_{cpt} \times E_{crt}}{E_{cpt} + E_{crt}} \quad (8)$$

where TP, FN, and FP are the pixel numbers of true positives, false negatives, and false positives, respectively, in converted 2D georeferenced images. Completeness describes how complete the extracted road markings are, correctness

is the percentage of valid extracted road markings, and the F measure indicates an overall score taking into consideration both precision and recall.

As shown in Table 1, our approach achieved an average completeness of 0.840, correctness of 0.774, and F measure of 0.804, indicating a reliable extraction result. The other two methods achieved higher scores for completeness but much lower scores for both correctness and F measure. The average F measure for both of the other methods is below 0.4 because of their terrible extraction results (shown in Figure 11).

Table 1. Quantitative assessment of road-marking extraction results.

Method	Data Set	Completeness	Correctness	F Measure
Ours	1	0.943	0.856	0.897
	2	0.816	0.842	0.829
	3	0.761	0.624	0.686
	Average	0.840	0.774	0.804
Otsu (1979)	1	0.954	0.746	0.847
	2	0.911	0.047	0.089
	3	0.957	0.102	0.184
Average	0.941	0.298	0.373	
Yu <i>et al.</i> (2015)	1	0.970	0.404	0.570
	2	0.954	0.104	0.188
	3	0.936	0.089	0.162
Average	0.953	0.199	0.307	

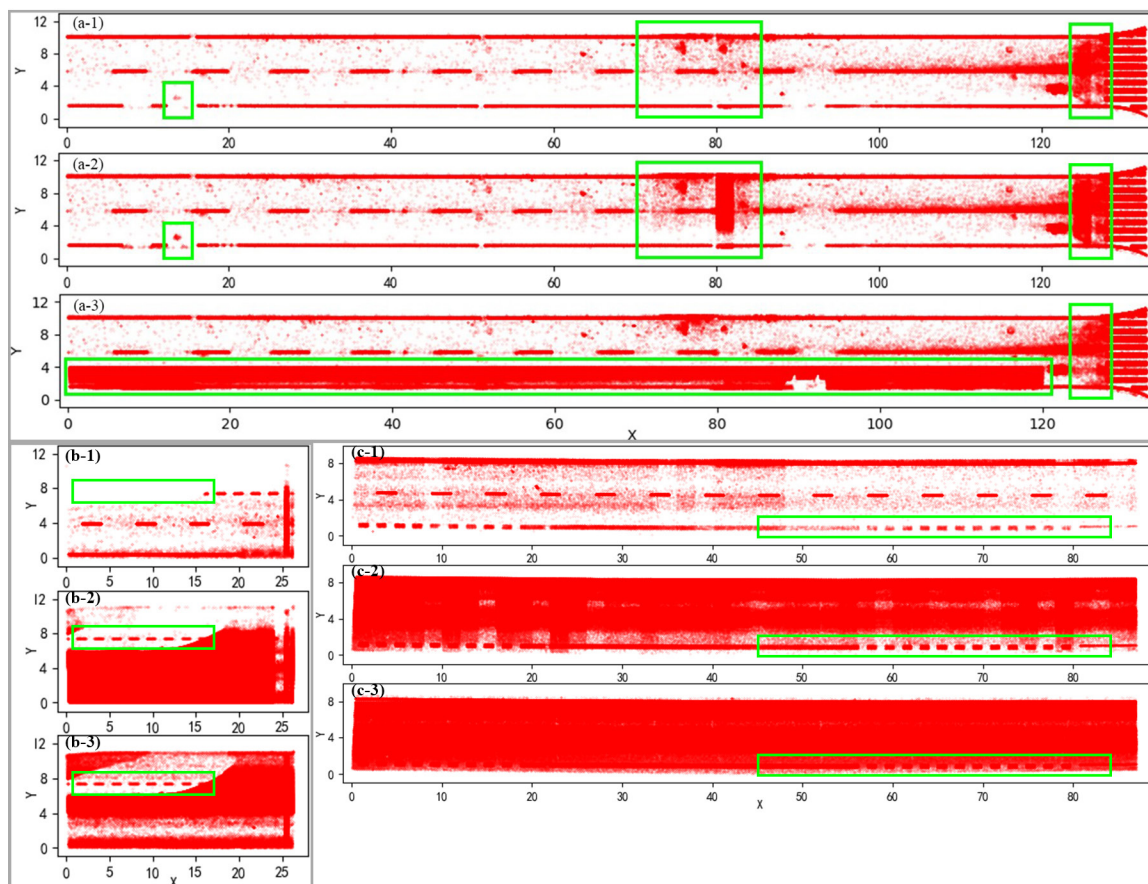


Figure 11. Road-marking extraction results using different methods for Data sets 1, 2, and 3. (a1, b1, c1) The proposed method, (a2, b2, c2) Otsu's (1979) method, (a3, b3, c3) Yu *et al.* (2015) method.

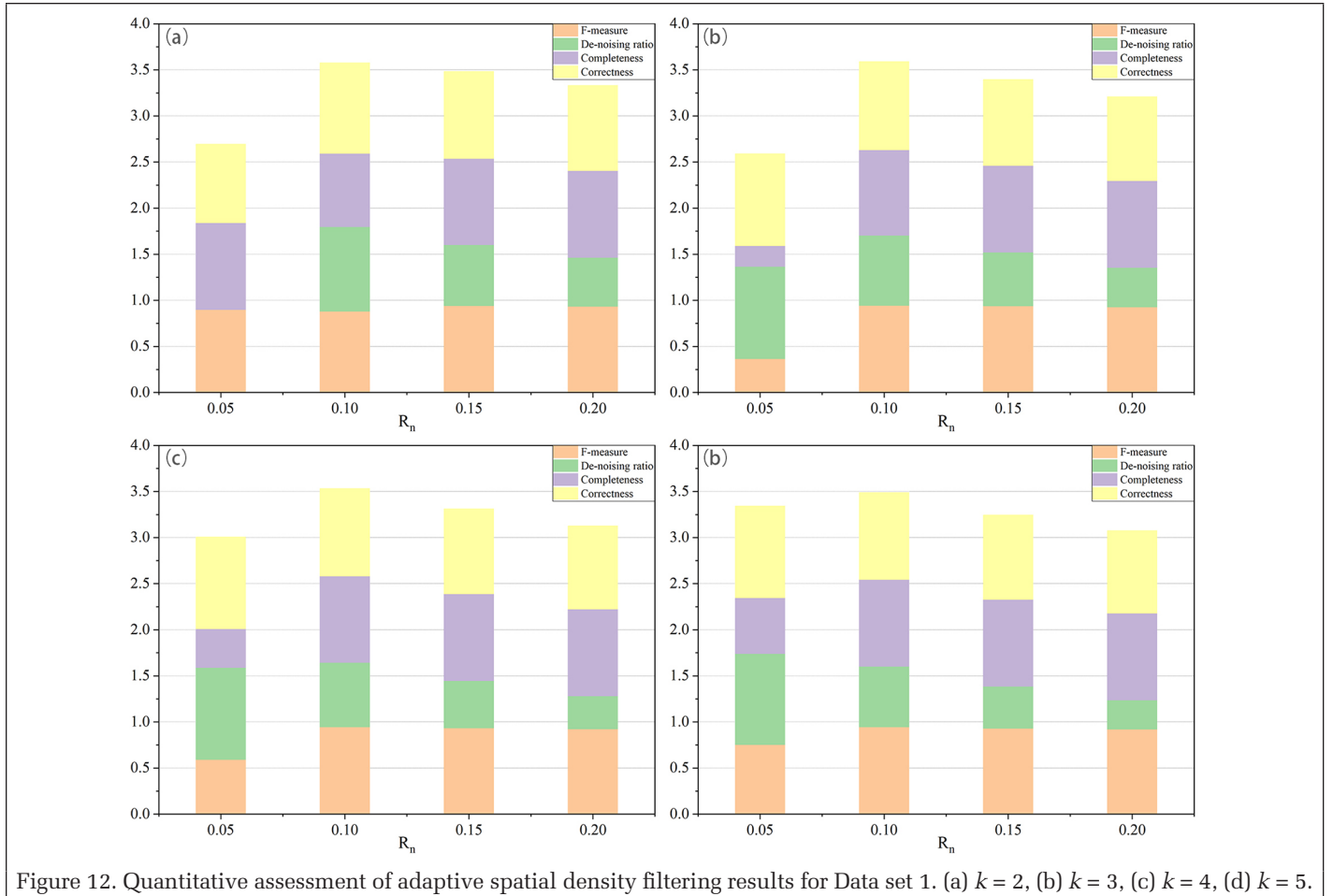


Figure 12. Quantitative assessment of adaptive spatial density filtering results for Data set 1. (a) $k = 2$, (b) $k = 3$, (c) $k = 4$, (d) $k = 5$.

Adaptive Spatial Density Filtering

Before directly analyzing the results of adaptive spatial density filtering, we take into consideration the neighborhood R_n and coefficient k , using Data set 1 as our experimental data. Because the width of standard road markings ranges from 0.1 to 0.15 m, according to the Code for the Layout of Urban Road Traffic Signs and Markings of China (GB 51038-2015), R_n is set as 0.05, 0.1, 0.15, and 0.2 m, with an interval of 0.05 m. The Coefficient k depends on the density of the point cloud; in our experiments we set it to 2, 3, 4, and 5. To further quantitatively evaluate the filtering results obtained using different parameters, we introduced another measure—the denoising ratio E_{dnr} —which indicates the percentage of noise eliminated:

$$E_{dnr} = \frac{N_b - N_a}{N_b} \quad (9)$$

where N_b and N_a are the pixel numbers of noise before and after filtering, respectively.

As can be seen in Figure 12, the denoising ratio and correctness decrease, while completeness increases, as R_n gets bigger in most cases. When R_n equals 0.1 m, both the F measure and denoising ratio show good performance. So we created Figure 13 to find out the influence of the coefficient k . As the figure shows, a high denoising ratio and correctness occur with a low F measure and completeness when k equals 2, which seriously affects road markings. Although other results indicate slight differences when k equals 3, 4, and 5, there is still a little superiority when k equals 3. Therefore, we recommend $k = 3$ and $R_n = 0.1$ m for Data set 1. The same parameters fit Data set 2 well, because the density distribution is similar for the two data sets. However, for Data set 3 a reliable

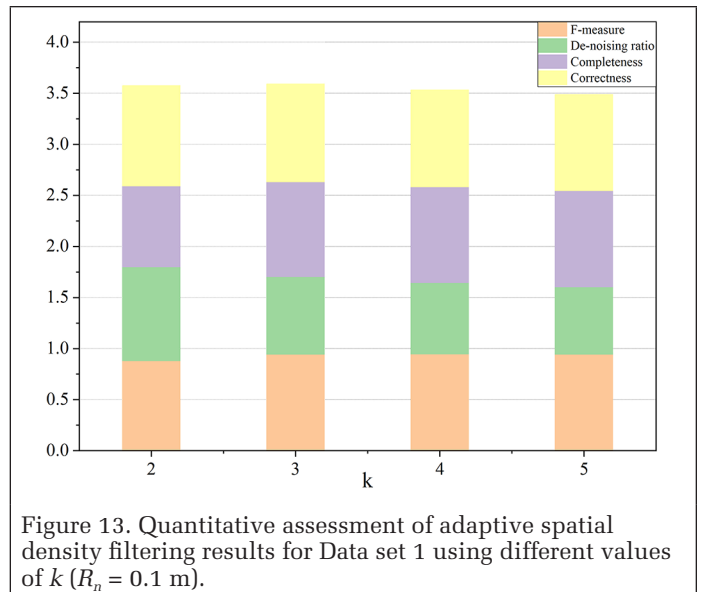


Figure 13. Quantitative assessment of adaptive spatial density filtering results for Data set 1 using different values of k ($R_n = 0.1$ m).

filtering result is obtained when $k = 6$ and $R_n = 0.1$ m, because the point-cloud density is less than that in Data sets 1 and 2.

After k and R_n are determined, we can discuss the filtering results in more detail. As Figure 14 shows, most of the dispersed noise is eliminated, with a few road markings affected, using an adaptive spatial density filter based on the density distribution of point clouds. The filtering results of the comparative study are seen in Figure 15, which shows less noise

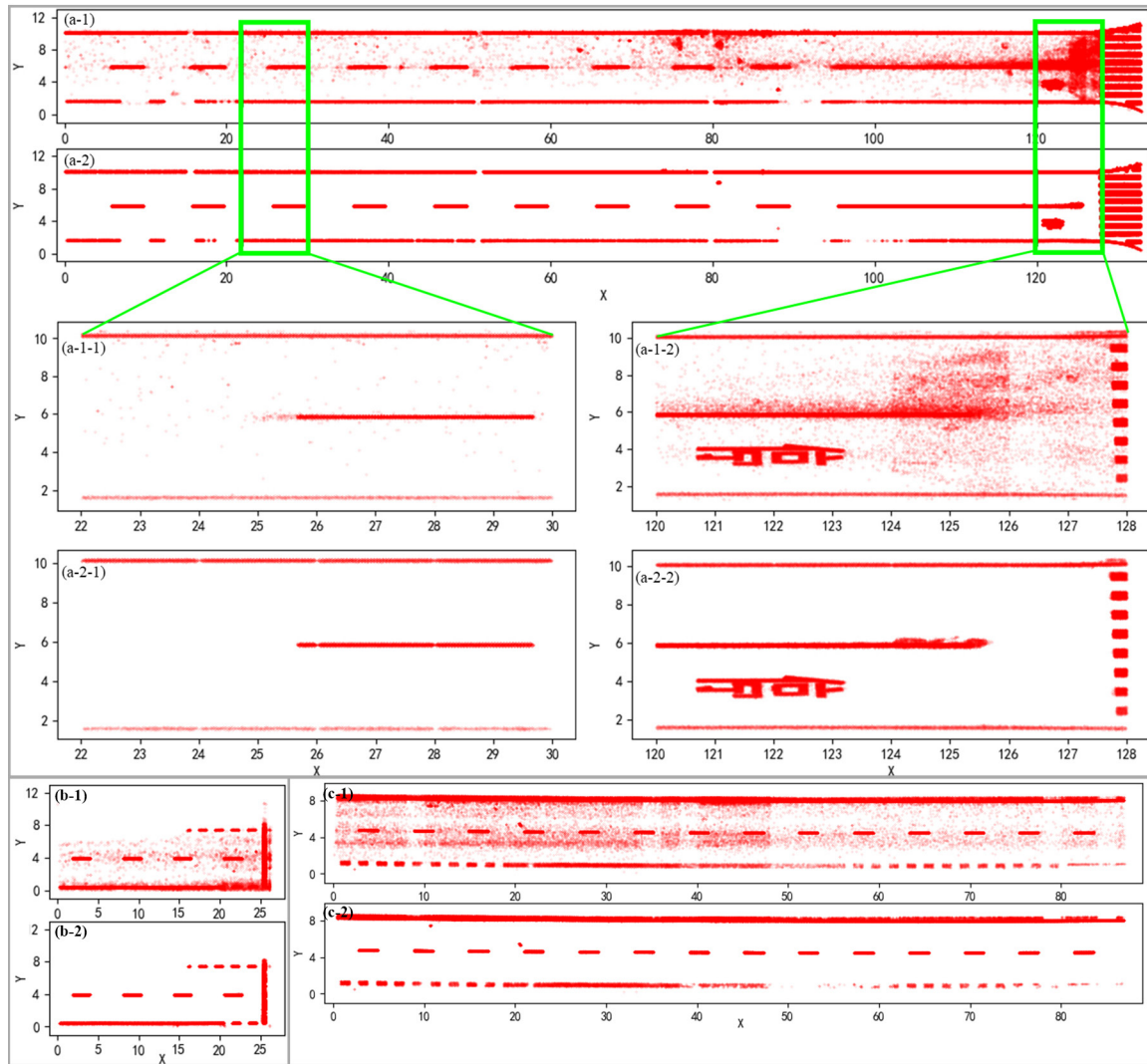


Figure 14. Adaptive spatial density filtering results for Data set 1, 2, and 3. (a1, b1, c1) Road-marking extraction results, (a2, b2, c2) adaptive spatial density filtering results.

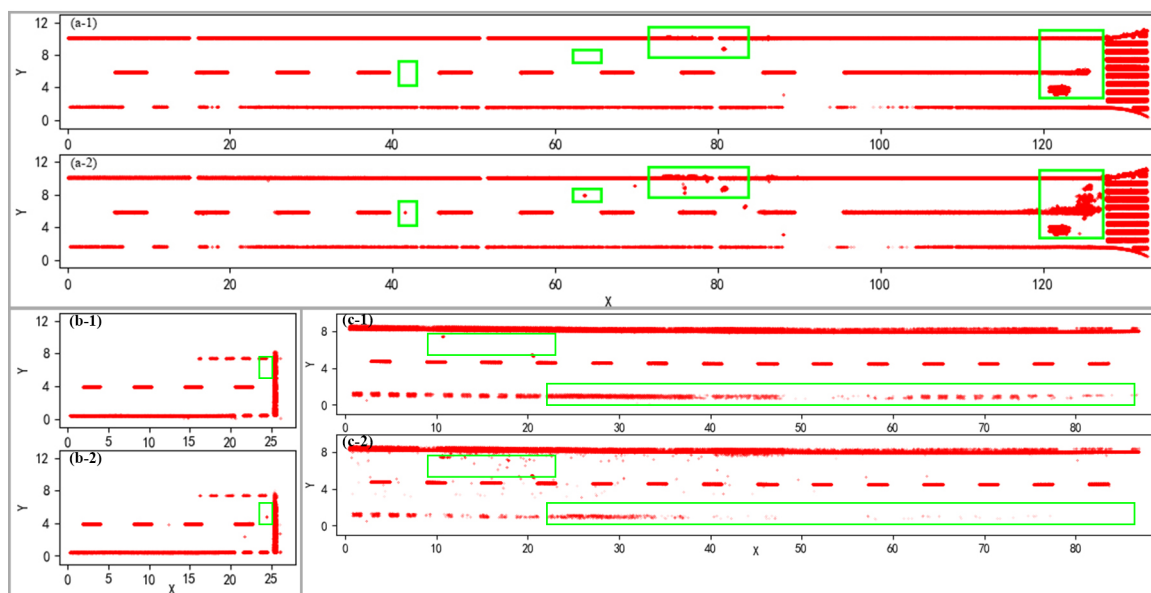


Figure 15. Filtering results for Data sets 1, 2, and 3 using different methods. (a1, b1, c1) Our proposed method, (a2, b2, c2) spatial density filtering method using a fixed density threshold.

using our proposed filtering method than a method with a fixed density threshold. The four indices already mentioned are computed to quantitatively evaluate the filtering results.

From Table 2, we can see that most indicators are higher using our method than a traditional fixed spatial density threshold method. These quantitative results show that our proposed adaptive spatial density filter has reliable performance in eliminating noise and retaining road markings compared to the traditional method.

Table 2. Quantitative assessment of filtering results.

Method	Data	F	Denoising		
	Set	Measure	Ratio	Completeness	Correctness
Ours	1	0.943	0.761	0.926	0.961
	2	0.875	0.785	0.803	0.961
	3	0.745	0.424	0.751	0.740
	Average	0.854	0.657	0.827	0.887
Fixed density threshold	1	0.926	0.501	0.930	0.922
	2	0.866	0.780	0.790	0.959
	3	0.718	0.435	0.705	0.731
	Average	0.837	0.572	0.808	0.871

Conclusions

Because the characteristics of point clouds themselves are ignored in most cases, current road-marking extraction methods have poor adaptability and robustness, especially for uneven point-cloud data. This study developed a simple and robust double adaptive intensity-threshold method to extract road markings from road-surface point clouds. We divided the road-surface point clouds into three categories (low, medium, high) according to reflection intensity and proposed a new strategy to extract road markings by removing low-reflection-intensity point clouds first. Moreover, an adaptive spatial density filter was used to eliminate false road-marking points based on the uneven density distribution of point clouds after road markings were extracted. Finally, we used data sets acquired by a RIEGL VMX-450 mobile lidar system to validate our road-marking extraction method. In quantitative evaluation, the proposed method achieved an average completeness, correctness, and F measure of 0.827, 0.887, and 0.854, respectively, for the three data sets. Comparative studies demonstrated that the proposed method performs more reliably than two other methods. Our method provides an alternative solution for extracting road information and constructing 3D HD maps.

Acknowledgments

This work was supported in part by the National Natural Science Foundation of China under grant 42071411 the Second Tibetan Plateau Scientific Expedition and Research Program under grant 2019QZKK0902, the Strategic Priority Research Program of the Chinese Academy of Sciences under grant XDA23090203, and a program of the Chengdu Science and Technology Bureau. The authors would like to thank Professor Jonathan Li of the University of Waterloo, Canada, for providing the data sets.

References

Aijazi, A. K., P. Checchin and L. Trassoudaine. 2013. Segmentation based classification of 3D urban point clouds: A super-voxel based approach with evaluation. *Remote Sensing* 5(4):1624–1650. <https://doi.org/10.3390/rs5041624>.

- Balado, J., L. Díaz-Vilariño, P. Arias and H. González-Jorge. 2018. Automatic classification of urban ground elements from mobile laser scanning data. *Automation in Construction* 86:226–239. <https://doi.org/10.1016/j.autcon.2017.09.004>.
- Bartels, M. and H. Wei. 2010. Threshold-free object and ground point separation in LIDAR data. *Pattern Recognition Letters* 31(10):1089–1099. <https://doi.org/10.1016/j.patrec.2010.03.007>.
- Bétaille, D. and R. Toledo-Moreo. 2010. Creating enhanced maps for lane-level vehicle navigation. *IEEE Transactions on Intelligent Transportation Systems* 11(4):786–798. <https://doi.org/10.1109/tits.2010.2050689>.
- Boyko, A. and T. Funkhouser. 2011. Extracting roads from dense point clouds in large scale urban environment. *ISPRS Journal of Photogrammetry and Remote Sensing* 66(6 suppl.):S2–S12. <https://doi.org/10.1016/j.isprsjprs.2011.09.009>.
- Che, E., J. Jung and M. J. Olsen. 2019. Object recognition, segmentation, and classification of mobile laser scanning point clouds: A state of the art review. *Sensors* 19(4):810. <https://doi.org/10.3390/s19040810>.
- Cheng, M., H. Zhang, C. Wang and J. Li. 2017. Extraction and classification of road markings using mobile laser scanning point clouds. *IEEE Journal of Selected Topics in Applied Earth Observations and Remote Sensing* 10(3):1182–1196. <https://doi.org/10.1109/jstars.2016.2606507>.
- Gao, Y., R. Zhong, T. Tang, L. Wang and X. Liu. 2017. Automatic extraction of pavement markings on streets from point cloud data of mobile LiDAR. *Measurement Science and Technology* 28(8):085203.
- Geospatial Media and Communications. 2018. *European Geospatial Business Outlook Report*. <<https://geospatialmedia.net/report/EGBS-report-digital.pdf>> Accessed DD Month YYYY.
- Guan, H., J. Li, Y. Yu, M. Chapman and C. Wang. 2015. Automated road information extraction from mobile laser scanning data. *IEEE Transactions on Intelligent Transportation Systems* 16(1):194–205. <https://doi.org/10.1109/tits.2014.2328589>.
- Guan, H., J. Li, Y. Yu, C. Wang, M. Chapman and B. Yang. 2014. Using mobile laser scanning data for automated extraction of road markings. *ISPRS Journal of Photogrammetry and Remote Sensing* 87:93–107.
- Holgado-Barco, A., D. González-Aguilera, P. Arias-Sanchez and J. Martínez-Sánchez. 2015. Semiautomatic extraction of road horizontal alignment from a mobile LiDAR system. *Computer-Aided Civil and Infrastructure Engineering* 30(3):217–228. <https://doi.org/10.1111/mice.12087>.
- Jung, J., E. Che, M. J. Olsen and C. Parrish. 2019. Efficient and robust lane marking extraction from mobile lidar point clouds. *ISPRS Journal of Photogrammetry and Remote Sensing* 147:1–18. <https://doi.org/10.1016/j.isprsjprs.2018.11.012>.
- Kumar, P., C. P. McElhinney, P. Lewis and T. McCarthy. 2013. An automated algorithm for extracting road edges from terrestrial mobile LiDAR data. *ISPRS Journal of Photogrammetry and Remote Sensing* 85:44–55. <https://doi.org/10.1016/j.isprsjprs.2013.08.003>.
- Kumar, P., C. P. McElhinney, P. Lewis and T. McCarthy. 2014. Automated road markings extraction from mobile laser scanning data. *International Journal of Applied Earth Observation and Geoinformation* 32:125–137. <https://doi.org/10.1016/j.jag.2014.03.023>.
- Ma, L., Y. Li, J. Li, Z. Zhong and M. A. Chapman. 2019. Generation of horizontally curved driving lines in HD maps using mobile laser scanning point clouds. *IEEE Journal of Selected Topics in Applied Earth Observations and Remote Sensing* 12(5):1572–1586. <https://doi.org/10.1109/jstars.2019.2904514>.
- Otsu, N. 1979. A threshold selection method from gray-level histograms, *IEEE Transactions on Systems, Man, and Cybernetics* SMC-9(1):62–66.
- Pirasteh, S. and J. Li. 2017. Landslides investigations from geoinformatics perspective: Quality, challenges, and recommendations. *Geomatics, Natural Hazards and Risk* 8(2):448–465.

- Pirasteh, S., P. Rashidi, H. Rastiveis, S. Huang, Q. Zhu, G. Liu, Y. Li, J. Li and E. Seydipour. 2019. Developing an algorithm for buildings extraction and determining changes from airborne LiDAR, and comparing with R-CNN method from drone images. *Remote Sensing* 11(11):1272.
- Pirasteh, S., G. Shamsipour, G. Liu, Z. Qing and C. Ye. 2020. A new algorithm for landslide geometric and deformation analysis supported by digital elevation models. *Earth Science Informatics* 13(2):361–375. <https://doi.org/10.1007/s12145-019-00437-5>.
- Pu, S., M. Rutzinger, G. Vosselman and S. O. Elberink. 2011. Recognizing basic structures from mobile laser scanning data for road inventory studies. *ISPRS Journal of Photogrammetry and Remote Sensing* 66(6 suppl.):S28–S39. <https://doi.org/10.1016/j.isprsjprs.2011.08.006>.
- Rastiveis, H., A. Shams, W. A. Sarasua and J. Li. 2020. Automated extraction of lane markings from mobile LiDAR point clouds based on fuzzy inference. *ISPRS Journal of Photogrammetry and Remote Sensing* 160:149–166. <https://doi.org/10.1016/j.isprsjprs.2019.12.009>.
- Rodríguez-Cuenca, B., S. García-Cortés, C. Ordóñez and M. C. Alonso. 2015. An approach to detect and delineate street curbs from MLS 3D point cloud data. *Automation in Construction* 51:103–112. <https://doi.org/10.1016/j.autcon.2014.12.009>.
- Soilán, M., B. Riveiro, J. Martínez-Sánchez and P. Arias. 2017. Segmentation and classification of road markings using MLS data. *ISPRS Journal of Photogrammetry and Remote Sensing* 123:94–103. <https://doi.org/10.1016/j.isprsjprs.2016.11.011>.
- Soilán, M., L. Truong-Hong, B. Riveiro and D. Laefer. 2018. Automatic extraction of road features in urban environments using dense ALS data. *International Journal of Applied Earth Observation and Geoinformation* 64:226–236. <https://doi.org/10.1016/j.jag.2017.09.010>.
- Wang, J., H. Zhao, D. Wang, Y. Chen, Z. Zhang and H. Liu. 2018. GPS trajectory-based segmentation and multi-filter-based extraction of expressway curbs and markings from mobile laser scanning data. *European Journal of Remote Sensing* 51(1):1022–1035. <https://doi.org/10.1080/22797254.2018.1533388>.
- Wang, R., J. Peethambaran and D. Chen. 2018. LiDAR point clouds to 3-D urban models: A review. *IEEE Journal of Selected Topics in Applied Earth Observations and Remote Sensing* 11(2):606–627.
- Wen, C., X. Sun, J. Li, C. Wang, Y. Guo and A. Habib. 2019. A deep learning framework for road marking extraction, classification and completion from mobile laser scanning point clouds. *ISPRS Journal of Photogrammetry and Remote Sensing* 147:178–192. <https://doi.org/10.1016/j.isprsjprs.2018.10.007>.
- Yadav, M., A. K. Singh and B. Lohani. 2017. Extraction of road surface from mobile LiDAR data of complex road environment. *International Journal of Remote Sensing* 38(16):4655–4682. <https://doi.org/10.1080/01431161.2017.1320451>.
- Yan, L., H. Liu, J. Tan, Z. Li, H. Xie and C. Chen. 2016. Scan line based road marking extraction from mobile LiDAR point clouds. *Sensors* 16(6):903.
- Yang, B., L. Fang, Q. Li and J. Li. 2012. Automated extraction of road markings from mobile lidar point clouds. *Photogrammetric Engineering & Remote Sensing* 78(4):331–338.
- Yang, B., Y. Liu, Z. Dong, F. Liang, B. Li and X. Peng. 2017. 3D local feature BKD to extract road information from mobile laser scanning point clouds. *ISPRS Journal of Photogrammetry and Remote Sensing* 130:329–343. <https://doi.org/10.1016/j.isprsjprs.2017.06.007>.
- Yang, M., Y. Wan, X. Liu, J. Xu, Z. Wei, M. Chen and P. Sheng. 2018. Laser data based automatic recognition and maintenance of road markings from MLS system. *Optics & Laser Technology* 107:192–203. <https://doi.org/10.1016/j.optlastec.2018.05.027>.
- Ye, C., J. Li, H. Jiang, H. Zhao, L. Ma and M. Chapman. 2020. Semi-automated generation of road transition lines using mobile laser scanning data. *IEEE Transactions on Intelligent Transportation Systems* 21(5):1877–1890.
- Yu, Y., J. Li, H. Guan, F. Jia and W. Cheng. 2015. Learning hierarchical features for automated extraction of road markings from 3-D mobile LiDAR point clouds. *IEEE Journal of Selected Topics in Applied Earth Observations and Remote Sensing* 8(2):709–726.

Estimating Regional Soil Moisture with Synergistic Use of AMSR2 and MODIS Images

Majid Rahimzadegan, Arash Davari, and Ali Sayadi

Abstract

Soil moisture content (SMC), product of Advanced Microwave Scanning Radiometer 2 (AMSR2), is not at an adequate level of accuracy on a regional scale. The aim of this study is to introduce a simple method to estimate SMC while synergistically using AMSR2 and Moderate Resolution Imaging Spectroradiometer (MODIS) measurements with a higher accuracy on a regional scale. Two MODIS products, including daily reflectance (MYD021) and nighttime land surface temperature (LST) products were used. In 2015, 1442 *in situ* SMC measurements from six stations in Iran were used as ground-truth data. Twenty models were evaluated using combinations of polarization index (PI), index of soil wetness (ISW), normalized difference vegetation index (NDVI), and LST. The model revealed the best results using a quadratic combination of PI and ISW, a linear form of LST, and a constant value. The overall correlation coefficient, root-mean-square error, and mean absolute error were 0.59, 4.62%, and 3.01%, respectively.

Introduction

Soil moisture content (SMC) has a lot of applications in short-term weather prediction (Drusch 2007), hydrological research (Al Bitar *et al.* 2012), drought monitoring (Choi *et al.* 2013), and climate changes studies (Al Bitar *et al.* 2012; Koster *et al.* 2004; Wu *et al.* 2016). Hence, continuous spatiotemporal SMC data sets are of utmost importance (Robock *et al.* 2000). Common *in situ* measurements are performed with lots of time and cost only at certain stations, in which the stations are not sufficient neither in number nor in distribution. Therefore, using a method to estimate SMC with high quality and low cost is of great importance. In this regard, remote sensing SMC estimations can be helpful. Remote sensing SMC estimation methods based on the used electromagnetic wavelength can be categorized into optical methods, microwave methods, and synergistic methods. A summary of the literature of SMC remote sensing methods along with a summary of their advantages and disadvantages are represented in Table 1 (see next page).

In the optical wavelength range, some studies on SMC extraction were performed (Table 1). For instance, Liu *et al.* (2009) developed a new SMC estimation method to calculate a quantitative relationship between soil reflectance and moisture of black soils in northeast China, and by so doing, they proved that the soil moisture can be estimated from soil reflectance in the black soil region. Gao *et al.* (2013) estimated SMC with soil with red and near-infrared band reflectance values from Landsat images over vegetation cover in Beijing, China. They used a linear decomposition algorithm of a mixture of pixels to derive soil reflectance. Afterwards, they acquired relationships between SMC and soil reflectance values in the red and near-infrared bands. They evaluated

the acquired SMC in Walnut Creek, Calif., which showed the correlation coefficient of more than 0.80. Qin *et al.* (2013) developed an upscaling algorithm using extracted apparent thermal inertia (ATI) from Moderate Resolution Imaging Spectroradiometer (MODIS) in the central Tibetan Plateau. They upscaled area-averaged SMC using Bayesian linear regression applied to *in situ* measurements as independent variables. The evaluation results using a network of *in situ* moisture sensors showed that the root-mean-square error (RMSE) was reduced from 0.023 m³/m³ to 0.013 m³/m³ after upscaling. Similarly, Soliman *et al.* (2013) and Lei *et al.* (2014) used ATI to extract SMC on a local scale, which proved the performance of ATI in estimating SMC.

Moreover, regarding the passive microwave wavelength range, various investigations proved that the SMC could be retrieved by passive microwave measurements (Bolten *et al.* 2010). Initial studies about the algorithms of extracting SMC from microwave measurements were performed with experimental research using airborne (Ulaby *et al.* 1983) and ground-based microwave radiometers (Maeda and Taniguchi 2013). The major challenge in microwave remote sensing of SMC is the prominent amount of errors in estimations around coastlines and salty soils. Singh and Srivastav (1990) recommended L-band satellite radiometers for detection of water-logged and saline soils. Njoku and Entekhabi (1996) showed that microwave measurements were largely unaffected by cloud cover and variable surface solar illuminations. Davenport *et al.* (2008) investigated the heterogeneity effect on SMC derived from passive microwave observations. They proved that the different microwave frequencies have various sensitivities to each material. Calvet *et al.* (2011) found that microwave L-band has the least error in the estimation of soil moisture and vegetation water content. The *Soil Moisture and Ocean Salinity* (SMOS) sensor provides a new opportunity for deriving SMC using microwave L-band. Al Bitar *et al.* (2012) evaluated SMOS SMC product all over the North American continent using Soil Climate Analysis Network (SCAN)/SNOWpack TElemetry (SNOTEL) *in situ* data in 2010. Results showed underestimation of SMOS SMC compared to *in situ* measurements with an error about 0.04 m³/m³.

The Advanced Microwave Scanning Radiometer 2 (AMSR2) has provided SMC with 10 km spatial resolution by using microwave bands since 2012. An advantage of AMSR2 is the low effect of sunlight, clouds, and dust on measurements (Merrikhpour and Rahimzadegan 2017b). SMC product derived from AMSR2 Japan Aerospace Exploration Agency (JAXA) algorithm was evaluated by Wu *et al.* (2016) within a three-year period (July 2012 to June 2015) in the United States. Evaluation was made by 598 *in situ* soil moisture data sets from the International Soil Moisture Network. The results showed that AMSR2 product underestimated soil moisture.

Department of Water Resources Engineering and Management, Faculty of Civil Engineering, K. N. Toosi University of Technology, Tehran, Iran (rahimzadegan@kntu.ac.ir).

Contributed by Dongdong Wang, September 9, 2020 (sent for review November 23, 2020; reviewed by Ji Zhou, C. Jeganathan).

Photogrammetric Engineering & Remote Sensing
Vol. 87, No. 9, September 2021, pp. 649–660.
0099-1112/21/649–660

© 2021 American Society for Photogrammetry
and Remote Sensing
doi: 10.14358/PERS.20-00085

Table 1. Summary of the different remote sensing estimation methods of soil moisture content as well as their advantages and disadvantages.

Wavelength Range	Methods	Advantages	Disadvantages	Spatial Scale	Sample Studies
Optical	Reflectance-based methods	10 m to 500 m spatial resolution, multiple satellites are available, hyperspectral sensors are promising	Improper performance to estimate SMC in dense vegetation cover, not applicable in cloudy conditions and at nighttime, improper temporal resolution	Catchment scale, local scale, regional scale	Liu <i>et al.</i> (2009), Gao <i>et al.</i> (2013)
	Thermal infrared-based methods	100 m to 1 km spatial resolution, multiple satellites available, methods relating SMC to thermal inertia are promising	Improper performance to estimate SMC in dense vegetation cover, not applicable in cloudy conditions, improper temporal resolution	Local scale, regional scale, global scale	Qin <i>et al.</i> (2013), Soliman <i>et al.</i> (2013), Lei <i>et al.</i> (2014)
Passive Microwave	Various methods	Promising results in SMC estimation particularly over bare soil surfaces, use not limited by clouds and/or daytime conditions, high temporal resolution	10 km to 50 km spatial resolution, SMC retrieval is influenced by vegetation cover and surface roughness	Local scale, regional scale, global scale	de Jeu <i>et al.</i> (2014)
Active Microwave	Various methods (empirical, semi-empirical, physically-based)	1 m to 1 km spatial resolution, use not limited by clouds and/or daytime conditions	SMC retrieval is influenced by surface roughness and vegetation cover, improper temporal resolution	Catchment scale, local scale	Callens <i>et al.</i> (2006), Al-Bakri <i>et al.</i> (2014), Panciera <i>et al.</i> (2014), Vereecken <i>et al.</i> (2014)
Synergistic Methods	Optical and thermal infrared	10 m to 1 km spatial resolution, a multiplicity of satellites are available, simple, and straightforward implementation	Most of methods are empirical, limited to cloud-free and daytime conditions, improper temporal resolution, low penetration depth	Catchment scale, local scale, regional scale	Wang <i>et al.</i> (2007), Holzman <i>et al.</i> (2014), Zhang <i>et al.</i> (2014)
	Active and passive MW	Combining the high spatial resolution images of active MW with the lower resolution of images of passive MW, improved temporal resolution and SMC retrieval	SMC scaling and validation needs caution, different SMC measurement depths	Catchment scale, local scale, regional scale	Lee and Anagnostou (2004), Narayan <i>et al.</i> (2006)
	MW and optical	Vegetation and surface roughness effects can be minimized, promising in SMC retrievals	SMC scaling and validation needs caution, different SMC measurement depths	Catchment scale, local scale, regional scale, global scale	Chauhan <i>et al.</i> 2003, Choi and Hur 2012, Mattar <i>et al.</i> 2012, Qu <i>et al.</i> 2021

SMC = soil moisture content; MW = microwave.

Active microwave measurements were also used in some studies to extract SMC (Table 1). Al-Bakri *et al.* (2014) evaluated the performance of empirical and semi-empirical models to extract SMC from the *RADARSAT-2* data over the Yarmouk basin in Jordan. They showed the spatial agreement of 55% to 65% between SMC maps in which the maps were reclassified based on intervals of 5% SMC for both models. Some other researchers such as Callens *et al.* (2006), Panciera *et al.* (2014), and Vereecken *et al.* (2014) studied the performance of the radar data on a local scale.

The satellite measurement in various wavelength ranges were synergistically used to extract SMC by some researchers, which include using satellite measurements in the wavelength ranges of: (1) optical and thermal infrared (Holzman *et al.* 2014; Wang *et al.* 2007; Zhang *et al.* 2014), (2) active and passive microwave (Lee and Anagnostou 2004; Liu *et al.* 2009; Narayan *et al.* 2006), and (3) microwave and optical (Zhao and Li 2013).

Numerous studies were performed using a combination of passive microwave and optical data to minimize the errors due to environmental conditions in an SMC estimation. Chauhan *et al.* (2003) investigated an approach to estimate SMC at high resolution using satellite microwave data from the Special Sensor Microwave Imager and optical/infrared data from Advanced Very High Resolution Radiometer. They used universal triangle approach to disaggregate microwave SMC into high resolution SMC in conjunction with high-resolution

normalized difference vegetation index (NDVI), surface albedo, and land surface temperature (LST). Their results showed that the predicted SMC at high resolution was in a good agreement with low resolution results. Mattar *et al.* (2012) introduced a method to correct the effect of vegetation in the SMC estimation of L-band passive microwave observations. They used a semi-empirical relationship between SMC and the effect of the vegetation optical depth, which was modeled using the NDVI. They proved that NDVI is useful for the estimation of SMC through the semi-empirical regressions. Choi and Hur (2012) developed a synergistic approach to disaggregate the Advanced Microwave Scanning Radiometer—Earth Observing System (AMSR-E) SMC from 25 to 1 km spatial resolution using MODIS data. Their results showed that the synergistic method is a feasible method to improve the spatial distributions of AMSR-E SMC products. Qu *et al.* (2021) compared several SMC downscaling methods based on polynomial fitting, physical model, machine learning, and geostatistics over the Qinghai-Tibet plateau. The results proved that the method based on a physical model, which in the case of that study was the disaggregation based on physical and theoretical scale change method, has the best performance to preserve the coarse-scale feature of the original microwave SMC product.

When all the effective parameters on SMC algorithm are known, AMSR2 SMC has been estimated from the observed brightness temperatures (TBs) using a radiative transfer model (RTM) in an inverse analysis method, which is known as the

look-up-table (LUT) method (Maeda and Taniguchi 2013). As previous studies indicate, the accuracy of estimated SMC by AMSR2 is relatively low (an RMSE ranging from 5% to 10%), which makes it not useful in practical studies (Wu *et al.* 2016). The reason for this is the lack of access to vegetation ratio and vegetation water content (VWC) maps at most areas, which results in the lack of access to the LUTs. On the other hand, soil moisture is affected by some other factors such as physical LST, which is not considered in the AMSR2 standard product (Wu *et al.* 2016). In this regard, synergistic use of other satellite sensors with a higher spatial resolution such as MODIS (spatial resolution of 1 km) along with its products, which are extensively available everywhere, can be useful. Moreover, MODIS can consider the effects of some environmental parameters such as vegetation cover and land surface temperature on SMC. Furthermore, standard SMC estimation of AMSR2 is relatively complicated and produced using LUT data on a global scale, which may not consider regional conditions

of a country such Iran with a diverse climatic conditions from semi-arid to semihumid climates. Hence, a new procedure of SMC estimation with better accuracy will be introduced, considering regional considerations. Therefore, the aim of this study is representing a new product of SMC with higher accuracy specifically for semi-arid to semihumid regions in Iran with concurrent use of AMSR2 TB values and MODIS NDVI and LST products, not having been investigated in the previous studies.

Materials and Methods

Study Area

The study area is Iran, located between 44° to 64° eastern longitude and 25° to 40° northern latitude (Figure 1). Iran is situated in a semi-arid region in the Middle East. The average precipitation of Iran is 250 mm, that is about one-third of the world's average (Merrikhpour and Rahimzadegan 2017b). Land cover

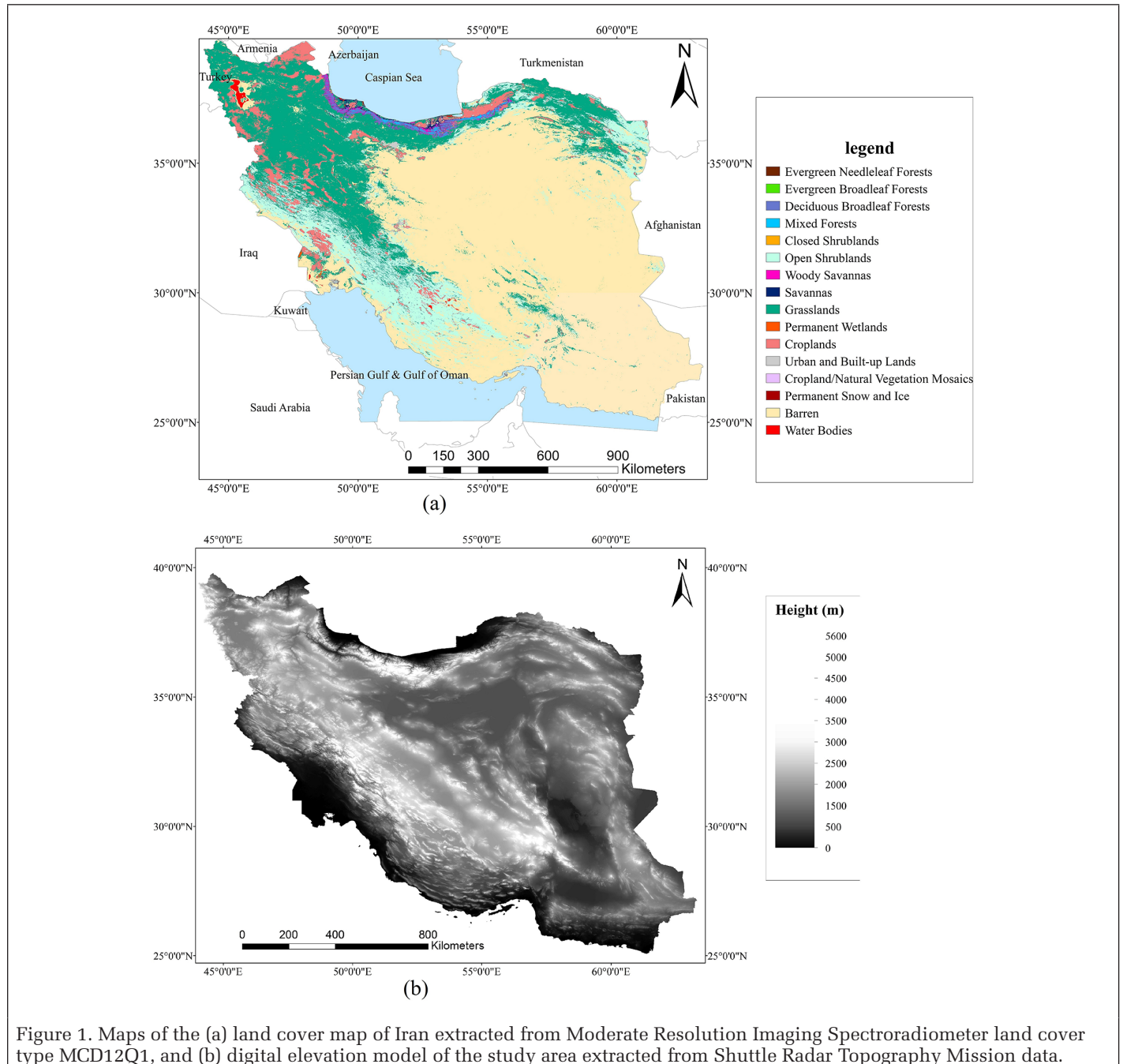


Figure 1. Maps of the (a) land cover map of Iran extracted from Moderate Resolution Imaging Spectroradiometer land cover type MCD12Q1, and (b) digital elevation model of the study area extracted from Shuttle Radar Topography Mission data.

map of Iran is shown in Figure 1a based on the International Geosphere Biosphere Programme global vegetation classification scheme (land cover type 1). This land cover map was adopted from MODIS (land cover type MCD12Q1) (Sulla-Menashe and Friedl 2018). Digital elevation model of the study area is presented in Figure 1b, prepared by Shuttle Radar Topography Mission (SRTM) with 30 m resolution acquired in 2007 (USGS XXXX).

Data Used

In this study, SMC measurements from 21 stations in the year 2015 were obtained from the Iran meteorological organization. Measurements from 15 stations were excluded due to lack of the recorded SMC measurements (missing days forming over two thirds of the year) and also because of their locations that were amidst and locating in the agricultural field. Measurements in the agricultural field cannot represent the general condition of the study area due to irrigation activities. Eventually, six stations were selected to perform this study, where SMC is measured on bare soil or outside farms. The locations of the selected stations are displayed in Figure 2.

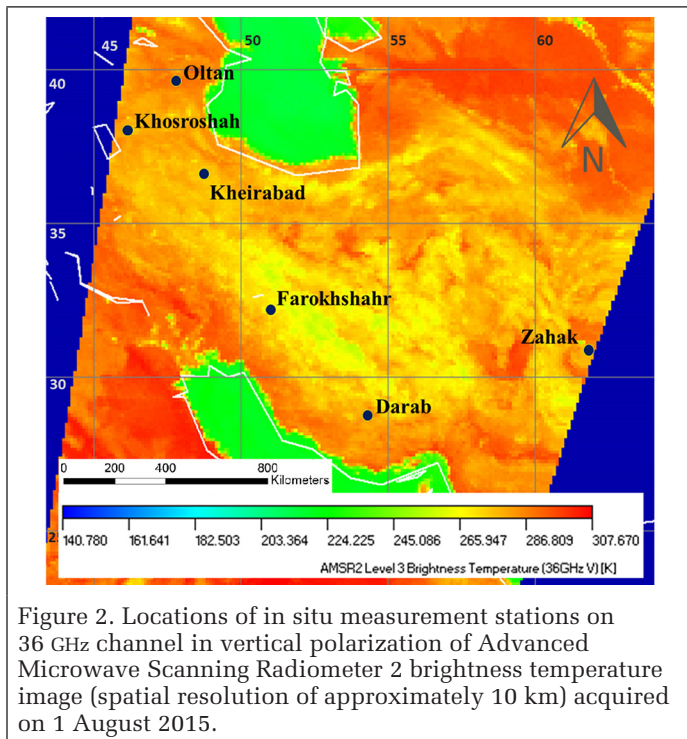


Figure 2. Locations of in situ measurement stations on 36 GHz channel in vertical polarization of Advanced Microwave Scanning Radiometer 2 brightness temperature image (spatial resolution of approximately 10 km) acquired on 1 August 2015.

In these stations, SMC is measured four times a day at 3:00 A.M., 6:00 A.M., 9:00 A.M., and 3:00 P.M. (local time, Greenwich Mean Time +3:30) in an unsaturated state, by using the time-domain reflectometry 6050X1 TRASE instrument. Since AMSR2 overpass time over the study region is at 5:00 A.M. local time, 3:00 A.M. station measurements were used. Moreover, as AMSR2 measurements can extract SMC near the surface, station measurements at the depth of 0–5 cm were considered. Furthermore, utilizing ground data at 3:00 A.M. can also lead to the reduction of the effect of sunlight, and consequently surface evaporation on surface SMC compared to measurements at the other times. From a total of 1979 SMC *in situ* measurements at the depth of 0–5 cm, 1442 measurements correspond to the selected AMSR2 images that were considered for this study. The reduction in SMC measurements from 1979 to 1442 was due to the fact that SMC measurements were not performed in some stations at 3:00 A.M., and SMC measurements were available at the other local times. In this study, 60% of the data was randomly selected as the training data. The remaining 40% has been used to validate the results (test data).

AMSR2 Data Sets

In this study, the level 2 TBs of AMSR2 on board the *Global Change Observation Mission–Water-1* (GCOM-W1) satellite and the AMSR2 SMC product were used. Figure 2 shows a sample track of an AMSR2 TB image regarding the 36 GHz channel in vertical polarization, acquired on 01 August 2015.

364 days of the year of 2015 were dedicated to this study. AMSR2 data was lacking for just one day in 2015 (3 December). AMSR2 data is released with an averaged spatial resolution of 10 km (0.1°). AMSR2 images are acquired two times per day at 1:30 P.M. and 1:30 A.M. (local solar time) in ascending and descending modes, respectively. To reduce the effect of sunlight, nighttime data (descending mode) was used. AMSR2 images can be downloaded from the GCOM-W1 data providing service (JAXA XXXX).

Among TB data, measurements at the frequencies of 10 and 36 GHz with horizontal and vertical polarizations in Kelvin (K) were used in this study. The level 3 AMSR2 TB product is produced for each day by combining all-round image scenes of the earth. Furthermore, the daily AMSR2 surface SMC was another part of the data used in this study, which provides the percentage of soil volumetric water content. The performance of the introduced new product of SMC in this study will be compared with the daily AMSR2 surface SMC to prove the performance of the introduced method.

MODIS Data Sets

MODIS was launched on-board Terra and Aqua platforms in 1999 and 2002, respectively (Merrikhpour and Rahimzadegan 2017a). MODIS images include 36 spectral bands, making it capable of providing various information about the atmosphere, land, and ocean (Choi and Hur 2012). Spatial resolution of the MODIS varies from 250 m for bands 1 and 2, through 500 m for bands 3 to 7, and to 1 km for bands 8 to 36 (Peters *et al.* 2011).

Aqua passes over the study area at 1:30 A.M. and 1:30 P.M. local solar time in descending and ascending modes, respectively. In this study, Aqua products were selected to be used in practice. The daily surface reflectance product of Aqua MODIS (MYD021) was used for calculating required vegetation indices. Moreover, the nighttime Aqua-MODIS LST level-2 product (MYD11-L2) was used to retrieve LST information, which is close to AMSR2 imaging time (1:30 A.M. local solar time). Wan (2014) proved that the accuracy of MODIS LST of the collection-6 level-2 product, calculated using refined split-window algorithm, was from ± 0.6 K to 1.9 K, which is acceptable for this study. In the MYD11-L2 product, clouds are masked by the MODIS science team (Merrikhpour and Rahimzadegan 2017a). The required MODIS images were prepared from the Level-1 and Atmosphere Archive & Distribution System (LAADS) Distributed Active Archive Center (DAAC) database (NASA xxxxx).

AMSR2 SMC Retrieval Algorithm

The AMSR2 SMC retrieval algorithm was initially introduced by Fujii *et al.* (2009). It is performed by using the L1R TB and a LUT. This algorithm used 10 and 36 GHz frequency channels to estimate SMC from AMSR2 measurements. As the water content of the vegetation affects the measured TB in AMSR2 images, a method is used to simultaneously extract SMC and VWC. This is accomplished by using polarization index (PI) and index of soil wetness (ISW), which are polarization and frequency differences divided by average values of TBs, respectively. These two indices are calculated as (Maeda and Taniguchi 2013):

$$PI = \frac{TB_{V,j} - TB_{H,j}}{\frac{1}{2}(TB_{V,j} + TB_{H,j})} \quad (1)$$

$$ISW = \frac{TB_{H,i} - TB_{H,j}}{\frac{1}{2}(TB_{H,i} + TB_{H,j})} \quad (2)$$

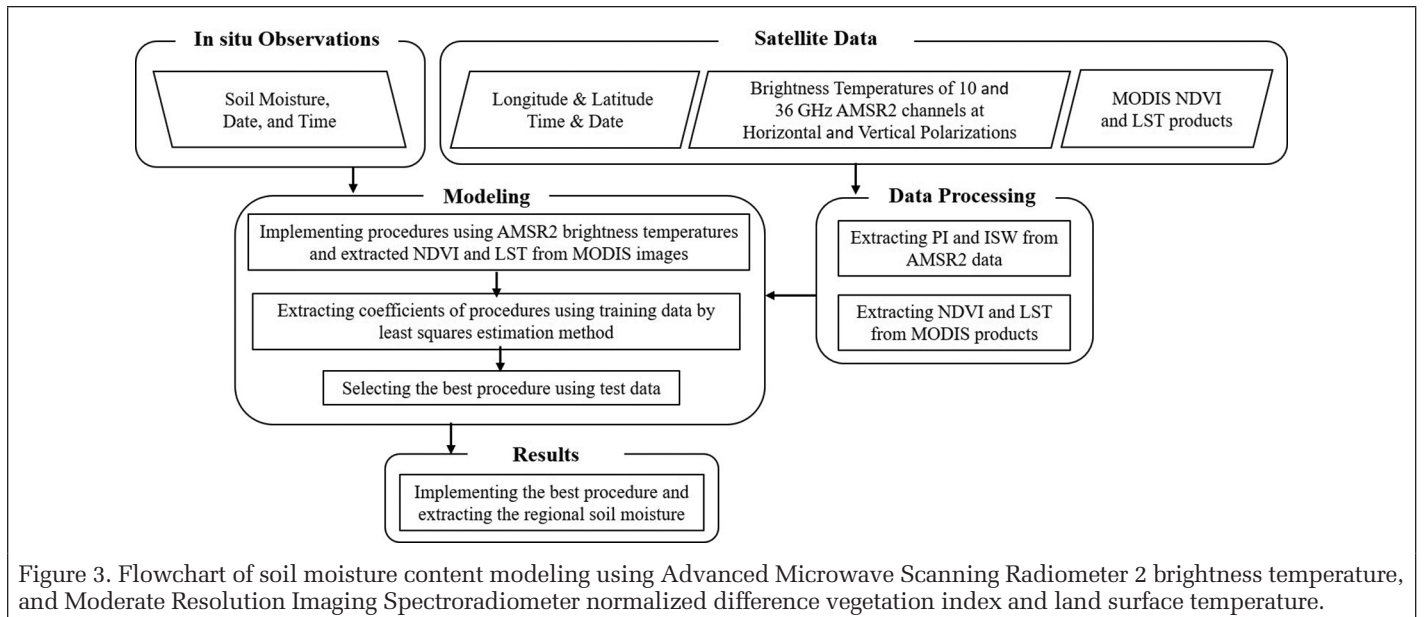


Figure 3. Flowchart of soil moisture content modeling using Advanced Microwave Scanning Radiometer 2 brightness temperature, and Moderate Resolution Imaging Spectroradiometer normalized difference vegetation index and land surface temperature.

where T_{B_V} and T_{B_H} are the TBs with vertical and horizontal polarizations, respectively. Moreover, subscripts i and j denote high (36 GHz) and low (10 GHz) frequencies, respectively. As the equations of PI and ISW show, the normalization equations used in these indices lead to a range of [-2 to 2].

Afterwards, the vegetation ratio was estimated using NDVI values (the NDVI values range from -1 to 1). In the AMSR2 products, NDVI values were extracted from the vegetation indices product of MODIS (16-day L3 global 1km V5), generated by the land processes of DAAC (Maeda and Taniguchi 2013). Finally, SMC and VWC are determined using the LUT method. LUTs are results of inverse analysis, which can be used for retrieving SMCs and VWCs from the microwave TBs. These tables are generated for different fractional vegetation covers using RTM simulations (Fujii *et al.* 2009).

SMC Estimation Using MODIS NDVI and LST

Some improvements were made in this study to overcome the problems faced by AMSR2 SMC estimations stated in the “Introduction” section. In this regard, in the context of a new procedure of SMC estimation with better accuracy, NDVI and LST data were used in the modeling processes. NDVI was considered to replace the vegetation cover factor of LUTs in the AMSR2 SMC product. LST was used to involve the effect of the physical temperature of the land on the modeling process. In this regard, mean value of 10×10 pixels of MODIS NDVI and LST product related to each AMSR2 pixel was calculated. These mean values were used as NDVI and LST in the SMC estimation.

In the SMC estimations of this study, five procedures were considered. In the first procedure, just calculated PI and ISW were used to determine SMC; in the second one, NDVI was used accompanied by PI and ISW; in the third procedure, PI and ISW were used along with LST; and in the fourth procedure, PI and ISW were used for SMC derivation in the dry season, and the modeling was performed just using dry season data. Finally, the fifth procedure was the same as the fourth procedure despite that the wet season data was used in place of dry season data.

Each of these procedures was evaluated by using four different procedures. In total, 20 models (M-1 to M-20) were introduced. These four methods include the combination of linear and quadratic form PI, ISW, NDVI, and LST along with a constant value in the models as summarized in Figure 3 and Table 2. The calculations of parameters of all the models were performed using least squares estimation. Moreover, the spatial accuracy of 0.1 degrees is used to find the corresponding image pixels of the measurements at the observation stations. To

do this, soil moisture content estimation of each measurement of the stations was extracted using nearest neighbor method, having been used by the previous studies (de Jeu *et al.* 2014; Fujii *et al.* 2009; Merrikhpour and Rahimzadegan 2017b).

Table 2. Implemented procedures and models of this research.

Procedure	Model	Equation
1: estimation using simple ISWPI model	M-1	$SMC = \alpha \times PI + \beta \times ISW$
	M-2	$SMC = \alpha \times PI + \beta \times ISW + \gamma$
	M-3	$SMC = \alpha \times PI + \beta \times ISW + \theta \times PI^2 + \lambda \times ISW^2$
	M-4	$SMC = \alpha \times PI + \beta \times ISW + \theta \times PI^2 + \lambda \times ISW^2 + \gamma$
2: estimation using ISW, PI, and NDVI	M-5	$SMC = \alpha \times PI + \beta \times ISW + \eta \times NDVI$
	M-6	$SMC = \alpha \times PI + \beta \times ISW + \eta \times NDVI + \gamma$
	M-7	$SMC = \alpha \times PI + \beta \times ISW + \theta \times PI^2 + \lambda \times ISW^2 + \eta \times NDVI$
	M-8	$SMC = \alpha \times PI + \beta \times ISW + \theta \times PI^2 + \lambda \times ISW^2 + \eta \times NDVI + \gamma$
3: estimation using ISW, PI, and LST	M-9	$SMC = \alpha \times PI + \beta \times ISW + \omega \times LST$
	M-10	$SMC = \alpha \times PI + \beta \times ISW + \omega \times LST + \gamma$
	M-11	$SMC = \alpha \times PI + \beta \times ISW + \theta \times PI^2 + \lambda \times ISW^2 + \omega \times LST$
	M-12	$SMC = \alpha \times PI + \beta \times ISW + \theta \times PI^2 + \lambda \times ISW^2 + \omega \times LST + \gamma$
4: estimation of SMC in the dry season	M-13	$SMC = \alpha_{wet} \times PI + \beta_{wet} \times ISW$
	M-14	$SMC = \alpha_{wet} \times PI + \beta_{wet} \times ISW + \gamma_{wet}$
	M-15	$SMC = \alpha_{wet} \times PI + \beta_{wet} \times ISW + \theta_{wet} \times PI^2 + \lambda_{wet} \times ISW^2$
	M-16	$SMC = \alpha_{wet} \times PI + \beta_{wet} \times ISW + \theta_{wet} \times PI^2 + \lambda_{wet} \times ISW^2 + \gamma_{wet}$
5: estimation of SMC in the wet season	M-17	$SMC = \alpha_{dry} \times PI + \beta_{dry} \times ISW$
	M-18	$SMC = \alpha_{dry} \times PI + \beta_{dry} \times ISW + \gamma_{dry}$
	M-19	$SMC = \alpha_{dry} \times PI + \beta_{dry} \times ISW + \theta_{dry} \times PI^2 + \lambda_{dry} \times ISW^2$
	M-20	$SMC = \alpha_{dry} \times PI + \beta_{dry} \times ISW + \theta_{dry} \times PI^2 + \lambda_{dry} \times ISW^2 + \gamma_{dry}$

ISWPI = index of soil wetness (ISW); polarization index (PI); NDVI = normalized difference vegetation index; LST = land surface temperature; SMC = soil moisture content.

MYD021 products were used to calculate the NDVI and LST information was extracted from the MYD11-L2 product using header information of the image.

The reason behind separating procedures 4 and 5 into two dry and wet seasons was the independent calculation of the model parameters for the two general conditions of the environment with low and high humidity. In the dry season, rainfall is low, the temperature is high, and the average SMC is less

than the SMC in the wet season. Differentiation of the two seasons is not definitely possible, because the changes between these two periods take place gradually. However, the 1 to 120 and 300 to 365 Julian days were considered as the wet period and 121 to 299 Julian days as the dry period. Then, a separate model was made for each period. 60% of data was considered as the training set and the remaining as the test set.

Evaluation Method of SMC Models

The evaluation process was carried out using three criteria including RMSE, mean absolute error (MAE), and Pearson correlation coefficient (R) as:

$$RMSE = \sqrt{\frac{\sum_{i=1}^n (y_i - \hat{y}_i)^2}{n}} \quad (3)$$

$$MAE = \frac{1}{n} \sum_{i=1}^n |\hat{y}_i - y_i| = \frac{1}{n} \sum_{i=1}^n |e_i| \quad (4)$$

$$R(Y, \hat{Y}) = \frac{\text{cov}(Y, \hat{Y})}{\sigma_Y \sigma_{\hat{Y}}} = \frac{E[(Y - \mu_Y)(\hat{Y} - \mu_{\hat{Y}})]}{\sigma_Y \sigma_{\hat{Y}}} \quad (5)$$

where n is the total number of evaluated data; \hat{y}_i and y_i are estimated and *in situ* measured SMC, respectively; e_i denotes the difference between evaluations and observations; E refers to expected value; cov is covariance; and σ is the standard deviation.

The whole study including programming was made using MATLAB, version x.x software.

Results and Discussion

AMSR2 SMC Evaluation

Initially, AMSR2 SMC products were evaluated using *in situ* observations (Table 3). As seen in Table 3, the correlation values vary greatly for different stations. The correlation, RMSE,

and MAE values of all the estimated SMC and *in situ* measurements are 0.25, 7.20%, and 4.85%, respectively. As the range of acquired AMSR2 SMC is approximately between 3% and 22%, those RMSE and MAE values are not acceptable. This means the calculated RMSE value is about 33% to 250% of the SMC values and MAE value is about 62% to 453% of the SMC values, which indicates the weak performance of the AMSR2 product. Moreover, the correlation value is below 0.5, and the fact indicates that AMSR2 SMC cannot be correlated to *in situ* measurements by a linear equation. Furthermore, the correlation, RMSE, and MAE values vary according to station (Table 3). Figure 4 shows the scatterplots of AMSR2 SMC against *in situ* measurements for the year 2015 over the selected stations. As it is obvious, the performance of the AMSR2 SMC is different in various stations. Therefore, a method is required to improve the SMC estimation.

Table 3. Evaluation results of Advanced Microwave Scanning Radiometer 2 product of soil moisture content.

Station Name	R	RMSE (%)	MAE (%)
Darab	0.51	2.92	2.11
Kheirabad	0.00	9.63	6.99
Khosroshah	0.33	3.83	2.87
Zahak	0.44	10.21	7.54
Farokhshahr	0.24	7.32	4.90
Oltan	0.08	6.00	4.75
Overall	0.25	7.20	4.85

R = Pearson correlation coefficient; RMSE = root-mean-square error; MAE = mean absolute error.

Figure 5 shows an example of satellite and *in situ* SMC time series for Darab and Khosroshah stations. As shown in the figure, in the Julian days 1 to 90 and 300 to 365, the standard product estimates lower SMC values than *in situ* data (the graph of AMSR2 SMC has fallen below the observation graph) in both stations. Conversely, in the other Julian days of the time series at Darab and Khosroshah stations, overestimation

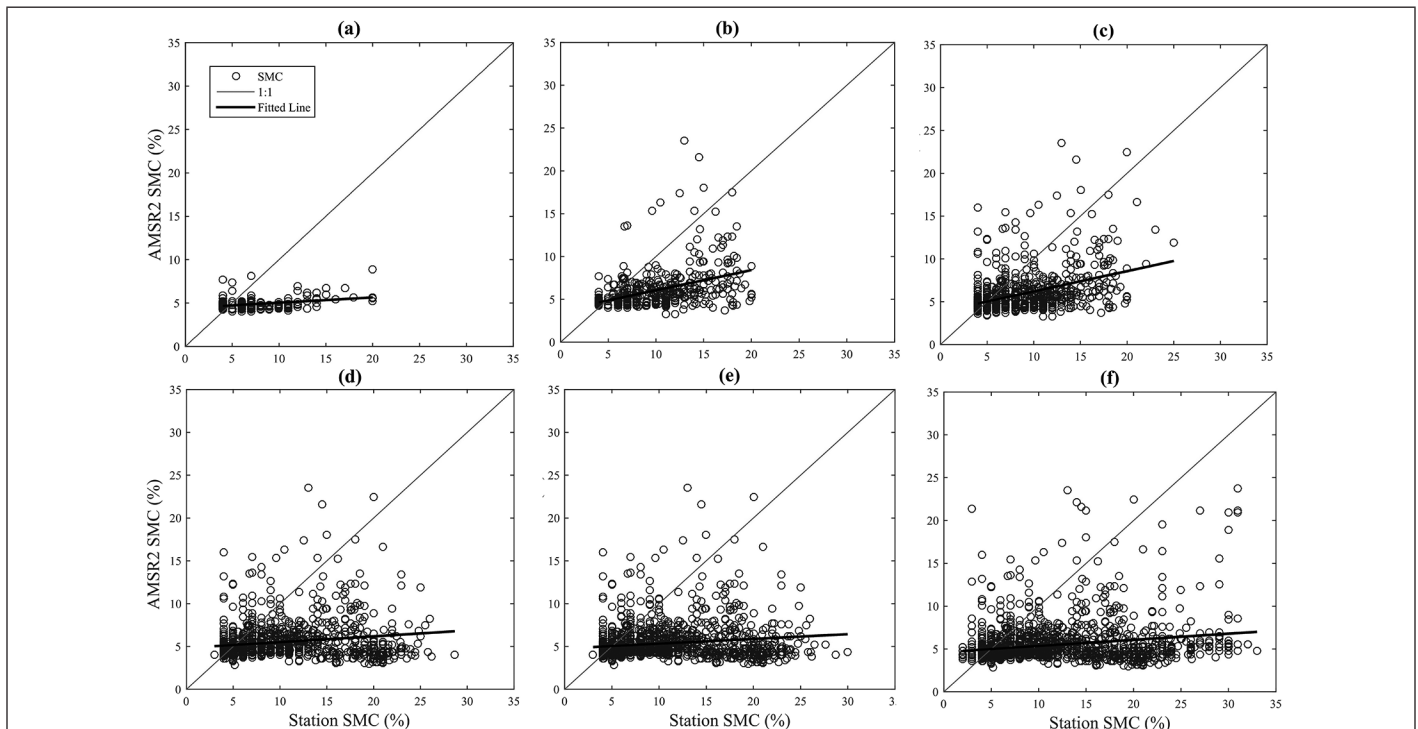


Figure 4. Scatterplots of Advanced Microwave Scanning Radiometer 2 soil moisture content (%) against *in situ* measurements (%) for the year 2015 over the stations of (a) Darab, (b) Oltan, (c) Khosroshah, (d) Kheirabad, (e) Farokhshahr, and (f) Zahak.

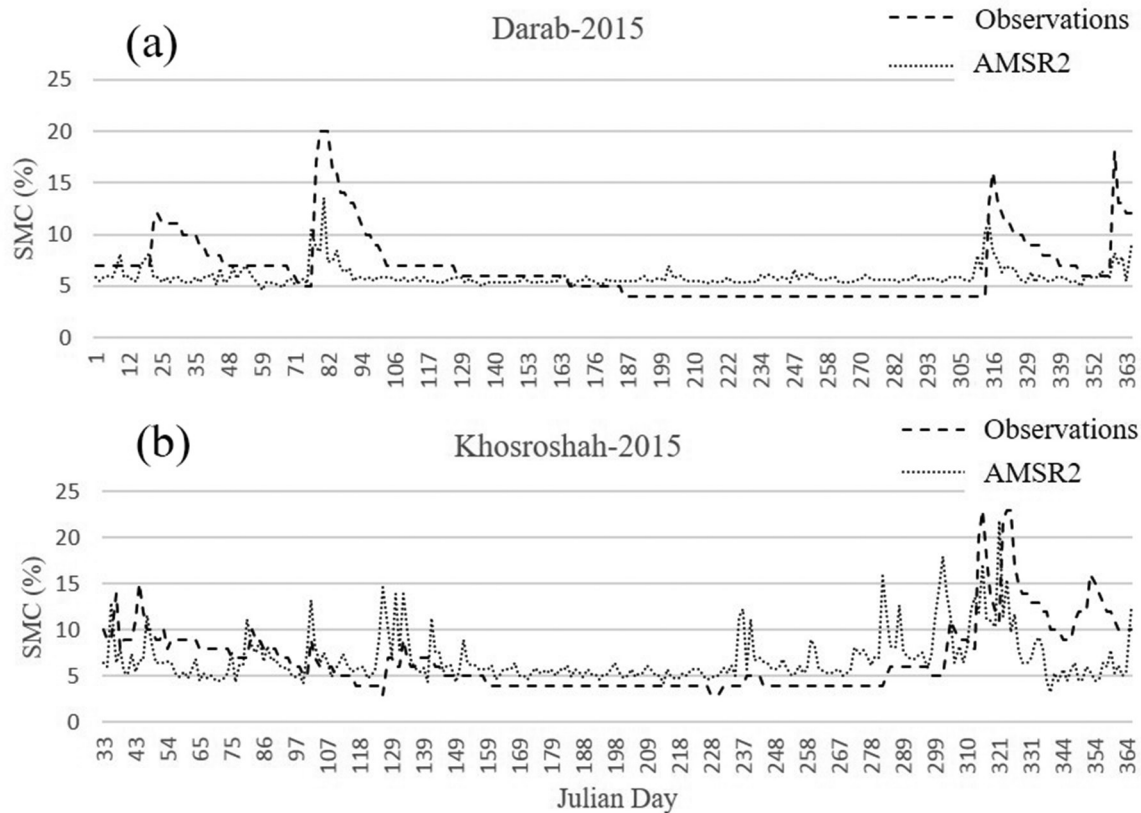


Figure 5. Soil moisture content values of Advanced Microwave Scanning Radiometer 2 estimation and in situ observation of the year 2015 for stations of (a) Darab and (b) Khosroshah.

occurs (the graph of AMSR2 SMC has fallen above the observation graph in Figure 5). In the cold and wet seasons there is a considerable difference between estimation and observation. However, despite the relatively large differences between estimated and observed SMC, the algorithm can often detect the peak points properly.

Procedure 1: SMC Estimation Using Simple ISWPI Model

The performance of this procedure was evaluated with the combinations of linear and quadratic terms of PI and ISW with constant values (Table 4). In this table, “Case 0” denotes the AMSR2 standard product of soil moisture. The results indicated that the simple index of soil wetness polarization index (ISWPI) model provides no considerable improvement in correlation. In this procedure, despite a slight decrease in the overall RMSE value, MAE increases. From among the models of this procedure, Model 4 (quadratic equation with constant value) has the best results.

Procedure 2: SMC Estimation Using ISW, PI, and NDVI

In this procedure, NDVI values were used to consider vegetation cover effects on the estimation of SMC for the brightness temperatures of mixed pixels. NDVI values range from 1 to 1 in this study and those values were used on the days with a clear sky condition (without cloud) for all the four proposed models. This index was linearly added to the simple ISWPI model in the training and test processes (Table 5).

As it can be seen in Table 5, using NDVI did not improve the estimations of the AMSR2 SMC standard product (Case 0). The correlation coefficient in “Case 0” was 0.21, which was not improved in any cases of M-5 to M-8. Moreover, the RMSE and MAE values are not improved remarkably in any of the four proposed models (M-5 to M-8). This can be due to the very large pixels of the AMSR2 image (about 10 km), that

Table 4. Evaluation of models 1 to 4 in procedure 1 (using polarization index and index of soil wetness).

Station Name	Evaluation Criterion	Case 0	M-1	M-2	M-3	M-4
Darab	<i>R</i>	0.50	0.12	0.43	0.35	0.44
	RMSE (%)	2.90	3.15	4.34	3.75	3.88
	MAE (%)	2.09	2.33	3.94	3.23	3.48
Kheirabad	<i>R</i>	0.03	0.37	0.04	0.30	-0.10
	RMSE (%)	9.64	8.71	7.88	7.45	8.29
	MAE (%)	7.01	6.67	6.98	6.30	7.18
Khosroshah	<i>R</i>	0.36	0.57	0.29	-0.12	0.43
	RMSE (%)	3.91	5.27	4.71	5.20	4.32
	MAE (%)	2.89	4.74	4.12	4.54	3.68
Zahak	<i>R</i>	0.37	0.50	0.45	0.14	0.36
	RMSE (%)	10.39	9.60	9.84	10.24	9.53
	MAE (%)	7.77	8.61	8.45	8.81	8.05
Farokhshahr	<i>R</i>	0.25	0.21	0.29	0.39	0.36
	RMSE (%)	7.06	5.92	5.42	5.21	5.58
	MAE (%)	4.77	4.12	4.18	4.12	4.20
Oltan	<i>R</i>	0.13	0.14	0.22	0.19	-0.02
	RMSE (%)	5.62	8.33	4.29	6.46	4.12
	MAE (%)	4.56	7.47	3.45	5.43	3.28
Overall	<i>R</i>	0.24	0.14	0.16	0.11	0.23
	RMSE (%)	7.17	7.14	6.47	6.69	6.39
	MAE (%)	4.84	5.59	5.25	5.39	5.04

R = Pearson correlation coefficient; RMSE = root-mean-square error; MAE = mean absolute error.

brings an increase to the number of mixed pixels of soil and vegetation cover. Moreover, NDVI cannot consider the background soil effect on the reflected energy to the sensor, and it may have inaccurate values in sparse vegetation cover condition (Alhammadi and Glenn 2008).

Procedure 3: SMC Estimation Using ISW, PI, and LST

Similar to the previous procedure, MODIS LST data were used linearly in the models of this procedure and the results were evaluated (Table 6). The initial correlation (AMSR2 product) was 0.46, which increases as 28% in the M-12 and improves to 0.59. Moreover, regarding to the RMSE and MAE values, the highest improvement regarding the errors occurred in this model. Thus, RMSE decreases to 4.62% with an improvement of 16% and MAE decreases to 3.01% with an improvement of 9%.

The M-12 with overall correlation value, RMSE, and MAE of respectively 0.59, 4.62, and 3.01 better performed, which can be due to considering the effect of LST on SMC (Table 6). Then, LST can be a good proxy for some ignored effects of land on the measured brightness temperatures in the PI and ISW values.

Procedure 4 and 5: Estimation SMC in Dry and Wet Seasons

As mentioned before, SMC is related with different variables that often change in different seasons and require separate modeling for each season. Then, all variables were used separately for dry and wet seasons. Due to reduction in number of the used data, seasonal study of NDVI and LST was not performed. The results of models compared with the satellite SMC product are presented in Table 7.

The results recommended higher correlation and less error for the dry season. In fact, the AMSR2 algorithm had a much better performance in the dry season compared to the wet season. On average, the correlation of SMC in the dry season was 3.38 times higher than the wet season, and the RMSE and MAE were about a quarter of the wet season. The fourth model of this procedure had the highest improvement in correlation for both seasons. The mean correlation of the M-16 model (wet season) with about a 54% increase, improves from 0.13 to 0.20 and in the M-20 model (dry season) with a 32% increase, this improves from 0.44 to 0.58. Despite the improvements in both seasons, the correlation of the results is still low for the wet season. The results indicate a decrease in RMSE and MAE values in both seasons. M-16 and M-20 recommend the best improvement in error values for dry and wet seasons, respectively.

Selecting the Best Model

The comparison between the overall SMC of the proposed models and AMSR2 product recommended that the fourth model in each procedure would provide the best results. In the first procedure, this method used the quadratic equation of PI and ISW accompanied with a constant value. In other procedures, the NDVI and LST variables were added separately, or seasonal modeling was performed.

In Table 8, the correlation and error changes of the quadratic model with constant values in different modeling procedures are compared. The best results are acquired by using LST (M-12) and also in seasonal modeling. Since the dry season model has good results for half of the year, despite its acceptable results, it is not considered as the selected model. Then, M-12 is selected as the best model. This model results in correlation, RMSE, and MAE values of 0.59, 4.62%, and 3.01%, respectively. On the other hand, correlation, RMSE, and MAE values are acquired as, respectively, 0.46, 5.51%, and 3.31% for AMSR2 products of SMC. Hence, M-12 model can improve the correlation, RMSE, and MAE of the standard AMSR2 products of soil moisture as 30.06%, 16.25%, and 9.10%, respectively. Parameters of all of the models are presented in Table 9.

Table 5. Evaluation of models 5 to 8 in procedure 2 (using normalized difference vegetation index).

Station	Evaluation					
	Criterion	Case 0	M-5	M-6	M-7	M-8
Darab	<i>R</i>	0.37	0.03	0.46	0.49	0.47
	RMSE (%)	2.72	2.95	3.30	3.12	3.02
	MAE (%)	2.09	2.46	3.05	2.78	2.78
Kheirabad	<i>R</i>	-0.11	-0.32	-0.10	0.21	0.22
	RMSE (%)	8.39	8.65	7.63	8.64	9.90
	MAE (%)	5.92	6.67	6.10	6.81	7.45
Khosroshah	<i>R</i>	0.13	-0.10	0.28	-0.23	0.04
	RMSE (%)	3.26	5.26	3.86	6.14	4.19
	MAE (%)	2.40	4.86	3.37	4.45	2.88
Zahak	<i>R</i>	0.35	0.66	0.36	0.25	0.25
	RMSE (%)	9.54	8.73	9.12	9.19	9.24
	MAE (%)	6.53	7.46	7.57	7.17	7.27
Farokhshahr	<i>R</i>	-0.06	-0.28	-0.17	0.22	0.41
	RMSE (%)	5.65	4.75	4.28	4.18	4.09
	MAE (%)	3.89	3.49	3.31	3.24	3.12
Oltan	<i>R</i>	0.13	-0.07	0.43	0.38	0.25
	RMSE (%)	4.97	5.39	4.84	5.56	4.52
	MAE (%)	3.83	4.18	3.88	4.57	3.58
Overall	<i>R</i>	0.21	0.02	0.06	0.14	0.21
	RMSE (%)	6.47	6.42	6.09	6.62	6.59
	MAE (%)	4.19	4.92	4.68	4.89	4.65

R = Pearson correlation coefficient; RMSE = root-mean-square error; MAE = mean absolute error.

Table 6. Evaluation of models 9 to 12 in procedure 3 (using land surface temperature).

Station	Evaluation					
	Criterion	Case 0	M-9	M-10	M-11	M-12
Darab	<i>R</i>	0.49	0.77	0.76	0.79	0.70
	RMSE (%)	2.58	1.89	2.65	2.64	2.30
	MAE (%)	2.03	1.50	2.12	2.01	1.84
Kheirabad	<i>R</i>	0.12	0.52	0.65	0.69	0.48
	RMSE (%)	4.71	4.62	3.92	3.84	4.16
	MAE (%)	2.55	2.40	3.00	2.02	3.04
Khosroshah	<i>R</i>	0.69	0.67	0.64	0.65	0.59
	RMSE (%)	1.26	1.61	1.97	1.66	1.85
	MAE (%)	1.16	1.24	1.61	1.31	1.44
Zahak	<i>R</i>	0.49	0.58	0.58	0.51	0.57
	RMSE (%)	8.44	7.61	7.40	7.50	7.16
	MAE (%)	5.75	6.09	5.06	5.32	4.99
Farokhshahr	<i>R</i>	0.84	0.74	0.73	0.80	0.71
	RMSE (%)	3.75	3.04	2.83	2.40	3.08
	MAE (%)	1.95	2.04	2.05	1.75	2.15
Oltan	<i>R</i>	0.04	0.40	0.56	0.40	0.60
	RMSE (%)	5.60	9.24	5.76	8.16	3.40
	MAE (%)	4.41	8.64	4.97	7.34	2.63
Overall	<i>R</i>	0.46	0.38	0.51	0.44	0.59
	RMSE (%)	5.51	5.52	4.93	5.24	4.62
	MAE (%)	3.31	3.69	3.32	3.37	3.01

R = Pearson correlation coefficient; RMSE = root-mean-square error; MAE = mean absolute error.

Table 7. Evaluation of Models 13 to 20 in procedures 4 and 5 (seasonal modeling).

Station	Evaluation Criterion	Wet Season					Dry Season				
		Case 0	M-13	M-14	M-15	M-16	Case 0	M-17	M-18	M-19	M-20
Darab	<i>R</i>	0.56	0.06	0.37	0.35	0.38	-0.20	-0.31	-0.19	-0.30	0.11
	RMSE (%)	3.73	3.73	5.66	4.56	5.38	1.39	1.40	2.34	2.81	1.57
	MAE (%)	2.79	2.67	5.08	3.97	4.80	1.23	1.24	2.11	2.51	1.33
Kheirabad	<i>R</i>	0.10	0.27	0.17	0.17	-0.17	0.23	0.03	0.39	0.00	0.50
	RMSE (%)	12.78	9.25	7.08	6.91	7.17	1.18	1.95	1.43	1.14	1.45
	MAE (%)	11.55	8.39	6.58	6.30	6.61	1.05	1.66	1.29	0.93	1.31
Khosroshah	<i>R</i>	0.18	0.40	0.22	-0.27	0.25	0.42	0.17	-0.22	-0.10	0.09
	RMSE (%)	4.80	8.17	6.08	6.87	5.80	2.35	2.54	1.42	2.59	1.52
	MAE (%)	3.88	7.45	5.43	6.19	5.12	1.90	1.65	1.07	1.74	0.90
Zahak	<i>R</i>	0.24	0.33	0.29	-0.31	0.26	0.62	0.68	0.47	0.44	0.67
	RMSE (%)	13.72	10.40	11.00	11.52	10.79	3.86	4.47	3.98	3.81	3.69
	MAE (%)	11.53	9.42	9.73	10.16	9.58	3.22	4.09	2.73	2.65	2.99
Farokhshahr	<i>R</i>	0.08	-0.13	0.01	0.14	0.21	0.23	-0.03	0.34	0.09	0.65
	RMSE (%)	9.99	7.11	5.85	5.74	5.90	1.51	2.77	1.28	1.85	1.77
	MAE (%)	8.31	5.53	4.93	4.92	4.85	1.18	2.32	1.00	1.32	1.56
Oltan	<i>R</i>	0.29	0.22	0.28	0.28	-0.20	0.35	-0.07	0.21	-0.12	0.32
	RMSE (%)	7.36	10.04	3.47	6.91	3.41	3.27	6.71	3.42	5.15	2.62
	MAE (%)	6.82	9.68	2.84	6.34	2.71	2.53	6.07	2.66	4.29	1.99
Overall	<i>R</i>	0.13	0.11	0.10	0.05	0.20	0.44	-0.10	0.40	0.02	0.58
	RMSE (%)	9.56	8.26	6.95	7.30	6.84	2.47	3.76	2.52	3.16	2.24
	MAE (%)	7.47	6.99	5.88	6.22	5.73	1.85	2.83	1.79	2.22	1.67

R = Pearson correlation coefficient; RMSE = root-mean-square error; MAE = mean absolute error.

Table 8. Comparison of the overall correlation and errors in Advanced Microwave Scanning Radiometer 2 soil moisture content and the best models.

	<i>R</i>			RMSE			MAE		
	AMSR2	quadratic model with	Improvement (%)	AMSR2	quadratic model with	Improvement (%)	AMSR2	quadratic model with	Improvement (%)
		constant value			constant value			constant value	
Normal	0.24	0.23	-4.42	7.17	6.39	10.83	4.84	5.04	-4.02
NDVI	0.21	0.21	-0.06	6.47	6.59	-1.93	4.19	4.65	-10.86
LST	0.46	0.59	30.06	5.51	4.62	16.25	3.31	3.01	9.10
Wet	0.13	0.20	56.02	9.56	6.84	28.44	7.47	5.73	23.33
Dry	0.44	0.58	29.95	2.47	2.24	9.27	1.85	1.67	10.11

R = Pearson correlation coefficient; RMSE = root-mean-square error; MAE = mean absolute error; AMSR2 = Advanced Microwave Scanning Radiometer 2; NDVI = normalized difference vegetation index; LST = land surface temperature.

Table 9. The acquired parameters of models.

Case	Model	Model Parameters						
		PI	PI2	ISW	ISW2	LST	NDVI	Constant
Normal	M-1	119.29	-	3.38	-	-	-	-
	M-2	8.79	-	32.61	-	-	-	8.24
	M-3	233.76	-1320.48	-46.47	1500.51	-	-	-
	M-4	-120.78	820.01	-11.70	516.19	-	-	12.93
NDVI	M-5	81.70	-	5.54	-	-	10.94	-
	M-6	21.12	-	41.78	-	-	-0.88	6.41
	M-7	183.88	-1166.62	-89.24	3711.57	-	4.65	-
	M-8	-108.87	624.91	-64.11	2386.15	-	-3.22	12.61
LST	M-9	91.19	-	75.28	-	-0.17	-	-
	M-10	17.64	-	88.89	-	-0.29	-	7.27
	M-11	165.95	-878.37	54.71	1975.39	-0.22	-	-
	M-12	-373.79	2576.53	117.92	-609.59	-0.29	-	19.73
Wet	M-13	168.83	-	-49.14	-	-	-	-
	M-14	23.09	-	7.61	-	-	-	11.11
	M-15	309.36	-1569.65	-70.16	1203.12	-	-	-
	M-16	-54.41	468.79	-7.63	188.55	-	-	13.79
Dry	M-17	45.16	-	99.38	-	-	-	-
	M-18	-46.53	-	63.89	-	-	-	7.41
	M-19	157.15	-1344.58	50.68	1375.39	-	-	-
	M-20	-299.57	1842.05	61.56	-548.53	-	-	15.26

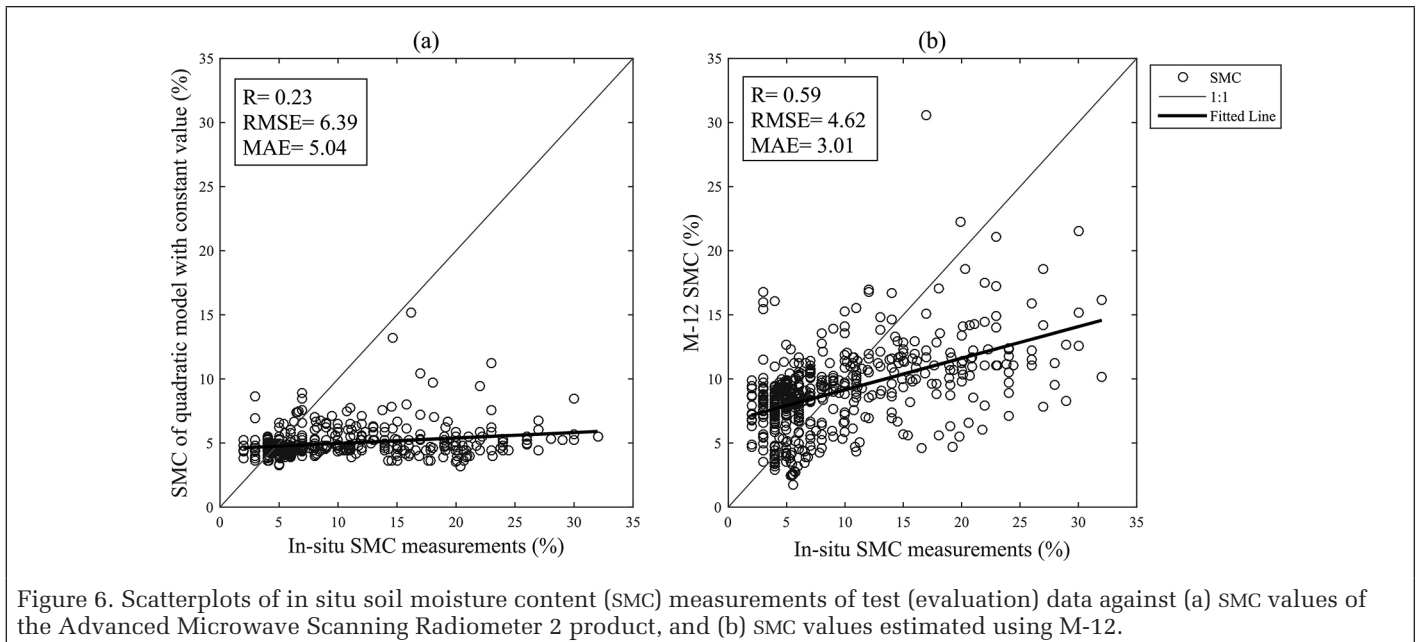


Figure 6 shows the scatterplots of SMC measurements of test data at the stations against AMSR2 SMC product and model with best performance of this study (M-12). This figure shows that the M12 has a better SMC approximation against *in situ* measurements and the fitted-line passing through this data is closer to the 1:1 line.

Figure 7 shows the SMC map, which was generated using the M-12 model. As it can be seen in this figure, coastal regions have relatively higher values of SMC. Moreover, the SMC values are not determined in some regions such as northern, central, and eastern regions due to the presence of cloud cover.

Uncertainty Sources

The results showed that in nearly all models, high values of SMC (values in the range of 25% to 40% in some case) were acquired for central deserts of Iran. This is due to the sensitivity of microwave brightness temperature to the saline soils (Merrikhpour and Rahimzadegan 2020). This is one of the uncertainty factors of the models' outputs. Moreover, this can be due to the lack of SMC measurement stations in these areas. Furthermore, for every image, the oceans, seas, free waters, lakes, and also coastal areas are masked. This masking is due to rapid and very high changes of SMC, which can result in a high grade of error in the models for these areas. Another uncertainty source of this study is the noise in the NDVI and LST data of MODIS data, which can affect the performance of the proposed models of this study. MODIS images may be contaminated by cloud effect, which may decrease applicability of the proposed model. Moreover, atmospheric phenomena such as atmospheric aerosols may contaminate MODIS images and reduce the performance of the proposed model. On the other hand, spatial mismatch in comparing ground station measurements and estimated SMC from AMSR2 data and inhomogeneity of land cover in AMSR2 pixels is another uncertainty source of this study.

Conclusion

The AMSR2 SMC product has some shortcomings, which may render some of its practical applications impossible. Two main shortcomings are low accuracy and complexity of the used model. Thus, the purpose of this study is the evaluation of the AMSR2 SMC product in Iran, and improvement of a model to extract SMC from synergistic use of the AMSR2 TBs and MODIS measurement with an acceptable accuracy.

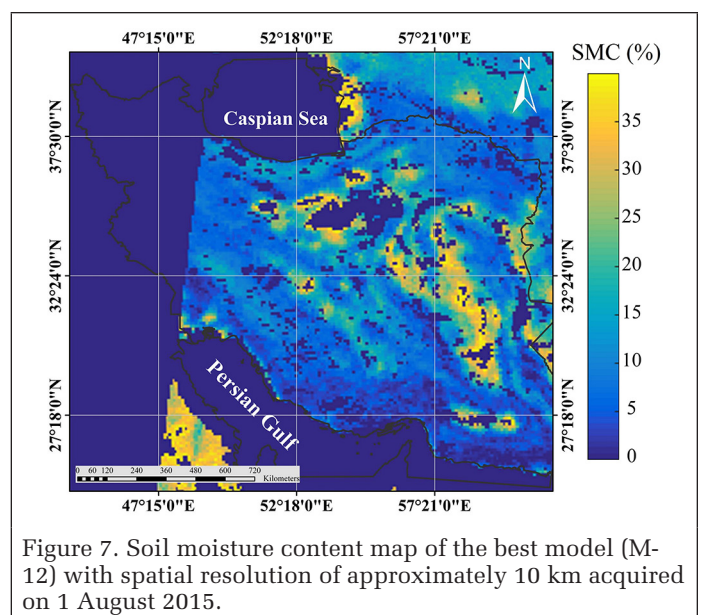


Figure 7. Soil moisture content map of the best model (M-12) with spatial resolution of approximately 10 km acquired on 1 August 2015.

In this regard, five different procedures, each comprising of four different methods (totaling 20 models) were developed for the SMC estimation. The methods were acquired by the combination of linear, quadratic equations, and a constant value. In the first procedure, SMC estimation was made only by using the PI and ISW. To consider the effect of vegetation on microwave radiation emitted from the soil, the NDVI was linearly applied besides PI and ISW in the second procedure. For the third procedure, the LST was used along with PI and ISW in modeling. In the fourth and fifth procedures, procedure 1 was individually implemented for the wet and dry seasons, respectively. The results proved that the performance of procedure 1 was close to the results of the AMSR2 SMC product with the overall correlation of 0.23, and RMSE and MAE of 6.39% and 5.04%, respectively. For the second procedure, the overall correlation of 0.21, and RMSE and MAE of 6.59% and 4.65% were acquired. These results indicated that the SMC estimation accuracy was not improved by taking into account the NDVI. In the third procedure, the best results were

obtained in the quadratic equation using a combination of PI and ISW along with LST, as well as a constant value. These results in the best model showed a correlation of 0.59 and RMSE and MAE values of 4.62% and 3.01%, respectively. Results obtained for the dry season model (fifth procedure) were similar to those of the previous procedure, but since the wet season did not produce satisfactory results, the two last procedures cannot be considered as a general model. By seasonal modeling, the correlation in the wet season was 0.20 and in the dry season it reached 0.58. Finally, a comparison of results of different models indicates that the M-12 model (using PI, ISW, and LST) provides the best results as a comprehensive model, since this does not require separate seasonal modeling. According to the results, it seems that using optical MODIS LST images along with AMSR2 passive microwave data leads to better results in SMC estimation. Therefore, it is possible to use the AMSR2 TBs along with MODIS LST data in a simple equation to improve the accuracy of the soil moisture estimations.

References

- Al-Bakri, J., A. Suleiman and A. Berg. 2014. A comparison of two models to predict soil moisture from remote sensing data of RADARSAT II. *Arabian Journal of Geosciences* 7:4851–4860.
- Al Bitar, A., D. Leroux, Y. H. Kerr, O. Merlin, P. Richaume, A. Sahoo and E. F. Wood. 2012. Evaluation of SMOS soil moisture products over continental US using the SCAN/SNOTEL network. *IEEE Transactions Geoscience Remote Sensing* 50:1572–1586.
- Alhammedi, M. and E. Glenn. 2008. Detecting date palm trees health and vegetation greenness change on the eastern coast of the United Arab Emirates using SAVI. *International Journal of Remote Sensing* 29:1745–1765.
- Bolten, J. D., W. T. Crow, X. Zhan, T. J. Jackson and C. A. Reynolds. 2010. Evaluating the utility of remotely sensed soil moisture retrievals for operational agricultural drought monitoring. *IEEE Journal of Selected Topics in Applied Earth Observations and Remote Sensing* 3:57–66.
- Callens, M., N. E. Verhoest and M. W. Davidson. 2006. Parameterization of tillage-induced single-scale soil roughness from 4-m profiles. *IEEE Transactions Geoscience Remote Sensing* 44:878–888.
- Calvet, J.-C., J.-P. Wigneron, J. Walker, F. Karbou, A. Chanzy and C. Albergel. 2011. Sensitivity of passive microwave observations to soil moisture and vegetation water content: L-band to W-band. *IEEE Transactions Geoscience Remote Sensing* 49:1190–1199.
- Chauhan, N. S., S. Miller and P. Ardanuy. 2003. Spaceborne soil moisture estimation at high resolution: A microwave-optical/IR synergistic approach. *International Journal of Remote Sensing* 24:4599–4622. <https://doi:10.1080/0143116031000156837>.
- Choi, M. and Y. Hur. 2012. A microwave-optical/infrared disaggregation for improving spatial representation of soil moisture using AMSR-E and MODIS products. *Remote Sensing of Environment* 124:259–269.
- Choi, M., J. M. Jacobs, M. C. Anderson and D. D. Bosch. 2013. Evaluation of drought indices via remotely sensed data with hydrological variables. *Journal of Hydrology* 476:265–273.
- Davenport, I. J., M. J. Sandells and R. J. Gurney. 2008. The effects of scene heterogeneity on soil moisture retrieval from passive microwave data. *Advances in Water Resources* 31:1494–1502.
- de Jeu, R. A., T. R. Holmes, R. M. Parinussa and M. Owe. 2014. A spatially coherent global soil moisture product with improved temporal resolution. *Journal of Hydrology* 516:284–296.
- Drusch, M. 2007. Initializing numerical weather prediction models with satellite-derived surface soil moisture: Data assimilation experiments with ECMWF's Integrated Forecast System and the TMI soil moisture data set. *Journal of Geophysical Research: Atmospheres* 112(D3). <https://doi.org/10.1029/2006JD007478>.
- Fujii, H., T. Koike and K. Imaoka. 2009. Improvement of the AMSR-E algorithm for soil moisture estimation by introducing a fractional vegetation coverage dataset derived from MODIS data. *Journal of the Remote Sensing Society of Japan (Japan)* 29:282–292.
- Gao, Z., X. Xu, J. Wang, H. Yang, W. Huang and H. Feng. 2013. A method of estimating soil moisture based on the linear decomposition of mixture pixels. *Mathematical and Computer Modelling* 58:606–613.
- Holzman, M. E., R. Rivas and M. Piccolo. 2014. Estimating soil moisture and the relationship with crop yield using surface temperature and vegetation index. *International Journal of Applied Earth Observation* 28:181–192.
- Japan Aerospace Exploration Agency (JAXA). xxxx. Webpage Title. <<http://gcom-w1.xxxxxx.jaxa.jp>> Accessed day Month year.
- Koster, R. D., P. A. Dirmeyer, Z. Guo, G. Bonan, E. Chan, P. Cox, C. T. Gordon, S. Kanae, E. Kowalczyk, D. Lawrence, P. Liu, C.-H. Lu, S. Malyshev, B. McAvaney, K. Mitchell, D. Mocko, T. Oki, K. Oleson, A. Pitman, Y. C. Sud, C. M. Taylor, D. Verseghy, R. Vasic, Y. Xue and T. Yamada. 2004. Regions of strong coupling between soil moisture and precipitation. *Science* 305:1138–1140.
- Lee, K.-H. and E. N. Anagnostou. 2004. A combined passive/active microwave remote sensing approach for surface variable retrieval using Tropical Rainfall Measuring Mission observations. *Remote Sensing of Environment* 92:112–125.
- Lei, S.-g., Z.-f. Bian, J. L. Daniels and D.-l. Liu. 2014. Improved spatial resolution in soil moisture retrieval at arid mining area using apparent thermal inertia. *Transactions of Nonferrous Metals Society of China* 24:1866–1873.
- Liu, H.-J., Y.-Z. Zhang, X.-L. Zhang, B. Zhang, K.-S. Song, Z.-M. Wang and N. Tang. 2009. Quantitative analysis of moisture effect on black soil reflectance. *Pedosphere* 19:532–540.
- Maeda, T. and Y. Taniguchi. 2013. Descriptions of GCOM-W1 AMSR2 Level 1R and Level 2 Algorithms. Ibaraki, Japan: Japan Aerospace Exploration Agency Earth Observation Research Center.
- Mattar, C., J.-P. Wigneron, J. A. Sobrino, N. Novello, J. C. Calvet, C. Albergel, P. Richaume, A. Mialon, D. Guyon, J. C. Jimenez-Munoz and Y. Kerr. 2012. A combined optical-microwave method to retrieve soil moisture over vegetated areas. *IEEE Transactions Geoscience Remote Sensing* 50:1404–1413.
- Merrikhpour, M. H. and M. Rahimzadegan. 2017a. Improving the algorithm of extracting regional total precipitable water vapor over land from MODIS images. *IEEE Transactions Geoscience Remote Sensing* 55:5889–5898. <https://doi:10.1109/TGRS.2017.2716414>.
- Merrikhpour, M. H. and M. Rahimzadegan. 2017b. An introduction to an algorithm for extracting precipitable water vapor over land from AMSR2 images. *IEEE Journal of Selected Topics in Applied Earth Observations and Remote Sensing* 10:3975–3984. <https://doi:10.1109/JSTARS.2017.2716403>.
- Merrikhpour, M. H. and M. Rahimzadegan. 2020. A synergistic use of AMSR2 and MODIS images to detect saline soils (study area: Iran). *Comptes Rendus Géoscience* 352:127–138. <https://doi:10.5802/crgeos.11>.
- Narayan, U., V. Lakshmi and T. J. Jackson. 2006. High-resolution change estimation of soil moisture using L-band radiometer and radar observations made during the SMEX02 experiments. *IEEE Transactions Geoscience Remote Sensing* 44:1545–1554.
- National Aeronautics and Space Administration (NASA). xxxx. Level-1 and Atmosphere Archive & Distribution System, Distributed Active Archive Center. <https://ladsweb.modaps.eosdis.xxxxxx.nasa.gov/> Accessed day Month year.
- Njoku, E. G. and D. Entekhabi. 1996. Passive microwave remote sensing of soil moisture. *Journal of Hydrology* 184:101–129.
- Panciera, R., M. A. Tanase, K. Lowell and J. P. Walker. 2014. Evaluation of IEM, Dubois, and Oh radar backscatter models using airborne L-band SAR. *IEEE Transactions Geoscience Remote Sensing* 52:4966–4979.
- Peters, J., B. De Baets, E. M. De Clercq, E. Ducheyne and N. E. Verhoest. 2011. The potential of multitemporal Aqua and Terra MODIS apparent thermal inertia as a soil moisture indicator. *International Journal of Applied Earth Observation* 13:934–941.
- Qin, J., K. Yang, N. Lu, Y. Chen, L. Zhao and M. Han. 2013. Spatial upscaling of in-situ soil moisture measurements based on MODIS-derived apparent thermal inertia. *Remote Sensing of Environment* 138:1–9.

- Qu, Y., Z. Zhu, C. Montzka, L. Chai, S. Liu, Y. Ge, J. Liu, Z. Lu, X. He, J. Zheng and T. Han. 2021. Inter-comparison of several soil moisture downscaling methods over the Qinghai-Tibet Plateau, China. *Journal of Hydrology* 592:125616. <https://doi.org/10.1016/j.jhydrol.2020.125616>.
- Robock, A. K. Y. Vinnikov, G. Srinivasan, J. K. Entin, S. E. Hollinger, N. A. Speranskaya, S. Liu and A. Namkhai. 2000. The global soil moisture data bank. *Bulletin of the American Meteorological Society* 81:1281–1299.
- Singh, R. and S. Srivastav. 1990. Mapping of waterlogged and salt-affected soils using microwave radiometers. *Remote Sensing* 11:1879–1887.
- Soliman, A., R. J. Heck, A. Brenning, R. Brown and S. Miller. 2013. Remote sensing of soil moisture in vineyards using airborne and ground-based thermal inertia. *Data Remote Sensing* 5:3729–3748.
- Sulla-Menashe, D. and M. A. Friedl. 2018. *User Guide to Collection 6 MODIS Land Cover (MCD12Q1 and MCD12C1) Product*. Reston, Va.: USGS.
- Ulaby, F. T., M. Razani and M. C. Dobson. 1983. Effects of vegetation cover on the microwave radiometric sensitivity to soil moisture. *IEEE Transactions Geoscience Remote Sensing*:51–61.
- United States Geological Survey. xxxx. Webpage Title. <<https://earthexplorer.usgs.gov/>> Accessed day Month year.
- Vereecken, H., J. A. Huisman, Y. Pachepsky, C. Montzka, J. van der Kruk, H. Bogena, L. Weihermüller, M. Herbst, G. Martinez and J. Vanderborght. 2014. On the spatio-temporal dynamics of soil moisture at the field scale. *Journal of Hydrology* 516:76–96.
- Wan, Z. 2014. New refinements and validation of the collection-6 MODIS land-surface temperature/emissivity product. *Remote Sensing of Environment* 140:36–45. <https://doi.org/10.1016/j.rse.2013.08.027>.
- Wang, L., J. Qu, S. Zhang, X. Hao and S. Dasgupta. 2007. Soil moisture estimation using MODIS and ground measurements in eastern China. *International Journal of Remote Sensing* 28:1413–1418.
- Wu, Q., H. Liu, L. Wang and C. Deng. 2016. Evaluation of AMSR2 soil moisture products over the contiguous United States using *in situ* data from the International Soil Moisture Network. *International Journal of Applied Earth Observation* 45:187–199.
- Zhang, D., R. Tang, W. Zhao, B. Tang, H. Wu, K. Shao and Z.-L. Li. 2014. Surface soil water content estimation from thermal remote sensing based on the temporal variation of land surface temperature. *Remote Sensing* 6:3170–3187.
- Zhao, W. and Z.-L. Li. 2013. Sensitivity study of soil moisture on the temporal evolution of surface temperature over bare surfaces. *International Journal of Remote Sensing* 34:3314–3331.

Optimal Regularization Method Based on the L-Curve for Solving Rational Function Model Parameters

Guoqing Zhou, Man Yuan, Xiaozhu Li, Hongjun Sha, Jiasheng Xu, Bo Song, and Feng Wang

Abstract

Rational polynomial coefficients in a rational function model (RFM) have high correlation and redundancy, especially in high-order RFMs, which results in ill-posed problems of the normal equation. For this reason, this article presents an optimal regularization method with the L-curve for solving rational polynomial coefficients. This method estimates the rational polynomial coefficients of an RFM using the L-curve and finds the optimal regularization parameter with the minimum mean square error, then solves the parameters of the RFM by the Tikhonov method based on the optimal regularization parameter. The proposed method is validated in both terrain-dependent and terrain-independent cases using Gaofen-1 and aerial images, respectively, and compared with the least-squares method, L-curve method, and generalized cross-validation method. The experimental results demonstrate that the proposed method can solve the RFM parameters effectively, and their accuracy is increased by more than 85% on average relative to the other methods.

Introduction

It is of prime importance to use sensor models to precisely define the mathematical relationship between two-dimensional image space and three-dimensional object space in a remote sensing field (Zhou *et al.* 2017; Liu *et al.* 2019). Sensor models fall into two categories (Zhou 2020; Zhou *et al.* 2021): physical and generic (i.e., rational function models [RFMs]). Physical sensor models are sensor dependent, which increases the difficulty of image processing and application. Conversely, generic sensor models can describe various remote sensing systems in a unified framework due to their independence. There are four generic sensor models defined by the Open GIS Consortium (2004): polynomial, grid interpolation, rational function, and universal image geometry. Investigators have demonstrated that RFMs are more complete and universal than the other models (L. Zhang *et al.* 2011). An RFM mainly consists of four 3D polynomials that contain numerous correlated terms (Ma *et al.* 2018; Moghaddam *et al.* 2018), which are usually used to extract spatial information

from an image. An RFM possesses the following characteristics (Tong *et al.* 2010; Zhou *et al.* 2016; R. Zhang *et al.* 2018):

- It is independent of sensor and coordinate systems, and can fit all kinds of physical sensor models well without coordinate conversion.
- Its accuracy is almost the same as that of rigorous physical models in stereo mapping, orthophoto correction, digital elevation model (DEM) extraction, and so on.
- It has superior interpolation properties.

The parameters of an RFM are known as rational polynomial coefficients (RPCs); they can be solved in terrain-independent cases using rigorous sensor models, and in terrain-dependent cases using ground control points (GCPs). Tao and Hu (2001a, 2001b) proposed a direct least-squares method and an iterative least-squares method for solving the parameters of an RFM. D. Li *et al.* (2006) proposed a linear solution of unknown RFM parameters based on a global DEM. However, in solving high-order RFM parameters, these methods may involve ill-conditioned problems caused by inhomogeneous distribution of GCPs or overparametrization of the RFM; specifically, overparametrization represents superfluous RPCs in the RFM. It is necessary to address these ill-conditioned problems to solve RFM parameters, which is the focus of this article.

Regularization has proven to be the primary approach for solving these ill-conditioned problems, and is suitable for weakening or even eliminating the complex collinearity hazard (C. Li *et al.* 2017). The Tikhonov regularization method is usually used to mitigate the problem of multicollinearity in linear regression, which commonly occurs in models with large numbers of parameters, and to do so it needs to select an appropriate regularization parameter (Edwards and Stoll 2018). There are many methods to select regularization parameters, which leads to various methods for solving RFM parameters. The common methods for solving RFM parameters are the L-curve and GCV (generalized cross-validation) methods (Hansen and O'Leary 1993). The L-curve method for determining the regularization parameters was first proposed by Hansen (1992). The L-curve is so named for its shape, consisting of a relatively vertical segment and a relatively horizontal line in an ideal setting. The maximum curvature of the corner point in the curve is defined as the regularization parameter. The L-curve method is a well-defined numerical problem, rarely affected by correlated errors. But it is difficult to determine the corner point exactly that has the maximum curvature. So the GCV method was proposed by Golub *et al.* (1979). The independent variable corresponding to the

Guoqing Zhou is with the Guangxi Key Laboratory of Spatial Information and Geomatics, Guilin University of Technology, Guilin, China (gzhou@glut.edu.cn).

Man Yuan, Jiasheng Xu, Bo Song, and Feng Wang are with the Guilin University of Technology, Guilin, China.

Xiaozhu Li is with the Hubei Geomatics Technology Group Stock Co., Ltd, Wuhan, China.

Hongjun Sha is with the School of Remote Sensing and Information Engineering, Wuhan University, Wuhan, China.

Contributed by Rongjun Qin, August 7, 2020 (sent for review January 22, 2021; reviewed by Rongjun Qin, Linfu Xie).

Photogrammetric Engineering & Remote Sensing
Vol. 87, No. 9, September 2021, pp. 661–668.
0099-1112/21/661–668

© 2021 American Society for Photogrammetry
and Remote Sensing
doi: 10.14358/PERS.20-00072

minimum value of the GCV function is the regularization parameter. However, the value in the left part of the GCV function may be too small, which will cause the plot to be too flat and make it difficult to find the correct minimum value.

With this analysis, this article proposes an improved optimal regularization method based on the L-curve to obtain a more stable solution for solving the ill-conditioned problems.

Optimal Regularization Method Based on the L-Curve

Model of Optimal Regularization Method With the L-Curve

For any type of image, the RFM positive formula (Jabari and Zhang 2016; Wang *et al.* 2016; Shen *et al.* 2017) is

$$\begin{cases} y_n = \frac{P_1(X_n, Y_n, Z_n)}{P_2(X_n, Y_n, Z_n)} \\ x_n = \frac{P_3(X_n, Y_n, Z_n)}{P_4(X_n, Y_n, Z_n)} \end{cases} \quad (1)$$

where (y_n, x_n) are pixel coordinates, (X_n, Y_n, Z_n) are the corresponding 3D coordinates in a given geodetic coordinate system, n is the number of collected points, and $P_i(X_n, Y_n, Z_n)$, $i = (1, 2, 3)$, represents a polynomial equation that is a function of X , Y , and Z . When a third-order polygonal equation is used, the coefficients of the polynomials P_1, P_2, P_3 , and P_4 are a_i, b_i, c_i , and d_i ($i = 0, \dots, 19$). Therefore, there are 78 unknown RPCs in Equation 1 (default $b_0 = 1$ and $d_0 = 1$), which means that the number of RFM parameters is also 78.

Three different orders of polynomials corresponding to three different denominator configurations are listed in Table 1, which means that different models correspond to different numbers of unknown RFM parameters. Accordingly, different numbers of GCPs are needed to solve the RPCs.

Table 1. Nine rational function models (Tao and Hu 2001).

Polynomial Order	Denominator	Number of RPCs	Minimum Number of GCPs
1	$P_2 = P_4 = 1$	8	4
	$P_2 = P_4$	11	6
	$P_2 \neq P_4$	14	7
2	$P_2 = P_4 = 1$	20	10
	$P_2 = P_4$	29	15
	$P_2 \neq P_4$	38	19
3	$P_2 = P_4 = 1$	40	20
	$P_2 = P_4$	59	30
	$P_2 \neq P_4$	78	39

GCP = ground control point; RPC = rational polynomial coefficient.

Equation 1 can be rewritten as observation equations in the form

$$l = BX + V \quad (2)$$

where $l \in R^r$ is the vector of observations, $B \in R^{n \times t}$ is the design matrix, $X \in R^t$ is the vector of unknown parameters, and $V \in R^n$ is the vector of random errors.

When the number of observations is greater than the number of unknown parameters ($n \geq t$) and the columns of B are linearly independent, the unknown parameters X can be determined by the least-squares solution (Tao and Hu 2001a, 2001b), and a linear solution can be obtained on the basis of a global DEM (Groddecki and Dial 2003; Fraser and Hanley 2005; H. Zhang *et al.* 2016). However, when n is less than t (see Table 1), the matrix B is rank deficient and its columns are multicollinear, which results in overparametrization, especially in

high-order RFM parameters. In this case, serious ill-conditioned problems will occur with the traditional least-squares method.

Therefore, in order to get a more stable and accurate solution under the ill-conditioned equation, Tikhonov regularization (Neumaier 1998; Surnin 2018) is used in this article. Determination of a suitable regularization parameter is an important task in the Tikhonov method. Generally, the L-curve or GCV method is used to determine the regularization parameter, which is either the maximum curvature of the corner of the L-curve or the independent variable corresponding to the minimum value of the GCV function. However, it is difficult to exactly determine the corner of the L-curve and the minimum value of the GCV function, which results in the deviation of regularization parameters obtained by these methods.

With this analysis, an improved optimal regularization method is proposed based on the L-curve to solve an optimal regularization parameter with the minimum mean square error. The process of our method is as follows:

A statistical model for solving Equation 2 can be written as

$$\begin{cases} E(l) = BX \\ D(l) = \Sigma_l = \sigma_0^2 I_n \end{cases} \quad (3)$$

According to the optimal linear uniformity estimate or the regularization estimate (Cai *et al.* 2001), the estimates \hat{X} of X are

$$\hat{X} = (B^T \Sigma_l^{-1} B + \alpha^2 S^{-1})^{-1} B^T \Sigma_l^{-1} l \quad (4)$$

When $S = \sigma_0^2 I_m$ (where m is the number of columns in B),

$$\begin{aligned} \hat{X} &= \left(B^T \frac{1}{\sigma_0^2} I_n B + \alpha^2 \frac{1}{\sigma_0^2} I_m \right)^{-1} B^T \frac{1}{\sigma_0^2} I_n l \\ &= (B^T B + \alpha^2 I_m)^{-1} B^T l \end{aligned} \quad (5)$$

The variance estimate is

$$\begin{aligned} D(\hat{X}) &= (B^T B + \alpha^2 I_m)^{-1} B^T \Sigma_l \left[(B^T B + \alpha^2 I_m)^{-1} B^T \right]^T \\ &= (B^T B + \alpha^2 I_m)^{-1} B^T B (B^T B + \alpha^2 I_m)^{-1} \sigma_0^2 \end{aligned} \quad (6)$$

The mean β of the deviation between the estimated value and the true value is

$$\begin{aligned} \beta &= E(\hat{X} - X) \\ &= (B^T B + \alpha^2 I_m)^{-1} B^T E(l) - X \\ &= -\alpha^2 (B^T B + \alpha^2 I_m)^{-1} X \end{aligned} \quad (7)$$

Therefore, the mean square error is:

$$\begin{aligned} \text{MSE}(\hat{X}) &= E\left[(\hat{X} - X)(\hat{X} - X)^T \right] \\ &= D(\hat{X}) + \beta\beta^T \\ &= (B^T B + \alpha^2 I_m)^{-1} B^T B (B^T B + \alpha^2 I_m)^{-1} \sigma_0^2 + \alpha^4 (B^T B + \alpha^2 I_m)^{-1} X X^T (B^T B + \alpha^2 I_m)^{-1} \end{aligned} \quad (8)$$

In terms of $\text{MSE}(\hat{X}) = \min \Leftrightarrow \text{tr} \text{MSE}(\hat{X}) = \min$, the trace of the minimum mean square error of the estimate of X , the function $f(\alpha)$ about α is constructed as follows:

$$f(\alpha) = \text{tr} \left((B^T B + \alpha^2 I_m)^{-1} B^T B (B^T B + \alpha^2 I_m)^{-1} \sigma_0^2 + \text{tr} \left((B^T B + \alpha^2 I_m)^{-1} X X^T (B^T B + \alpha^2 I_m)^{-1} \right) \alpha^4 \right) \quad (9)$$

The optimal regularization parameter $\alpha (\alpha \in (0, 1))$ corresponds to the minimum value of the function $f(\alpha)$ on the

fitting function. As shown in Equation 9, it is only necessary for us to determine X and the identity weight variance σ_0^2 in solving $f(\alpha)$, where σ_0^2 can be obtained from \hat{X} :

$$\sigma_0^2 = \frac{(B\hat{X} - I)^T (B\hat{X} - I)}{n - \text{rank}(B)} \quad (10)$$

with X replaced by \hat{X} ($X = \hat{X}$). Thus, \hat{X} is important for solving . However, in the ill-posed case, the value of $f(\alpha)$ will be unstable due to the unstable \hat{X} (a few elements too large or a few elements too small), which will affect the determination of the minimum value of $f(\alpha)$. Therefore, we propose an optimal solution of \hat{X} with the L-curve method as follows.

First, \hat{X} can be solved by Equation 5:

$$\hat{X}_{\text{L-curve}} = (B^T B + \alpha_{\text{L-curve}}^2 I_m)^{-1} B^T I \quad (11)$$

where the regularization parameters can be obtained by the maximum curvature of the L-curve:

$$k = \frac{\mu'v'' - \mu''v'}{(\mu'^2 + v'^2)^{3/2}} \quad (12)$$

Second, the value of \hat{X} is used to obtain X and σ_0^2 , and the optimal regularization parameter is solved by Equation 9.

With this analysis, the \hat{X} obtained by the L-curve method is more stable for determining the minimum value of $f(\alpha)$, which ensures the stability and reliability of the solved optimal regularization parameter. Thus, the accuracy of RFM parameters based on the improved optimal regularization method would be significantly increased.

Analysis and Discussion

In order to further analyze the advantages and disadvantages of the proposed method, a comparison analysis of four methods is depicted in Table 2. It can be analyzed theoretically as follows.

The proposed method has advantages over the least-squares method:

- For the parameters, adding α^2 as the main diagonal entries of the coefficient matrix of the normal equation can make the matrix more stable.
- For the order number of the RFM, it is suitable for solving high-order RFM parameters.

It has advantages over the L-curve method:

- For the parameters, \hat{X} is optimized based on the L-curve method, which can effectively determine the minimum value of the function about with the minimum mean square error, and further obtains the most reliable optimal regularization parameters.
- For the results, even if the \hat{X} obtained by the L-curve has a slight error, it only causes the value of $f(\alpha)$ to be slightly larger or smaller overall; it does not affect the determination of extreme points of the function. As a result, α can be accurately determined.

It has advantages over the GCV method:

- For the parameters, the determination of the minimum value of the function is more reliable and accurate, which ensures the stability and reliability of the optimal regularization parameter α obtained.
- For the results, the RFM parameters obtained are more stable.

Experiments and Analysis

The proposed method was validated through both terrain-dependent and terrain-independent solutions. In the terrain-independent solution, the 3D virtual control grid is built based on the parameters of the rigorous imaging model, and the RFM parameters are solved by fitting. This method does not need real GCPs on the Earth's surface.

In the terrain-dependent solution, well-distributed GCPs are collected—a certain number with uniform distribution can be directly obtained on large-scale digital maps—and the least-squares method is used to solve the unknown parameters.

Terrain-Independent Solution

Data Description

An aerial image covering Denver, Colorado, was used to validate the proposed method. The aerial image was obtained on 17 April 2000 using an RC30 aerial camera with a focal length of 153.022 mm (Figure 1). The internal and external orientation elements of the camera are shown in Table 3. The scale of aerial image is approximately 1:7200 at an average flight altitude of 1650 m, and the size of aerial image is 17 054×17 054 pixels.

The steps of the terrain-independent solution for validating the proposed method are as follows:

1. Divide an original image with m rows and n columns into points on an equal-size grid with image point coordinates (x, y) (Figure 2).
2. Calculate the elevation difference R covering the same image extent and then divide R into k layers of height $\text{int}(R/k)$ (Figure 2).

Table 2. Characteristics of four methods for solving rational function model (RFM) parameters.

Method	Solving RFM Parameters (X)	Key to Determining Regularization Parameter	Advantages	Challenges	Solution Stability
Least-squares	$(B^T B)^{-1} B^T I$	Null	Intuitive and simple	Solution of high-order RFM parameters is unstable	Unstable
L-curve		Maximum curvature of curve	Well-defined numerical problem; uninfluenced by correlated errors	Difficult to accurately determine the corner point with maximum curvature	Stable
Generalized cross-validation	$(B^T B + \alpha^2 I)^{-1} B^T I$	Minimum value of the generalized cross-validation function	Very robust against nonhomogeneity of variance and non-Gaussian errors	Affected by correlated errors; difficult to accurately determine the minimum value of the function	Less stable
Improved optimal regularization		$\hat{X}_{\text{L-curve}}$ and the minimum value of the function $f(\alpha)$	More stable and reliable	Calculation is more complicated	More stable



Figure 1. The original aerial image of Denver, Colorado, USA.

Table 3. Internal and external orientation elements of the camera.

Parameter	Value
f	153.022 mm
x_0	0.002 mm
y_0	-0.004 mm
X_S	3 143 040.487 824 465 ft
Y_S	1 696 520.187 562 254 ft
Z_S	9073.690 373 855 898 ft
ϕ	1.705 248 003 481 724°
ω	0.087 068 798 164 338 63°
κ	89.024 747 465 774 55°

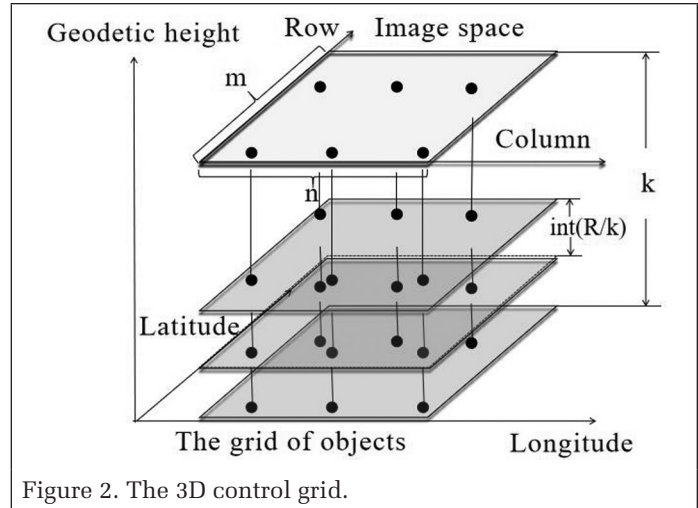


Figure 2. The 3D control grid.

3. Calculate the geodetic coordinates (X, Y, Z) of each image point coordinate (x, y) in each layer on the basis of the rigorous sensor model, establishing the 3D control grid (Figure 2).
4. Establish the 3D check grid—with twice as many layers and double each grid size length of the control grid—by repeating Steps 1–3.
5. Calculate the unknown RFM parameters according to the image point coordinates (x, y). The RFM parameters of the control grid are used to calculate the image point coordinates (x', y') of the check grid. The accuracy evaluation will be conducted by comparing the difference of the image coordinates between the original image and those calculated from the RFM.

Validation Using Nine RFMs

In order to verify the accuracy of RFM parameters, we designed nine RFMs. The size of the horizontal control grid is set to 20×20 pixels, and there are five elevation layers. Meanwhile, the size of the horizontal check grid is set to double each side of the control grid's—that is, 40×40 pixels—with twice as

Table 4. Rational function model error with the least-squares method versus our method.

Polynomial Order	Denominator	Method	X (pixels)		Y (pixels)		Z (pixels)	
			Maximum Residual Error	Mean Square Error	Maximum Residual Error	Mean Square Error	Maximum Residual Error	Mean Square Error
1	$P_2 \neq P_4$	Ours	2.0009×10^{-10}	1.1435×10^{-10}	8.1745×10^{-11}	4.0002×10^{-11}	2.1703×10^{-10}	1.2132×10^{-10}
		Least-squares	2.1100×10^{-10}	1.1538×10^{-10}	8.1855×10^{-11}	4.0007×10^{-11}	2.1813×10^{-10}	1.2212×10^{-10}
	$P_2 = P_4$	Ours	2.0636×10^{-10}	1.1446×10^{-10}	8.7231×10^{-11}	3.8271×10^{-11}	2.1256×10^{-10}	1.2057×10^{-10}
		Least-squares	2.0736×10^{-10}	1.1466×10^{-10}	8.7311×10^{-11}	3.8573×10^{-11}	2.1353×10^{-10}	1.2097×10^{-10}
	$P_2 = P_4 = 1$	Ours	3.8025×10^2	9.2681×10^1	2.9267×10^2	8.5699×10^1	4.8011×10^2	1.2509×10^2
		Least-squares	3.8047×10^2	9.2783×10^1	2.9362×10^2	8.5819×10^1	4.8059×10^2	1.2639×10^2
2	$P_2 \neq P_4$	Ours	2.1828×10^{-10}	1.1692×10^{-10}	1.0914×10^{-10}	3.7946×10^{-11}	2.3756×10^{-10}	1.2292×10^{-10}
		Least-squares	—	—	—	—	—	—
	$P_2 = P_4$	Ours	2.1282×10^{-10}	1.1295×10^{-10}	9.0949×10^{-11}	3.5859×10^{-11}	2.1689×10^{-10}	1.1851×10^{-10}
		Least-squares	—	—	—	—	—	—
	$P_2 = P_4 = 1$	Ours	1.2093×10^1	1.8671	8.0198	1.6472	1.4389×10^1	2.5129
		Least-squares	1.2293×10^1	1.8875	8.0378	1.6876	1.4688×10^1	2.5319
3	$P_2 \neq P_4$	Ours	4.5657×10^{-10}	1.7356×10^{-10}	6.7303×10^{-11}	2.7944×10^{-11}	4.5832×10^{-10}	1.7580×10^{-10}
		Least-squares	—	—	—	—	—	—
	$P_2 = P_4$	Ours	2.8558×10^{-10}	1.1150×10^{-10}	5.0932×10^{-11}	1.9344×10^{-11}	2.8595×10^{-10}	1.1316×10^{-10}
		Least-squares	—	—	—	—	—	—
	$P_2 = P_4 = 1$	Ours	3.0581×10^{-01}	3.6971×10^{-2}	1.7212×10^{-1}	3.3411×10^{-2}	3.6859×10^{-1}	5.0291×10^{-2}
		Least-squares	3.2541×10^{-1}	3.8982×10^{-2}	1.9252×10^{-1}	3.4401×10^{-2}	3.7809×10^{-1}	5.1991×10^{-2}

— = no solution.

Table 5. Influence of grid size on rational function model accuracy.

Grid Size (pixels)	x (pixels)		y (pixels)		Plane $\left(\sqrt{x^2 + y^2}\right)$ (pixels)	
	Maximum Residual Error	Mean Square Error	Maximum Residual Error	Mean Square Error	Maximum Residual Error	Mean Square Error
10×10	7.4215×10^{-10}	3.5251×10^{-10}	3.4470×10^{-10}	1.7327×10^{-10}	7.8669×10^{-10}	3.9279×10^{-10}
20×20	6.8349×10^{-10}	3.4585×10^{-10}	3.5999×10^{-10}	1.7350×10^{-10}	7.4976×10^{-10}	3.8693×10^{-10}
30×30	7.4942×10^{-10}	3.4608×10^{-10}	3.9336×10^{-10}	1.7344×10^{-10}	8.0754×10^{-10}	3.8711×10^{-10}
40×40	7.8671×10^{-10}	3.4751×10^{-10}	4.1291×10^{-10}	1.7511×10^{-10}	8.4970×10^{-10}	3.8913×10^{-10}
50×50	7.5534×10^{-10}	3.4651×10^{-10}	4.2201×10^{-10}	1.7457×10^{-10}	8.5141×10^{-10}	3.8800×10^{-10}

many elevation layers (10). The least-squares method and the proposed method were applied to solve the RFM parameters. The experimental results are shown in Table 4.

As can be observed, the least-squares method is only able to solve low-order RFM parameters, but high-order ones, which is caused by ill-conditioned problems. However, the proposed method can effectively solve high-order RFM parameters with little error.

Influence of Grid Size on RFM Parameter Accuracy

In order to verify the stability and influence of the grid size on the accuracy of the RFM parameters in the proposed method, we set five control grid sizes—10×10, 20×20, 30×30, 40×40, and 50×50 pixels—with five elevation layers. Accordingly, check grid sizes were set to 20×20, 40×40, 60×60, 80×80, and 100×100 pixels, with 10 elevation layers.

As can be observed from Table 5 and Figure 3, the residuals remained almost unchanged with increasing control grid size. This demonstrates that the grid size has little impact on the RFM parameter accuracy, with the smallest residual error at 20×20 pixels.

Terrain-Dependent Solution

Data Description

A *Gaofen-1* (GF-1) image of the Yunnan region of China was used to validate the proposed method, with the panchromatic image at 2-m resolution and the multispectral image at 8-m resolution (Figure 4). The panchromatic image was 18 000×18

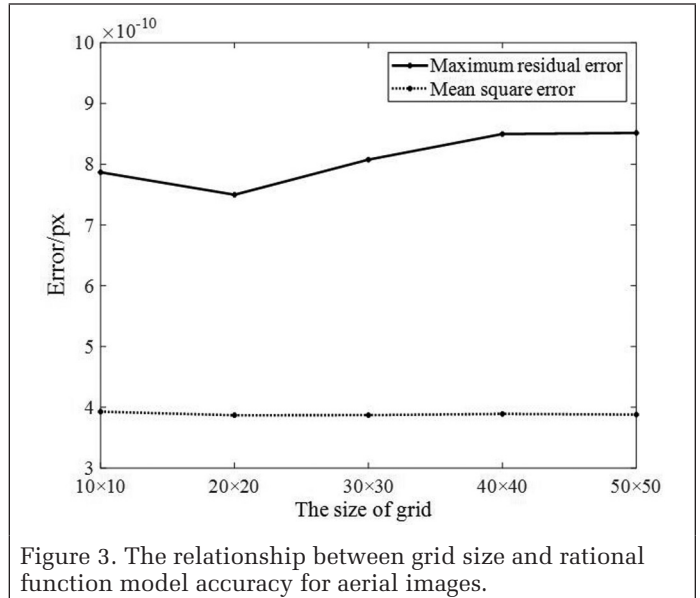


Figure 3. The relationship between grid size and rational function model accuracy for aerial images.

192 pixels, and the multispectral image was 4500×4548 pixels, corresponding to a ground size of approximately 36×36 km. The processing level of the GF-1 data was Level 1A—i.e., with radiometric correction, and thus an .rpb file.

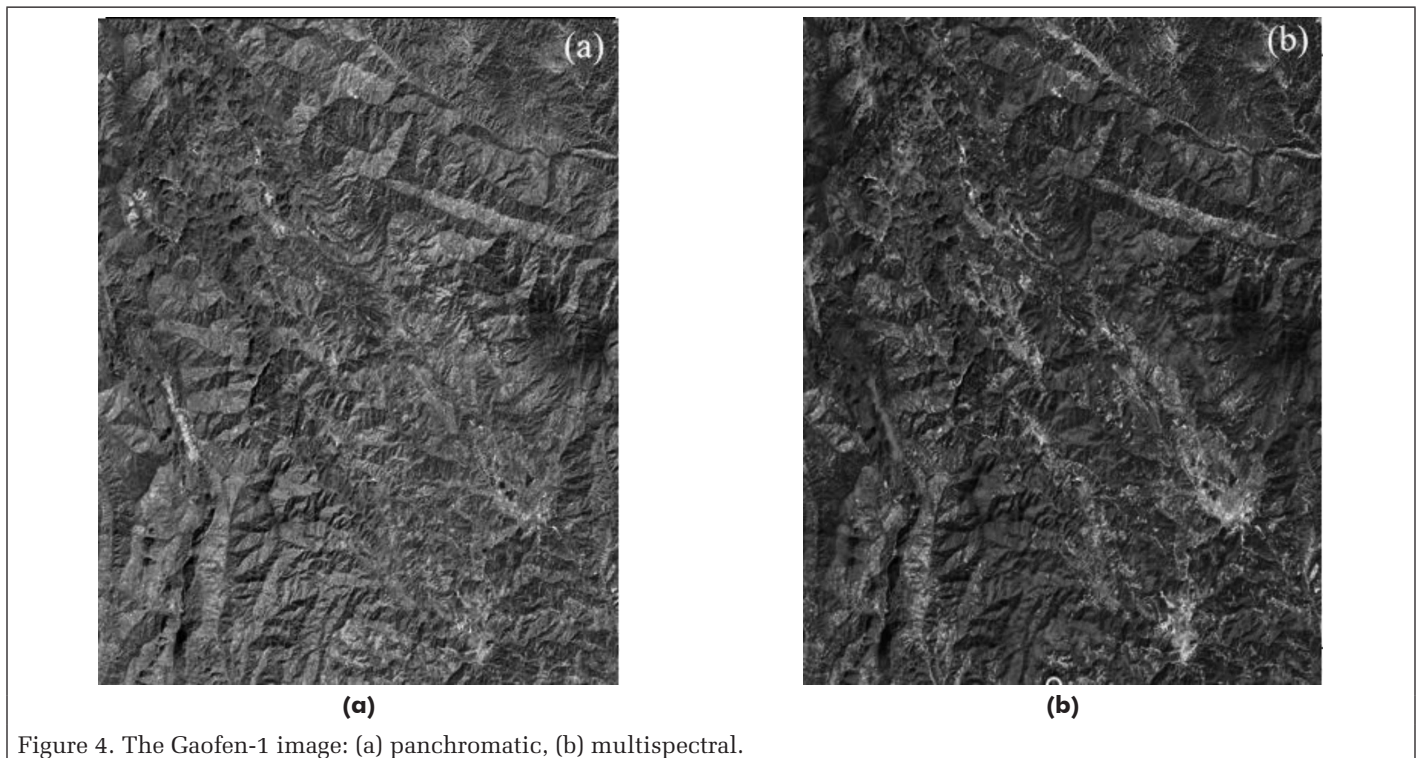


Figure 4. The Gaofen-1 image: (a) panchromatic, (b) multispectral.

GCP Acquisition From GF-1 Satellite Imagery

When the RFM parameters are solved by the terrain-dependent solution, the distribution and quantity of GCPs are crucial to the RFM parameter accuracy.

The XY-coordinates of 152 GCPs with uniform distribution were collected from Google Earth in the covered image area, and the elevation of each GCP was obtained through DEM interpolation at 30-m ground resolution. The RPCs in the standard .rpb file for the GF-1 panchromatic image were used to compute the pixel coordinates of each GCP, which were taken as true values. Then the pixel coordinates of the panchromatic image were converted into corresponding pixel coordinates of the multispectral image by bilinear transformation. Finally, the geographical coordinates of the 152 GCPs were obtained. The reason for this process is that the resolution of the panchromatic image is higher than that of the multispectral image.

Similarly, appropriate checkpoints were obtained for error analysis. Although the GF-1 image used in the experiment already had RPCs in the .rpb auxiliary file, the vendor provided only the first-order RFM—i.e., ill-conditioned problems for high-order RFMs, such as second or third order, still existed (Table 6). For this reason, the least-squares method was used in the low-order case for solving RFM parameters, and our method was used in the high-order case. In the end, 152 GCPs and 13 checkpoints were selected to evaluate the accuracy of different RFMs (Figure 5, Table 6).

Influence of Different RFM Conditions on RFM Accuracy

The accuracy of the RFM is evaluated by calculating the residuals of the pixel coordinates relative to the known checkpoints. The maximum residuals in x and y were used to evaluate the accuracy of the RFM.

Influence of the Number of GCPs on RFM Accuracy

Different numbers of GCPs—40, 60, 80, 100, 120, 140, 160, 180, 200, 300, 400, 500, and 1000—with 40 checkpoints were selected to investigate the effect of the number of GCPs on RFM accuracy (Table 6). The RFM accuracy in the GF-1 image was highest when the denominator of the third-order RFM was used. With different numbers of GCPs, the RFM accuracy changed as shown in Figure 6. Through experiments with 13 groups of GCPs, we found that when the number of GCPs was greater than or equal to 100, the residuals and mean square errors of the checkpoints gradually became stable and the RFM accuracy increased.

Comparison Analysis

For the terrain-independent solution, the control grid size was set at 20×20 pixels, with five elevation layers; and accordingly, the check grid size was set to 40×40 pixels with 10 elevation layers. We obtained RFM parameters by the L-curve method, the GCV method, and our method when the denominator of the third-order RFM changed. The stability

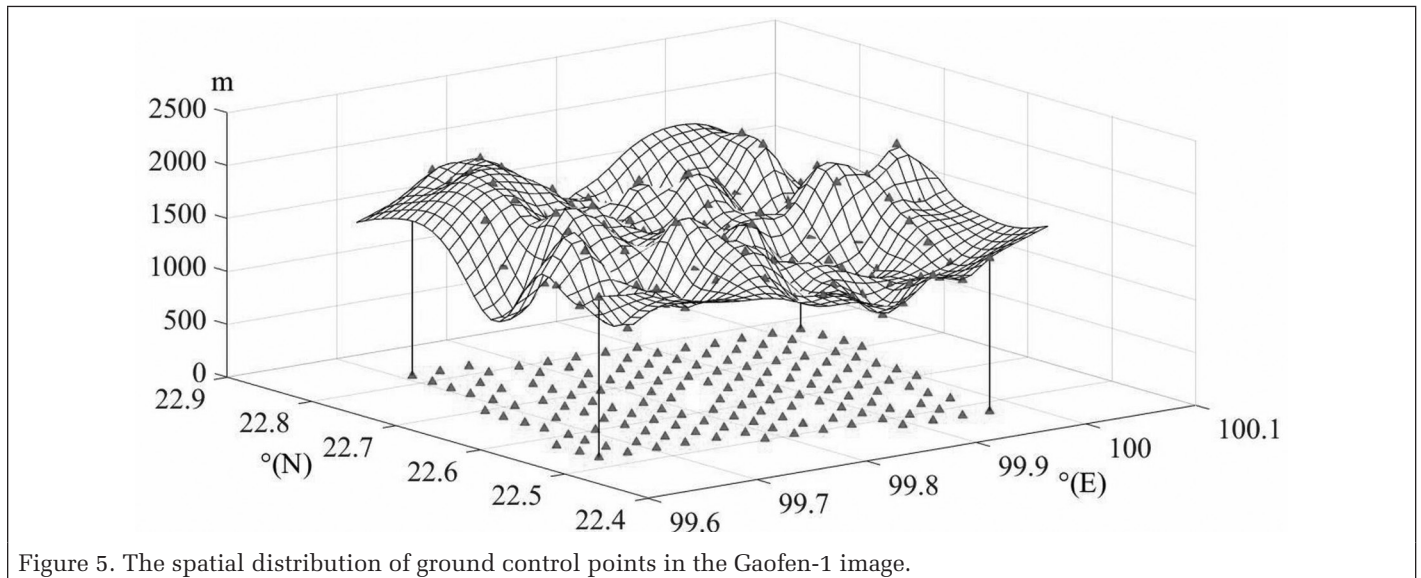


Figure 5. The spatial distribution of ground control points in the Gaofen-1 image.

Table 6. Rational function model residuals for the Gaofen-1 image.

Polynomial Order	Denominator	x (pixels)		y (pixels)		Plane $(\sqrt{x^2 + y^2})$ (pixels)		Parameter of Regularization
		Maximum Residual Error	Mean Square Error	Maximum Residual Error	Mean Square Error	Maximum Residual Error	Mean Square Error	
1	$P_2 \neq P_4$	4.1575	1.9930	-1.5743	1.2526	4.2308	0.9386	Not ill-conditioned
	$P_2 = P_4$	4.3781	2.0930	-2.1999	1.5325	4.4957	1.0515	
	$P_2 = P_4 = 1$	4.6939	2.2378	-1.7633	1.3631	4.7887	1.1099	
2	$P_2 \neq P_4$	0.2600	0.0825	-0.0475	0.0243	0.2626	0.0717	5.4344×10^{-4}
	$P_2 = P_4$	-2.5502	1.2799	1.5102	0.9806	2.9335	0.7519	1.2549×10^{-2}
	$P_2 = P_4 = 1$	4.6267	2.2071	0.2335	0.1169	4.6268	1.5339	Not ill-conditioned
3	$P_2 \neq P_4$	0.2600	0.0823	-0.0475	0.0198	0.2626	0.0540	1.8614×10^{-7}
	$P_2 = P_4$	0.1604	0.0775	-0.0577	0.0330	0.1949	0.0537	8.6034×10^{-4}
	$P_2 = P_4 = 1$	0.2061	0.0846	-0.0544	0.0253	0.2087	0.0614	Not ill-conditioned

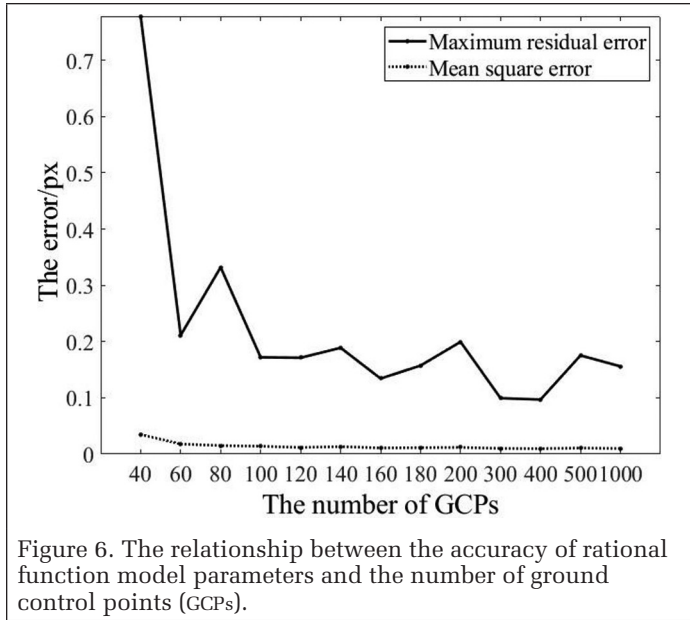


Figure 6. The relationship between the accuracy of rational function model parameters and the number of ground control points (GCPs).

and accuracy of RFM parameters from the three methods were validated, with results are depicted in Figure 7 and errors shown in Table 7.

As can be seen from Table 7, a few large errors (gross errors) occurred with both the least-squares method and the GCV method. This means that those two methods cannot detect and delete gross errors effectively. The GCV method additionally cannot solve the ill-conditioned equation, due to deviation in determining regularization parameters. The L-curve method and our method, by contrast, can solve the ill-posed problems and thus can obtain stable and highly accurate parameters. The RFM parameters solved by our method had the highest accuracy, an average 85% increase over the traditional L-curve method. This demonstrates that our method can effectively solve ill-conditioned equations.

Conclusion

This article proposes an improved optimization regularization method with the L-curve based on the solutions of RFM parameters in both terrain-independent and terrain-dependent cases. This method takes the solutions obtained by the L-curve method as the initial value to find the optimal regularization parameter with the minimum mean square error, and then solves the RFM parameters by the Tikhonov method with the optimal regularization parameter. We compared our method with the least-squares, L-curve, and GCV methods. The major innovation of the proposed method is optimizing RPC estimation using the L-curve.

The accuracy of RFM parameters solved using our proposed method is higher than that obtained with the general least-squares, L-curve, and GCV methods. In the terrain-dependent case, the accuracy of the parameters in the third-order RFM is highest out of the nine RFMs we tested when the denominators are not equal ($P_2 \neq P_4$). In the terrain-dependent case, when the number of GCPs exceeds 100, the accuracy of the RFM parameters is significantly improved. However, after that threshold, increasing numbers of GCP do not significantly increase the accuracy of the RFM parameters. The GCV and least-squares method will sometimes be invalid for solving RFM parameters. Moreover, the GCV method cannot solve ill-conditioned problems well due to deviation in determining the regularization parameter.

Table 7. Regularization parameters and rational function model parameters from different methods.

Method	Parameter (α)	Accuracy (pixels)	
		x (Column)	y (Row)
Least-squares	0	2.9482×10^7	2.1687×10^5
L-curve	1.3603×10^{-2}	4.8267×10^{-2}	3.8576×10^{-2}
Generalized cross-validation	3.1565×10^{-5}	5.6383×10^6	4.9432×10^5
Our method	2.0570×10^{-3}	7.8948×10^{-3}	5.8548×10^{-3}

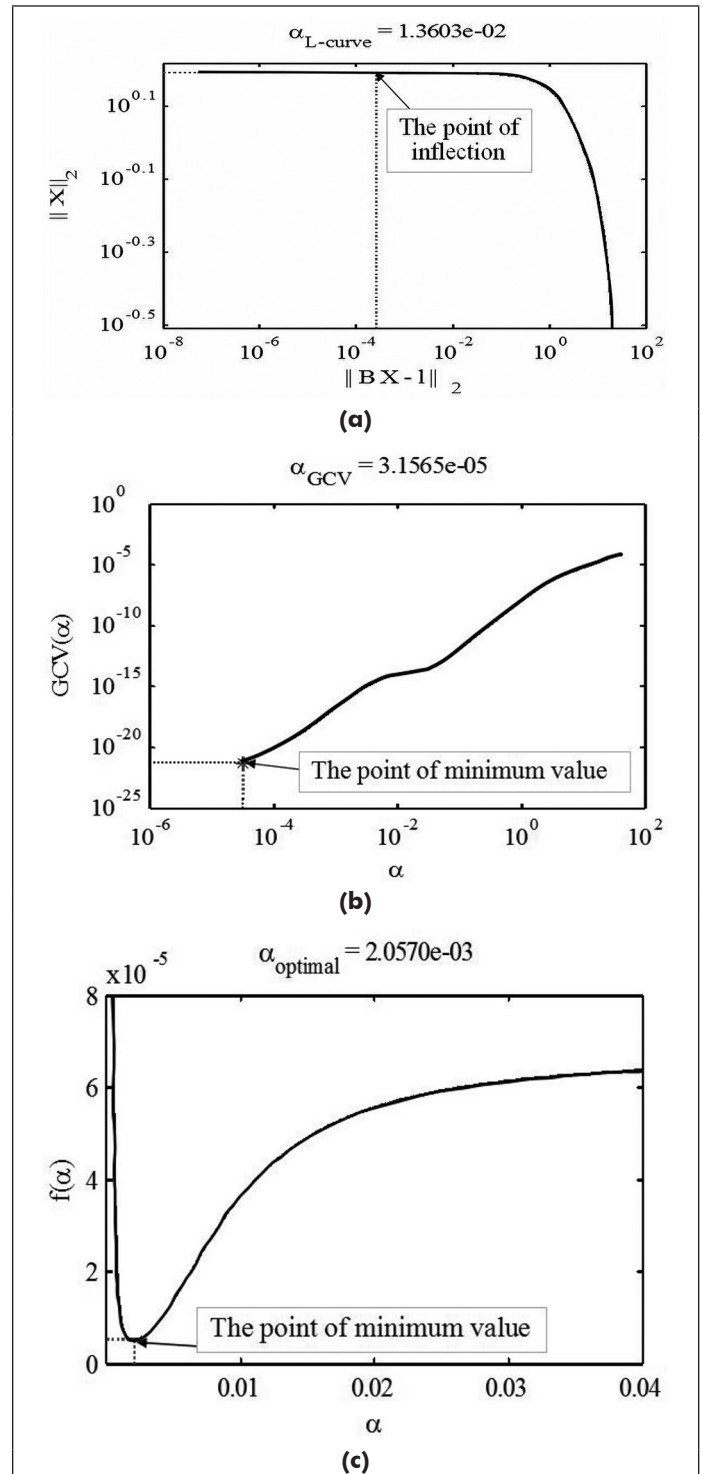


Figure 7. The regularization parameters of three methods: (a) L-curve, (b) generalized cross-validation, (c) proposed method.

Acknowledgments

This work was financially supported by the National Natural Science Foundation of China (grants 41961065 and 41431179), the Guangxi Science and Technology Base and Talent Project (grant Guike AD19254002), the Guangxi Innovative Development Grand Program (grants GuikeAA18118038 and GuikeAA18242048), the Guangxi Natural Science Foundation for Innovation Research Team (grant 2019GXNSFGA245001), the Guilin Research and Development Plan Program (grant 201902102), the National Key Research and Development Program of China (grant 2016YFB0502501), and the BaGuiScholars program of Guangxi.

References

- Cai, J. 2004. *Statistical Inference of the Eigenspace Components of a Symmetric Random Deformation Tensor*. Ph.D. dissertation, University of Stuttgart.
- Cai, J., E. Grafarend and B. Schaffrin. 2001. The λ -weighted BLE of the direct observations of a symmetric random tensor—Simulated case study: 2-dimensional strain. Pages PP–PP in *Geodetic Week*, Köln, held in Köln, Germany, 18–21 September 2001. Edited by J. Editor. Location: Publisher.
- Edwards, T. H. and S. Stoll. 2018. Optimal Tikhonov regularization for DEER spectroscopy. *Journal of Magnetic Resonance* 288:58–68.
- Fraser, C. S. and H. B. Hanley. 2005. Bias-compensated RPCs for sensor orientation of high-resolution satellite imagery. *Photogrammetric Engineering and Remote Sensing* 71(8):909–915.
- Golub, G. H., M. Heath and G. Wahba. 1979. Generalized cross-validation as a method for choosing a good ridge parameter. *Technometrics* 21(2):215–223.
- Grodecki, J. and G. Dial. 2003. Block adjustment of high-resolution satellite images described by rational polynomials. *Photogrammetric Engineering and Remote Sensing* 69(1):59–68.
- Hansen, P. C. 1992. Analysis of discrete ill-posed problems by means of the L-curve. *SIAM Review* 34(4):561–580.
- Hansen, P. C. and D. P. O’Leary. 1993. The use of the L-curve in the regularization of discrete ill-posed problems. *SIAM Journal on Scientific Computing* 14(6):1487–1503.
- Jabari, S. and Y. Zhang. 2016. RPC-based coregistration of VHR imagery for urban change detection. *Photogrammetric Engineering and Remote Sensing* 82(7):521–534.
- Li, C., X. Liu, Y. Zhang and Z. Zhang. 2017. A stepwise-then-orthogonal regression (STOR) with quality control for optimizing the RFM of high-resolution satellite imagery. *Photogrammetric Engineering and Remote Sensing* 83(9):611–620.
- Li, D., G. Zhang, W. Jiang and X. Yuan. 2006. SPOT-5 HRS satellite imagery block adjustment without GCPs or with single GCP. *Geomatics and Information Science of Wuhan University* 31(5):377–381.
- Liu, D., G. Zhou, J. Huang, R. Zhang, L. Shu, X. Zhou and C. S. Xin. 2019. On-board georeferencing using FPGA-based optimized second-order polynomial equation. *Remote Sensing* 11(124):124.
- Ma, Z., W. Song, J. Deng, J. Wang and C. Cui. 2018. A rational function model based geo-positioning method for satellite images without using ground control points. *Remote Sensing* 10(2):182.
- Moghaddam, S.H.A., M. Mokhtarzade, A. A. Naeini and A.R. Amiri-Simkooei. 2018. A statistical variable selection solution for RFM ill-posedness and overparameterization problems. *IEEE Transactions on Geoscience and Remote Sensing* 56(7):3990–4001.
- Neumaier, A. 1998. Solving ill-conditioned and singular linear systems: A tutorial on regularization. *SIAM Review* 40(3):636–666.
- Open GIS Consortium. 2004. *Some Image Geometry Models*. <http://portal.opengeospatial.org/files/?artifact_id=7257> Accessed 12 October 2010.
- Shen, X., Q. Li, G. Wu and J. Zhu. 2017. Bias compensation for rational polynomial coefficients of high-resolution satellite imagery by local polynomial modeling. *Remote Sensing* 9(3):200.
- Surmin, Y. V. 2018. Correction to: Decomposition and regularization of the solution of ill-conditioned inverse problems in processing of measurement information. Part 1. A theoretical evaluation of the method. *Measurement Techniques* 61(4):418.
- Tao, C. V. and Y. Hu. 2001a. A comprehensive study of the rational function model for photogrammetric processing. *Photogrammetric Engineering and Remote Sensing* 67(12):1347–1357.
- Tao, C. V. and Y. Hu. 2001b. Use of the rational function model for image rectification. *Canadian Journal of Remote Sensing* 27(6):593–602.
- Tong, X., S. Liu and Q. Weng. 2010. Bias-corrected rational polynomial coefficients for high accuracy geo-positioning of QuickBird stereo imagery. *ISPRS Journal of Photogrammetry and Remote Sensing* 65(2):218–226.
- Wang, T., G. Zhang, Y. Jiang, S. Wang, W. Huang and L. Li. 2016. Combined calibration method based on rational function model for the Chinese GF-1 wide-field-of-view imagery. *Photogrammetric Engineering and Remote Sensing* 82(4):291–298.
- Zhang, H., R. Pu and X. Liu. 2016. A new image processing procedure integrating PCI-RPC and ArcGIS-Spline tools to improve the orthorectification accuracy of high-resolution satellite imagery. *Remote Sensing* 8(10):827.
- Zhang, L., X. He, T. Balz, X. Wei and M. Liao. 2011. Rational function modeling for spaceborne SAR datasets. *ISPRS Journal of Photogrammetry and Remote Sensing* 66(1):133–145.
- Zhang, R., G. Zhou, G. Zhang, X. Zhou and J. Huang. 2018. RPC-based orthorectification for satellite images using FPGA. *Sensors* 18(8):2511.
- Zhou, G. 2020. *Urban High-Resolution Remote Sensing: Algorithms and Modeling*. Boca Raton, Fla.: CRC Press.
- Zhou, G., X. Bao, S. Ye, H. Wang and H. Yan. 2021. Selection of optimal building facade texture images from UAV-based multiple oblique image flows. *IEEE Transactions on Geoscience and Remote Sensing* 59(2):1534–1552.
- Zhou, G., Y. Wang, Y. Tao, S. Ye and W. Wang. 2017. Building occlusion detection from ghost images. *IEEE Transactions on Geoscience and Remote Sensing* 55(2):1074–1084.
- Zhou, G., T. Yue, Y. Shi, R. Zhang and J. Huang. 2016. Second-order polynomial equation-based block adjustment for orthorectification of DISP imagery. *Remote Sensing* 8(8):680.

Scene-Change Detection Based on Multi-Feature-Fusion Latent Dirichlet Allocation Model for High-Spatial-Resolution Remote Sensing Imagery

Xiaoman Li, Yanfei Zhong, Yu Su, and Richen Ye

Abstract

With the continuous development of high-spatial-resolution ground observation technology, it is now becoming possible to obtain more and more high-resolution images, which provide us with the possibility to understand remote sensing images at the semantic level. Compared with traditional pixel- and object-oriented methods of change detection, scene-change detection can provide us with land use change information at the semantic level, and can thus provide reliable information for urban land use change detection, urban planning, and government management. Most of the current scene-change detection methods are based on the visual-words expression of the bag-of-visual-words model and the single-feature-based latent Dirichlet allocation model. In this article, a scene-change detection method for high-spatial-resolution imagery is proposed based on a multi-feature-fusion latent Dirichlet allocation model. This method combines the spectral, textural, and spatial features of the high-spatial-resolution images, and the final scene expression is realized through the topic features extracted from the more abstract latent Dirichlet allocation model. Post-classification comparison is then used to detect changes in the scene images at different times. A series of experiments demonstrates that, compared with the traditional bag-of-words and topic models, the proposed method can obtain superior scene-change detection results.

Introduction

Scene understanding of remote sensing images refers to the acquisition of the complex semantic information of important scene areas in the images (Q. Zhu *et al.* 2016; Ni and Wu 2020). Compared with pixel- and object-oriented image expression, scene understanding can make up for the problem of the semantic gap between low-level features and high-level semantic information of remote sensing images (Pang *et al.* 2019), allowing us to further abstract the image information. Meanwhile, along with the continuous development of high-spatial-resolution (HSR) technology, it is now becoming possible to obtain more and more HSR images, which enables

us to interpret image scenes through the spatial-arrangement information and the structural characteristics of the different objects, which can be clearly seen in the high-resolution images (Ni and Wu 2020).

Scene classification is an important task in scene understanding. At first, most scene-classification methods mainly focused on the use of low-level features, such as color, texture, and shape, to build the scene-classification model, and then used a classifier to derive high-level information. Although this low-level feature-based approach does not require any external knowledge, its lack of mid-level semantic representation means that it has poor generalization capabilities. To overcome the semantic gap between low-level visual features and high-level semantics, methods of modeling scene semantics based on the mid-level features have attracted widespread attention, in both semantic objective-based expression and semantic visual-words-based expression. The semantic objective-based description method needs to effectively recognize the various targets in the scene. When the recognition accuracy is insufficient, the subsequent classification accuracy will be reduced. As a result, generalized mid-level representation methods, which directly learn scene content from the images, have been the subject of more attention. The bag-of-visual-words (BOVW) model (Sivic and Zisserman 2003) is one representative method. It evolved from the bag-of-words (BOW) model, which was first applied in the field of text analysis. It first extracts the low-level manual features of the image, which are called visual words, and learns bases from them through dictionary learning (Zhong *et al.* 2017). Then, based on mid-level feature coding, the low-level features of the region are mapped to the dictionary. Finally, the spatial-layout statistics are obtained through pooling or another method to obtain the final mid-level feature expression. The BOVW model can achieve better recognition in scene understanding, but it faces the problem of high-dimensional expression of the mid-level features of the scene, which reduces the storage efficiency and transmission efficiency of the scene expression. Therefore, semantic attribute-based topic models, such as probabilistic latent semantic analysis (PLSA; Hofmann 2001) and latent Dirichlet allocation (LDA; Blei *et al.* 2003), have been proposed to further abstract the visual words.

The topic model learns a few topics from the mid-level features that express the scene through probability and statistics

Xiaoman Li, Yu Su, and Richen Ye are with the State Key Laboratory of Information Engineering in Surveying, Mapping, and Remote Sensing, Wuhan University, Wuhan, China.

Yanfei Zhong (corresponding author) is with the State Key Laboratory of Information Engineering in Surveying, Mapping, and Remote Sensing, Wuhan University, Wuhan, China; and Hubei Provincial Engineering Research Center of Natural Resources Remote Sensing Monitoring, Wuhan University, Wuhan, China (zhongyanfei@whu.edu.cn).

Contributed by Zhenfeng Shao, June 8, 2020 (sent for review November 16, 2020; reviewed by Peng Fu, Kaimin Sun).

Photogrammetric Engineering & Remote Sensing
Vol. 87, No. 9, September 2021, pp. 669–681.
0099-1112/21/669–681

© 2021 American Society for Photogrammetry
and Remote Sensing
doi: 10.14358/PERS.20-00054

theory, and at the same time obtains the distribution of the scene on the topic as the topic features of the scene to achieve scene modeling (V duva *et al.* 2013). Since the number of topics acquired based on the probabilistic topic model is small, the topic feature dimension describing the scene is also relatively small, which has the effect of reducing the dimension of the scene-expression features compared to the BOVW model. However, the existing designs of both BOVW and topic models are based on single-feature extraction, and in some complex scene-classification tasks, the expressive ability of topic models based on a single feature is still limited. In recent years, scene classification based on deep feature extraction by deep learning has also made great progress. Convolutional neural networks (Li *et al.* 2017; Cheng *et al.* 2018; H. Sun *et al.* 2020), AlexNet (J. Sun *et al.* 2016), ResNet (Liu *et al.* 2019), and other deep-learning frameworks have been widely used in scene-classification studies. However, for specific scene-classification problems in certain areas, we need to perform new sample labeling for the model training. At the current time, the large amount of sample data necessary for deep learning is beyond our reach.

Compared to interpreting a single image scene, the implementation of scene-change detection between scene images acquired at different times can allow us to ascertain the land use change in a certain area over a certain period of time, thereby providing effective support for land planning (Bulatov *et al.* 2019; Wan *et al.* 2019) and government management (Du *et al.* 2018). In urban research, urban change detection is a significant supporting technology for sustainable urban development (Shao *et al.* 2020). To date, most of the research and algorithms for change detection have mainly focused on pixel-based and object-oriented change-detection methods (J. Zhu *et al.* 2017), such as principal component analysis (Atasever *et al.* 2016), change vector analysis (Polykretis *et al.* 2020), multivariate alteration detection (Nielsen 2007), and Markov random-field-based methods (Lu *et al.* 2019). However, studies of scene-change detection are relatively rare, and most of the existing works in multi-class scene-change detection are based on mid-level scene-classification results, which leads to many challenges due to the complexity of the scenes. First of all, scenes are often diverse, particularly for HSR remote sensing images. Due to the increase in image spatial resolution, the complexity and changeability of the landscape become more obvious. The same scenes may have different feature-distribution patterns, and different scenes may also have certain similarities in their internal structure (L. Li *et al.* 2012), which can bring much confusion to the scene classification. Second, it should be stressed that these mid-level models are designed for use with a single type of feature. The expression of the scene is more complicated than in traditional pixel- and object-oriented expressions (Li *et al.* 2017), and the existing feature-extraction methods often cannot fully mine the underlying semantic information of the scenes. These factors all bring great difficulties to the development of scene classification and scene-change detection methods for HSR imagery.

Wu *et al.* (2016) proposed the first framework for scene-change detection, based on the BOVW model. In this method, the original pixel information and the spectral features are extracted for simple overlying fusion, and the BOW model is applied to classify the multi-temporal image scenes. Post-classification is then used to obtain the final scene-change detection results. In follow-up work (Wu *et al.* 2017), because of the lack of temporal correlation in the BOVW scene-change detection framework, the authors took into account the temporal correlation between images in different phases and introduced the idea of kernel slow feature analysis. Then, to make up for the shortcomings of high-dimensional scene expression and the need for prior knowledge in these BOVW-based methods, Du *et al.* (2018) proposed an unsupervised framework for scene-change detection based on the LDA topic

model and multi-variate alteration detection. Most of the existing methods are focused on the high-dimensional BOVW model or the topic model based a strategy of single-feature extraction, and they are unable to fully and effectively take different feature information into consideration. It is therefore logical that a combination of multiple complementary features for the LDA model should be able to make up for the multi-feature research gap and improve the performance of scene classification (Zhao *et al.* 2016a), as well as the subsequent scene-change detection task.

In the proposed approach, the multi-feature-fusion latent Dirichlet allocation (MFLDA) model is used to fuse multiple image features and extract the topic features of every single scene image to complete the scene expression. On this basis, post-classification change detection between the multi-temporal HSR remote sensing images is implemented to obtain the final “from-to” change information. The contributions of this article can be summarized as follows:

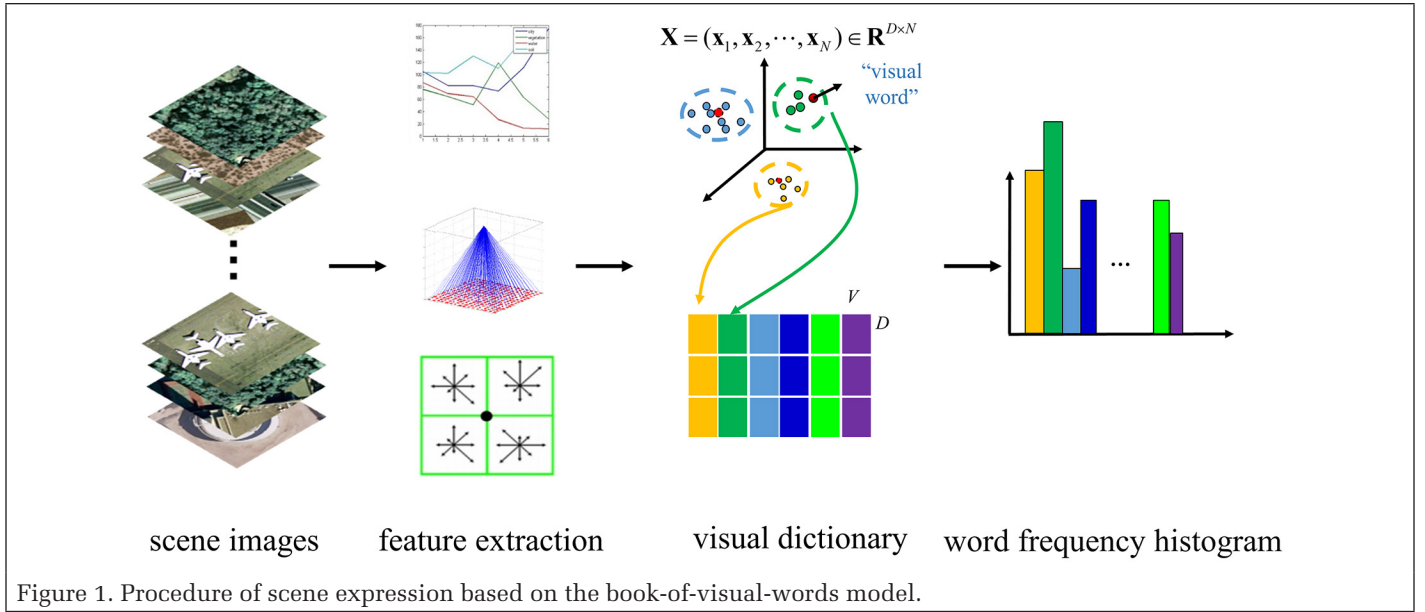
- A scene-change detection framework based on MFLDA is proposed. The proposed framework separately extracts spectral, texture, and structural features of the scene images. Based on the LDA model, the topic feature expression of these features is implemented in the topic space, and then the scene-classification results are obtained based on the topic features. Post-classification is then applied to complete the scene-change detection task and obtain the final change information.
- The MFLDA model first relies on the expression of the BOW model to represent the extracted multiple features of the scene image as multiple 1D histograms. Compared with the expression method of directly using visual words, MFLDA effectively reduces the feature dimensions of the final image expression, to obtain superior scene-classification results. At the same time, it does not need to use a large volume of sample data, as in deep-learning training, and only a small number of samples is required to solve the model parameters, complete the model training process, and perform the classification task.
- The MFLDA model fuses different kinds of features by generating topic spaces for features with different distributions, and then maps the underlying features into the topic space, which has probabilistic significance. Compared with the previous feature-fusion approach of directly superimposing feature vectors, MFLDA is less affected by different feature distributions when fusing multiple local and global features. Thus, the multi-feature-fusion strategy can obtain more useful information in complex urban-scene applications.

The rest of this article is organized as follows. The next section presents the basic methodologies applied in this work. After that, the MFLDA model and the scene-change detection method based on it are described in detail. The following section describes the data sets and data settings used in the experiments, followed by the final change-detection results and an analysis of the sensitivity of the model parameters. Finally, we give our conclusions and the future outlook for scene-change detection.

Related Methodology

BOVW-Based Scene Expression

The BOW model was proposed by Sivic (Sivic and Zisserman 2003) in the field of text analysis. It assumes that the word order, grammar, syntax, and other factors of a document are ignored, with the document treated instead as just a collection of words. In recent years, some scholars have been influenced by the idea of expressing documents using word frequency and have applied the BOW model to the processing of remote sensing images (Cheng *et al.* 2013), aiming to



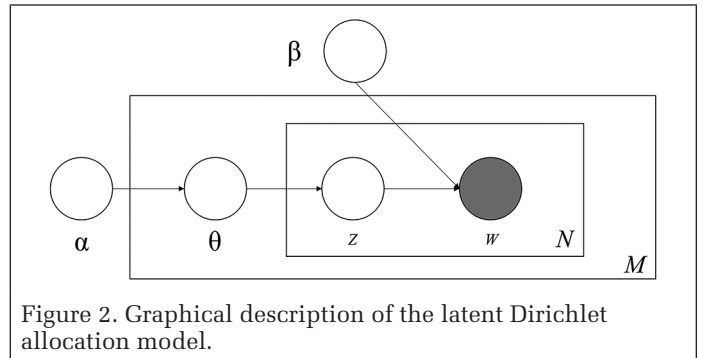
use the statistical frequency of the visual words as the image characteristics to represent the scene information.

The technological process of scene expression based on the BOVW model is shown in Figure 1. BOVW expression of scene images first requires feature extraction, which plays a crucial part in the model expression (Lu *et al.* 2019). The scene image block obtained by a sampling method such as uniform grid sampling or random sampling on the original scene image is used to achieve low-level expression of the scene through a feature-extraction method. Common means of feature extraction are the gray-level co-occurrence matrix (GLCM; Zheng *et al.* 2018), the scale-invariant feature transform (SIFT; Sedaghat and Ebadi 2015), and the statistical method based on mean and standard deviation (MeanStd; Lienou *et al.* 2010). GLCM realizes the texture feature analysis through calculating the spatial correlation between the gray levels of two pixels at a certain distance and direction from each other. SIFT is a local feature descriptor that extracts the structural features by detecting key points in the image. MeanStd is a method of extracting spectral features by calculating the mean and standard deviation of the spectral values of each band.

Dictionary learning is then applied according to the low-level scene feature information obtained from the feature extraction to build the visual dictionary. In the proposed method, the selected training images are used to build the visual dictionary by a clustering method such as k-means clustering (Zhao *et al.* 2016b). In the feature-coding step, every single scene image patch is encoded with the corresponding visual words based on the final visual dictionary generated by dictionary learning. Finally, all of the scene images are expressed as frequency histograms that show the frequencies of the visual words.

The Latent Dirichlet Allocation (LDA) Model

Although the scene-classification methods based on mid-level feature coding can achieve good recognition in scene understanding, they often face the problem that the mid-level feature dimension of the scene expression is too high. The scene-understanding methods based on the probabilistic topic model can learn a few topics from high-dimensional mid-level features through probability statistics theory, and describe the scene with lower-dimensional topic features (Zang *et al.* 2015), thereby making up for the shortcomings of the high feature dimensions brought by mid-level feature-coding methods.



Commonly used probabilistic topic models include PLSA and LDA. LDA was developed on the basis of PLSA, but its scalability is greatly enhanced due to its complete probability statistics framework (Blei 2012). In the process of semantic mining via LDA, it is assumed that there is no order problem between the text words or image visual vocabulary—i.e., the semantic mining is considered to have nothing to do with the word order or visual vocabulary. Meanwhile, it is also assumed that the number of potential topics in the text is fixed, and that the topics are independent of each other.

LDA is a kind of generative probabilistic topic model. It is assumed that the scene image set is $D = \{d_i\}_{i=1}^N$ and each image consists of a sequence of M words $w_i = (w_{i,1}, w_{i,2}, \dots, w_{i,M})$. As shown in the probability model in Figure 2, θ is the topic distribution of a certain image, α corresponds to the discrete probability value of the topic, z is the topic assignment of the corresponding image, w refers to the observed words, and the hyperparameter β is the probability distribution of words about a topic. Based on this probability graph representation, the generative process of LDA can be expressed as follows:

1. Select the θ of the probability distribution of the subject in the image from the Dirichlet prior distribution.
2. For any $w_i = (w_{i,1}, w_{i,2}, \dots, w_{i,M})$:
 - a. Select $z_{i,j}$ that follows the polynomial distribution $z_{i,j} \sim \text{Multinomial}(\theta)$.
 - b. Select $w_{i,j}$ that follows the conditional probability distribution $p(w_{i,j} | z_{i,j}, \beta)$.

Then the likelihood function of the scene image can be written as

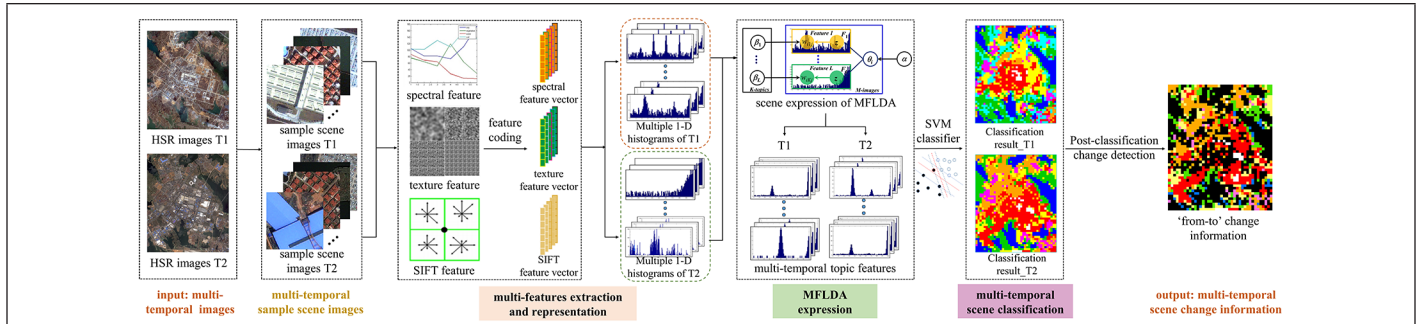


Figure 3. Flowchart of scene-change detection based on multi-feature-fusion latent Dirichlet allocation.

$$p(w_i | \alpha, \beta) = \int p(\theta_i | \alpha) \left(\prod_{j=1}^N \sum_{z_{i,j}} p(z_{i,j} | \theta_i) p(w_{i,j} | z_{i,j}, \beta) \right) d\theta_i \quad (1)$$

From this analysis, it can be seen that the core problem of the LDA model is calculating the posterior distribution probability of the hidden variables θ and z in a specific image with the given hyperparameters. However, due to the coupling of θ and β on the topic, an accurate calculation cannot be performed. In the actual solution process, the variational algorithm and Markov approximations are often used.

LDA has been extensively used in the extraction and interpretation of remote sensing image information. For example, Bratasanu *et al.* (2011) used it to perform semantic mining of feature combinations to achieve semantic analysis; Lienou *et al.* (2010) used it in text semantic mining and applied it to the scene classification and semantic annotation of HSR remote sensing imagery; and Bahmanyar *et al.* (2018) used it with multi-sensor data fusion to complete land cover classification.

The MFLDA-Based Scene-Change Detection Model

When fusing multiple sets of visual words with different types of features, the existing LDA model based on single-feature classification generates only one set of potential topic variables, and uses the same type of probability distribution to model all the visual word sets, which affects its ability to fuse visual words with multiple features. In the proposed MFLDA model, in order to overcome this shortcoming, different potential topic spaces are generated for the different types of features through the same Dirichlet prior, and each scene is represented by the different probability distributions of the potential topic variables—i.e., the topic features. In the fusion process, the weights of the different topic features of each scene are optimized by maximizing the likelihood function of the scene, and multiple types of features are thus effectively fused by fusing the topic features. In addition, since the topic features complete the further description of the visual-word distribution, MFLDA has the ability to reduce the dimension of the feature vector used for HSR scene representation (Zhao *et al.* 2016a; Zhong *et al.* 2018).

The overall flowchart of the MFLDA-based scene-change detection model for HSR remote sensing imagery is displayed in Figure 3. There are three main parts in the process: multi-feature extraction and representation, MFLDA expression and scene classification, and post-classification comparison for change detection.

Thus, the specific process of multi-temporal scene image processing based on the MFLDA model can be summarized as follows:

1. Multi-feature extraction and representation. The spectral, structural, and textural features of the scene images are extracted. The multiple features are then expressed as 1D histograms.

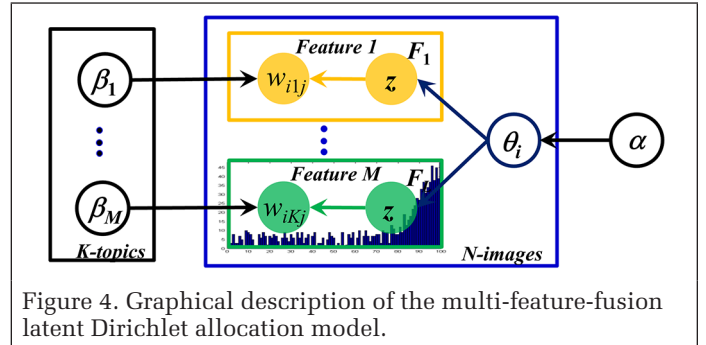


Figure 4. Graphical description of the multi-feature-fusion latent Dirichlet allocation model.

2. Training process. Some of the original images are selected as the training images, and then the multi-feature histogram expressions of all the training images are used for training the MFLDA model. The hyperparameter β of the MFLDA model and the topic feature expressions of each training image are acquired. These topic features are then used for training the support vector machine (SVM) classifier. To obtain a better result, we run each case 10 times and compute the statistical averages. The connection is thus built among the scene's multi-feature histograms, topic features, and scene categories.
3. Classification test process. For a multi-feature histogram of a new test scene image, the hyperparameter β is used to extract its topic features, which are finally used as the input of the trained SVM classifier to determine the scene labels of the test images.
4. Post-classification scene-change detection. For multi-temporal scene images of a specific research area, the MFLDA model is used to complete the multi-feature expression of the scene images, and then the post-classification change-detection method is applied to obtain the multi-temporal scene-change information.

MFLDA Model Construction and Derivation

The indices that need to be used in the interpretation of the MFLDA model should be first stated. Each scene image is represented by the letter s , and the number of images is represented by i . The visual words are represented by letter w , the final cluster types of visual words are represented by v , and the total number of visual words is represented by V . The type of feature is represented by m , and the total number of features used is denoted by M . The topic is denoted by k , and thus for the m -th feature, the topic number can be denoted as K_m and the visual-word number as V_m . The number of visual words corresponding to the m -th feature in the i -th image is represented by $F_{i,m}$. It is assumed that the scene image set with N images is $S = \{s_i\}_{i=1}^N$. Then for the m -th feature, the visual words of the i -th scene image s_i can be denoted as $w_{i,m} = \{w_{i,m,1}, w_{i,m,2}, \dots, w_{i,m,F_{i,m}}\}$, $w_{i,m,j} \in C = \{1, 2, \dots, V\}$.

To model the multiple features of the scene, the proposed MFLDA model uses the same Dirichlet prior distribution to generate a topic space for each feature in the scene, and maps each feature into the relevant topic space. A graphical description of MFLDA is shown in Figure 4, where α and β are the hyperparameters of the model, θ and z are the hidden variables, and w is the visual words of the scene images. As a probability generation model, the generative process is as follows:

For any scene image S_i :

1. Select the θ_i for each feature from the Dirichlet prior distribution.
2. For any $w_{i,m,j}$ of the images:
 - a. Extract a topic from the polynomial distribution $\text{Multi}(\theta_i)$.
 - b. Extract $w_{i,m,j}$ to obey the conditional probability distribution $p(w_{i,m,j} | z_{i,m,j}, \beta)$, where β records the probability of each topic generating $w_{i,m,j}$.

In MFLDA, $w_{i,m,j}$ is the observed variable and $\{\theta_i\}$ and $\{z_{i,m,j}\}$ are the implicit variables. Therefore, the likelihood function of MFLDA is expressed as

$$p(w_i | \alpha, \beta) = \int p(\theta_i | \alpha) \left(\prod_{m=1}^M \prod_{j=1}^{F_{i,m}} \sum_{z_{i,m,j}} p(z_{i,m,j} | \theta_i) p(w_{i,m,j} | z_{i,m,j}, \beta) \right) d\theta_i \quad (2)$$

As in the LDA model, the likelihood function of MFLDA cannot be accurately evaluated because of the coupling of the hidden variables θ and z . To this end, the variational expectation-maximization algorithm (Figure 5) is used for the calculation and parameter estimation. By introducing the variation parameters γ and φ to cut off the relationship between the hidden variables θ and z , an approximate calculation of the likelihood function of the MFLDA model can be realized.

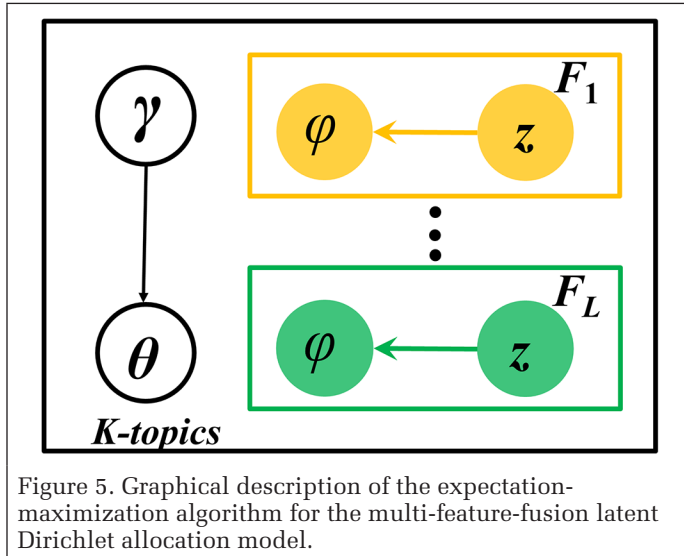


Figure 5. Graphical description of the expectation-maximization algorithm for the multi-feature-fusion latent Dirichlet allocation model.

For each scene image S_i , the variational distribution can be written as

$$q(\theta_i, z_i | \gamma_i, \varphi_i) = q(\theta_i | \gamma_i) \prod_{m=1}^M \prod_{j=1}^{F_{i,m}} q(z_{i,m,j} | \varphi_i) \quad (3)$$

Using Jensen's inequality to modify the likelihood function, the lower bound of the MFLDA likelihood function can be obtained as

$$\begin{aligned} \log p(w_i | \alpha, \beta) &= \log \int \sum_{\theta, z} p(\theta, z, w_i | \alpha, \beta) d\theta \\ &= \log \int \sum_{\theta, z} \frac{p(\theta, z, w_i | \alpha, \beta)}{q(\theta, z)} q(\theta, z) d\theta \\ &= \log \int \sum_{\theta, z} \frac{p(\theta, z, w_i | \alpha, \beta)}{q(\theta, z)} q(\theta, z) d\theta \geq \int \sum_{\theta, z} q(\theta, z | \gamma, \varphi) \log p(\theta, z, w_i | \alpha, \beta) d\theta - \int \sum_{\theta, z} q(\theta, z | \gamma, \varphi) \log q(\theta, z | \gamma, \varphi) d\theta \\ &= E_{\gamma} [\log p(\theta, z, w_i | \alpha, \beta)] - E_{\gamma} [\log q(\theta, z | \gamma, \varphi)] \end{aligned} \quad (4)$$

According to this above representation, we can verify that the difference between the left and right sides of the inequality is the Kullback–Leibler divergence between the variational distribution and the true posterior distribution. Expressing the right side of the inequality as $L(\gamma, \varphi, \alpha, \beta)$, we can obtain

$$\log p(w_i | \alpha, \beta) = L(\gamma, \varphi, \alpha, \beta) + D(q(\theta, z | \gamma, \varphi) \| q(\theta, z | w_i, \alpha, \beta)) \quad (5)$$

The variational expectation-maximization method is then used to maximize the lower bound of the variational distribution function on the variational parameters φ and γ . In step E, the parameters $\varphi_{i,m,v,k}$ and $\gamma_{i,m,k}$ are separated. The restriction of $\sum_{k=1}^{K_m} \varphi_{i,m,v,k} = 1$ is then added to find the optimal variational free parameters:

$$\varphi_{i,m,v,k} \propto \beta_{m,v,k} \exp \left(\Psi(\gamma_{i,m,k}) - \Psi \left(\sum_{m=1}^M \sum_{k=1}^{K_m} \gamma_{i,m,k} \right) \right) \quad (6)$$

$$\gamma_{i,m,k} = \alpha_{m,k} + \sum_{v=1}^{V_m} n_{i,v} \phi_{i,m,v,k} \quad (7)$$

Through maximization of the lower bound of the log likelihood with respect to $\gamma_{i,m,k}$, the update function of the variational Dirichlet variable $\gamma_{i,m,k}$ can be obtained. Thus, each image can acquire a group of $\gamma_{i,m,k}$, which are finally regarded as the topic features for the scene classification.

In step M, the two variational parameters are fixed and the lower bounds of the model parameters α and β are maximized. The parameter $\beta_{k,v}$ is then separated from $L(\gamma, \varphi, \alpha, \beta)$, and the following formula obtained:

$$\beta_{m,v,k} \propto \sum_{i=1}^N \sum_{m=1}^M \sum_{v=1}^{V_m} n_{i,m,v} \phi_{i,m,v,k} \quad (8)$$

$$\sum_{v=1}^{V_m} \beta_{m,v,k} = 1 \quad (9)$$

When the total likelihood function of all the scene images reaches the maximum value, the estimated values of the LDA model parameters are obtained—i.e., the model parameter β and the topic features $\gamma_{i,m,k}$ of each image. The topic features are then inputted into the SVM classifier to obtain the final scene categories. For multi-temporal scene images, the topic-feature expression is performed through the MFLDA model, and then the final classification results for the multi-temporal scene images are acquired.

Multi-Feature Extraction and Representation

The understanding of HSR remote sensing imagery based on the MFLDA model first requires us to express the multiple features—i.e., texture feature extraction based on GLCM (Zheng *et al.* 2018), structural feature extraction based on the SIFT operator (Sedaghat and Ebadi 2015), and spectral feature extraction based on MeanStd (Lienou *et al.* 2010)—in the form of multiple 1D histograms. When the features are locally continuous, such as spectral features and structural features, they can be clustered by a clustering method (such as k-means), and the 1D histogram expression of the scene image can be obtained by counting the frequency of each cluster category in the scene image. When the feature is globally discrete, such as

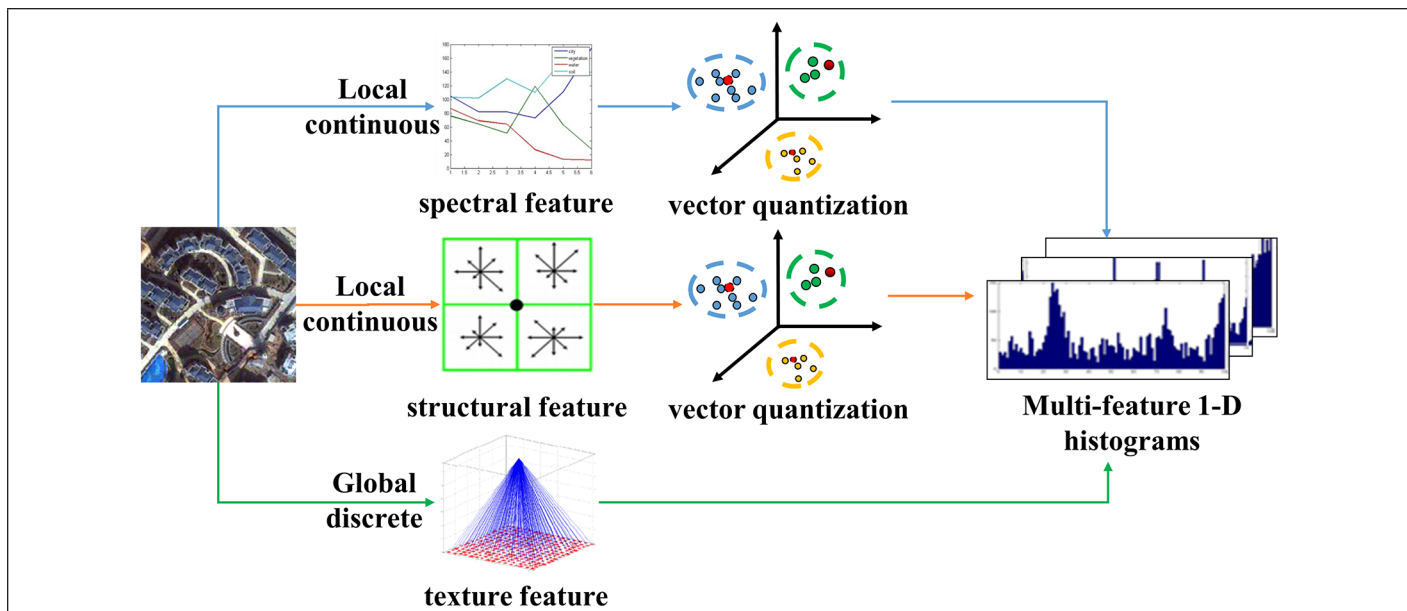


Figure 6. Multi-feature 1D histogram expression of scene images.

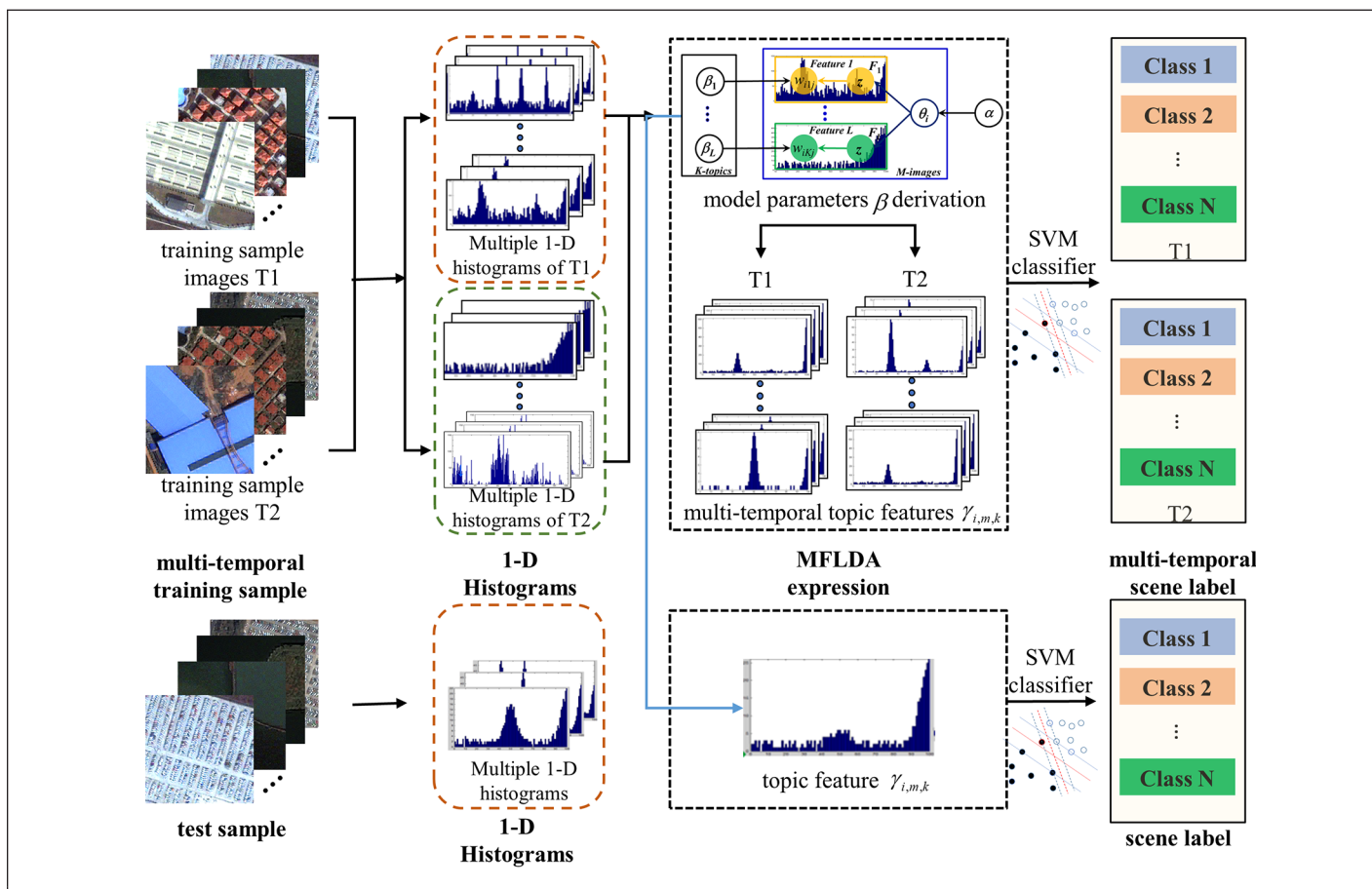


Figure 7. Multi-feature fusion and scene classification with the multi-feature-fusion latent Dirichlet allocation model.

the texture feature, it can be directly expressed as a 1D histogram of the scene image (Figure 6).

Through counting of the visual words with the same value, the visual words of each type of feature can be transformed into a 1D histogram $f_{i,m} = (f_{i,m,1}, f_{i,m,2}, \dots, f_{i,m,V})$, $\sum_{v=1}^V f_{i,m,v} = F_{i,m}$,

where V is the dimension of the 1D histogram as well as the number of the visual words, and $f_{i,m,v}$ represents the frequency corresponding to the v -th type of visual word in the histogram.

Multi-feature Fusion and Scene Classification

After the multi-feature extraction and representation, all the types of features are represented as multiple 1D histograms, which are then used to estimate the model parameters of the MFLDA model. Different potential topic spaces are generated

for the different types of features through the same Dirichlet prior. The topic features $\gamma_{i,m,k}$ with different probability distributions are used to finally represent the scene image, and are inputted to the classifier, such as SVM (Chang and Lin 2011). In the fusion process, the weights of the different topic features of each scene are optimized by maximizing the likelihood function of the scene, and multiple types of features are thus effectively fused by fusing the topic features. The MFLDA-based scene-classification method (Figure 7) is as follows:

1. The training and test images are represented by multiple 1D histograms corresponding to the multiple types of features.
2. The collection of multiple 1D histograms of the training images is used to train the model to obtain the model parameter β and topic features $\gamma_{i,m,k}$. The training of the specific classifier (such as SVM) is then completed based on the topic features.
3. In the test process, using the trained MFLDA model, multiple 1D histograms of the test image are used to infer the topic features $\gamma_{i,m,k}$ of the test image. Finally, the trained classifier is applied to classify the topic features obtained from the test images to obtain the corresponding scene-classification labels.

Post-classification Scene Change Detection

After the final multi-temporal scene-classification results are obtained through the multi-feature-fusion LDA model, post-classification comparison is used to complete the scene-change detection. Based on the classification results, post-classification comparison is performed to obtain the “from-to” change information of the scenes from different time periods and to obtain the land use change of the study area at the semantic level during the study period.

Experimental Settings

Data-Set Description

In order to evaluate the performance of the proposed MFLDA-based scene-change detection method, we performed relevant experiments. The first data set was the MtS-WH data set (Figure 8) built by Wu *et al.* (2016), which was mainly used for verification of the scene-change detection. It is made up of two HSR images covering the Hanyang District of Wuhan, Hubei province, China, from February 2002 and June 2009. It was obtained by the Ikonos sensor, with a spatial resolution of 1 m. The image size is 7200×6000. The large original images were divided using a 150×150 uniform grid, generating 1920 small scene images in each phase. In total, 55.52% and 74.01% of these small scene images were labeled as the ground-truth maps for 2002 and 2009, respectively. There

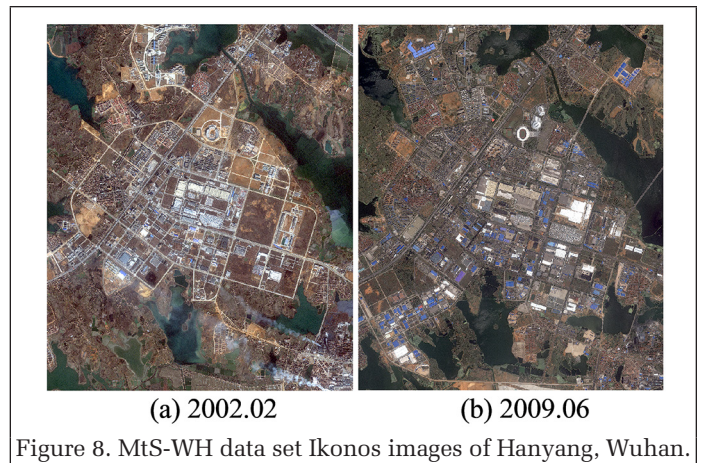
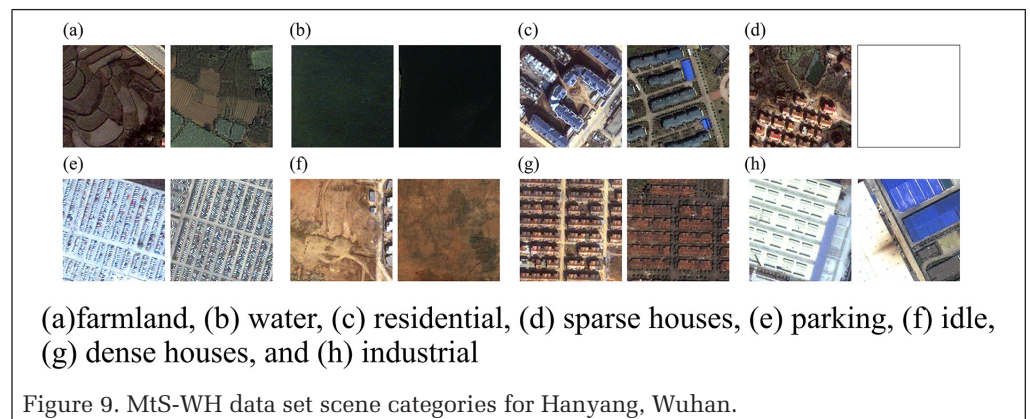


Figure 8. MtS-WH data set Ikonos images of Hanyang, Wuhan.



(a)farmland, (b) water, (c) residential, (d) sparse houses, (e) parking, (f) idle, (g) dense houses, and (h) industrial

Figure 9. MtS-WH data set scene categories for Hanyang, Wuhan.

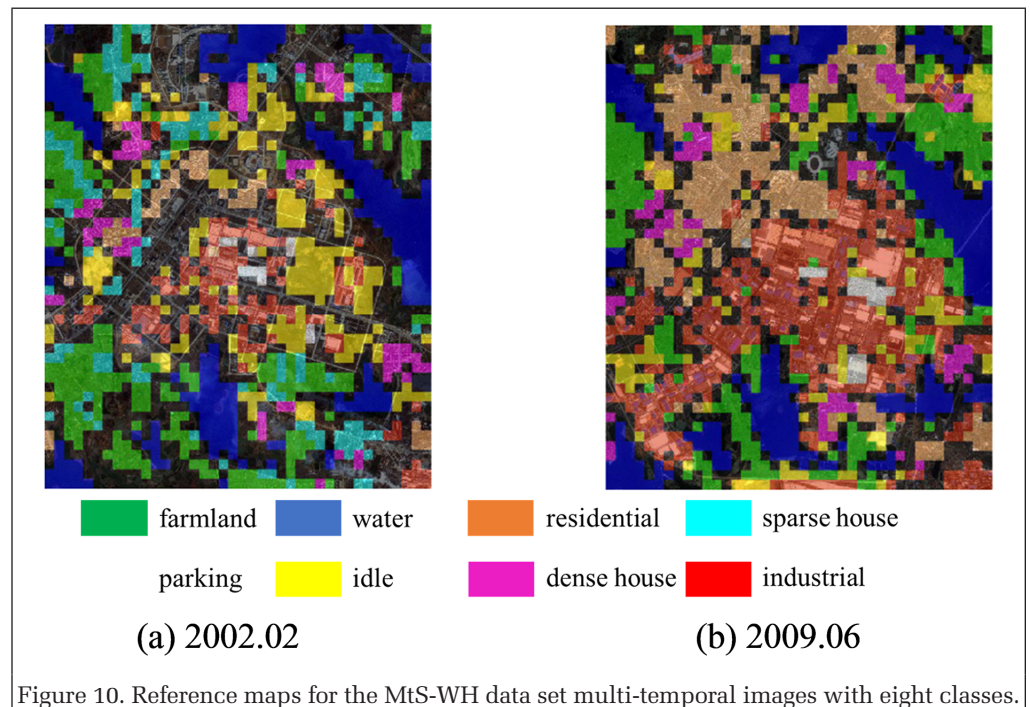


Figure 10. Reference maps for the MtS-WH data set multi-temporal images with eight classes.

are eight scene categories in the study area: farmland, water, residential, sparse houses, parking, idle, dense houses, and industrial (Figure 9). What needs to be mentioned is that there is no scene category of sparse houses in the image from 2009, so this is indicated by blank space. (For reference maps of the MtS-WH data-set images, see Figure 10.)

The second data set, which we refer to as the Google Earth Wuhan center data set, was made up of two HSR images

covering the city-center area of Wuhan, Hubei province, China, from June 2010 and June 2018, which were collected from Google Earth (Figure 11). The image size is 15 000×12 000, with a spatial resolution of 0.5 m. In this data set, a 300×300 uniform grid was again applied to divide the large annotated images, generating 2000 small scene images in each phase. In total, 53.7% and 48.05% of these small scene images were labeled as the ground-truth maps for 2010 and 2018, respectively. Twelve scene categories were selected in this study area: bare land, commercial, dense residential, harbor, industrial, medium residential, green land, parking lot, sports, school, sparse residential, and water (Figure 12).

Experimental Settings

In the experiments, for each data set, 80% of the labeled scene images of each phase were randomly selected as training images, and the remaining images were used as the test images. In the feature-extraction stage, the patch size was set to 8×8, keeping an overlap of four pixels. For the continuous MeanStd spectral feature and SIFT structural feature, the k-means method was used for clustering, and the cluster center (the visual dictionary size) was set to 1000. Since the dictionary was learned by randomly selected patches, we ran each case 10 times and computed the statistical averages.

In addition, a series of comparative experiments were set up, including single-feature-based BOVW, PLSA, LDA, and the different fusion strategy of MFLDA. BOVW is the main basis of the multi-level scene expression. PLSA uses the BOW expression to mine the potential semantics of the scene. On the basis of PLSA, LDA develops a complete probability generation model. During the experiments, we also changed the number of topics in the topic model, varying from 50 to 240, to output the scene-classification results. For PLSA, LDA, and MFLDA,

the kernel of the SVM classifier utilized a histogram intersection kernel because of its simplicity and good performance in image classification. The penalty parameter of the SVM was optimally set to 300.

Experimental Results and Analysis

Experiment 1: The MtS-WH Data Set

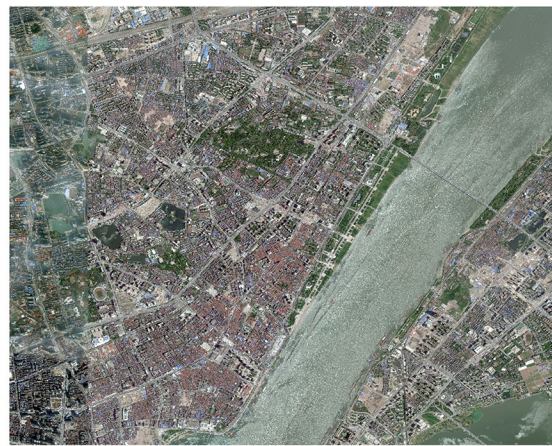
Table 1. Quantitative evaluation of the classification and change-detection results for the MtS-WH data set.

Method	2002		2009		Change Map	
	OA (%)	kappa (%)	OA (%)	kappa (%)	OA (%)	κ (%)
Wu <i>et al.</i> (2016)	85.65	—	84.03	—	76.43	—
BOVW_mstd	85.46	81.96	83.07	80.78	73.97	65.06
BOVW_sift	77.68	72.54	79.49	74.43	70.37	62.92
BOVW_siti	79.98	75.30	78.05	73.02	72.27	64.68
PLSA_mstd	71.54	64.92	80.86	76.26	63.44	55.06
PLSA_sift	75.79	70.23	70.68	64.06	65.97	54.47
PLSA_siti	61.33	50.73	64.80	53.65	51.44	41.00
LDA_mstd	83.37	79.44	88.45	85.43	76.39	67.33
LDA_sift	74.70	68.85	75.60	69.76	71.69	65.33
LDA_siti	77.92	72.80	77.27	71.87	72.03	67.18
MFLDA_mstd_sift	88.86	86.16	90.11	87.49	78.28	70.42
MFLDA_mstd_siti	87.31	84.23	90.15	87.52	77.06	69.91
MFLDA_sift_siti	82.31	78.15	81.34	76.76	73.54	64.98
MFLDA_mstd_sift_siti	91.03	88.82	92.46	90.40	80.32	71.33

BOVW = bag of visual words; LDA = latent Dirichlet allocation; MFLDA = multi-feature-fusion latent Dirichlet allocation; mstd = MeanStd spectral feature; OA = overall accuracy; PLSA = probabilistic latent semantic analysis; sift = scale-invariant feature transform structural feature; siti = gray-level co-occurrence matrix texture feature.

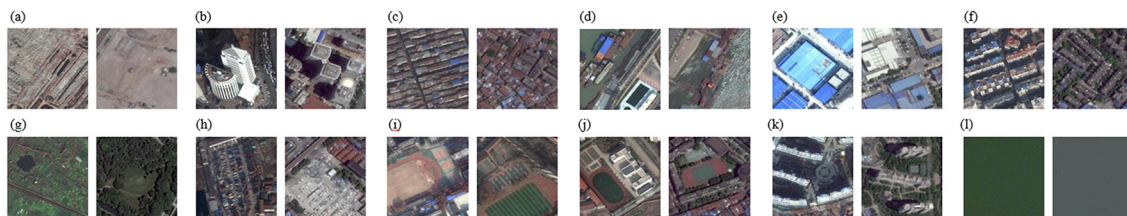


(a) 2010.06



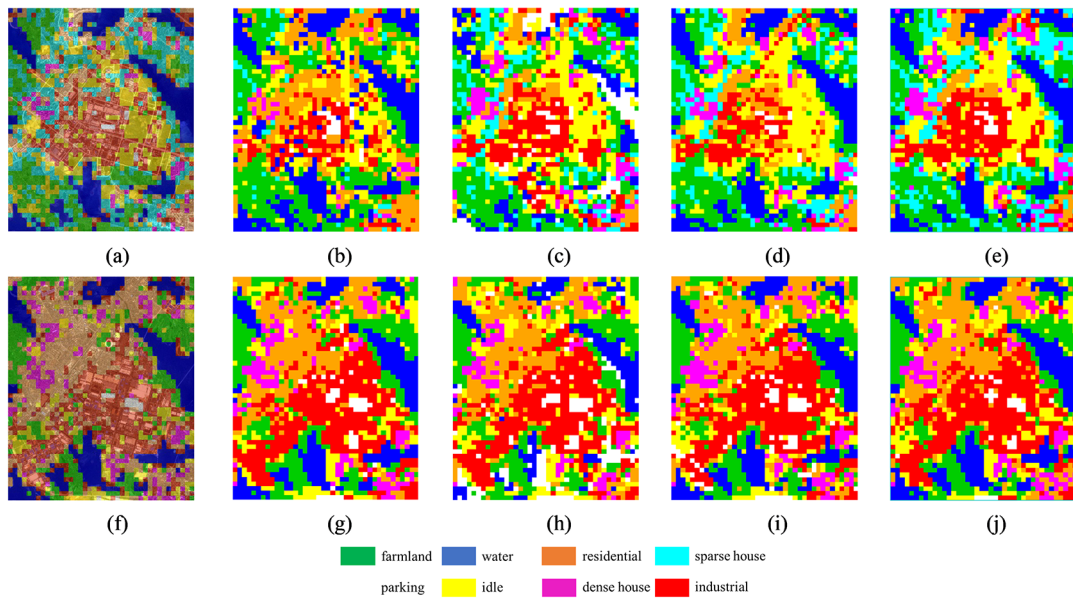
(b) 2018.06

Figure 11. Google Earth Wuhan center data set images.

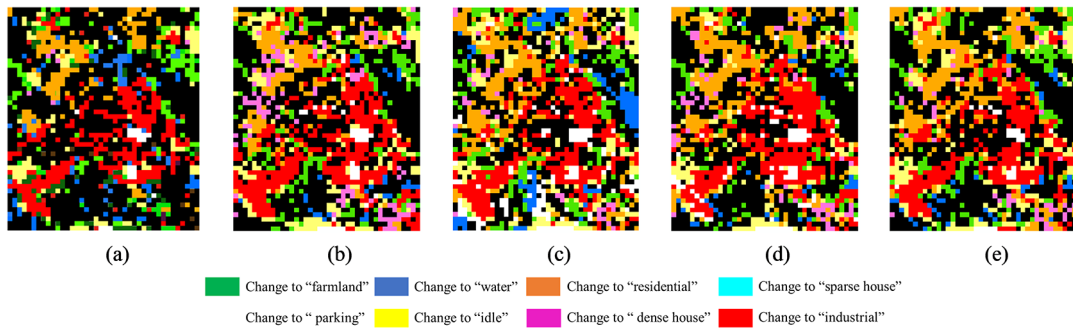


(a) bare land, (b) commercial, (c) dense residential, (d) harbor, (e) industrial, (f) medium residential, (g) greenland, (h) parking lot, (i) sports, (j) school, (k) sparse residential, (l) water.

Figure 12. Scene categories of the Google Earth Wuhan center data set.



(I) The scene classification results for the MtS-WH dataset in 2002 ((a)–(e)) and 2009 ((f)–(j)) obtained using the method of Wu *et al.* (2016), BOVW, PLSA, LDA, and MFLDA.



(II) The scene change detection results for the MtS-WH dataset obtained using the method of Wu *et al.* (2016), BOVW, PLSA, LDA, and MFLDA ((a)–(e)).

Figure 13. Classification and change-detection maps for the MtS-WH data set.

Table 2. Transition matrix for the MtS-WH data set with multi-feature-fusion latent Dirichlet allocation.

	Farmland	Water	Residential	Sparse Houses	Parking	Idle	Dense Houses	Industrial
Farmland	155	23	4	91	0	36	4	11
Water	30	272	0	8	2	1	0	4
Residential	29	13	86	68	1	70	29	79
Parking	6	1	0	4	5	12	0	5
Idle	74	9	9	66	1	68	13	16
Dense Houses	3	0	12	23	0	4	82	6
Industrial	74	1	21	57	13	145	3	171

Table 1 provides the quantitative comparison of the classification and change-detection results for the method of Wu *et al.* (2016), the single-feature-based BOVW, PLSA, LDA, and the proposed MFLDA. A visual comparison is displayed in Figure 13.

The specific performances of the different features obtained through the single-feature-based BOVW model and topic model were first compared. As can be seen in the quantitative results, the MeanStd spectral feature performs the best in the single-feature-based BOVW and LDA models, and the SIFT structural feature performs the best in the single-feature-based PLSA model. In view of this, the multi-feature-fusion strategy is aimed at attempting to realize the complementary advantages of the different features and realize full extraction

of the scene information. From the perspective of the multi-feature-fusion strategy, the multi-feature BOVW framework proposed by Wu *et al.* (2016) and the proposed MFLDA method are the representative methods that were compared with the single-feature strategy. The multi-feature-fusion BOVW model obtains overall accuracies of 85.65% and 84.03% for the 2002 and 2009 images, respectively, which is better than the optimal accuracy of the single-feature BOVW model, confirming the effectiveness of multi-feature fusion. The proposed MFLDA model also performs better than the single-feature LDA method and the other feature-fusion strategies, with overall accuracies of 91.03% and 92.46% for scene classification in 2002 and 2009, respectively, and 80.32% for scene-change

detection. It also shows an accuracy advantage over the existing multi-feature BOVW method. This verifies the effectiveness of the proposed method. Since the post-classification method for scene-change detection is dependent on the classification result, error in the classification results will accumulate in the change detection. As we evaluated the overall accuracy and kappa of the multi-class scene-change detection, the accumulation of errors between categories had a significant impact on the accuracy of the change-detection results. Therefore, the change-detection overall accuracy of 80.32% is explainable and acceptable.

At the same time, from the visualization results of each method with the best accuracy (Figure 13), it can be seen that the classification results of the MFLDA method contain less noise in each scene category, and the scene boundaries of each category are clearer than with the other methods. In addition, the change-detection result based on the scene classification is also similar to the ground-truth map.

In order to express the specific scene changes in the study area in more detail, the transition matrix for the MtS-WH data set is provided in Table 2. The main scene types for the Hanyang District of Wuhan are farmland, water, and industrial.

Table 3. Time-cost comparison for the MtS-WH data set.

Method	2002 (s)	2009 (s)
Wu et al. (2016)	—	—
BOVW_mstd	189.2	174.3
BOVW_sift	290.1	280.7
BOVW_siti	120.2	120.4
PLSA_mstd	255.8	226.9
PLSA_sift	866.0	863.2
PLSA_siti	890.5	780.2
LDA_mstd	549.6	430.9
LDA_sift	903.6	800.9
LDA_siti	867.2	793.9
MFLDA_mstd_sift	824.1	722.8
MFLDA_mstd_siti	805.2	712.1
MFLDA_sift_siti	810.1	718.0
MFLDA_mstd_sift_siti	891.5	787.2

BOVW = bag of visual words; LDA = latent Dirichlet allocation; MFLDA = multi-feature-fusion latent Dirichlet allocation; mstd = MeanStd spectral feature; PLSA = probabilistic latent semantic analysis; sift = scale-invariant feature transform structural feature; siti = gray-level co-occurrence matrix texture feature.

During the study period from 2002 to 2009, the scene category of sparse houses disappeared and was mainly converted to farmland. Other scene changes focused on the conversion from idle and farmland to industrial, and from farmland to water and residential. The Hanyang District is a typical industrial zone in Wuhan, and thus the obtained scene-change information is consistent with reality. The conclusion also conforms to existing findings in urban research, that building is one of the fastest-changing land use type in cities (Shao *et al.* 2020).

Finally, the computational efficiency of the HSR image processing is important. Therefore, the calculation cost of the proposed MFLDA model and those of the other methods are compared in Table 3. It can be seen that the single-feature-based BOVW method costs the least computation time, and MFLDA costs the most. Since the LDA model achieves dimensionality reduction through topic features in the processing, it naturally takes more time than the BOVW model. In addition, for the multi-feature-fusion strategies, as the number of features in the fusion increases, the computational efficiency decreases. However, it can be seen that the feature-fusion

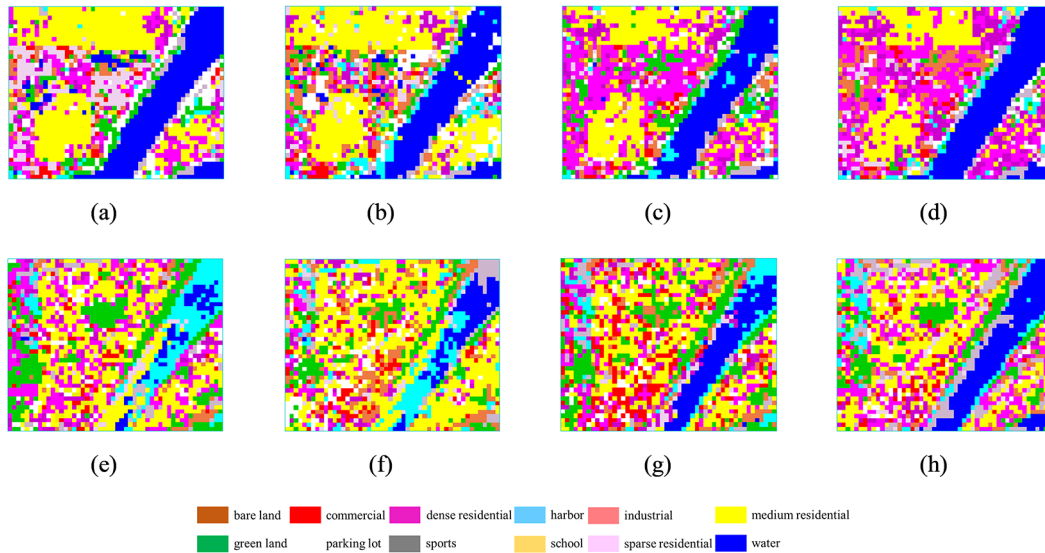
Table 4. Quantitative evaluation of the classification and change-detection results for the Google Earth Wuhan center data set.

Method	2010		2018		Change Map	
	OA (%)	kappa (%)	OA (%)	kappa (%)	OA (%)	kappa (%)
BOVW_mstd	73.92	65.86	79.68	72.06	62.68	51.22
BOVW_sift	76.57	69.31	75.73	66.91	65.78	58.61
BOVW_siti	73.63	65.67	72.63	63.23	64.25	56.68
PLSA_mstd	68.98	58.69	74.69	65.89	59.57	52.31
PLSA_sift	64.33	54.99	75.13	67.45	57.16	46.69
PLSA_siti	62.06	51.84	69.34	58.87	54.59	41.46
LDA_mstd	78.78	71.97	80.65	73.41	69.39	62.94
LDA_sift	74.47	66.57	75.17	67.47	65.58	54.28
LDA_siti	70.17	61.38	68.46	57.90	60.38	52.96
MFLDA_mstd_sift	79.37	72.38	81.31	74.40	71.59	65.40
MFLDA_mstd_siti	78.55	71.84	80.26	72.98	70.03	63.82
MFLDA_sift_siti	78.43	71.55	80.92	73.60	71.23	64.68
MFLDA_mstd_sift_siti	80.18	73.73	81.84	74.74	72.70	66.85

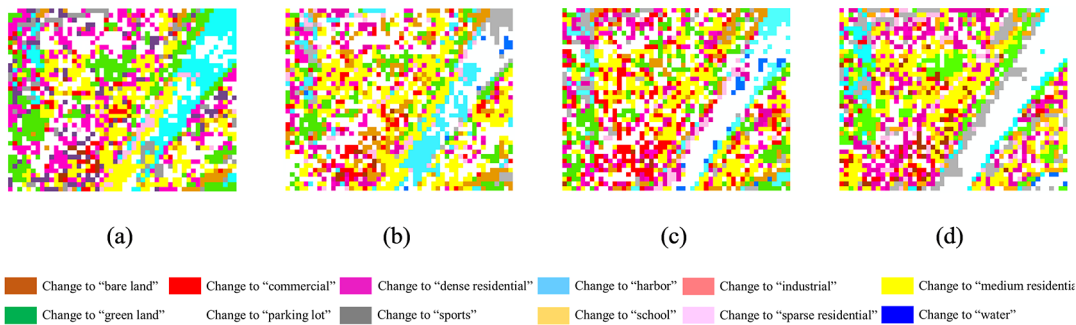
BOVW = bag of visual words; LDA = latent Dirichlet allocation; MFLDA = multi-feature-fusion latent Dirichlet allocation; mstd = MeanStd spectral feature; OA = overall accuracy; PLSA = probabilistic latent semantic analysis; sift = scale-invariant feature transform structural feature; siti = gray-level co-occurrence matrix texture feature.

Table 5. Transition matrix for the Google Earth Wuhan center data set with multi-feature-fusion latent Dirichlet allocation.

	Dense Residential		Green Land		Parking Lot		Sparse Residential		Medium Residential		Bare Land		Water
Sports	8	19	2	4	15	37	3	3	0	26	7	66	
Dense residential	8	95	0	6	12	6	10	19	3	95	27	0	
School	0	0	1	0	0	0	0	1	1	1	0	0	
Green land	27	50	0	18	5	15	30	6	0	19	39	3	
Harbor	6	12	0	4	7	9	4	5	1	6	16	32	
Industrial	2	9	4	1	2	11	2	4	11	13	5	0	
Parking lot	1	14	0	1	3	4	1	5	6	26	4	0	
Sparse residential	1	15	0	0	1	16	1	5	1	29	7	1	
Commercial	2	19	1	1	2	12	3	2	8	8	5	2	
Medium residential	6	194	0	4	6	77	5	35	8	108	27	-	
Bare land	9	15	1	7	12	24	10	1	2	36	8	4	
Water	3	0	0	0	0	0	2	0	0	0	0	282	



(I) The scene classification results for the Google Earth Wuhan center dataset in 2010 ((a)–(d)) and 2018 ((e)–(h)) obtained using the methods of BOVW, PLSA, LDA, and MFLDA.



(II) The scene change detection results for the Google Earth Wuhan center obtained using the methods of BOVW, PLSA, LDA, and MFLDA.

Figure 14. Classification and change-detection maps for the Google Earth Wuhan center data set.

strategy of the 1D histogram used in MFLDA makes its processing time less than that of the single-feature-based LDA model in some cases. Therefore, it can be concluded that although the proposed MFLDA process is not the fastest, it is acceptable to take time, considering the accuracy of the results.

Experiment 2: The Google Earth Wuhan Center Data Set

Table 4 presents the quantitative comparison of the single-feature-based BOVW, PLSA, LDA, and the proposed MFLDA model. A visual comparison is displayed in Figure 14. In this experiment, as we can see from the comparison of the single-feature-based BOVW and topic model results, the different feature-extraction methods have different optimal expressions in both model and data diversity. At the same time, the MFLDA method again achieves the best performance at both scene classification and change detection.

The transition matrix for the data set is provided in Table 5. The main scene types for the center area of Wuhan are medium residential, dense residential, and water. During the study period from 2010 to 2018, the main scene change was conversion from dense residential to medium residential and commercial. The planned land in the center area of Wuhan is mainly residential and commercial, and with the continuous development of the city, these main land types in the main urban area will likely be constantly converted.

Table 6. Time-cost comparison for the Google Earth Wuhan center data set.

Method	2010 (s)	2018 (s)
BOVW_mstd	230.6	257.9
BOVW_sift	310.1	305.4
BOVW_siti	205.3	200.8
PLSA_mstd	558.3	557.2
PLSA_sift	1335.0	1276.0
PLSA_siti	938.1	945.9
LDA_mstd	1733.8	1623.8
LDA_sift	4095.6	4119.2
LDA_siti	3056.9	3093.4
MFLDA_mstd_sift	3760.8	3592.5
MFLDA_mstd_siti	1723.8	1720.5
MFLDA_sift_siti	3804.1	3624.7
MFLDA_mstd_sift_siti	2979.2	2919.8

BOVW = bag of visual words; LDA = latent Dirichlet allocation; MFLDA = multi-feature-fusion latent Dirichlet allocation; mstd = MeanStd spectral feature; PLSA = probabilistic latent semantic analysis; sift = scale-invariant feature transform structural feature; siti = gray-level co-occurrence matrix texture feature.

The calculation costs for the data set are summarized in Table 6. The BOVW method again takes the shortest time. For PLSA, LDA, and MFLDA, some of the feature-fusion strategies in the MFLDA comparison take less time than in PLSA and LDA. Thus, in this experiment, MFLDA obtains a better balance between time cost and accuracy.

Sensitivity Analysis for the MFLDA Method

To analyze the sensitivity of the MFLDA scene-classification method to the topic number, we obtained the classification accuracy curves for PLSA, LDA, and MFLDA with the best feature-extraction method for the two data sets by changing the number of topics K (Figures 15 and 16). As the number of topics increases, the classification accuracy curve of MFLDA does not greatly fluctuate, which indicates that the scene classification of MFLDA has a certain robustness. MFLDA generates topic spaces for features with different distributions. The topic features generated through this process have probabilistic meaning and can better realize feature fusion. Therefore, compared with the other multi-feature-fusion methods, the types of features that can be used in MFLDA are not limited to local/global or discrete/continuous, thereby achieving superior classification.

Conclusions

In this article, a scene-change detection method based on the multi-feature-fusion latent Dirichlet allocation model has been proposed. This method extracts the spectral, textural, and spatial features of multi-temporal scene images and represents them as 1D histograms. The topic features of the scene are then obtained based on multi-feature topic expression. Finally, the “from-to” change information of the scenes is acquired through post-classification comparison. This

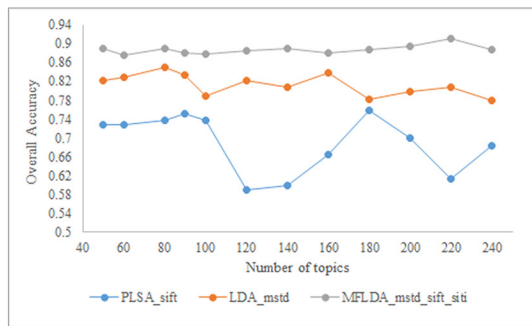
method fully utilizes the feature information of the original images and makes up for the drawbacks of the existing single-feature-based methods and the topic-model-based methods of scene-change detection. The method of automatically extracting deep features via deep learning is advantageous for scene classification and scene-change detection. Therefore, in our future work we will further extend our research to consider deep learning, while combining scene-level and pixel-level change detection, to build a pixel-parcel-scene multi-level change-detection framework and further improve scene-change detection performance. Additionally, the scene changes of urban green land can be detected with a combination of HSR imagery and lidar (Zhang and Shao 2021), and the accuracy of urban scene-change detection can be further improved to a certain extent.

Acknowledgments

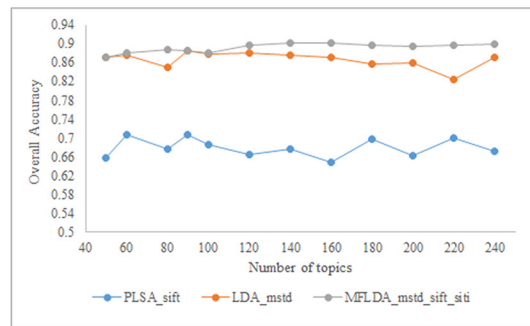
This work was supported by National Natural Science Foundation of China under grants 41771385 and 42071350.

References

- Atasever, U. H., M. H. Kesikoglu and C. Ozkan. 2016. A new artificial intelligence optimization method for PCA based unsupervised change detection of remote sensing image data. *Neural Network World* 26(2):141–154.
- Bahmanyar, R., D. Espinoza-Molina and M. Datcu. 2018. Multisensor earth observation image classification based on a multimodal latent Dirichlet allocation model. *IEEE Geoscience and Remote Sensing Letters* 15(3):459–463.
- Blei, D. M. 2012. Probabilistic topic models. *Communications of the ACM* 55(4):77–84.

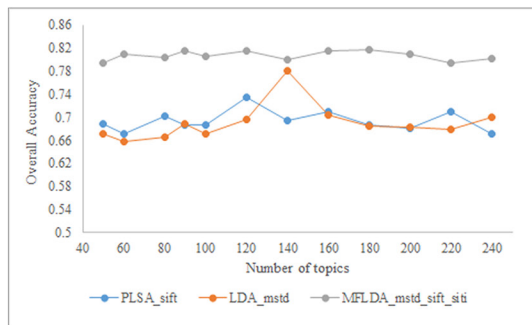


(a) 2002.02

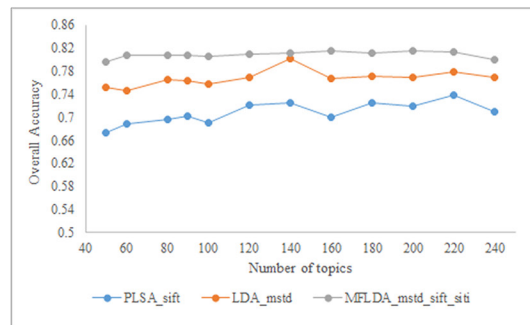


(b) 2009.06

Figure 15. Accuracy curves for scene classification versus number of topics for the MtS-WH data set.



(a) 2010.06



(b) 2018.06

Figure 16. Accuracy curves for scene classification versus number of topics for the Google Earth Wuhan center data set.

- Blei, D. M., A. Y. Ng and M. I. Jordan. 2003. Latent Dirichlet allocation. *Journal of Machine Learning Research* 3:993–1022.
- Bratananu, D., I. Nedelcu and M. Datcu. 2011. Bridging the semantic gap for satellite image annotation and automatic mapping applications. *IEEE Journal of Selected Topics in Applied Earth Observations and Remote Sensing* 4(1):193–204.
- Bulatov, D., G. Häufel, L. Lucks and M. Pohl. 2019. Land cover classification in combined elevation and optical images supported by OSM data, mixed-level features, and non-local optimization algorithms. *Photogrammetric Engineering and Remote Sensing* 85(3):179–195.
- Chang, C.-C. and C.-J. Lin. 2011. LIBSVM: A library for support vector machines. *ACM Transactions on Intelligent Systems and Technology* 2(3):27.
- Cheng, G., L. Guo, T. Zhao, J. Han, H. Li and J. Fang. 2013. Automatic landslide detection from remote-sensing imagery using a scene classification method based on BoVW and pLSA. *International Journal of Remote Sensing* 34(1):45–59.
- Cheng, G., C. Yang, X. Yao, L. Guo and J. Han. 2018. When deep learning meets metric learning: Remote sensing image scene classification via learning discriminative CNNs. *IEEE Transactions on Geoscience and Remote Sensing* 56(5):2811–2821.
- Du, B., Y. Wang, C. Wu and L. Zhang. 2018. Unsupervised scene change detection via latent Dirichlet allocation and multivariate alteration detection. *IEEE Journal of Selected Topics in Applied Earth Observations and Remote Sensing* 11(12):4676–4689.
- Hofmann, T. 2001. Unsupervised learning by probabilistic latent semantic analysis. *Machine Learning* 42(1–2):177–196.
- Li, E., J. Xia, P. Du, C. Lin and A. Samat. 2017. Integrating multilayer features of convolutional neural networks for remote sensing scene classification. *IEEE Transactions on Geoscience and Remote Sensing* 55(10):5653–5665.
- Li, L., S. Jiang and Q. Huang. 2012. Learning hierarchical semantic description via mixed-norm regularization for image understanding. *IEEE Transactions on Multimedia* 14(5):1401–1413.
- Li, Q., X. Huang, D. Wen and H. Liu. 2017. Integrating multiple textural features for remote sensing image change detection. *Photogrammetric Engineering and Remote Sensing* 82(2):109–121.
- Lienou, M., H. Maitre and M. Datcu. 2010. Semantic annotation of satellite images using latent Dirichlet allocation. *IEEE Geoscience and Remote Sensing Letters* 7(1):28–32.
- Liu, S., G. Tian and Y. Xu. 2019. A novel scene classification model combining ResNet based transfer learning and data augmentation with a filter. *Neurocomputing* 338:191–206.
- Lu, P., Y. Qin, Z. Li, A. C. Mondini and N. Casagli. 2019. Landslide mapping from multi-sensor data through improved change detection-based Markov random field. *Remote Sensing of Environment* 231:111235.
- Lu, X., W. Ji, X. Li and X. Zheng. 2019. Bidirectional adaptive feature fusion for remote sensing scene classification. *Neurocomputing* 328:135–146.
- Ni, K. and Y. Wu. 2020. Scene classification from remote sensing images using mid-level deep feature learning. *International Journal of Remote Sensing* 41(4):1415–1436.
- Nielsen, A. A. 2007. The regularized iteratively reweighted MAD method for change detection in multi- and hyperspectral data. *IEEE Transactions on Image Processing* 16(2):463–478.
- Pang, Y., Y. Li, J. Shen and L. Shao. 2019. Towards bridging semantic gap to improve semantic segmentation. Pages 4230–4239 in *2019 IEEE/CVF International Conference on Computer Vision (ICCV)*, held in Seoul, South Korea, 27 October–2 November 2019. Edited by J. Editor. City, ST: IEEE.
- Polykretis, C., M. G. Grillakis and D. D. Alexakis. 2020. Exploring the impact of various spectral indices on land cover change detection using change vector analysis: A case study of Crete island, Greece. *Remote Sensing* 12(2):319.
- Sedaghat, A. and H. Ebadi. 2015. Remote sensing image matching based on adaptive binning SIFT descriptor. *IEEE Transactions on Geoscience and Remote Sensing* 53(10):5283–5293.
- Shao, Z., N. S. Sumari, A. Portnov, F. Ujoh, W. Musakwa and P. J. Mandela. 2020b. Urban sprawl and its impact on sustainable urban development: A combination of remote sensing and social media data. *Geo-spatial Information Science*. <https://doi.org/10.1080/10095020.2020.1787800>.
- Shao, Z., P. Tang, Z. Wang, N. Saleem, S. Yam and C. Sommai. 2020a. BRNNet: A fully convolutional neural network for automatic building extraction from high-resolution remote sensing images. *Remote Sensing* 12(6):1050.
- Sivic, J. and A. Zisserman. 2003. Video Google: A text retrieval approach to object matching in videos. Pages 1470–1477 in *Proceedings Ninth IEEE International Conference on Computer Vision*, held in Nice, France, 13–16 October 2003. Edited by J. Editor. City, ST: IEEE.
- Sun, H., S. Li, X. Zheng and X. Lu. 2020. Remote sensing scene classification by gated bidirectional network. *IEEE Transactions on Geoscience and Remote Sensing* 58(1):82–96.
- Sun, J., X. Cai, F. Sun and J. Zhang. 2016. Scene image classification method based on Alex-Net model. Pages 363–367 in *2016 3rd International Conference on Informative and Cybernetics for Computational Social Systems (ICCSS)*, held in Jinzhou, China, 26–29 August 2016. Edited by J. Editor. City, ST: IEEE.
- V duva, C., I. Gav t and M. Datcu. 2013. Latent Dirichlet allocation for spatial analysis of satellite images. *IEEE Transactions on Geoscience and Remote Sensing* 51(5):2770–2786.
- Wan, H., Y. Shao, J. B. Campbell and X. Deng. 2019. Mapping annual urban change using time series Landsat and NLCD. *Photogrammetric Engineering and Remote Sensing* 85(10):715–724.
- Wu, C., L. Zhang and B. Du. 2017. Kernel slow feature analysis for scene change detection. *IEEE Transactions on Geoscience and Remote Sensing* 55(4):2367–2384.
- Wu, C., L. Zhang and L. Zhang. 2016. A scene change detection framework for multi-temporal very high resolution remote sensing images. *Signal Processing* 124:184–197.
- Zang, M., D. Wen, K. Wang, T. Liu and W. Song. 2015. A novel topic feature for image scene classification. *Neurocomputing* 148:467–476.
- Zhang, Y. and Z. Shao. 2021. Assessing of urban vegetation biomass in combination with LiDAR and high-resolution remote sensing images. *International Journal of Remote Sensing* 42(3):964–985.
- Zhao, B., Y. Zhong, G.-S. Xia and L. Zhang. 2016a. Dirichlet-derived multiple topic scene classification model for high spatial resolution remote sensing imagery. *IEEE Transactions on Geoscience and Remote Sensing* 54(4):2108–2123.
- Zhao, B., Y. Zhong and L. Zhang. 2016b. A spectral-structural bag-of-features scene classifier for very high spatial resolution remote sensing imagery. *ISPRS Journal of Photogrammetry and Remote Sensing* 116:73–85.
- Zheng, G., X. Li, L. Zhou, J. Yang, L. Ren, P. Chen, H. Zhang and X. Lou. 2018. Development of a gray-level co-occurrence matrix-based texture orientation estimation method and its application in sea surface wind direction retrieval from SAR imagery. *IEEE Transactions on Geoscience and Remote Sensing* 56(9):5244–5260.
- Zhong, Y., R. Huang, J. Zhao, B. Zhao and T. Liu. 2018. Aurora image classification based on multi-feature latent Dirichlet allocation. *Remote Sensing* 10(2):233.
- Zhong, Y., S. Wu and B. Zhao. 2017. Scene semantic understanding based on the spatial context relations of multiple objects. *Remote Sensing* 9(10):1030.
- Zhu, J., Y. Su, Q. Guo and T. C. Harmon. 2017. Unsupervised object-based differencing for land-cover change detection. *Photogrammetric Engineering and Remote Sensing* 83(3):225–236.
- Zhu, Q., Y. Zhong, B. Zhao, G.-S. Xia and L. Zhang. 2016. Bag-of-visual-words scene classifier with local and global features for high spatial resolution remote sensing imagery. *IEEE Geoscience and Remote Sensing Letters* 13(6):747–751.

IN-PRESS ARTICLES

- Lisa M. LaForest, Tian Zhou, Seyyed Meghdad Hasheminasab, and Ayman Habib. System Calibration Including Time Delay Estimation for GNSS/INS-Assisted Push-Broom Scanners Onboard UAV Platforms.
- He Yanjun, Xu Jun, Li Jiansong, Peng Hao, Wu Bin. Information Extraction from High-resolution Remote Sensing Images Based on Multi-scale Segmentation and Case-based Reasoning.
- Radhika Ravi, Ayman Habib. Least Squares Adjustment with a Rank-deficient Weight Matrix and its Applicability towards Image/LiDAR Data Processing.
- Saket Gowravaram, Haiyang Chao, Andrew Molthan, Tiebiao Zhao, Pengzhi Tian, Harold Flanagan, Lori Schultz, and Jordan Bell. Spectral Reflectance Estimation of UAS Multispectral Imagery Using Satellite Cross-Calibration Method.
- Toshihiro Sakamoto. Early Classification Method for US Corn and Soybean by Incorporating MODIS-Estimated Phenological Data and Historical Classification Maps in Random-Forest Regression Algorithm.
- Mehdi Khoshboresh-Masouleh and Reza Shah-Hosseini. A Deep Multi-Modal Learning Method and a New RGB-Depth Data Set for Building Roof Extraction.
- Weining Zhu, Zeliang Zhang, Zaiqiao Yang, Shuna Pang, Jiang Chen, Qian Cheng. Spectral Probability Distribution of Closed Connected Water and Remote Sensing Statistical Inference for Yellow Substance.
- Abdullah Kayı, Bülent Bayram, and Dursun Zafer Şeker. The Analysis on the Annual Change of Digital Aerial Camera's IMUs Boresight Misalignment.
- Huan Xie, Binbin Li, Shijie Liu, Xiaohua Tong, Hong Tang, Xu Wang. A Method of Extracting High-accuracy Elevation Control Points from ICESat-2 Altimetry Data.
- Forrest Corcoran, Christopher Parrish. Diffuse Attenuation Coefficient (Kd) from ICESat-2 ATLAS Spaceborne Lidar Using Random Forest Regression.
- Samia Boukir, Li Guo, Nesrine Chehata. Improving remote sensing multiple classification by data and ensemble selection.
- Hari Shankar, Arijit Roy, Prakash Chauhan. Persistent Scatterer Interferometry for Pettimudi (India) Landslide Monitoring using Sentinel-1A Images.
- Ying Dong, Bo Yu, Fang Chen, Lei Wang, Ning Wang, Aqiang Yang. MSegnet, a practical network for building detection from high spatial resolution images.
- Lei Yan, Feizhou Zhang, Xufang Liu, Yun Xiang, Zihan Zhang, Siyuan Liu. Estimation of rock characteristics based on polarization spectra: surface roughness, composition and density.
- Ningning Zhu, Bisheng Yang, Zhen Dong, Chi Chen, Xia Huang, Wen Xiao. Automatic Registration of MMS LiDAR Points and Panoramic Image Sequence by Relative Orientation Model.
- Zhenfeng Shao, Qing Ding, Xiao Huang, Orhan Altan, Yewen Fan. Improving Urban Land Cover Mapping with the Fusion of Optical and SAR Data Based on Feature Selection Strategy.
- Clement Akumu, Eze Amadi. Examining the Integration of Landsat Operational Land Imager (OLI) with Sentinel-1 and Vegetation Indices in Mapping Southern Yellow Pines (Loblolly, Shortleaf and Virginia Pines).
- Steven Martinez Vargas, Claudio Delrieux, Katy Lorena Blanco, Alejandro Vitale. Dense Bathymetry in Turbid Coastal Zones using Airborne Hyperspectral.
- Qunming Wang, Xinyu Ding. Augmented Samples-based Real-time Spatio-temporal Spectral Unmixing.

WHO'S WHO IN ASPRS

BOARD OF DIRECTORS

BOARD OFFICERS

President

Jason M. Stoker, Ph.D.
U.S. Geological Survey

President-Elect

Christopher Parrish, Ph.D.
Oregon State University

Vice President

Lorraine B. Amenda, PLS, CP
Towill, Inc.

Past President

Jeff Lovin
Woolpert

Treasurer

Stewart Walker, Ph.D.
photogrammetry4u

Secretary

Harold Rempel
ESP Associates, Inc.

BOARD MEMBERS

Sustaining Members Council

Chair: Joe Cantz
<https://www.asprs.org/sustaining-members-council.html>

Technical Division Directors Council

Chair: Bandana Kar, Ph.D.
Vice Chair: Denise G. Theunissen

Committee Chairs Council

Chair: Mike Zoltek

Early-Career Professionals Council

Chair: Melissa Martin

Region Officers Council

Chair: Demetrio Zourarakis
Vice Chair: Jason Krueger

Student Advisory Council

Chair: Evan Vega
Vice Chair: Lauren McKinney
<http://www.asprs.org/Students/Student-Advisory-Council.html>

TECHNICAL DIVISION OFFICERS

Geographic Information Systems Division

Director: Denise Theunissen
Assistant Director: Briana Williams
www.asprs.org/Divisions/GIS-Division.html

Lidar Division

Director: Josh Nimetz, CMS
Assistant Director: Ajit Sampath
www.asprs.org/Divisions/Lidar-Division.html

Photogrammetric Applications Division

Director: Kurt Rogers
Assistant Director: Benjamin Wilkinson
www.asprs.org/Divisions/Photogrammetric-Applications-Division.html

Primary Data Acquisition Division

Director: Greg Stensaas
Assistant Director: Srinu Dharmapuri
www.asprs.org/Divisions/Primary-Data-Acquisition-Division.html

Professional Practice Division

Director: Bill Swope
Assistant Director: Hope Morgan
www.asprs.org/Divisions/Professional-Practice-Division.html

Remote Sensing Applications Division

Director: Amr Abd-Ehrahman
Assistant Director: Tao Liu
www.asprs.org/Divisions/Remote-Sensing-Applications-Division.html

Unmanned Autonomous Systems (UAS)

Director: Dan Hubert
Assistant Director: Jacob Lopez
<https://www.asprs.org/divisions-committees/uas-division>

REGION PRESIDENTS

Alaska Region

Cascadia Region

Robert Hariston-Porter

Eastern Great Lakes Region

Michael Joos, CP, GISP
<http://egl.asprs.org>

Florida Region

Xan Fredericks
<http://florida.asprs.org>

Heartland Region

Whit Lynn
<http://heartland.asprs.org/>

Intermountain Region

Robert T. Pack
<https://asprsintermountain.weebly.com>

Mid-South Region

David Hughes
<https://www.asprs.org/all-regions/mid-south.html>

Northeast Region

North Atlantic Region

<http://natlantic.asprs.org>

Pacific Southwest Region

John Erickson, PLS, CP
<https://pswasprs.org>

Potomac Region

Dave Lasko
<http://www.asprspotomac.org>

Rocky Mountain Region

<http://www.asprs-rmr.org/>

Western Great Lakes Region

Adam Smith
<http://wgl.asprs.org/>

SUSTAINING MEMBERS

ACI USA Inc.

Weston, Florida
<https://acicorporation.com/>
 Member Since: 2/2018

Aerial Services, Inc.

Cedar Falls, Iowa
www.AerialServicesInc.com
 Member Since: 5/2001

Ayres Associates

Madison, Wisconsin
www.AyresAssociates.com
 Member Since: 1/1953

Dewberry

Fairfax, Virginia
www.dewberry.com
 Member Since: 1/1985

Environmental Research Incorporated

Linden, Virginia
www.eri.us.com
 Member Since: 8/2008

Esri

Redlands, California
www.esri.com
 Member Since: 1/1987

F.R. Aleman & Associates, Inc.

Miami, Florida
<https://fr-aleman.com>
 Member Since: 7/2020

GeoCue Group

Madison, Alabama
<http://www.geocue.com>
 Member Since: 10/2003

Geographic Imperatives LLC

Centennial, Colorado
<http://geographicimperativesllc.com>
 Member Since: 9/2021

GeoWing Mapping, Inc.

Richmond, California
www.geowingmapping.com
 Member Since: 12/2016

GPI Geospatial Inc.

formerly Aerial Cartographics of America, Inc. (ACA)
 Orlando, Florida
www.aca-net.com
 Member Since: 10/1994

Green Grid Inc.

San Ramon, California
www.greengridinc.com
 Member Since: 1/2020

Half Associates, Inc.

Richardson, Texas
www.half.com
 Member Since: 8/2021

Keystone Aerial Surveys, Inc.

Philadelphia, Pennsylvania
www.kasurveys.com
 Member Since: 1/1985

Kucera International

Willoughby, Ohio
www.kucerainternational.com
 Member Since: 1/1992

L3Harris Corporation

Broomfield, Colorado
www.harris.com
 Member Since: 6/2008

NV5 Geospatial

Sheboygan Falls, Wisconsin
www.quantumspatial.com
 Member Since: 1/1974

Pickett and Associates, Inc.

Bartow, Florida
www.pickettusa.com
 Member Since: 4/2007

Robinson Aerial Surveys, Inc.(RAS)

Hackettstown, New Jersey
www.robinsonaerial.com
 Member Since: 1/1954

Sanborn Map Company

Colorado Springs, Colorado
www.sanborn.com
 Member Since: 10/1984

Scorpius Imagery Inc.

Newark, Delaware
aerial@scorpiusimagery.com
 Member Since: 6/2021

Surdex Corporation

Chesterfield, Missouri
www.surdex.com
 Member Since: 12/2011

Surveying And Mapping, LLC (SAM)

Austin, Texas
www.sam.biz
 Member Since: 12/2005

T3 Global Strategies, Inc.

Bridgeville, Pennsylvania
<https://t3gs.com/>
 Member Since: 6/2020

Terra Remote Sensing (USA) Inc.

Bellevue, Washington
www.terraremote.com
 Member Since: 11/2016

Towill, Inc.

San Francisco, California
www.towill.com
 Member Since: 1/1952

Wingtra

Zurich, Switzerland
<https://wingtra.com/>
 Member Since: 6/2020

Woolpert LLP

Dayton, Ohio
www.woolpert.com
 Member Since: 1/1985

SUSTAINING MEMBER BENEFITS

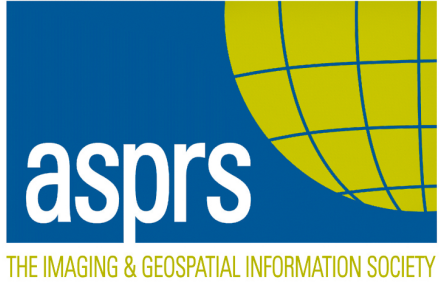
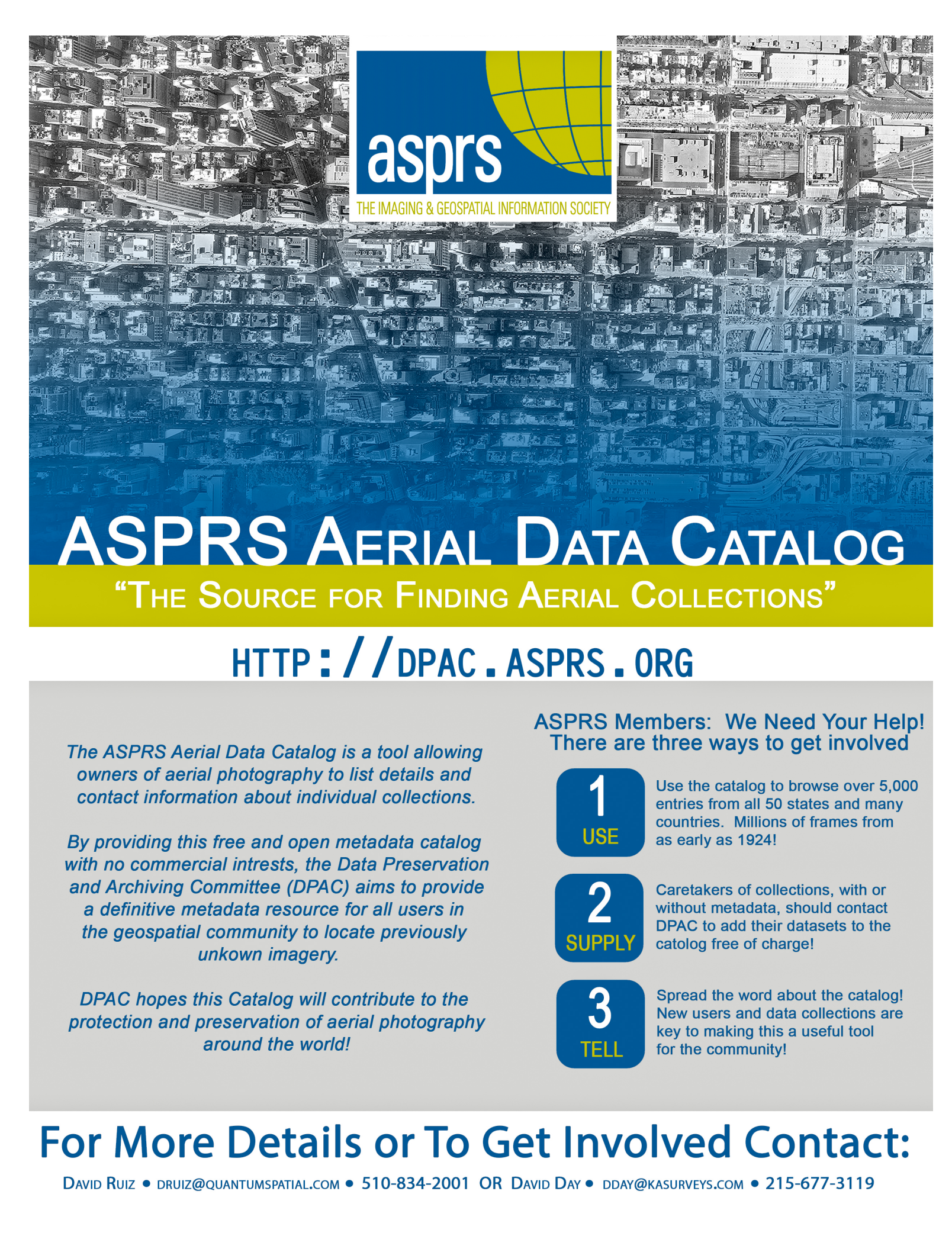
Membership

- ✓ Provides a means for dissemination of new information
- ✓ Encourages an exchange of ideas and communication
- ✓ Offers prime exposure for companies

Benefits of an ASPRS Membership

- Complimentary and discounted Employee Membership*
- E-mail blast to full ASPRS membership*
- Professional Certification Application fee discount for any employee
- Member price for ASPRS publications
- Discount on group registration to ASPRS virtual conferences
- Sustaining Member company listing in ASPRS directory/website
- Hot link to company website from Sustaining Member company listing page on ASPRS website
- Press Release Priority Listing in *PE&RS* Industry News
- Priority publishing of Highlight Articles in *PE&RS* plus, 20% discount off cover fee
- Discount on *PE&RS* advertising
- Exhibit discounts at ASPRS sponsored conferences (exception ASPRS/ILMF)
- Free training webinar registrations per year*
- Discount on additional training webinar registrations for employees
- Discount for each new SMC member brought on board (Discount for first year only)

*quantity depends on membership level



asprs

THE IMAGING & GEOSPATIAL INFORMATION SOCIETY

ASPRS AERIAL DATA CATALOG

“THE SOURCE FOR FINDING AERIAL COLLECTIONS”

[HTTP://DPAC.ASPRS.ORG](http://dpac.asprs.org)

The ASPRS Aerial Data Catalog is a tool allowing owners of aerial photography to list details and contact information about individual collections.

By providing this free and open metadata catalog with no commercial interests, the Data Preservation and Archiving Committee (DPAC) aims to provide a definitive metadata resource for all users in the geospatial community to locate previously unknown imagery.

DPAC hopes this Catalog will contribute to the protection and preservation of aerial photography around the world!

ASPRS Members: We Need Your Help!
There are three ways to get involved

1

USE

Use the catalog to browse over 5,000 entries from all 50 states and many countries. Millions of frames from as early as 1924!

2

SUPPLY

Caretakers of collections, with or without metadata, should contact DPAC to add their datasets to the catalog free of charge!

3

TELL

Spread the word about the catalog! New users and data collections are key to making this a useful tool for the community!

For More Details or To Get Involved Contact:

DAVID RUIZ • DRUIZ@QUANTUMSPATIAL.COM • 510-834-2001 OR DAVID DAY • DDAY@KASURVEYS.COM • 215-677-3119

LEARN
DO
GIVE
BELONG

ASPRS Offers

- » Cutting-edge conference programs
- » Professional development workshops
- » Accredited professional certifications
- » Scholarships and awards
- » Career advancing mentoring programs
- » *PE&RS*, the scientific journal of ASPRS

asprs.org

ASPRS